Investigations on the Evolution of Zn Dust into ZnO Nanostructures, Electroceramics and Polymer Matrix Composite Dielectrics

Thesis Submitted to
Cochin University of Science and Technology (CUSAT)
in Partial Fulfilment of the Requirements for the Degree of
DOCTOR OF PHILOSOPHY IN PHYSICS
Under the Faculty of Science

By
JEEN MARIA MATHEWS
(Reg. No. 4568)

Under the Guidance of
Dr. S. Ananthakumar

Functional Materials Section
Materials Science and Technology Division
CSIR-National Institute for Interdisciplinary Science and Technology
(CSIR-NIIST)
Thiruvananthapuram, Kerala, India – 695019

June 2018

Dedicated to My Beloved Family......................

DECLARATION

I, Jeen Maria Mathews, hereby declare that the work presented in the Ph. D. thesis entitled **"Investigations on the Evolution of Zn Dust into ZnO Nanostructures, Electroceramics and Polymer Matrix Composite Dielectrics"** is an independent research work carried out by me for the award of degree of Doctor of Philosophy in Physics, under the Faculty of Science, Cochin University of Science and Technology (CUSAT), under the guidance of Dr. S. Ananthakumar, Senior Principal Scientist, Functional Materials Section, Material Science and Technology Division, CSIR-National Institute of Science and Technology (CSIR-NIIST), Thiruvananthapuram. I further declare that this thesis or any part of it has not been submitted anywhere else for any other degree, diploma, or other similar title.

JEEN MARIA MATHEWS

Place: Thiruvananthapuram
Date: 12-06-2018

COUNCIL OF SCIENTIFIC AND INDUSTRIAL RESEARCH
NATIONAL INSTITUTE FOR INTERDISCIPLINARY SCIENCE AND TECHNOLOGY (CSIR-NIIST)
Industrial Estate P. O., Pappanamcode,
Thiruvananthapuram-695019, Kerala, INDIA
www.niist.res.in

Dr. S. Ananthakumar
Senior Principal Scientist
Functional Materials Section
Materials Science and Technology Division

☎ Off: 0471-2515289
Mob: 09497271547
Fax: +91-471-2491712
Email: ananthakumar70@gmail.com

CERTIFICATE

This is to certify that the work embodied in the thesis entitled, "**Investigations on the Evolution of Zn Dust into ZnO Nanostructures, Electroceramics and Polymer Matrix Composite Dielectrics"** is an authentic record of the research work carried out by **Ms Jeen Maria Mathews**, Functional Materials Section, Materials Science and Technology Division, CSIR-National Institute for Interdisciplinary Science and Technology (CSIR-NIIST), Thiruvananthapuram under my supervision in partial fulfilment of the requirement for the degree of Doctor of Philosophy in Physics, under the Faculty of Science, Cochin University of Science and Technology (CUSAT). It is further certified that no part of this thesis has been presented previously anywhere else for the award of any other degree. All the relevant corrections and modifications suggested by the audience during the pre-synopsis seminar and recommended by the Doctoral committee have been incorporated in this thesis.

Dr. S. Ananthakumar
(Research Guide)

Place: Thiruvananthapuram
Date: 12-06-2018

Acknowledgments

First and foremost, I would like to express my profound gratitude to God Almighty for giving me the strength, patience and opportunity to undertake this research study and to persevere and complete it satisfactorily.

I would like to express my sincere gratitude to all the people who have helped me in this journey of completing the thesis work. First of all, I have great pleasure to express my deep sense of gratitude to Dr. S. Ananthakumar, my research supervisor, for his guidance, constant encouragement, intellectual support, constructive criticism and above all, the freedom he gave me during the course of my research studies. I am greatly indebted to him for all the efforts he has put in for the successful completion of this thesis.

I express my sincere gratitude to our Director Dr. A. Ajayghosh for providing the excellent facilities at CSIR-NIIST. I also thank the former Director Dr. Suresh Das.

I also gratefully acknowledge Dr. P. Prabhakar Rao, Head of Material Science and Technology Division (MSTD) for the valuable suggestions and timely help. The former heads of the Division Dr. M.L.P Reddy, and Dr. M.T Sebastian are thankfully remembered for their valuable suggestions and support during the period of research.

I extend my sincere thanks to Dr. K. G. K. Warrier, Emeritus Scientist (Rtd.) Dr. U. S. Hareesh, Dr. Balagopal, Dr. S. K. Ghosh, Dr. K. G. Nishanth, and Dr. K.P Surendran from Functional Materials Section, for their support, suggestions and advices during the course of my work. I would also like to thank all the other scientists from MSTD for their help and support.

I express my sincere gratitude to my external expert from CUSAT Dr.K.P Vijayakumar, Professor (Rtd.), Department of Physics, CUSAT for his help to conduct my presynopsis presentation and all formalities in CUSAT. I would like to extend my sincere gratitude to Dr. T. P. D Rajan (Principal Scientist and DC member), for all the help and support.

I extend my special thanks to Mr. A. Peer Mohamed, Senior Technical officer for providing me the technical support and encouragement throughout the research period.

I am also immensely thankful to Mr. Kiran Mohan and Mr. Robert Philip for the TEM analysis, Mr. M. R. Chandran (Rtd.), Mrs. Lucy Pau (Rtd.)l, Mrs. Soumya, and Mr. V. Harish Raj for SEM analysis, Mr. P. Guruswamy and Mr. Prithviraj for XRD.

I thank my senior colleagues Dr. S. Anas, Dr. K.V Mahesh, Dr. Linsha Vazhayal, Dr. S. Soumya, Dr. P.S Suchithra, Dr. K.B. Jaimy, Dr. V.S Smitha, Dr.Manju, Dr. Sree Remya, Dr. K. Asha Dr. S. Sankar for their support and valuable suggestions.

I thank all my colleagues, Mrs. Babitha K.B, Ms. K.A Shuhailath, Ms. N Minju, Mrs. N. V Sheemol, Mr. Y. Dhaneesh, Mr. S. Vaisakh Mr. Vishnu Prasad for the useful discussions, friendship and precious time that we spend together at NIIST.I also warmly acknowledge the support of former colleagues Mr.S. Sujith, Mr. Akhil Das, Mr. Goutham, Mr. Raimond, Mr. Shinto Alex, Ms. B. Susheela, Mr. Vishnu Mr. Gokul for their kind corporation.

I would like to acknowledge friendship with Ms. Minju Thomas, Mr. M. Firoz, Ms. K. Shijina, Ms. Gayatri Prabhu, Mrs. P Suyana, Mrs. Ann Rose Sunny, Mr. S Rahul, Mrs. Arya Das, Mr. Akhil S Karun, Dr. Manu Jose,, Ms. Swetha, Dr. Harsha Ms. Nimisha, , Mrs. Megha Joy for their warm support and help.

I am thankful to the help and support provided by the Masters Project students Mr. Esposito Kevin, Angel Rose Rajan and Sherin Banu.

I would like to thank Mr. Balanand Santhosh for his warm support and technical help for which I am always indebted.

I have to acknowledge all my teachers who laid foundation for me to pursue higher studies.

I would also like to thanks all the staff members of various departments of CSIR-NIIST for rendering their help during my work.

At this moment, I remember with gratitude my parents Mr. Mathews and Mrs. Mariyakutty, my dearest sister Deepa Alphonce and family and brother Martine Mathews and family, for their wholehearted support and prayers to achieve this goal in my life. I heart fully thank my in laws Mr. Kurian Kurian and Mrs. Annie Kurian for their love, prayers and support.

I am also thankful to all my relatives and friends especially, Sr. Lourd Maria and Sr. Prasoona for their motivation and prayers.

I wish to specially thank Mr. Majo Kurian, my beloved husband, for his care, unfailing support, tremendous patience and trust that helped for the successful completion of my thesis. At this juncture, I would also like to remember Baby Helan, my dearest daughter who missed my care during the final stages of my research.

I acknowledge the Council of Scientific and Industrial Research, New Delhi, for financial assistance and CSIR-NIIST for providing me platform to work on.

Jeen Maria Mathews

CONTENTS

Temperature Synthesis of Nano ZnO

CHAPTER 6: Application studies of Zn/ZnO Cermet Reactant Mixture for the development of Ultrafine Grained ZnO Varistors and Multi-Functional Micro-Varistor Fillers for PVC Composites 200

List of Figures

List of Tables

List of Abbreviations

0D	Zero dimensional
1D	One dimensional
2D	Two dimensional
3D	Three dimensional
a.u.	Arbitrary unit
BPMR	Ball to Powder Mass Ratio
CNSL	Cashew nut shell liquid
CNT	Carbon nano tube
CTO	Conventional thermal oxidation
CTAB	cetyltrimethylammonium bromide
e^-	electron
EDX	Energy dispersive X-ray spectroscopy
e.g.	Exempli gratia (for example)
et al.	Et alaia (and others)
etc.	Et cetera(and so on)
GNP	Graphite Nanoplatelet
HRTEM	High resolution transmission electron microscopy
i.e.	In est (in other words)
JCPDS	Joint committee of powder diffraction standards
J_L	Leakage current
MV	Micro varistor
MW	Microwave
nm	Nano metre
NIR	Near infra-red
PZT	lead zirconate titanate
PVC	Poly(vinyl chloride)
PVA	Polyvinyl alcohol
PVP	Polyvinylpyrrolidone
RPM	Revolution per minute
SAED	Selected area electron spectroscopy

SEM	Scanning electron microscopy
TEM	Transmission electron microscopy
TGA	Thermogravimetric analysis
UV-Vis	Ultra-violet visible
via	Through or By way of
XRD	X-ray diffraction
ZnO	Zinc oxide

List of Symbols

Å	Angstrom
A	Ampere
%	Percentage
^{o}C	Degree celsius
2θ	Diffraction angle in degrees
g	Gram
J_L	Leakage current
min	Minute
mL	Milliliter
λ	Wavelength
wt %	Weight percentage
h	Hour
μm	Micrometer
nm	Nanometer
mg	Milligram
α	Non-linear coefficient
s	Seconds
vs.	Versus
θ	Contact angle/Bragg angle
mol	Mole
Hz	Hertz
V_b	Breakdown voltage
S	Siemens
W	Watt

Preface

Over the years, great demand is seen with ZnO based nanostructures and nanocomposites. Experts recommend ZnO for transparent electrodes in liquid crystal display, lead free piezoelectric, biosensors and also in energy-saving or heat-protecting smart windows. It has innumerable physical properties like optical transparency, remarkable UV shielding and IR reflectance impressive electron mobility, and strong room temperature luminescence which makes ZnO and its nanostructures as candidates for futuristic electrical / electronic and functional applications. The advanced breakthroughs in fundamental research of ZnO have made its bulk and low cost production as a necessary step towards its large scale production and applications. This thesis explored the possibilities of deriving high quality ZnO and its derivatives from an environmentally viable and economically cheap source, metallic Zn dust for large scale industrial applications. The whole thesis is centred around a thematic concept on "*effective and efficient utilization of a partially avoided industrial by-product, Zn dust*". The content of this thesis have been described in seven chapters.

Chapter 1 gives an account of synthesis strategies reported in literature for obtaining nano scale ZnO for various functional and electronic applications. The chapter concludes with the research statement and different targets aimed in the Ph.D work.

Chapter 2 of the thesis comprises a brief description of various instrumentation and characterization techniques employed for the characterization of products at different stages of the investigation.

In Chapter 3, bulk processing of nano ZnO has been attempted via a facile green synthesis approach namely 'Aqueous Mechanical-Oxidation **[AMOx]'.** The technique resulted in voluminous production of H_2 gas as a by-product. This catalyst-free water-splitting reaction was confirmed during milling of Zn dust. Further the effect of surfactant assisted milling on ZnO morphology was studied. The effect of sintering and grain growth evolution was also monitored. Nano scale ZnO by direct aqueous mechanical milling, without any further thermal or calcination steps is reported for the first time. The associated release of H_2 gas is a complementary by-product in **AMOx** technique.

Chapter 4 deals with bulk production of ZnO nanostructures *via* thermal oxidation of mechanically activated Zn dust. This chapter is devided into three parts. In the section **1**, thermal oxidation of Zn dust via conventional route is studied. Effect of reaction temperature on the direct oxidation of Zn dust (72 h milled) into different ZnO nanostructures was investigated. The sequential evolution of ZnO nanostructures from metallic Zn dust was studied from 700 to 1000 ^{o}C and the growth of various morphologies such as nanosheets, tetrapod, nanowire and multipods are reported. At 1000 ^{o}C the growth of well-defined nanowire and multipods with several micrometer length was confirmed.

In the **section 2** oxidation of mechanically activated Zn dust *via* ultra-fast microwave heating is studied. The 72 h mechanical activation of Zn dust creates a ZnO seed layer on Zn particle. Zn dust with ZnO seed nuclei on its surface transformed into interesting ZnO nanostructures. By varying microwave irradiation time and power using a domestic microwave oven, with a power of 750W, series of ZnO nanostructures viz. nanorod, tetrapod, multipod *etc*. were obtained within 15 min. This study reveals microwave thermal oxidation is a potential catalyst-free/rapid technique for the production of nano ZnO.

resin; cashew nut shell liquid (CNSL) and surface coatings were developed over glass and a highly sensitive magnesium alloy metal substrates. ZnO incorporated CNSL resin coatings were further studied for NIR reflectance, optical transparency, hydrophobic surface property and corrosion resistance. The paint showed about 33% enhancement in NIR shielding and about 156% improvement in corrosion resistance when compared to their uncoated counterparts.

Section 3 of **Chapter 4** describes the formulation of functional paints and coatings developed with nano ZnO synthesized via direct thermal oxidation. Paint formulation was made by blending the as synthesized nano ZnO with a natural organic resin; cashew nut shell liquid (CNSL) and surface coatings were developed over glass and a highly sensitive magnesium alloy metal substrates. ZnO incorporated CNSL resin coatings were further studied for NIR reflectance, optical transparency, hydrophobic surface property and corrosion resistance. The paint showed about 33% enhancement in NIR shielding and about 156% improvement in corrosion resistance when compared to their uncoated counterparts.

Chapter 5 devotes to study the influence of Zn-ZnO cermet particles as functional filler for epoxy composites. The effect of cermet architectures on the dielectric properties of epoxy composite was investigated. Surface oxidized Zn dust forms ZnO layer on the surface of Zn particles. The thickness of ZnO layer is controlled by varying the temperature and time. The ZnO layer on Zn surfaces act as an interlayer which prevent direct contact of metal core and thus alter the dielectric loss. The developed Zn-ZnO/epoxy polymer composites resulted in high dielectric constant and low loss with enhanced thermal conductivity. Such composites are potential candidate for embedded passive component applications.

Chapter 6 is divided into two parts. **Part 1** addresses the fabrication ultrafine grained ZnO varistors via cermet route. Cermet route involves the mechanical blending of metallic Zn dust with La_2O_3, CeO_2 rare earth oxides along with varistor forming minor additives. At 1250 °C, Zn dust derived cermet composition showed 99% theoretical density with an average sintered grain size ~ 2.5 μm. Such varistors resulted in breakdown voltage $V_b = 477$ V mm^{-1} with the non-linear coefficient $\alpha = 38$.

Section 2 of **Chapter 6** describes the fabrication varistor reinforced flexible polymer composites. Zn dust derived ZnO microvaristors is introduced in PVC matrix to obtain UV resistant, flexible PVC dielectric composites. The composites exhibit conductivity in the range 2.2×10^{-7} to $3.8\ 10^{-5}$ S/mm with increasing amount of varistor filler loading from 0 to 70 wt %.

The main findings and future perspectives of the present thesis work are summarized in **Chapter 7**.

CHAPTER 1

Nano ZnO: Introduction to Properties, Processing and Applications

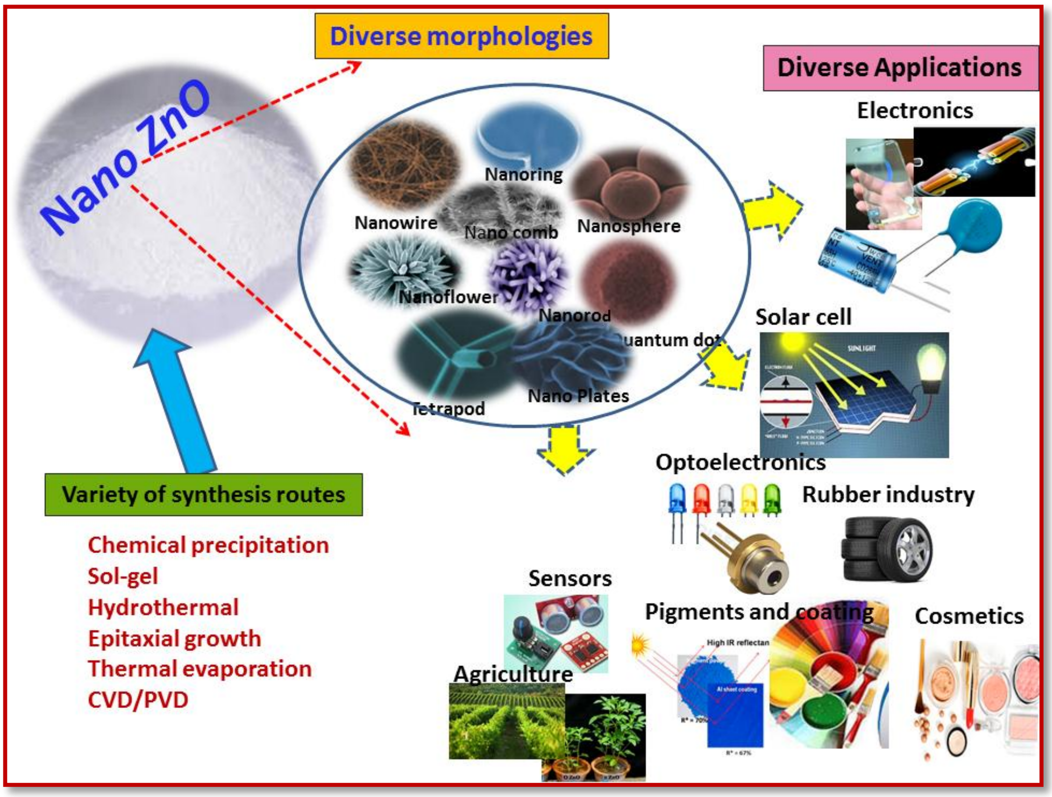

This thesis has a major focus on the synthesis of high quality nano ZnO via an economic and eco-friendly approach from a low cost and environmentally viable source Zn dust. Zn dust is a partially avoided industrial by-product and this thesis put forward certain technologies for its efficient and effective utilization. The introductory chapter describes fundamental knowledge about properties, conventional processing routes and applications of nano ZnO with the support of previous literatures. With this back drop the objectives of the present work and scope of the thesis are described at the end.

Nano ZnO: Introduction to Properties, Processing and Applications

1.1 ZnO Nanomaterials

Since the development of nanotechnology the investigations of material properties at nanoscale has become the leading edge of material research. The nano-structured materials with unique and fascinating properties have motivated the scientific world to a great extend to explore them for a wide range of applications. The individual molecules and interacting groups of molecules are responsible for the bulk macroscopic properties of the material at nano scale. The introduction of novel electrical, optical, chemical and mechanical properties with size reduction is resulted from the much believed surface and quantum confinement effect [1-3]. In the last few decades ZnO nanostructure has gained wide attention triggered by their technological potential in various fields. Nano ZnO has revolutionized the field of material research because of their promising applications in electronics, non-linear optics, catalysis, solar energy conversion, optoelectronic devices *etc.* [4-13]. ZnO is a group II-VI binary compound semiconductor with wide band gap energy of 3.37 eV and exhibit n-type conductivity [2, 14, 15]. It possesses large free exciton binding energy of 60 meV, which is ~3 times higher than that of the well-known GaN based semiconductors. This enables the effective room temperature excitonic emission in the case of ZnO [16].

Among the various wide band gap semiconductors such as GaN, SiC, TiO_2, CeO_2, SnO_2 and ZnS, ZnO has been attracted much attention due to several reasons. For instance, ZnO is prepared in rather pure form after Ge and Si semiconductors. Also it can be easily grown into different nanoscale forms including one dimensional, two dimensional and three dimensional structures which has not been claimed in other semiconducting material [17-21]. The typical properties of wurtzite ZnO are listed in the Table 1.1.

Table 1.1: Properties of ZnO

Property	**Value**
Mineral	Zincite
Density	5.606 g/cm^3
Lattice parameters at 300 K: a_0 c_0 a_0/c_0	 0.32495 nm 0.52069 nm 1.602 (1.633 for ideal hexagonal structure)
Stable phase at 300 K	Wurtzite
Lattice	Hexagonal
Space Group	$P6_3mc$ or C^4_{6v}
Energy gap	3.4 eV (direct)
Refractive index	2.008, 2.029
Melting point	1975°C
Exciton binding energy	60 m eV
Static dielectric constant	8.656
Thermal conductivity	0.6, 1-1.2 W.m^{-1}. K^{-1}
Heat Capacity, Cp	9.6 cal mol^{-1}. K^{-1}

The properties of ZnO those differentiate it from other metal oxide semiconductor and contribute for various applications are listed below.

i) *Wide and direct band-gap and opportunities for band gap engineering:* ZnO possess band gap of 3.44 eV and 3.37 eV at low temperature and room temperature respectively [22] and those values exhibited by GaN are 3.50 eV and 3.44 eV respectively [23]. Wide band gap allowed absorption in the UV range and higher electron mobility. This qualifies ZnO for the applications in optoelectronic devices including, laser light, photo detector, light emitting diode *etc.* [24-28]. For optoelectronic applications band gap engineering of semiconductors is a crucial step. The band gap engineering of a semiconductor can be done by alloying it with another materials having different band gap and thus changing the wavelength of excitonic emission [29]. The band gap of ZnO can be tuned *via* divalent substitution on the cation site to produce heterostructures. For ZnO, alloying with MgO and CdO is an effective approach to increase and decrease its band gap energy respectively. Cd doping can decrease the band gap to as low as ~3.0 eV, whereas Mg doping can increase the band gap to as high as ~4.0 eV [30-34].

ii) *Electrical properties:* The electrical properties of the ZnO varied with respect to the quality of the sample available [35]. ZnO is reported to be an intrinsic semiconductor, and occurs naturally as *n*-type. The presence of native defects such as O vacancies and Zn interstitials are responsible for the n-type conductivity of ZnO. In the case of ZnO it is very difficult to get stable and reproducible p-type conductivity. The electron effective mass and hole effective mass of ZnO are $0.24m_0$ and $0.59m_0$ respectively [35].

iii) *Wide range of morphologies:* Large number of nano and micro morphologies possessed by ZnO is one of the most inviting characteristics of ZnO. The various morphologies include nanowire, nanorod, nanospring, nanocomb, nanoring, nanobelt, nanoflower *etc.* [37, 38]. The polar surfaces and non-central symmetry of ZnO resulted in the evolution of large number of morphologies at different experimental conditions [38]. Among the various nanostructures one-dimensional ZnO nanostructures have attracted special attention for the fabrication of highly sophisticated devices due to their unique properties which are different from those of their bulk counterparts [40-43].

iv) *Higher exciton binding energy:* ZnO possess large exciton binding energy of 60 meV compared with 25 meV for GaN [44, 16, 23]. This results in intense near-band-edge excitonic emission at room and even above the room temperatures, since this value is 2.4 times higher than the thermal energy at room-temperature (RT), k_BT=25 meV [46,47]. The electron hole transitions in ZnO is much lower than the oscillator strength of exciton and this makes it as a promising material for excitonic effect based optical devices [46].

v) *Non-linear current-voltage characteristics of polycrystalline ZnO:* The working of ZnO varistors are based on non-linear current-voltage characteristics of ZnO [48, 49]. The non-linear behaviour is attributed to the presence of grain boundaries in the varistor microstructure and is controlled by the various varistor additives.

vi) *Piezoelectric property:* The tetrahedral coordination leads to a non-centro-symmetric structure in ZnO crystals [45]. The lack of symmetry along with large electromechanical coupling in wurtzite ZnO results in piezoelectric properties [29]. And this can be used for device applications including transducers, actuators and sensors [50-55].

vii) *Luminescence property:* ZnO possess strong luminescence property in the green-white region of the electromagnetic spectrum which makes it a promising material for phosphor applications [56]. The luminescence properties of ZnO are attributed to Zn interstitials or oxygen vacancies [56, 57]. The defect Zn vacancies are acceptors and leads to the n-type conductivity in ZnO and make it suitable for field emission displays and vacuum florescent displays [58, 59].

viii) *Amenability to wet chemical etching:* The possibility for wet chemical etching of ZnO is greatly benefited the semiconductor industry by adding flexibility to designing, processing and integration of various semiconductor devices [60, 61]. ZnO films can be etched in both acidic and alkaline solutions [62].

ix) *Radiation hardness:* The radiation hardness is an essential requirement for high altitude applications. ZnO possesses relatively higher radiation hardness [24, 63].

x) *Large single crystal availability:* Single crystals with large area and epi-ready substrate are important requirements for the application in semiconductor industry [64]. The growth of ZnO thin film on native substrate reduced the extended defect concentration and can lead to the growth of high quality thin film [65]. This property distinguished ZnO from GaN for which native substrate do not present [66].

xi) *Thermal conductivity:* For a semiconductor, thermal conductivity is an important property while considering high temperature or high power applications [67]. The point defects in ZnO crystal have a significant effect on its thermal conductivity. Typically the thermal conductivity of ZnO falls in the range 0.6–1W. m^{-1}. K^{-1} [68].The high thermal conductivity of ZnO makes them to use as a functional filler in polymer composite to improve the heat dissipation properties of polymer matrix and resulting in efficient heat removal during device operation [69].

The extensive interest in nano ZnO research in recent years is based on its potential to develop:

- A material to replace GaN for blue/UV optoelectronic devices like laser diode and light emitting diode.

- Ferromagnetic material developed by doping with V, Co, Mn *etc.* for spintronics.
- A material with radiation hardness for the fabrication of electronic devices.
- A cost effective material for transparent conducting oxide (TCO) by doping with Al, In, Ga *etc.* to replace indium tin oxide (ITO).

1.2 Crystal Structure of ZnO

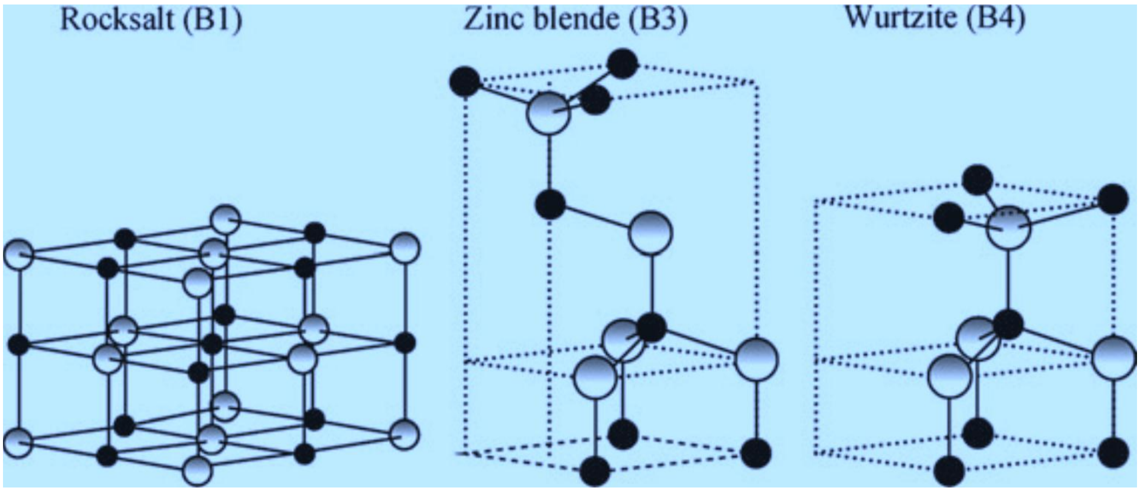

Figure1.1: The crystal structures of ZnO. The grey and black spheres represent Zn and O atoms, respectively (reproduced from https://onlinelibrarywiley.com /doi/abs/10.1111/j.1744-7402.2012.02795.x).

ZnO crystalizes in three forms hexagonal wurtzite, cubic zinc blende and cubic rocksalt [70]. The crystal structures of ZnO are schematically shown in Figure 1.1. At ambient conditions, thermodynamically most stable form is hexagonal wurtzite and it is the most common form of ZnO crystals. The zinc blende form of ZnO crystals are observed for ZnO grown on substrate having cubic lattice structure. The rocksalt form of ZnO crystal is observed at relatively higher pressure. Wurtzite ZnO possess hexagonal unit cell with lattice parameters a = 3.24 Å and c = 5.21 Å. A tetrahedral unit of ZnO is formed by the O^{2-} and Zn^{2+} ion and it lacks central symmetry. ZnO has a polar hexagonal c-axis. Thus simply the structure of ZnO composed of alternate interpenetrating planes of tetrahedrally coordinated Zn^{2+} and O^{2-} ions stacked along the c-axis [71]. Each Zn ion is tetrahedrally surrounded by four O ions. In ZnO the tetrahedral coordination results in non-central symmetric structure [71, 72]. Another important characteristics of ZnO is polar surfaces and the most common polar surface is basal plane (0001) and this plane support one-dimensional growth of ZnO along (0001) direction [70].

Positively charged Zn-(0001) and negatively charged O-(0001) surfaces are produced by the oppositely charged ions Zn and O, leads to a dipole moment and spontaneous polarization along the c-axis. The surface energy diversity and spontaneous polarization along ± (0001), ± $(0\bar{1}11)$ have been of wide interest in describing evolution of ZnO nanostructures. The morphological diversity in the case of ZnO is attributed to its growth along the directions (0001), $(0\bar{1}10)$, and $(2\bar{1}10)$ along with polar surfaces ± (0001) [73, 74]. However most common and fastest growth direction is <0001>.

1.3 Synthesis of Nano ZnO

ZnO possess richest variety of nanostructures including nanowire, nanorod, nanospring, nano belt, nanocomb *etc*. These varieties of morphologies of ZnO can be grown by different synthesis route ranging from vacuum based sophisticated techniques to low cost, low temperature chemical synthesis routes [75-85]. In the last decade substantial effort has been devoted to the development of new synthetic methodologies and modification of the existing ones. For the synthesis of ZnO nanostructures two strategies are generally pursued: “top-down” and “bottom-up” approaches. The processing conditions, like solvent, temperature, and additives have critical role in obtaining a variety of ZnO nanostructures having different sizes and shapes. The different mechanism in each synthesis technique resulted in bulk crystal growth at different rates and direction and leads to diverse morphologies with exciting properties. Typically the synthesis technique of ZnO nanostructures can be divided into two, vapour phase growth process and solution phase growth process. The gaseous or vapour phase processes are considered as the low cost synthesis route for the large scale production of ZnO nanostructures. Liquid phase synthesis routes are flexible in terms of controlled variation of morphological, structural and compositional properties of synthesised nano product.

1.3.1 Vapour Phase Growth Process

Vapour phase growth processes are the most versatile group of techniques for the production of size, morphology and property tuned ZnO nanostructures. The vapour phase methods involves crystal growth in which crystal is grown by depositing gaseous or vapour phase material directly. In the vapour phase synthesis the reaction is performed in the temperature range 500-1500 ^{o}C and the growth mechanisms are attributed to vapour solid (VS), vapour-solid-solid (VSS) and vapor-liquid-solid (VLS) mechanisms [87]. In order to control various properties of ZnO nanostructures various vapour phase growth methods have explored till date [86, 87, 88]. These incudes pulsed laser deposition (PLD), chemical vapour deposition(CVD), thermal evaporation, thermal chemical vapour deposition, cyclic chemical vapour deposition, metal organic chemical vapour deposition (MOCVD) *etc*.

1.3.1.1 Pulsed-Laser Deposition (PLD)

In PLD technique material from the surface of the target is evaporated using laser pulses having high energy. The material vaporised from the surface of target is deposited as thin film on the substrate placed opposite to the target. The PLD technique allows the growth of high quality ZnO film at lower temperatures in the range 200-800 ^{o}C [89]. Tsoutsouva *et al.* prepared ZnO thin film on soda lime glass substrate by PLD. High quality polycrystalline ZnO films were deposited at low substrate temperature of 100 ^{o} C [90]. Highly transparent Al-doped ZnO film with low resistivity was grown *via* oxygen radical-assisted PLD by Matsubara *et al.* [91] The difficulty in obtaining film on substrate having large area and particulate formation have limited PLD to laboratory scale production of nano ZnO [92].

1.3.1.2 Chemical Vapour Deposition (CVD)

Chemical vapour deposition is a vapour phase synthesis route for nanomaterial in which the vapours of reactants produced at higher temperature transported *via* carrier gas and the chemical reactions on the substrate leads to the formation of thin film [2, 93]. It is widely used for producing high quality films and can be used for large scale fabrication. Several modifications of CVD are there depending on the type of precursor used. If the precursors used are metallo-organics or alkoxides the processing is called MOCVD and when halide or hybrid precursors are used it is called halide or hydride CVD [94]. Ataev *et al.* have successfully grown high quality ZnO film with good electrical and luminescence properties *via* hydride CVD in which they have used hydrogen as the carrier gas [95]. The reaction carried out under the pressure of < 133 Pa and the target was kept in the evaporation zone at 770 ^{o}C temperature. ZnO thin film was grown *via* halide CVD [96] in which $ZnCl_2$ or ZnI_2 and O_2 gas were used as the sources of Zn and oxygen respectively [97]. This technique provide high growth rate. In iodide system the ZnO film obtained shows good structural and optical properties. For chloride system the ZnO film obtained shows UV emission at room temperature. The MOCVD technique used metal alkyls like diethyl zinc or dimethyl zinc along with oxygen source and argon or nitrogen as carrier gas [98, 99]. But the higher reactivity of these Zn source with oxygen and water vapour resulted in white powder formation and degrade the quality of film obtained. Several modifications in MOCVD were reported. Ogata *et al.* demonstrate the growth of ZnO film in presence of nitrous oxide. Low reactivity allows the growth of high quality ZnO film with good crystalline and optical quality [100]. MOCVD is a catalyst free growth technique for growing ZnO nanowire where the growth rate can be controlled by changing the growth parameters. However, the CVD processes have some disadvantage. CVD demands volatile precursors at near room temperatures and also in most cases precursors are quite costly. CVD produced hazardous by-products. Since in CVD the film deposition takes place at elevated temperature there are some limitations on the kind of substrates that can be used. Also the difference in the thermal expansion coefficient of material deposited and substrate leads to development of stresses and resulted in mechanical instability of film deposited [101].

1.3.1.3 Thermal Evaporation

In thermal evaporation at higher temperature the vapours of powder or condensed reactants formed and at certain condition the condensation of these reactants vapour phases occur and form final product [2]. Temperature is the critical parameter responsible for the different morphologies obtained at different conditions [102]. Lee *et al*. synthesised ZnO nanorod, nanobelt and nanowire *via* thermal evaporation of milled ZnO at 1300 ^{o}C [103]. In another work Yao *et al*. reported the bulk production of ZnO nano ribbon, nanowire and needle like nanorods *via* thermal evaporation of ZnO graphite mixture [104]. Large scale production of nano and micro ZnO morphologies including microrod, microtube, nano belt and nanowire *via* microwave assisted thermal evaporation of Zn or ZnO source material was investigated by Cheng *et al*. [102]. Processing temperature, substrate and catalyst showed considerable impact on various morphologies obtained at different conditions.

1.3.2 Solution Phase Growth Methods

The solution phase growth method includes appropriate composition of precursor-solvent- additive system. The ZnO precursors used in chemical synthesis include metal-nitrate, metal halides and metal-carboilates in alcoholic/aqueous solution [105-

108].Typically, solution phase growth of ZnO nanostructures occur at comparatively lower temperatures (<200 °C) than that of vapor phase growth methods [109, 110]. Thus, solution phase growth methods permit for a wide range of substrates comprising organic and inorganic substrates. Some of the widely used solution phase growth methods for ZnO nanostructures are discussed below.

1.3.2.1 Precipitation method

Precipitation method involves the reduction of Zn salt solution using reducing agent followed by precipitation of ZnO precursor and then subjected to thermal treatment. Synthesis of ZnO nanoparticle *via* precipitation technique from zinc nitrate solution with amine additives like ethylenediamine, hexamethylenetetramine is a common approach in which pH, concentration of the solution and type of additives shows control over size and shape of particle obtained [108]. During reaction when the product get super saturated the nucleation starts. Then it grows into different nanostructures depending on various reaction conditions. Hong *et al.* synthesised ZnO nanoparticle with size 30-40 nm *via* precipitation technique using zinc acetate and ammonium carbonate as reagents [111]. Lanje *et al.* prepared ZnO nano particle using zinc nitrate and sodium hydroxide *via* precipitation technique as an attempt for the large scale production of ZnO without undesired impurities [112]. They have used starch molecule containing large number of hydroxyl group which could attach on the surface of nano particle to reduce the agglomeration between the particles. Wang *et al.* synthesised ZnO nano particle having size 9-20 nm by precipitation of zinc sulphate and ammonium carbonate aqueous solution. Thus precipitation method is simple and able to produce variety of ZnO nanostructures. However, the major drawback of precipitation technique is the difficulty in avoiding contamination due to the production of by-product during chemical reaction.

1.3.2.2 Sol-gel Synthesis

Sol-gel method is a versatile solution synthesis route for producing ZnO nanostructures. In sol-gel method a colloidal suspension of particles called sol is obtained by the hydrolysis of precursor solution [114]. After that a gel is formed which is an aggregate of particle. The thermal treatment of gel is carried out in order to obtain the final product. In a typical sol-gel processing of ZnO, zinc acetate solution is mixed with ethanolamine and 2- methoxyethanol and stirred at temperature below 100 ^{o}C [115]. Ristić *et al.* reported the sol-gel synthesis of nanocrstalline ZnO by adding tetramethyl ammonium hydroxide to zinc 2-ethylhexanoate in propan-2-ol resulting in the formation of ZnO nanoparticle with size 20–50 nm [116]. Using zinc acetate dihydrate and oxalic acid in ethanol solvent Benhebal *et al.* have prepared ZnO nano particle *via* sol-gel method [117]. The calcined ZnO having BET surface area 10 $m^2. g^{-1}$ with low porosity was obtained. Thus sol-gel technique is a widely accepted technique for the production of nano ZnO. However, since in sol-gel method the hydrolysis, condensation and drying takes place simultaneously the control over particle morphology and reproducibility of the product are difficult. Therefore the sol-gel route is highly recommended for the production of bulk metal oxides rather than nanoscale forms.

1.3.2.3 Hydrothermal synthesis

The hydrothermal synthesis carried out in autoclave in which the reactants are heated to100-300 ^{o}C and kept for several days. This process has many advantageous like free from organic solvent, low temperature processing, wide variety of morphologies, high degree of crystallinity and high purity of the product obtained [118,119]. Chen *et al.* have synthesised nano ZnO *via* hydrothermal method using $ZnCl_2$ and NaOH as reagents [120]. pH of the solution, reaction time and temperature have significant role on size and morphology of the particle obtained. Large numbers of reports are there on the significant benefits obtained by microwave assisted hydrothermal synthesis. For example the loss of energy as heat was reduced by heating the solution alone not the container during microwave assisted reaction. Thus microwave assisted hydrothermal synthesis leads to fast and voluminal heating of reactants and shorten the reaction time [121-123].

Table 1.2: A bird-view comparison of the processing conditions employed in various syntheses techniques to obtain nano ZnO.

Method	Precursor	Condition for synthesis	Properties	Ref.
Vapour deposition	ZnO/graphite, Au coated sapphire substrate	620– 890 ^{o}C, 30 min annealing	Vertically aligned ZnO nanowire	126
	Zinc acetylacetonate hydrate,silicon substrate	500 ^{o}C, N_2/O_2 as carrier gas	Well aligned nanorod with diameter 60-80nm	128
	Diethylzinc, N_2O as oxidizer	750-800 ^{o}C, Ar as carrier gas	Defect-free aligned ZnO nanorods with uniform length and diameter	129
Thermal Evaporation	High purity ZnO, Graphite, silicon substrate	Reaction: 900 ^{o}C/30 min, Ar as carrier gas	Flower-like ZnO nanorods (D- 50–80 nm and L- 1.5–2.0 µm	102
	Ball milled ZnO, silicon substrate	Reaction: 1380 ^{o}C/3h, Ar as carrier gas	nanobelts, nanorods, and nanowires were synthesized at three different substrate temperatures	103
	ZnO/graphite	Reaction: 1100 ^{o}C/30 min	nanowires, nanoribbons, and needle-like rods	104
Precipitation process	$Zn(CH_3COO)_2$, $(NH_4)_2CO_3$, PEG10000	Calcination: 450 °C/3h	Zincite structure; spherical particles (*D* ~ 30 nm)	111
	$ZnSO_4$, NH_4HCO_3, ethanol	Drying: overnight, 100 °C; calcination: 300–500 °C	Wurtize structure; crystallite size 9–20 nm; particle size *D*: ~12 nm,	113

	$Zn(CH_3COO)_2$, NaOH	Reaction: 30 in, 75 °C drying: overnight, room temperature	Hexagonal structure; flower shape	125
Sol-gel	$Zn(CH_3COO)_2$, oxalic acid ($C_2H_2O_4$), ethanol	Reaction: 50 °C, 60 min; dri ed of gel: 80 °C, 20 h; calcined: under flowing air for 4 h at 650 °C	Hexagonal wurtzite structure; uniform, spherically shaped particles	81
	$Zn(CH_3COO)_2$, diethanolamine, ethanol	Reaction: room temperature; annealing of sol: 2 h, 500 °C	Hexagonal wurtize structure; particles: nanotubes of 70 nm	82
	zinc 2-ethylhexanoate, TMAH ($(CH_3)_4NOH$), ethanol and 2-propanol	Reaction: room temperature; drying: 60 °C	cylinder-shaped crystallites, *D*: 25–30 nm; *L*: 35–45 nm	116
Hydrothermal	$Zn(CH_3COO)_2$, NaOH, HMTA (hexamethylenetetraamine)	Reaction: 5–10 h 10–200 °C; HMTA concentration: 0–200 ppm	Spherical shape; particles diameter: 55–110 nm	125
	$ZnCl_2$, NaOH	Reaction:100–220 °C in teflon-lined autoclave,5–10 h	Rod-like (100–200 nm), bullet-like (100–200nm), polyhedron (200–400 nm), sheet (50–200 nm).	120
	$ZnCl_2$, KOH, Urea	Microwave reactor Pressure-4 MPa pH=12	Nanocrystalline ZnO with grain size 10-200 nm	123

Limitations experienced in chemical techniques:

In all the above mentioned processing of ZnO nanoparticles the particle growth takes place in liquid, gas or vacuum and the complete separation of the product is not guaranteed at the end of the reaction. Moreover the control over particle size is poor due to the increased agglomeration tendency of particle during the growth stage. Also some of these methods often meet difficulties of tedious operation procedures, catalyst/templates removal, poor adhesion of nanostructures to the substrate, etc. Most of these chemical techniques are not very popular in industries when the mass-production of nano ZnO is considered. In various synthesis routes the main technological differences are in the precursors of zinc processing temperatures, the unit operations used and the scale of production. Considering the approaches shown in the Table 1.2 most of them use substrate and external gas supply to achieve ZnO nanoparticles and those methods are definitely promising for the production of high quality ZnO for highly sophisticated application. But for the bulk production of nanostructures for industrial application they are not suitable. Among the various pilot scale or laboratory technique reported till date for the production of nano ZnO only few of them are suitable for commercial interest. The mechano-chemical synthesis is one among them.

1.3.2.4 Mechano-chemical Synthesis using precursor salts

Milling technique is a facile, easy to scale up top-down approach for the production of high quality nano ZnO. For the nanomaterials processed *via* mechanical milling the agglomeration tendency is reduced to a great extent and good homogeneity is obtained in size and morphology of product. Due to the simplicity and low production cost the technique is promising for industrial scale production of ZnO nanostructures [127]. Also it does not use any organic solvent and hence from environmental point of view it is very attractive for the production of nanomaterial [128]. In mechanochemical process the precursors mainly used are $ZnCl_2$ and sodium carbonate. NaCl is used as the reaction medium. The particle size effectively reduces on the increase of milling time and good homogeneity in particle size and morphology can also be achieved under optimised milling conditions. The Good homogeneity is also possible in size and the morphology under optimized milling conditions. Table 1.3 compares some of the literature on mechanochemical synthesis of nano ZnO.

Table 1.3: Comparison of processing parameters of mechanochemical synthesis of ZnO.

Precursor	**Conditions for synthesis**			**Size of particle (nm)**	**Remarks**	**Ref.**
	Volume of chamber (mL)	**BPMR**	**rpm**			
$ZnCl_2$ +Na_2CO_3 (in dilute NaCl) Heat treatment @ (400-800) ^{o} C /2h	300	15:1 (steel balls 8,20 mm D and 40, 10 mm D)	600	18-36	Calcination followed by milling	129
$ZnSO_4$+NaOH (in Diluent NaCl) Milling,heat treatment and washing	-	15:1	300	50-80	Milling heat treatment and washing	130
$ZnSO_4.7H_2O$ +KCl + KOH 2 Step Grinding process (10+20 min) Paste state @Room Temperature Repeated Washing processes to remove Cl ions	-	-	-	22	Grinding followed by repeated washing steps	128
$ZnCl_2$ +$Ca(OH)_2$ Calcination @ 300-900 ^{o} C / 15 min-2h	500	10:1 (122 balls ,8mm D Alumina balls)	180	50-200	Calcination followed by milling	131
$Zn(OAc)_2.2H_2O$+NaOH 2 step process 45 min Grinding Washing centrifuging @ 600 rpm calcination @ 300 ^{o} C/ 2h	-	-	-	35	Grinding followed by washing, centrifuging and calcination	127
$Zn(NO_3)_2\cdot 6H_2O$ Polysaccharide 1:1 to 1:10 Zinc Milling for 30 min Calcination @ 600 ^{o} C/3 h	125	18 steel Balls, (10mm D)	350	50	Milling followed by calcination	132

Even though the mechano-chemical milling resulted in nano ZnO, the direct nucleation and growth of fully crystalline ZnO is evolved only after the calcination and the temperature usually vary in the range 500 to 700 ^{o}C. All these nanostructures are possible if the milling operation is effectively carried out. Ball milling is the simple industrially viable unit operation that can also be employed for mechanical activation followed by direct oxidation of Zn dust [133, 134]. The following section briefly describes the ball milling technique.

1.3.3 Mechanical milling: As an Activation Step and a Room Temperature Processing for ZnO Nanomaterial

For the synthesis of nano ZnO several chemical and physical routes have been explored till date. Majority of them are bottom –up approaches starting from appropriate precursor where the product yield is low and impurity level may high. The top-down approaches like ball milling are of relatively low cost and less explored for the synthesis of nanoparticle. It has been reported that a high temperature up to 1000 ^{o}C and several GPa pressure can be created inside the milling chamber as an impact of milling [135]. This enables milling process to be utilized as a mechanochemical process for the synthesis of variety of nano structures [136]. Ball milling is simple and effective technique for the synthesis of nanoparticle and is applicable to all classes of materials. In mechanical milling the material in the form of powder charged into milling chamber along with an appropriate milling media. During milling the powder particle is trapped between the colliding balls and inner surface of the milling chamber and undergo continuous deformation, cold welding and finally fracturing of the material. Milling breaks the chemical bonds and fresh surface with dangling bond become available for fast reaction. In mechanical milling the kinetics of milling is related to the energy transferred from colliding balls to the powder material and governed by ball to powder ratio (BPMR), rotation per minute (rpm), types of mill. The temperature in the milling chamber depending on the material properties of milling powder, kinetic energy of the balls and milling medium [137].

The mechanical milling is a non-equilibrium processing with controlled parameter and can be used for the production of alloys, composites with unique properties. Conventionally milling is used for size reduction of particles; it is also capable to tailor the chemistry of materials by triggering the surface activation at atomic level. Handful reports are available on the production various metal oxide *via* milling assisted technique from their chemical precursors. In future mechanical milling could become one of the main stream sustainable techniques for the production of nanomaterial because of its advantages like lower waste, less energy consumption, low capital cost, less organic solvent and enhanced selectivity.

Different types of high energy mills include vibratory mills, attrition mills, tumbler ball mills and planetary mills. A typical ball mill consists of a cylindrical hollow chamber which rotates about its axis. The material to be ground is charged into the milling chamber along with milling balls and milling medium. During milling inside the milling chamber the balls lifted up and drop down and the powder particles trapped between the balls undergoes structural transformation. The schematic representation of horizontal section of milling chamber during milling shown in Figure 1.2.

There are several parameters which determine the efficiency of milling process.

i) Rotation per minute (RPM) or Revolution speed

ii) Milling time

iii) Number of balls with respect to chamber size

iv) Ball to powder mass ratio

Under optimized conditions these parameters plays an important role for the best yield.

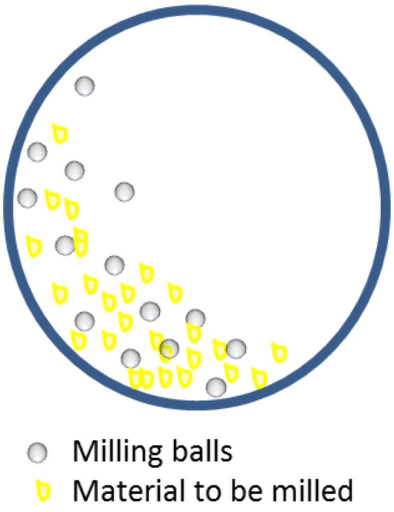

Figure 1.2: Schematic representation of horizontal section of milling chamber.

Mechanical milling can be an activation step allowing low temperature calcination for the completion of reaction. For example, Ye *et al*. reported that conventional synthesis of $CaZrO_3$ involving heating at 1100 ^oC and by mechanical activation of precursor powder calcination temperature can be reduced to 800 ^oC [138]. Similarly for the synthesis of $ZrTiO_4$ the temperature is reduced from 1400 ^oC to 1100 ^oC by activation of precursor *via* mechanical milling, reported by Gajovic *et al*. [139] From the Table 1.3 it is clear that for synthesis of ZnO also most of the approaches used milling process just as an activation step or as an initial treatment phase usually followed by a calcination stage. In the present study ball milling has been used both as an activation step before thermal oxidation of Zn and as a direct room temperature processing of ZnO from Zn dust.

In all the reported work on mechano-chemical synthesis of ZnO listed in the Table 1.3 they have used Zn salt and a base for mechanical activation followed by thermal treatment. The use of micronic Zn dust, an industrial by-product is not reported anywhere for the synthesis of nano ZnO for large scale applications.

1.3.4 Industrial Production of Nano ZnO

Large proportion of ZnO for industrial application is produced *via* hydrometallurgical or pyrometallurgical routes [45]. The Zn containing precursor to be selected will determine the production method. The pyrometallurgical route exploits Zn containing waste. This process produces ZnO of different grade, for example, gold seal ZnO which is pharmaceutical grade and high grade ZnO which is adequate for rubber industry. The ZnO produced through this route have high purity > 99%. However the product obtained may contains traces of Zn and may not suitable for some applications.

1.4 Direct oxidation of Metallic Zinc Dust into nano ZnO: An economical way for the bulk production of ZnO nanostructures

The use of ‘Zn dust’ recovered from secondary sources like sulphide zinc concentrates for the production of nano ZnO put forwards a ‘waste to wealth’ concept, indirectly reducing the environmental impact and at the same time making economic benefits. Zinc is the fourth widely used metal after iron, aluminium and copper. Zn is a non-ferrous metal widely used in textile metallurgical and chemical industries and is primarily recovered from its sulphide and oxide concentrates [140].

Table 1.4: Properties of Zn

Property	Value
Density	7.14 g/ cm^3
Crystal structure	Hexagonal close packed
Thermal conductivity	116 W. $m^{-1}.K^{-1}$
Melting point	420 ^oC
Boiling point	907 ^oC

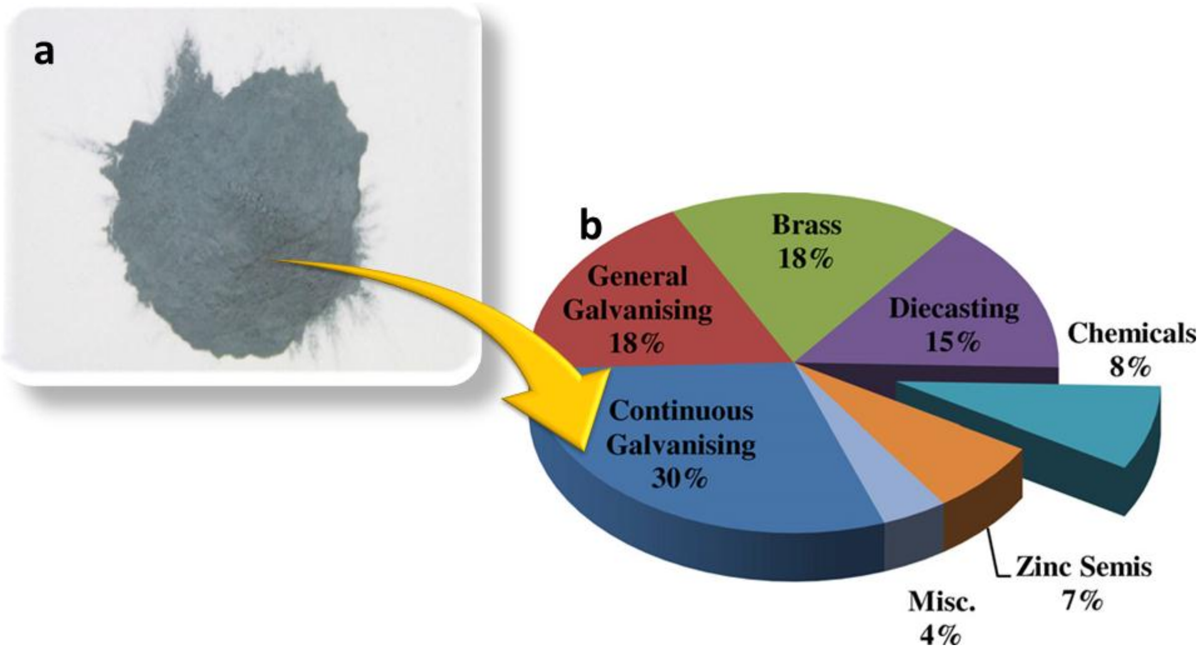

Figure 1.3: a) Mettalic Zn dust and b) Chart showing the various applications of zinc metal. (Reproduced from Ref. [45] with permission of Chemical Engineering Journal).

Zn also recovered from secondary sources like zinc ash, zinc dross produced in various metallurgical industries. ‘Zinc dust’ and ‘zinc ash’ are industrial by-products produced in bulk quantities *via* atomization during zinc alloy processing [140]. The properties of metallic Zn is summarised in Table 1.4. The ‘zinc dust’ is a ductile grey coloured powder (Figure 1.3(a)) and is a strongly recommended and a largely consumed product in Zn-primer paints. It is used in heavy-duty anti-corrosion protection coatings on textile, marine structures and steel sheets. The end use of metallic Zn in different fields is summarized in the Figure (1.4 (b)).

Commercially and industrially there exist a close relationship between Zn and ZnO. The production of ZnO mostly done by three distinct route, direct oxidation of Zn metal, production of Zn metal by reduction of Zn ore followed by the re-oxidation and precipitation of Zn precursors from the aqueous solution followed by calcination. Large number of reports are there on the production of nano ZnO *via* thermal oxidation of Zn in the form of foil, thin film, nanowire *etc*. [46, 86, 87]. The Table 1.5 summarizes the synthesis of ZnO nanostructures by thermal oxidation of Zn. Direct heating of Zn in O_2 atmosphere results in the formation of nano ZnO with a wide variety of morphologies. The temperature range reported for the ZnO nanostructure growth *via* thermal oxidation of zinc is 400-1000 ^{o}C. This covers the melting temperature (420 ^{o}C) and boiling temperature (907 ^{o}C) of metallic Zn.

Table 1.5: Synthesis of ZnO nanostructures *via* thermal oxidation of various Zn source.

Source of Zn	Morphology obtained	Thermal oxidation temperature	Substrate /carrier gas	Reference
Zinc metal thin films	Nanowire	500 ^{o}C	Silicon	142
Zn nano particle	ZnO nano particle	250-350 ^{o}C	-	143
Metallic Zn film	Nanowire with hexagonal structure	390 ^{o}C	N_2/O_2, water vapour congaing atmosphere	144
Zinc metal film	Nano needle	250-400 ^{o}C	-	146
Zinc foil	Bicrystalline nanowire, Single crystalline nanowire, tetrapod	200-1000 ^{o}C	Ar/O_2	87
Hexagonal nanodisc	Nano sheet and nanoneedles	250-400 ^{o}C	Silicon /N_2	145
Zn foil and Zn particle	Nanobelt	400-600 ^{o}C	Zinc	86

The mechanism behind the formation of ZnO nanostructures *via* thermal oxidation is depends on the temperature. In thermal oxidation, at temperature below the melting point of Zn the nanostructures are formed by solid-solid transformation [87]. At thermal oxidation temperature above boiling point of Zn the nanostructure are formed by vapour-solid mechanism. At temperatures between melting temperature and boiling temperature liquid-solid mechanism accounts for the nanostructure formation [87]. Lu *et al.* reported the synthesis of ZnO nanotube *via* catalyst free thermal oxidation of Zn nanowire at temperature 400 ^{o}C under the pressure 20 Pa [141]. The fabrication of bicrystalline ZnO nanowire arrays with enhanced field emission properties was studied by Zhao et al. *via* thermal oxidation of Zn film at 500 ^{o}C [142].

1.5 An overview of the Application of nano ZnO aimed in the Thesis

ZnO is a promising material for a wide range of applications due to its unique properties, variety of synthesis method and diverse morphologies. The large exciton binding energy and wide direct band gap made ZnO a promising candidate for optoelectronic device functioning in blue and ultraviolet region. Oxygen vacancies dependant conducting properties of ZnO enables it to use as transparent conducting material and piezoelectric material for sensors, solar cells, electrodes *etc.* Some of the applications relevant in the present thesis are discussed briefly below.

1.5.1 Pigments and coatings

ZnO is an inorganic white pigment [147]. The pigments derived from ZnO are known as Chinese white or zinc white. The white pigment shows lower absorbance of light and high dispersion of light in visible region [45]. Compared to the major white pigment TiO_2, ZnO has some advantages. It can be synthesized *via* simple chemical synthesis methods using inexpensive precursors. By controlling the processing parameters carefully wide variety of ZnO morphologies can be synthesised. About 90 % of incident near infrared will be reflected by ZnO and transmit light in the visible spectra. Doping of ZnO with Ga or Al induced modest electrical conductivity for ZnO and acquires the infrared radiation reflecting property. Thus ZnO is a potential candidate for energy-saving coating on windows [35]. The various coatings based on ZnO are briefed in Figure 1.4.

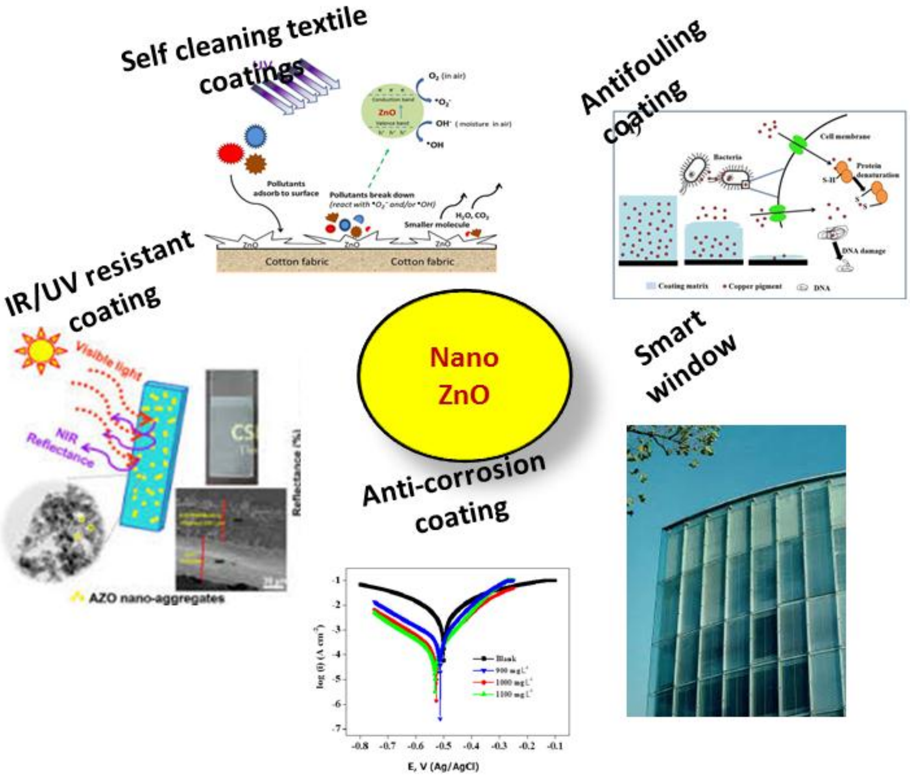

Figure 1.4: ZnO based coatings.

Due the UV/IR shielding property and optical transparency nano ZnO in polymer matrix has received much attention for developing surface coating having solar thermal control [148]. Soumya *et al.* reported IR and UV shielding coatings on textile surface by incorporating silane treated ZnO nanoparticle into poly (methyl methacrylate) PMMA matrix [149]. The coatings also offer hydrophobic nature and antifungal bio safe coatings.

ZnO is a well-known candidate for its multifunctional properties like antifungal/antibacterial and hydro-phobic properties. The ability of ZnO to neutralize acid formed during paint oxidation makes it useful for anti-fouling coatings [150,151]. The sulphide scavenging properties of ZnO make it useful for corrosion resistant coating for food packaging industry [152,153].

1.5.2 ZnO: Multifunctional Filler for Polymer Matrix

Inorganic micro and nanostructures particularly metal oxides are potential candidate to equip polymer matrix with desired properties. Size and shape of filler particle have a major role on tuning the properties of polymer matrix. ZnO, belongs to metal oxide family possess versatile nanostructures with multifunctional properties for various applications. ZnO is a widely available low cost metal oxide which can be used as multifunctional filler for polymer matrix composite. In polymer matrix composite the unique combination of filler and matrix properties resulted into superior properties compared to the properties resulted when filler or polymer matrix used alone. By using ZnO as filler in polymer matrix it will modify the properties of pristine polymer by virtue of the filler added. Large numbers of reports are there on the incorporation of ZnO as functional inorganic filler in various polymer matrixes to tailor the electrical, thermal, tribological, antimicrobial and optical properties of the composites.

ZnO is a semiconducting material with non-linear electrical conductivity. Yu *et al*. prepared silicone elastomeric composite with enhancement in capacity of energy generation and actuation by using ZnO as filler. For the optimal concentration of ZnO around 4 phr the properties are improved by six times compared to pure elastomer [154]. Oku *et al*. have added ZnO to polymer matrix as functional filler and reported that the resultant composites are able to shield and absorb electromagnetic wave and prevent static charge deposition [155]. Hong *et al*. prepared ZnO-low density polyethylene nanocomposites *via* melt mixing route. The interface between nanoparticle and polymer matrix contribute rescaled electrical properties at lower percolation limit with higher break down strength and resistivity at highest nanoparticle loading level [156].

Figure 1.5: Applications of nano/micro ZnO filled polymer composites.

ZnO possess high thermal conductivity of 50 W.m^{-1}. K^{-1} and is used as an additive to improve the thermal conductivity of polymer. Mu *et al*. showed that the thermal conductivity of pure silicone rubber increased from 0.165 W.m^{-1}. K^{-1} to 0.56 W.m^{-1}. K^{-1} with the incorporation of ZnO fillers [157]. Very recently Guo *et al*. prepared epoxy composite with tetrapod shaped ZnO whisker as filler *via* simple solution blending method. The resultant epoxy composite achieved a high thermal conductivity of 4.38 W.m^{-1}.k^{-1} for 50 wt% filler loading [158].

The biocompatibility and hydrophobicity of ZnO make it a promising candidate to be used as filler for antibacterial and hydrophobic coatings. Seo *et al.* showed the incorporation of ZnO particle into polypropylene carbonate have enhanced the oxygen and water barrier properties of pristine polymer and nanocomposites film showed good antibacterial properties also [159].

Large numbers of reports are there on the incorporation of ZnO particle into polymer matrix to enhance the mechanical and tribological properties of the matrix.

Needle shaped ZnO particle incorporated Polyimide composites film with enhanced thermal conductivity was fabricated by Uchida *et al.* The tensile strength and elongation at break of fibrous cellulose acetate nanocomposites film were improved by 446 and 56 % respectively with the addition of ZnO nanoparticle [160]. Hamad *et al*. prepared PMMA/ ZnO composite. ZnO is added to improve the antimicrobial property of pure PMMA. For 5 % loading of ZnO the composite shows good mechanical as well as antimicrobial characters [161]. The wear and friction characteristics of polytetraethylene (PTFE) composite filled with nano ZnO was investigated by Li *et al*. [162]. ZnO offers anti-wear mechanism to the polymer matrix by changing the structure of PTFE and best anti-wear property was obtained for PTFE loaded with 15 vol % nano ZnO.

To obtain high dielectric constant polymer composite with higher breakdown strength, ZnO has been used as filler in polymer matrices. Bouropoulos *et al*. describes the dielectric properties of ZnO/PVA composite fabricated *via* simple solution casting method by incorporating ZnO (having size 59, 82 and 150 nm) prepared *via* thermal decomposition method [163]. As the particle size decreasing the interfacial polarization shifts to higher frequencies with decreasing intensity. Hong *et al*. prepared ZnO/low density polyethylene nanocomposites. The high surface area of ZnO nanoparticle enables the introduction of surface modifying agent with high dielectric constant into composites and thereby modifies the dielectric properties of composite [156]. Vaishnav *et al.* prepared poly (aryletherketon)/ZnO composite *via* ball milling followed by hot pressing [164]. The dielectric properties and thermal stability of polymer increased significantly. Wu *et al.* introduced novel ZnO three dimensional superstructures into poly (vinylidene fluoride) (PVDF) matrix to obtain high-k polymer composite with high breakdown strength [165].

1.5.3 Electroceramics

Electroceramics are functional materials which have been technically utilized for their unique piezoelectric, ferroelectric, dielectric, electro-optic and pyroelectric properties [166]. The research and development in electroceramic field include investigations on wide spectrum of inorganic material from the level of crystalline lattice to the final device. The properties and applications of electroceramics rely on compositional and structural control, particle morphology and distribution of dopants. Electroceramics have become a key material for various technologies including, conversion and storage of energy, communication, power engineering, medicine and electronics [166]. Electroceramic materials include dielectric, conducting, semiconducting, superconducting and magnetic ceramics used in a variety of diverse applications. Comparatively high thermal conductivity, high heat capacity, high temperature stability, good electronic properties along with relatively lower expansion coefficient of ZnO are desirable for electroceramic applications [167]. ZnO is a promising semiconducting material for device applications. It possess direct wide band gap in the near-UV region and large free exciton binding energy which enables excitonic emission persists at or even above the room temperature [3]. This makes ZnO a potential material for various electronic and optoelectronic application [4, 5]. Among the various electroceramic devices based on ZnO, varistors attains intense attention due to its wide applications in electronics and communication systems.

1.5.3.1 Varistors

The lightning and electrostatic discharge resulted in sudden variation in the circuit voltage. Varistors are electroceramic devices used in electronics and communication field to sense and limit over voltages ranging from few to a several million volts [48]. ZnO varistor was invented by Matsuoka in 1970 [168]. Varistors are voltage dependant non-linear devices with electric characteristics similar to back-to-back zener diode. When over voltage comes the varistor resistance varies from an open circuit state to conducting state and limit the over voltage to a harmless level and protect the electronic components [48]. The unique non-linear electrical behaviour of varistors originated from the microstructure of varistor ceramics containing conducting ZnO grains bounded by electrically insulating grain boundary as shown in Figure 1.6 (a). In a typical varistor circuit the varistor is connected in parallel (Figure 1.6 (b)) with the component to be protected. When over voltage comes the varistor offers low resistant path and draws over current to the ground.

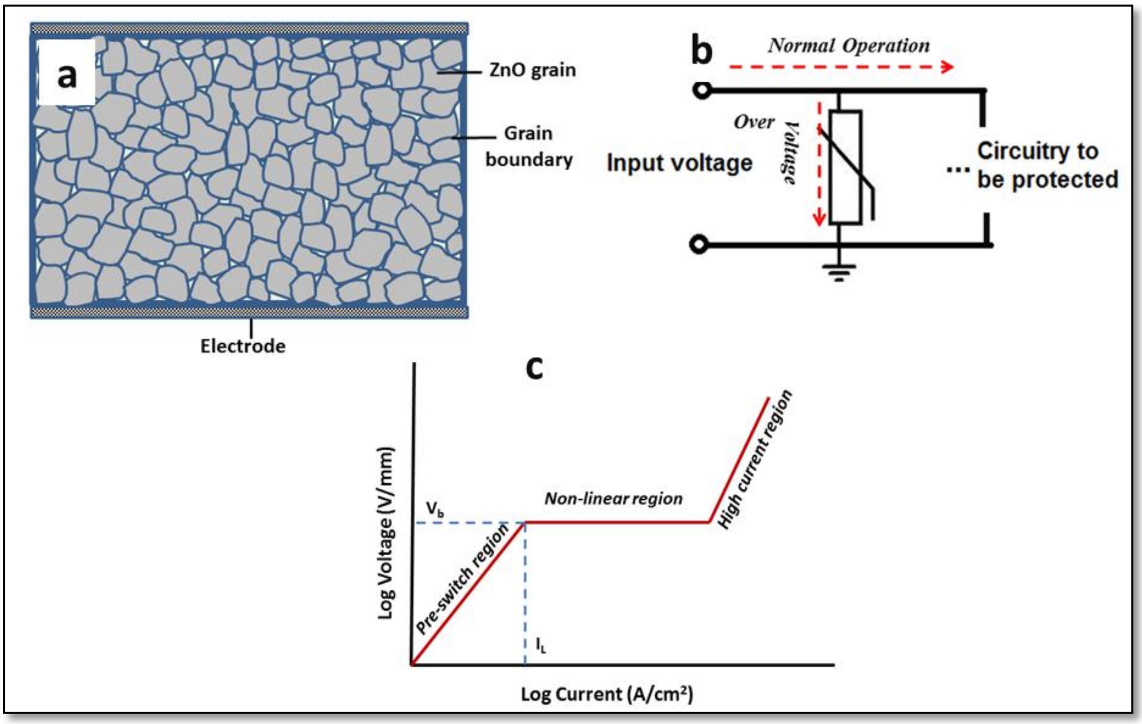

Figure 1.6: a) Typical microstructure of varistor showing grains and grain boundary, b) basis varistor circuit and c) current voltage characteristic of a typical varistor.

The current–voltage characteristic of varistor is shown in Figure 1.6 (c). As evidenced from the Figure 1.6 (c) the I-V curve of varistors are divided into three regions: pre-switch region, non-linear region and high current region [48]. In pre-switch region the resistivity of varistor is very high and behaves like an open circuit. The non-linear region is the varistor action region wherein for a large change in current, varistor voltage remains almost constant. The current-voltage characteristics of this region can be expressed by the Equation,

$$I=K\,(V)^{\alpha} \qquad (1.1)$$

K is the material constant and α is the non-linear coefficient and is given by the relation,

$$\alpha = \log(I_2/I_1)/\log(V_2/V_1) \qquad (1.2)$$

V_1 and V_2 are the voltages corresponding to the current I_1 and I_2. Higher the value of α better will be the device performance. Another important parameter for varistor performance is the break down voltage (V_b) which indicates the transition from linear region to non-linear region. In the high current region varistor acts like nearly short circuit.

Pure ZnO is a n-type semiconductor with ohmic behaviour. In order to make it non-linear material various metal oxides (Bi_2O_3, Sb_2O_3, MnO, Al_2O_3, CoO, and Cr_2O_3) are incorporated into ZnO [168]. These oxides have great effect on varistor properties, sintering temperature and grain growth.

1.5.5.1 Processing of Varistor Material

Conventionally ZnO varistors are prepared by mixing the precursors of ZnO and other varistor additives. The pressed varistor pellets are sintered at temperature 1100-1200 ^{o}C to obtain sintered dense ZnO varistors. New processing routes are designed to meet the demand for smaller varistors with improved performance for miniaturized electronic devices. By careful control of the varistor microstructure *via* chemical processing routes like precipitation route, sol-gel synthesis, plasma pyrolysis, micro emulsion method and combustion method it is possible to produce varistors with high break down voltage and optimum electrical characteristics. Novel sintering techniques such as spark plasma sintering, step sintering, microwave assisted sintering are also employed to tailor the microstructural properties of varistors.

Gas phase synthesis: Lin *et al*. have employed plasma pyrolysis for the synthesis of nanometer sized varistor precursor [169]. The resultant varistor sintered at 1050 ^{o}C showed excellent electronic properties with break down voltage of 500 V.mm^{-1} and non-linear coefficient of 54. However the high production cost prevents its implementation on an industrial scale. High quality ZnO varistor film was prepared from Zn powder *via* gas discharge activated reaction evaporation [170]. In this the varistor parameters are tuned by simply changing the synthesisconditions. The α value varies from 33-62 depending on the number of coating. It is interesting to note that this good varistor characteristic were obtained without the addition of any dopants. This method is promising for small scale device fabrication [170].

Combustion synthesis: The synthesis of doped nano crystalline ZnO *via* combustion synthesis with sucrose was reported by Hembram *et al*. [171]. A break down voltage 950 V. mm^{-1} and non-linear coefficient of 42 were obtained. The most important advantages of this synthesis is shorter processing time and potential for scale-up. The combustion synthesis demonstrates a single step fabrication of ZnO varistor with enhanced properties.

Liquid phase synthesis: The liquid phase processing possesses advantages of high purity, homogeneity in dopant distribution and low temperature of processing. The multi-dopant ZnO varistor system was prepared by mixing relevant metal salt along with ZnO precursor solution. In solution phase synthesis the dopant homogeneity in ZnO matrix can be achieved at atomic level. Some of the liquid phase method for varistor material synthesis is outlined below.

The varistor fabrication by *precipitation technique* is an inexpensive and has a potential for large scale production. Haile *et al.* synthesised spherical ZnO particles and are coated by dopant metal salt by precipitation technique [172]. The varistor fabricated shows a breakdown voltage of 180 V. mm^{-1} and non-linear coefficient 44. Viswanath *et al.* reported the fabrication of varistor material from zinc perchlorate *via precipitation technique* and doped with oxides of Bi, Sb, Co, Sn, B and Cu [173]. The material produced shows breakdown voltage 3000 V. mm^{-1} and non-linear coefficient value 50. Wang *et al.* reported the fabrication of low voltage varistor *via* co-precipitation route and a breakdown voltage of 87 V. mm^{-1} and non-linear coefficient of 32 were obtained [174]. The synthesis of ZnO nano particle *via* two step precipitation was reported by Yang *et al.* These particles were mixed with various varistor additives and sintered at 1200 ^{o}C [48]. The varistor obtained showed a break down voltage of 492 V. mm^{-1} with non-linear coefficient 56. Li *et al*. prepared varistor powder *via* precipitation reaction in organic solvent [175]. The obtained ZnO particles covered with dopants are calcined and sintered at 1050 ^{o}C. The varistor obtained shows a breakdown voltage of 540 V. mm^{-1} with a non-linear coefficient of 50.

Amine processing is another liquid phase processing route for preparing uniform powder for production of ZnO varistors. Hishita *et al.* prepared ZnO varistors *via* amine processing in which they have used diethylamine to co-precipitate all the reactants [176]. High breakdown voltage of 711 V. mm^{-1} and non-linear coefficient of 50 were achieved in this case.

Sol-gel processing of varistor material provides homogeneous distribution of dopants at molecular level. Generally sol-gel synthesis of varistor is carried out in two ways. In first method ZnO produced *via* sol-gel route and subsequently metal salt added into it. In the second route gel is prepared from Zn and metal salt precursor solution. Pillai *et al.*

synthesised ZnO nanoparticle *via* sol gel route and a core-shell type doped varistor particle were synthesised using ZnO particle and metal salt dopants [177]. The core-shell type varistor particle showed good varistor characteristics but the densification obtained was inadequate for industrial fabrication of varistors. Pillai *et al* adopted sol-gel based processing for the large scale production of varistors which produce fully dense varistor with superior properties [178]. The varistor obtained showed higher breakdown voltage of 941 V. mm^{-1} and higher densification at lower sintering temperature compared to other laboratory scale methods. Table (1.6) summarised various chemical processing for the fabrication of ZnO varistors and compared their varistor properties.

Table 1.6: Synthesis strategies for the varistor material and comparison of electrical properties.

Processing route	**Particle size**	**Sintering temperature (^{o}C)**	**Non-linear coefficient**	**Breakdown voltage (V/mm)**	**Ref.**
Plasma pyrolysis Lin	10-50 nm	1050	54	500	169
Combustion *Hembram et al.*	15-250 nm	1050	42	205	171
Amine processing *Hishita et al.*	200 nm	1050	50	711	176
Precipitation					
Viswanath	1-3µm	750	50	3000	173
Haile et al.	-	1200	44	180	172
Core-shell *Pillai et al.*	34 nm	1050	33	850	177
Sol-gel					
Pillai	15 nm	1050	33	859	178
Nobrega et al.		1100	26	800	179

Thus compared to the conventional industrial processing of varistor, chemical processing of varistors have remarkable benefits. However, for industrial scale production of varistors these methods are not suitable due to, 1) expensive precursor, 2) longer processing time, and 3) chemical synthesis requires large quantity of solvent.

1.6 Definition of the Present Research Problem

The promising large scale applications of nano ZnO in the fields of transparent conducting oxide coatings, UV/NIR shielding optical coatings on windows, antiglare/light reflective automobile window glass, water repellent/fungal growth resistant paints, filler material for various polymer matrix, high energy button varistors and other miniaturized electronic devices etc., have generated significant interest among the industries to produce high quality nano ZnO in a most economical way. Chemical techniques often produced sulphate, nitrate and chloride based effluents during bulk processing of ZnO. Physical methods require expensive processing equipment, presence of catalysts and reaction temperatures as high as 950 ^{o}C. Therefore, it is extremely important for the scientific community to identify a process for the large scale production of nano ZnO in a more environmental friendly manner. This triggered tremendous motivation to explore the possibilities of deriving high quality nano ZnO directly from an economically cheap source.

Zn dust is a by-product generated in bulk quantity by various chemical industries. Presently, the consumption of Zn dust is in the low-value products like primers and paints. Hence the industries are serious about the value addition of Zn dust mainly by converting Zn dust into nano ZnO. Number of works is reported on thermal oxidation of metallic Zn for producing ZnO nanostructures. However, most of them have used Zn in the form of Zn nanowire, Zn foil, Zn thin film *etc*. [Table 1.5]. The process became more economical if the Zn dust is directly transformed to nano ZnO. In the present thesis direct transformation of Zn dust into ZnO nanostructures is mainly investigated. The Zn dust was further explored for various high-end industrial applications including paint and coating, ZnO varistors, high-k dielectrics *etc.*

Research Problem: Explore Zn dust for the direct conversion to bulk ZnO nanostructures through environmentally friendly innovative methods; Investigate the conversion of Zn dust into ZnO *via* Aqueous mechanical oxidation [AMOx], Direct thermal oxidation [CTO], and Microwave assisted thermal oxidation [MTO] techniques and explore the Zn dust derived nano ZnO and cermet structures for potential industrial products such as functional coatings, high energy varistors and multifunctional filler for epoxy/PVC composites.

The major objectives of the thesis are as follows,

1.7 Objectives

- Room temperature synthesis of nano ZnO *via* direct oxidation of Zn dust
- Role of surfactants assisted milling on the morphological evolution and sintering behaviour of ZnO derived from Zn dust.
- Investigations on the oxidation of Zn dust *via* conventional thermal oxidation and microwave assisted thermal oxidation and asses the ZnO nanostructures for functional coatings.
- Design of Zn-ZnO metal-semiconductor cermet fillers for high-k epoxy composites.
- Processing of high energy varistors from Zn /ZnO cermet reactants and fabrication of PVC/microvaristor composites.

The research works were carried out under the above mentioned framework. The various research components covered in the current thesis are briefly described below;

Processing of nano ZnO has been attempted *via* a facile, green synthesis approach namely *'aqueous mechanical-oxidation'* of Zn dust. The mechanical deformation of Zn dust at different interval of time was investigated systematically. The mechanism of oxidation of Zn dust during aqueous milling was proposed and detection of gas produced in the milling chamber was also carried out. Effect of surfactant assisted milling on particle morphology and sintering of ZnO are also reported.

The evolution of ZnO nanostructures *via* thermal oxidation of mechanically activated Zn dust was carried out. The effects of conventional thermal oxidation and microwave assisted thermal oxidation on the evolution of various ZnO morphologies are investigated. The industrial applications of nano ZnO obtained were tested for corrosion resistant paints and NIR reflective coatings.

Design of Zn-ZnO metal–semiconductor cermet architectures *via* simple calcination was carried out at different temperatures. The effect of interface design by tuning of metal / semiconductor ratio of Zn/ZnO cermet particle was studied on dielectric properties of epoxy composites. The enhancement in heat dissipation property of epoxy composite by the addition of cermet particle was studied by measuring the thermal conductivity of the composite.

Fabrication of ultrafine grained ZnO varistor from Zn dust *via* cermet route was carried out. The advantages of Zn dust on sintering and varistor characteristic at different temperature were studied and were compared with that of commercial ZnO. Further the microvaristor filler derived from cermet source was used as multifunctional filler in PVC matrix. The effect of microvaristor filler on the dielectric properties, thermal stability, UV resistance and mechanical stability of PVC matrix were explored.

1.8 Novelty and Sustainability Factors of the Present Thesis

The novelty of the present thesis in general lies in the selection of low-cost Zn dust for the production of ZnO nanostructures and other functional architectures. From various reported works, the most common ZnO precursors used for the synthesis of nano ZnO *via* chemical route are listed in Table 1.3 and 1.5. Moreover, that chemical synthesis routes requires stringent processing conditions.

Table 1.6: Price comparison of ZnO precursors marketed by different suppliers.

Supplier	Product Name	Price/Kg
Sigma Aldrich[1]	Zinc acetate dihydrate	1233
	Zinc chloride	4952
	Zinc nitrate hexahydrate	3988
	Zinc sulfate	4300
	Zinc oxide	26075
	Zinc	8345
Alfa Aesar[2]	Zinc acetate dihydrate	3563
	Zinc chloride	9319
	Zinc nitrate hexahydrate	6044
	Zinc sulfate	6600
	Zinc oxide	4611
	Zinc	5821
Merck[3]	Zinc acetate dihydrate	7370
	Zinc chloride	8510
	Zinc nitrate hexahydrate	980
	Zinc sulfate	5250
	Zinc oxide	8700
	Zinc	1660
S D Fine[4]	Zinc acetate dihydrate	950
	Zinc chloride	728
	Zinc nitrate hexahydrate	1118
	Zinc sulfate	502
	Zinc oxide	1132
	Zinc	1036
Binani Zinc Pvt. Ltd.	Zinc dust	5-6

[1] *https://www.sigmaaldrich.com*, [2]*https://www.alfa.com*,[3]*www.merck.co.in/en/index.html*
[4] *www.sdfine.com/.*

Till date no reports are there on the use of Zn dust, a partially avoided industrial by product not only for synthesis of nano ZnO but also for any high-end applications. The starting material used in the entire study is Zn dust supplied by Binani Zinc Pvt Limited, India. It costs approximately Rs.6 per kilogram which is cheap and affordable for the bulk processing of nano ZnO.

The price comparison of various ZnO precursors from different suppliers used for the preparation of nano ZnO is given in the Table 1.6. Thus the choice of the low value precursor Zn dust in this work itself underlines a 'waste to wealth' engineering initiative. The value addition to this low cost product by a simple sustainable technique certainly would be an innovative step which many industries can take up with some least capital investment. Moreover, the whole thesis is dedicated to describe the direct conversion of Zn dust into ZnO nanostructures to produce exciting ZnO nano morphologies and high-end industrial products mainly functional paints, intelligent coatings, high-k composite dielectrics and high energy varistors.

References

[1] Dai, Z.R., Pan, Z.W. and Wang, Z.L. “Novel nanostructures of functional oxides synthesized by thermal evaporation.” *Advanced Functional Materials* 13.1 (2003): 9-24.

[2] Ahmad, M. and Zhu, J. "ZnO based advanced functional nanostructures: synthesis, properties and applications." *Journal of Materials chemistry* 21.3 (2011): 599-614.

[3] Wang, Z.L. "Zinc oxide nanostructures: growth, properties and applications." *Journal of physics: condensed matter* 16.25 (2004): R829.

[4] Kao, P.C., Chu, S.Y., Li, B.J., Chang, J.W., Huang, H.H., Fang, Y.C. and Chang, R.C. "Low temperature solution-synthesis and photoluminescence properties of ZnO nanowires." *Journal of Alloys and Compounds* 467.1-2 (2009): 342-346.

[5] Shen, X., Xu, W., Xu, J., Liang, G., Yang, H. and Yao, M. "Quasi-solid-state dye-sensitized solar cells based on gel electrolytes containing different alkali metal iodide salts." Solid State Ionics 179.35-36 (2008): 2027-2030.

[6] Khan, A., Jadwisienczak, W.M., Lozykowski, H.J. and Kordesch. "Catalyst-free synthesis and luminescence of aligned ZnO nanorods." *Physica E: Low-Dimensional Systems and Nanostructures* 39.2 (2007): 258-261.

[7] Zhang, Q., Yu, K., Bai, W., Wang, Q., Xu, F., Zhu, Z., Dai, N. and Sun, Y. "Synthesis, optical and field emission properties of three different ZnO nanostructures." *Materials Letters* 61.18 (2007): 3890-3892.

[8] Comini, E. "Metal oxide nano-crystals for gas sensing." *Analytica chimica acta* 568.1-2 (2006): 28-40.

[9] Zhang, Q., Zhang, Y., Yu, K. and Zhu, Z. "Photoluminescence and field-emission characteristics of ZnO nanowires synthesized by two-step method." *Vacuum* 82.1 (2007): 30-34.

[10] Pradhan, B., Batabyal, S.K. and Pal, A.J. "Vertically aligned ZnO nanowire arrays in Rose Bengal-based dye-sensitized solar cells." Solar Energy Materials and Solar Cells 91.9 (2007): 769-773.

[11] Black, K., Jones, A.C., Chalker, P.R., Gaskell, J.M., Murray, R.T., Joyce, T.B. and Rushworth, S.A. "MOCVD of ZnO thin films for potential use as compliant layers for GaN on Si." Journal of Crystal Growth310.5 (2008): 1010-1014.

[12] Song, J.K., Willer, U., Szarko, J.M., Leone, S.R., Li, S. and Zhao, Y. "Ultrafast upconversion probing of lasing dynamics in single ZnO nanowire lasers." *The Journal of Physical Chemistry C* 112.5 (2008): 1679-1684.

[13] Wang, M. and Zhang, L. "The influence of orientation on the photoluminescence behavior of ZnO thin films obtained by chemical solution deposition." *Materials Letters* 63.2 (2009): 301-303.

[14] Georgekutty, Reenamole, Michael K. Seery, and Suresh C. Pillai. "A highly efficient Ag-ZnO photocatalyst: synthesis, properties, and mechanism." *The Journal of Physical Chemistry C* 112.35 (2008): 13563-13570.

[15] Djurišić, A.B., Chen, X., Leung, Y.H. and Ng, A.M.C. "ZnO nanostructures: growth, properties and applications." *Journal of Materials Chemistry*22.14 (2012): 6526-6535.

[16] Bagnall, D.M., Chen, Y.F., Zhu, Z., Yao, T., Koyama, S., Shen, M.Y. and Goto, T. "Optically pumped lasing of ZnO at room temperature." Applied Physics Letters 70.17 (1997): 2230-2232.

[17] Banerjee, D., Lao, J.Y., Wang, D.Z., Huang, J.Y., Ren, Z.F., Steeves, D., Kimball, B. and Sennett, M. "Large-quantity free-standing ZnO nanowires." *Applied Physics Letters* 83.10 (2003): 2061-2063.

[18] Xu, S. and Wang, Z.L. "One-dimensional ZnO nanostructures: solution growth and functional properties." *Nano Research* 4.11 (2011): 1013-1098.

[19] Hahn, Y-B. "Zinc oxide nanostructures and their applications." *Korean Journal of Chemical Engineering* 28.9 (2011): 1797

[20] Wahab, R., Ansari, S.G., Kim, Y.S., Seo, H.K. and Shin, H.S. "Room temperature synthesis of needle-shaped ZnO nanorods via sonochemical method." *Applied Surface Science* 253.18 (2007): 7622-7626.

[21] Wu, J.J., Liu, S.C., Wu, C.T., Chen, K.H. and Chen, L.C. "Heterostructures of ZnO–Zn coaxial nanocables and ZnO nanotubes." *Applied Physics Letters*81.7 (2002): 1312-1314.

[22] Mang, A. and Reimann, K. "Band gaps, crystal-field splitting, spin-orbit coupling, and exciton binding energies in ZnO under hydrostatic pressure." *Solid state communications* 94.4 (1995): 251-254.

[23] Madelung, O, ed. *Semiconductors—basic data*. Springer Science & Business Media, 2012.

[24] Look, D. C. "MATER SCI ENG B." Mater. Sci. Eng., B 80 (2001): 383.

[25] Films, T. "Heterostructures for Oxide Electronics, edited by SB Ogale." (2005).

[26] Özgür, Ü., Alivov, Y.I., Liu, C., Teke, A., Reshchikov, M., Doğan, S., Avrutin, V.C.S.J., Cho, S.J. and Morkoc, H. "A comprehensive review of ZnO materials and devices." Journal of applied physics 98.4 (2005): 11.

[27] Jagadish, C. and Pearton, S.J. eds. *Zinc oxide bulk, thin films and nanostructures: processing, properties, and applications*. Elsevier, 2011.

[28] Zinc Oxide, A. "Material for Micro-and Optoelectronic Applications, ed. NH Nickel and E. Terukov." (2005).

[29] Janotti, A. and Van de Walle, C.G. "Fundamentals of zinc oxide as a semiconductor." *Reports on progress in physics* 72.12 (2009): 126501.

[30] Ohtomo, A., Kawasaki, M., Sakurai, Y., Ohkubo, I., Shiroki, R., Yoshida, Y., Yasuda, T., Segawa, Y. and Koinuma, H. "Fabrication of alloys and superlattices based on ZnO towards ultraviolet laser." *Materials Science and Engineering: B* 56.2-3 (1998): 263-266.

[31] Gruber, T., Kirchner, C., Kling, R., Reuss, F. and Waag, A. "ZnMgO epilayers and ZnO–ZnMgO quantum wells for optoelectronic applications in the blue and UV spectral region." *Applied physics letters* 84.26 (2004): 5359-5361.

[32] Jin, Y., Zhang, B., Yang, S., Wang, Y., Chen, J., Zhang, H., Huang, C., Cao, C., Cao, H. and Chang, R.P. "Room temperature UV emission of MgxZn1− xO films." *Solid State Communications* 119.6 (2001): 409-413.

[33] Gruber, T., Kirchner, C., Kling, R., Reuss, F., Waag, A., Bertram, F., Forster, D., Christen, J. and Schreck, M. "Optical and structural analysis of ZnCdO layers grown by metalorganic vapor-phase epitaxy." *Applied physics letters* 83.16 (2003): 3290-3292.

[34] Makino, T., Segawa, Y., Kawasaki, M., Ohtomo, A., Shiroki, R., Tamura, K., Yasuda, T. and Koinuma, H. "Band gap engineering based on Mg x Zn 1− x O and Cd y Zn 1− y O ternary alloy films." *Applied Physics Letters* 78.9 (2001): 1237-1239.

[35] Klingshirn, C. "ZnO: material, physics and applications." *ChemPhysChem* 8.6 (2007): 782-803.

[36] Yuliah, Y., Bahtiar, A., Fitrilawati and Sirega. "The optical band gap investigation of PVP-capped ZnO nanoparticles synthesized by sol-gel method." *AIP Conference Proceedings*. Vol. 1712. No. 1. AIP Publishing, 2016.

[37] Wang, Z. L. "Nanostructures of zinc oxide." *Materials today* 7.6 (2004): 26-33.

[38] Kumar, S.S., Venkateswarlu, P., Rao, V.R. and Rao, G.N. Synthesis, characterization and optical properties of zinc oxide nanoparticles. *International Nano Letters*, *3*(1), p.30.

[39]

[40] Kar, S. and Santra, S. "ZnO nanotube arrays and nanotube-based paint-brush structures: a simple methodology of fabricating hierarchical nanostructures with self-assembled junctions and branches." *The Journal of Physical Chemistry C* 112.22 (2008): 8144-8146.

[41] Kar, S., Pal, B.N., Chaudhuri, S. and Chakravorty, D. One-dimensional ZnO nanostructure arrays: Synthesis and characterization." *The Journal of Physical Chemistry B* 110.10 (2006): 4605-4611.

[42] Rao, C.N.R., Deepak, F.L., Gundiah, G. and Govindaraj, A. "Inorganic nanowires." *Progress in Solid State Chemistry* 31.1-2 (2003): 5-147.

[43] Xia, Y., Yang, P., Sun, Y., Wu, Y., Mayers, B., Gates, B., Yin, Y., Kim, F. and Yan, H. "One-dimensional nanostructures: synthesis, characterization, and applications." *Advanced materials* 15.5 (2003): 353-389.

[44] Reynolds, D.C., Look, D.C. and Jogai, B. "Optically pumped ultraviolet lasing from ZnO." *Solid State Communications* 99.12 (1996): 873-875.

[45] Moezzi, A., McDonagh, A.M. and Cortie, M.B. "Zinc oxide particles: Synthesis, properties and applications." *Chemical engineering journal* 185 (2012): 1-22

[46] Liang, H.Q., Pan, L.Z. and Liu, Z.J. "Synthesis and photoluminescence properties of ZnO nanowires and nanorods by thermal oxidation of Zn precursors." *Materials Letters* 62.12-13 (2008): 1797-1800.

[47] Djurišić, A.B., Ng, A.M.C. and Chen, X.Y. "ZnO nanostructures for optoelectronics: material properties and device applications." *Progress in quantum electronics* 34.4 (2010): 191-259.

[48] Pillai, S.C., Kelly, J.M., Ramesh, R. and McCormack, D.E "Advances in the synthesis of ZnO nanomaterials for varistor devices." *Journal of Materials Chemistry C* 1.20 (2013): 3268-3281.

[49] Look, D.C. "Recent advances in ZnO materials and devices." *Materials Science and Engineering: B* 80.1-3 (2001): 383-387.

[50] Molarius, J., Kaitila, J., Pensala, T. and Ylilammi, M. "Piezoelectric ZnO films by rf sputtering." *Journal of Materials Science: Materials in Electronics* 14.5-7 (2003): 431-435.

[51] Shiosaki, T. and Kawabata, A. "Low-frequency piezoelectric-transducer applications of ZnO film." *Applied Physics Letters* 25.1 (1974): 10-11.

[52] Lee, J.B., Lee, H.J., Seo, S.H. and Park, J.S. "Characterization of undoped and Cu-doped ZnO films for surface acoustic wave applications." *Thin Solid Films* 398 (2001): 641-646.

[53] Wang, J.X., Sun, X.W., Yang, Y., Huang, H., Lee, Y.C., Tan, O.K. and Vayssieres, L. "Hydrothermally grown oriented ZnO nanorod arrays for gas sensing applications." *Nanotechnology*17.19 (2006): 4995.

[54] Liu, C.H., Yiu, W.C., Au, F.C.K., Ding, J.X., Lee, C.S. and Lee, S.T. "Electrical properties of zinc oxide nanowires and intramolecular p–n junctions." *Applied physics letters*83.15 (2003): 3168-3170.

[55] Zhao, M.H., Wang, Z.L. and Mao, S.X. "Piezoelectric characterization of individual zinc oxide nanobelt probed by piezoresponse force microscope." *Nano Letters* 4.4 (2004): 587-590.

[56] Shionoya, S., Yen, W.M. and Yamamoto, H. eds. *Phosphor handbook*. CRC press, 2006.

[57] Rodnyi, P.A. and Khodyuk, I.V. "Optical and luminescence properties of zinc oxide." *Optics and Spectroscopy* 111.5 (2011): 776-785.

[58] Nakanishi, Y., Miyake, A., Kominami, H., Aoki, T., Hatanaka, Y. and Shimaoka, G. "Preparation of ZnO thin films for high-resolution field emission display by electron beam evaporation." *Applied Surface Science* 142.1-4 (1999): 233-236.

[59] Holloway, P.H., Sebastian, J., Trottier, T., Swart, H. and Petersen, R.O. "Production and control of vacuum in field emission flat panel displays." *Solid State Technology* 38.8 (1995): 47-52.

[60] Look, D.C., Reynolds, D.C., Litton, C.W., Jones, R.L., Eason, D.B. and Cantwell, G. Characterization of homoepitaxial p-type ZnO grown by molecular beam epitaxy. *Applied physics letters.*

[61] Yoo, D.G., Nam, S.H., Kim, M.H., Jeong, S.H., Jee, H.G., Lee, H.J., Lee, N.E., Hong, B.Y., Kim, Y.J., Jung, D. and Boo, J.H. "Fabrication of the ZnO thin films using wet-chemical etching processes on application for organic light emitting diode (OLED) devices." *Surface and Coatings Technology* 202.22-23 (2008): 5476-5479.

[62] Maki, H., Ikoma, T., Sakaguchi, I., Ohashi, N., Haneda, H., Tanaka, J. and Ichinose, N. "Control of surface morphology of ZnO (0 0 0 1) by hydrochloric acid etching." *Thin Solid Films* 411.1 (2002): 91-95.

[63] Coskun, C., Look, D.C., Farlow, G.C. and Sizelove, J.R. "Radiation hardness of ZnO at low temperatures." *Semiconductor science and technology* 19.6 (2004): 752.

[64] Liu, H.F., Chua, S.J., Hu, G.X., Gong, H. and Xiang, N. "Effects of substrate on the structure and orientation of ZnO thin film grown by rf-magnetron sputtering." *Journal of Applied Physics* 102.8 (2007): 083529.

[65] Heinze, S., Krtschil, A., Bläsing, J., Hempel, T., Veit, P., Dadgar, A., Christen, J. and Krost, A. "Homoepitaxial growth of ZnO by metalorganic vapor phase epitaxy in two-dimensional growth mode." *Journal of Crystal Growth* 308.1 (2007): 170-175.

[66] Dadgar, A., Schulze, F., Wienecke, M., Gadanecz, A., Bläsing, J., Veit, P., Hempel, T., Diez, A., Christen, J. and Krost, A. "Epitaxy of GaN on silicon—impact of symmetry and surface reconstruction." *New Journal of Physics* 9.10 (2007): 389.

[67] Sim, L., Ramanan, S.R., Ismail, H., Seetharamu, K.N. and Goh, T.J. "Thermal characterization of Al2O3 and ZnO reinforced silicone rubber as thermal pads for heat dissipation purposes." *Thermochimica acta* 430.1-2 (2005): 155-165.

[68] Mu, Q., Feng, S. and Diao, G. "Thermal conductivity of silicone rubber filled with ZnO." *Polymer composites* 28.2 (2007): 125-130.

[69] Vadivelu, M.A., Kumar, C.R. and Joshi, G.M. Ramesh Kumar, and Girish M. Joshi. "Polymer composites for thermal management: a review." *Composite Interfaces* 23.9 (2016): 847-872.

[70] Sahu, D.R., Liu, C.P., Wang, R.C., Kuo, C.L. and Huang, J.L. "Growth and application of ZnO nanostructures." *International Journal of Applied Ceramic Technology* 10.5 (2013): 814-838.

[71] Tasker, P. W. "The stability of ionic crystal surfaces." Journal of Physics C: Solid State Physics 12.22 (1979): 4977.

[72] Wang, Z.L. "Zinc oxide nanostructures: growth, properties and applications." *Journal of physics: condensed matter* 16.25 (2004): R829.

[73] Wander, A., Schedin, F., Steadman, P., Norris, A., McGrath, R., Turner, T.S., Thornton, G. and Harrison, N.M. "Stability of polar oxide surfaces." *Physical review letters* 86.17 (2001): 3811.

[74] Staemmler, V., Fink, K., Meyer, B., Marx, D., Kunat, M., Girol, S.G., Burghaus, U. and Wöll, C. "Stabilization of polar ZnO surfaces: validating microscopic models by using CO as a probe molecule." *Physical review letters* 90.10 (2003): 106102.

[75] Stanković, A., Veselinović, L.J., Škapin, S.D., Marković, S. and Uskoković, D. "Controlled mechanochemically assisted synthesis of ZnO nanopowders in the presence of oxalic acid." *Journal of materials science* 46.11 (2011): 3716-3724.

[76] Aghababazadeh, R., Mazinani, B., Mirhabibi, A. and Tamizifar, M. "ZnO nanoparticles synthesised by mechanochemical processing." *Journal of Physics: Conference Series*. Vol. 26. No. 1. IOP Publishing, 2006.

[77] Lanje, A.S., Sharma, S.J., Ningthoujam, R.S., Ahn, J.S. and Pode, R.B. "Low temperature dielectric studies of zinc oxide (ZnO) nanoparticles prepared by precipitation method." *Advanced Powder Technology* 24.1 (2013): 331-335.

[78] Hong, R., Pan, T., Qian, J. and Li, H. "Synthesis and surface modification of ZnO nanoparticles." *Chemical Engineering Journal* 119.2-3 (2006): 71-81.

[79] Ma, C.L. and Sun, X.D. "Preparation of nanocrystalline metal oxide powders with the surfactant-mediated method." *Inorganic Chemistry Communications* 5.10 (2002): 751-755.

[80] Li, P., Wei, Y., Liu, H. and Wang, X.K. "Growth of well-defined ZnO microparticles with additives from aqueous solution." *Journal of solid state chemistry* 178.3 (2005): 855-860.

[81] Benhebal, H., Chaib, M., Salmon, T., Geens, J., Leonard, A., Lambert, S.D., Crine, M. and Heinrichs, B. "Photocatalytic degradation of phenol and benzoic acid using zinc oxide powders prepared by the sol–gel process." *Alexandria Engineering Journal* 52.3 (2013): 517-523.

[82] Yue, S., Yan, Z., Shi, Y. and Ran, G. "Synthesis of zinc oxide nanotubes within ultrathin anodic aluminum oxide membrane by sol–gel method." *Materials Letters* 98 (2013): 246-249.

[83] Dem'Yanets, L.N., Li, L.E. and Uvarova, T.G. "Zinc oxide: hydrothermal growth of nano-and bulk crystals and their luminescent properties." *Journal of materials science* 41.5 (2006): 1439-1444.

[84] Hu, X.L., Zhu, Y.J. and Wang, S.W. "Sonochemical and microwave-assisted synthesis of linked single-crystalline ZnO rods." *Materials Chemistry and physics*88.2-3 (2004): 421-426.

[85] Li, X., He, G., Xiao, G., Liu, H. and Wang, M. "Synthesis and morphology control of ZnO nanostructures in microemulsions." *Journal of Colloid and Interface Science* 333.2 (2009): 465-473.

[86] Wen, X., Fang, Y., Pang, Q., Yang, C., Wang, J., Ge, W., Wong, K.S. and Yang, S. "ZnO nanobelt arrays grown directly from and on zinc substrates: synthesis, characterization, and applications." *The Journal of Physical Chemistry B* 109.32 (2005): 15303-15308.

[87] Yuan, L., Wang, C., Cai, R., Wang, Y. and Zhou, G. "Temperature-dependent growth mechanism and microstructure of ZnO nanostructures grown from the thermal oxidation of zinc." *Journal of Crystal Growth* 390 (2014): 101-108.

[88] Fang, F., Zhao, D.X., Zhang, J.Y., Shen, D.Z., Lu, Y.M., Fan, X.W., Li, B.H. and Wang, X.H. "The influence of growth temperature on ZnO nanowires." *Materials Letters* 62.6-7 (2008): 1092-1095.

[89] Hu, W.S., Liu, Z.G., Sun, J., Zhu, S.N., Xu, Q.Q., Feng, D. and Ji, Z.M. "Optical properties of pulsed laser deposited ZnO thin films." *Journal of Physics and Chemistry of Solids*58.6 (1997): 853-857.

[90] Tsoutsouva, M.G., Panagopoulos, C.N., Papadimitriou, D., Fasaki, I. and Kompitsas, M. "ZnO thin films prepared by pulsed laser deposition." *Materials Science and Engineering: B* 176.6 (2011): 480-483.

[91] Matsubara, K., Fons, P., Iwata, K., Yamada, A. and Niki, S. "Room-temperature deposition of Al-doped ZnO films by oxygen radical-assisted pulsed laser deposition." *Thin Solid Films* 422.1-2 (2002): 176-179.

[92] Morintale, E., Constantinescu, C. and Dinescu, M. "Thin films development by pulsed laser-assisted deposition." *Physics AUC* 20.1 (2010): 43-56.

[93] Kumar, G., Kumar, R. and Kumar, A. "ZnO Thin Films: Chemical Vapour Deposition, Growth and Functional Properties." *Reviews in Advanced Sciences and Engineering*5.2 (2016): 150-160.

[94] Wang, J.T. "Chemical Vapor Deposition and Its Applications in Inorganic Synthesis." *Modern Inorganic Synthetic Chemistry (Second Edition)*. 2017. 167-188.

[95] Ataev, B.M., Bagamadova, A.M., Mamedov, V.V., Omaev, A.K. and Rabadanov, M.R. "Highly conductive and transparent thin ZnO films prepared in situ in a low pressure system." *Journal of crystal growth* 198 (1999): 1222-1225.

[96] Takahashi, N., Kaiya, K., Nakamura, T., Momose, Y. and Yamamoto, H. "Growth of ZnO on sapphire (0001) by the vapor phase epitaxy using a chloride source." *Japanese journal of applied physics* 38.4B (1999): L454.

[97] Kaiya, K., Omichi, K., Takahashi, N., Nakamura, T., Okamoto, S. and Yamamoto, H. "Epitaxial growth of ZnO thin films exhibiting room-temperature ultraviolet emission by atmospheric pressure chemical vapor deposition." *Thin Solid Films* 409.1 (2002): 116-119.

[98] Heinze, S., Krtschil, A., Bläsing, J., Hempel, T., Veit, P., Dadgar, A., Christen, J. and Krost, A. "Homoepitaxial growth of ZnO by metalorganic vapor phase epitaxy in two-dimensional growth mode." Journal of Crystal Growth 308.1 (2007): 170-175.

[99] Morkoç, H. and Özgür, Ü. *Zinc oxide: fundamentals, materials and device technology*. John Wiley & Sons, 2008.

[100] Ogata, K., Kim, S.W., Fujita, S. and Fujita, S. "ZnO growth on Si substrates by metalorganic vapor phase epitaxy." *Journal of crystal growth* 240.1-2 (2002): 112-116.

[101] Creighton, J.R. and Ho, P. "Introduction to chemical vapor deposition (CVD)." *Chemical vapor deposition* 2 (2001): 1-22.

[102] Zheng, J.H., Jiang, Q. and Lian, J.S. "Synthesis and optical properties of flower-like ZnO nanorods by thermal evaporation method." *Applied Surface Science* 257.11 (2011): 5083-5087.

[103] Lee, J.S., Park, K., Kang, M.I., Park, I.W., Kim, S.W., Cho, W.K., Han, H.S. and Kim, S. "ZnO nanomaterials synthesized from thermal evaporation of ball-milled ZnO powders." *Journal of Crystal Growth* 254.3-4 (2003): 423-431.

[104] Yao, B.D., Chan, Y.F. and Wang, N. "Formation of ZnO nanostructures by a simple way of thermal evaporation." *Applied Physics Letters* 81.4 (2002): 757-759.

[105] Wahab, R., Ansari, S.G., Kim, Y.S., Seo, H.K., Kim, G.S., Khang, G. and Shin, H.S. "Low temperature solution synthesis and characterization of ZnO nano-flowers." *Materials Research Bulletin* 42.9 (2007): 1640-1648

[106] Liu, D. and Kelly, T.L. "Perovskite solar cells with a planar heterojunction structure prepared using room-temperature solution processing techniques." *Nature photonics* 8.2 (2014): 133.

[107] Singh, D. P. "Synthesis and growth of ZnO nanowires." *Science of Advanced Materials* 2.3 (2010): 245-272.

[108] Adl, A.H., Kar, P., Farsinezhad, S., Sharma, H. and Shankar, K. "Effect of sol stabilizer on the structure and electronic properties of solution-processed ZnO thin films." *RSC Advances* 5.106 (2015): 87007-87018.

[109] Gao, X., Li, X. and Yu, W. "Flowerlike ZnO nanostructures via hexamethylenetetramine-assisted thermolysis of zinc− ethylenediamine complex." *The Journal of Physical Chemistry B* 109.3 (2005): 1155-1161.

[110] Zhang, Y., Ram, M.K., Stefanakos, E.K. and Goswami, D.Y. "Synthesis, characterization, and applications of ZnO nanowires." *Journal of Nanomaterials*2012 (2012): 20.

[111] Hong, R., Pan, T., Qian, J. and Li, H. "Synthesis and surface modification of ZnO nanoparticles." *Chemical Engineering Journal* 119.2-3 (2006): 71-81.

[112] Lanje, A.S., Sharma, S.J., Ningthoujam, R.S., Ahn, J.S. and Pode, R.B. "Low temperature dielectric studies of zinc oxide (ZnO) nanoparticles prepared by precipitation method." *Advanced Powder Technology* 24.1 (2013): 331-335.

[113] Wang, Y., Zhang, C., Bi, S. and Luo, G. "Preparation of ZnO nanoparticles using the direct precipitation method in a membrane dispersion micro-structured reactor." *Powder Technology* 202.1-3 (2010): 130-136.

[114] Danks, A.E., Hall, S.R. and Schnepp, Z. "The evolution of 'sol–gel'chemistry as a technique for materials synthesis." *Materials Horizons* 3.2 (2016): 91-112.

[115] Adl, A.H., Kar, P., Farsinezhad, S., Sharma, H. and Shankar, K. "Effect of sol stabilizer on the structure and electronic properties of solution-processed ZnO thin films." *RSC Advances* 5.106 (2015): 87007-87018.

[116] Ristić, M., Musić, S., Ivanda, M. and Popović, S. "Sol–gel synthesis and characterization of nanocrystalline ZnO powders." *Journal of Alloys and Compounds* 397.1-2 (2005): L1-L4.

[117] Benhebal, H., Chaib, M., Salmon, T., Geens, J., Leonard, A., Lambert, S.D., Crine, M. and Heinrichs, B. "Photocatalytic degradation of phenol and benzoic acid using zinc oxide powders prepared by the sol–gel process." *Alexandria Engineering Journal* 52.3 (2013): 517-523.

[118] B Djurisic, A., Y Chen, X. and H Leung, Y. "Recent progress in hydrothermal synthesis of zinc oxide nanomaterials." *Recent patents on nanotechnology* 6.2 (2012): 124-134.

[119] Kołodziejczak-Radzimska, A. and Jesionowski, T. "Zinc oxide—from synthesis to application: a review." *Materials* 7.4 (2014): 2833-2881.

[120] Chen, D., Jiao, X. and Cheng, G. "Hydrothermal synthesis of zinc oxide powders with different morphologies." *Solid State Communications* 113.6 (1999): 363-366.

[121] Ma, J., Liu, J., Bao, Y., Zhu, Z., Wang, X. and Zhang, J. "Synthesis of large-scale uniform mulberry-like ZnO particles with microwave hydrothermal method and its antibacterial property." *Ceramics International* 39.3 (2013): 2803-2810.

[122] Bondioli, F., Ferrari, A.M., Braccini, S., Leonelli, C., Pellacani, G.C., Opalinska, A., Chudoba, T.,
Grzanka, E., Palosz, B., Łojkowski, W. “Microwave hydrothermal synthesis of nanocrystalline
pre-doped zirconia powders at pressures up to 8 MPa. Solid State Phenom.” 94 (2003): 193–196.

[123] Strachowski, T., Grzanka, E.,Palosz, B., Presz, A., Ślusarski, L., and Łojkowski, W. “Microwave
driven hydrothermal synthesis of zinc oxide nanopowders.” *Solid State Phenomena* 94 (2003): 189–192.

[124] Kumar, K.M., Mandal, B.K., Naidu, E.A., Sinha, M., Kumar, K.S. and Reddy, P.S. "Synthesis and characterisation of flower shaped zinc oxide nanostructures and its antimicrobial activity." *Spectrochimica Acta Part A: Molecular and Biomolecular Spectroscopy* 104 (2013): 171-174.

[125] Ismail, A.A., El-Midany, A., Abdel-Aal, E.A. and El-Shall, H. "Application of statistical design to optimize the preparation of ZnO nanoparticles via hydrothermal technique." *Materials Letters* 59.14-15 (2005): 1924-1928.

[126] Dalal, S.H., Baptista, D.L., Teo, K.B.K., Lacerda, R.G., Jefferson, D.A. and Milne, W.I. "Controllable growth of vertically aligned zinc oxide nanowires using vapour deposition." *Nanotechnology* 17.19 (2006): 4811.

[127] Anand, K., Varghese, S. and Kurian, T. "Synthesis of ZnO nano rods through mechano-chemical route: A solvent free approach." *International Journal of Theoretical and Applied Sciences* 6.1 (2014): 87.

[128] Lu, J., Ng, K.M. and Yang, S. "Efficient, one-step mechanochemical process for the synthesis of ZnO nanoparticles." *Industrial & engineering chemistry research*47.4 (2008): 1095-1101.

[129] Ao, W., Li, J., Yang, H., Zeng, X. and Ma, X. "Mechanochemical synthesis of zinc oxide nanocrystalline." *Powder Technology* 168.3 (2006): 148-151.

[130] Kakhaki, Z.M., Youzbashi, A. and Naderi, N. "Optical Properties of Zinc Oxide Nanoparticles Prepared by a One-Step Mechanochemical Synthesis Method." *Journal of Physical Science* 26.2 (2015): 41.

[131] Čeliković, A., Kandić, L., Zdujić, M. and Uskokovic, D.P. "Synthesis of ZnO and ZrO2 powders by mechanochemical processing." *Materials science forum*. Vol. 555. Trans Tech Publications, 2007.

[132] Francavilla, M., Pineda, A., Romero, A.A., Colmenares, J.C., Vargas, C., Monteleone, M. and Luque, R. "Efficient and simple reactive milling preparation of photocatalytically active porous ZnO nanostructures using biomass derived polysaccharides." *Green Chemistry* 16.5 (2014): 2876-2885.

[133] Maria, M.J., Balanand, S., Anas, S., Mohamed, A.P. and Ananthakumar, S. "Zn-dust derived ultrafine grained ZnO non-linear ceramic resistors via in-situ thermal oxidation of cermet reactant mixture." *Materials & Design* 92 (2016): 387-396.

[134] Balanand, S., Maria, M.J., Rajan, T.P.D., Mohamed, A.P. and Ananthakumar, S. "Bulk processing of ZnO nanostructures via microwave assisted oxidation of

mechanically seeded Zn dust for functional paints and coatings." *Chemical Engineering Journal* 284 (2016): 657-667.

[135] Chen, X.H., Yang, H.S., Wu, G.T., Wang, M., Deng, F.M., Zhang, X.B., Peng, J.C. and Li, W.Z. "Generation of curved or closed-shell carbon nanostructures by ball-milling of graphite." *Journal of crystal growth* 218.1 (2000): 57-61.

[136] Kaupp, G. "Mechanochemistry: the varied applications of mechanical bond-breaking." *CrystEngComm* 11.3 (2009): 388-403.

[137] Yadav, T.P., Yadav, R.M. and Singh, D.P. "Mechanical milling: a top down approach for the synthesis of nanomaterials and nanocomposites." *Nanoscience and Nanotechnology* 2.3 (2012): 22-48.

[138] Ye, G. and Tom, T. "Mechanochemical Activation-Assisted Low-Temperature Synthesis of $CaZrO_3$." *Journal of the American Ceramic Society* 90.1 (2007): 287-290.

[139] Gajović, A., Djerdj, I., Furić, K., Schlögl, R. and Su, D.S. "Preparation of nanostructured ZrTiO4 by solid state reaction in equimolar mixture of TiO2 and ZrO2." *Crystal Research and Technology* 41.11 (2006): 1076-1081.

[140] Jha, M.K., Kumar, V. and Singh, R.J. "Review of hydrometallurgical recovery of zinc from industrial wastes." *Resources, conservation and recycling* 33.1 (2001): 1-22.

[141] Lu, H.B., Li, H., Liao, L., Tian, Y., Shuai, M., Li, J.C., Hu, M.F., Fu, Q. and Zhu, B.P. "Low-temperature synthesis and photocatalytic properties of ZnO nanotubes by thermal oxidation of Zn nanowires." *Nanotechnology* 19.4 (2008): 045605.

[142] Zhao, C.X., Li, Y.F., Zhou, J., Li, L.Y., Deng, S.Z., Xu, N.S. and Chen, J. "Large-scale synthesis of bicrystalline ZnO nanowire arrays by thermal oxidation of zinc film: growth mechanism and high-performance field emission." *Crystal Growth & Design* 13.7 (2013): 2897-2905.

[143] Wang, Z.H., Geng, D.Y., Han, Z. and Zhang, Z.D. "Characterization and optical properties of ZnO nanoparticles obtained by oxidation of Zn nanoparticles." *Materials Letters* 63.29 (2009): 2533-2535.

[144] Xu, C.H., Lui, H.F. and Surya, C. "Synthetics of ZnO nanostructures by thermal oxidation in water vapor containing environments." *Materials letters* 65.1 (2011): 27-30.

[145] Guo, C.F., Wang, Y., Jiang, P., Cao, S., Miao, J., Zhang, Z. and Liu, Q. "Zinc oxide nanostructures: epitaxially growing from hexagonal zinc nanostructures." *Nanotechnology* 19.44 (2008): 445710.

[146] Mihailova, I., Gerbreders, V., Tamanis, E., Sledevskis, E., Viter, R. and Sarajevs, P. "Synthesis of ZnO nanoneedles by thermal oxidation of Zn thin films." Journal of Non-Crystalline Solids 377 (2013): 212-216.

[147] Buxbaum, G. ed. *Industrial inorganic pigments*. John Wiley & Sons, 2008.

[148] Gao, Y., Gereige, I., El Labban, A., Cha, D., Isimjan, T.T. and Beaujuge, P.M. "Highly transparent and UV-resistant superhydrophobic SiO2-coated ZnO nanorod arrays." *ACS applied materials & interfaces* 6.4 (2014): 2219-2223.

[149] Soumya, S., Kumar, S.N., Mohamed, A.P. and Ananthakumar, S. "Silanated nano ZnO hybrid embedded PMMA polymer coatings on cotton fabrics for near-IR reflective, antifungal cool-textiles." New Journal of Chemistry 40.8 (2016): 7210-7221.

[150] Yebra, D.M., Kiil, S., Weinell, C.E. and Dam-Johansen, K. "Dissolution rate measurements of sea water soluble pigments for antifouling paints: ZnO." *Progress in organic coatings* 56.4 (2006): 327-337.

[151] Yong, H.E., Krishnamoorthy, K., Hyun, K.T. and Kim, S.J. "Preparation of ZnO nanopaint for marine antifouling applications." *Journal of Industrial and Engineering Chemistry* 29 (2015): 39-42.

[152] Zeno, Jr. W.W.,. Frank, N.J., Pappas, S.P., Douglas, A.W. “Pigments, in: Organic Coatings” John Wiley & Sons, Inc. (2007) 417–434.

[153] Dhoke, S.K., Khanna, A.S. and Sinha, T.J.M. "Effect of nano-ZnO particles on the corrosion behavior of alkyd-based waterborne coatings." *Progress in Organic Coatings* 64.4 (2009): 371-382.

[154] Yu, L. and Skov, A.L. "ZnO as a cheap and effective filler for high breakdown strength elastomers." *RSC Advances* 7.72 (2017): 45784-45791.

[155] Oku, M., Kitano, M., Mastsuo, K., Yagi, J. and Imai, T. "Electro-conductive resin composition." U.S. Patent No. 5,141,982. 25 Aug. 1992.

[156] Hong, J.I., Winberg, P., Schadler, L.S. and Siegel, R.W. "Dielectric properties of zinc oxide/low density polyethylene nanocomposites." *Materials Letters* 59.4 (2005): 473-476.

[157] Mu, Q., Feng, S. and Diao, G. "Thermal conductivity of silicone rubber filled with ZnO." *Polymer composites* 28.2 (2007): 125-130

[158] Guo, L., Zhang, Z., Kang, R., Chen, Y., Hou, X., Wu, Y., Wang, M., Wang, B., Cui, J., Jiang, N. and Lin, C.T. "Enhanced thermal conductivity of epoxy composites filled with tetrapod-shaped ZnO." *RSC Advances* 8.22 (2018): 12337-12343.

[159] Seo, J., Jeon, G., Jang, E.S., Bahadar Khan, S. and Han, H. "Preparation and properties of poly (propylene carbonate) and nanosized ZnO composite films for packaging applications." Journal of Applied Polymer Science 122.2 (2011): 1101-1108.

[160] Uchida, S., Murakami, T., Iwamura, T., Ishige, R. and Ando, S. "Enhanced thermal conductivity in immiscible polyimide blend composites with needle-shaped ZnO particles." *RSC Advances* 7.25 (2017): 15492-15499.

[161] Hamad, W.N.F.W., Abdullah, A.M., and Mohamad, D. “Effect of zinc oxide on flexural and physical properties of PMMA composites.” AIP Conference Proceedings 1791 (2016): 020014.

[162] Li, F., Hu, K.A., Li, J.L. and Zhao, B.Y. "The friction and wear characteristics of nanometer ZnO filled polytetrafluoroethylene." *Wear* 249.10-11 (2001): 877-882.

[163] Bouropoulos, N., Psarras, G.C., Moustakas, N., Chrissanthopoulos, A. and Baskoutas, S. "Optical and dielectric properties of ZnO-PVA nanocomposites." *physica status solidi (a)* 205.8 (2008): 2033-2037.

[164] Vaishnav, D. and Goyal, R.K. "Thermal and dielectric properties of high performance polymer/ZnO nanocomposites." *IOP Conference Series: Materials Science and Engineering*. Vol. 64. No. 1. IOP Publishing, 2014.

[165] Wu, W., Huang, X., Li, S. and Jiang, P. "Novel three-dimensional zinc oxide superstructures for high dielectric constant polymer composites capable of withstanding high electric field." *The Journal of Physical Chemistry C* 116.47 (2012): 24887-24895.

[166] ,A.J. and Herbert, J.M. *Electroceramics: materials, properties, applications*. John Wiley & Sons, 2003.

[167] Setter, N. and Waser, R. "Electroceramic materials." Acta materialia 48.1 (2000): 151-178.

[168] Matsuoka, M. "Nonohmic properties of zinc oxide ceramics." Japanese Journal of Applied Physics 10.6 (1971): 736.

[169] Lin, Y., Zhang, Z., Tang, Z., Yuan, F. and Li, J. "Characterisation of ZnO-based varistors prepared from nanometre Precursor powders." *Advanced Materials for Optics and Electronics* 9.5 (1999): 205-209.

[170] Lu, H., Wang, Y. and Lin, X. "Structures, varistor properties, and electrical stability of ZnO thin films." *Materials Letters* 63.27 (2009): 2321-2323.

[171] Hembram, K., Sivaprahasam, D. and Rao, T.N. "Combustion synthesis of doped nanocrystalline ZnO powders for varistors applications." *Journal of the European Ceramic Society* 31.10 (2011): 1905-1913.

[172] Haile, S.M., Johnson, D.W., Wiseman, G.H. and Bowen, H.K. "Aqueous precipitation of spherical zinc oxide powders for varistor applications." *Journal of the American Ceramic Society* 72.10 (1989): 2004-2008.

[173] Viswanath, R.N., Ramasamy, S., Ramamoorthy, R., Jayavel, P. and Nagarajan, T. "Preparation and characterization of nanocrystalline ZnO based materials for varistor applications." *Nanostructured Materials* 6.5-8 (1995): 993-996.

[174] Wang, M-H., Yao, C., and Zhang, N-F. "Degradation characteristics of low-voltage ZnO varistor manufactured by chemical co-precipitation processing." *Journal of Materials Processing Technology* 202 (2008): 406-411.

[175] Li, Y., Li, G. and Yin, Q. "Preparation of ZnO varistors by solution nano-coating technique." *Materials Science and Engineering: B* 130.1-3 (2006): 264-268.

[176] Hishita, S., Yao, Y. and Shirasaki, S.I. "Zino Oxide Varistors Made from Powders Prepared by Amine Processing." *Journal of the American Ceramic Society* 72.2 (1989): 338-340.

[177] Pillai, S.C., Kelly, J.M., McCormack, D.E., O'Brien, P. and Ramesh, R. "The effect of processing conditions on varistors prepared from nanocrystalline ZnO." *Journal of Materials Chemistry* 13.10 (2003): 2586-2590.

[178] Pillai, S.C., Kelly, J.M., McCormack, D.E. and Ramesh, R. "High performance ZnO varistors prepared from nanocrystalline precursors for miniaturised electronic devices." *Journal of Materials Chemistry* 18.33 (2008): 3926-3932.

[179] Nobrega, M.C.S., Zolotar, M.S., Mannheimer, W.A. and Espinola, A. "ZnO varistors produced using colloidal-gel powders." *Journal of non-crystalline solids* 147 (1992): 803-807.

CHAPTER 2

Tools and Techniques for Material Characterizations

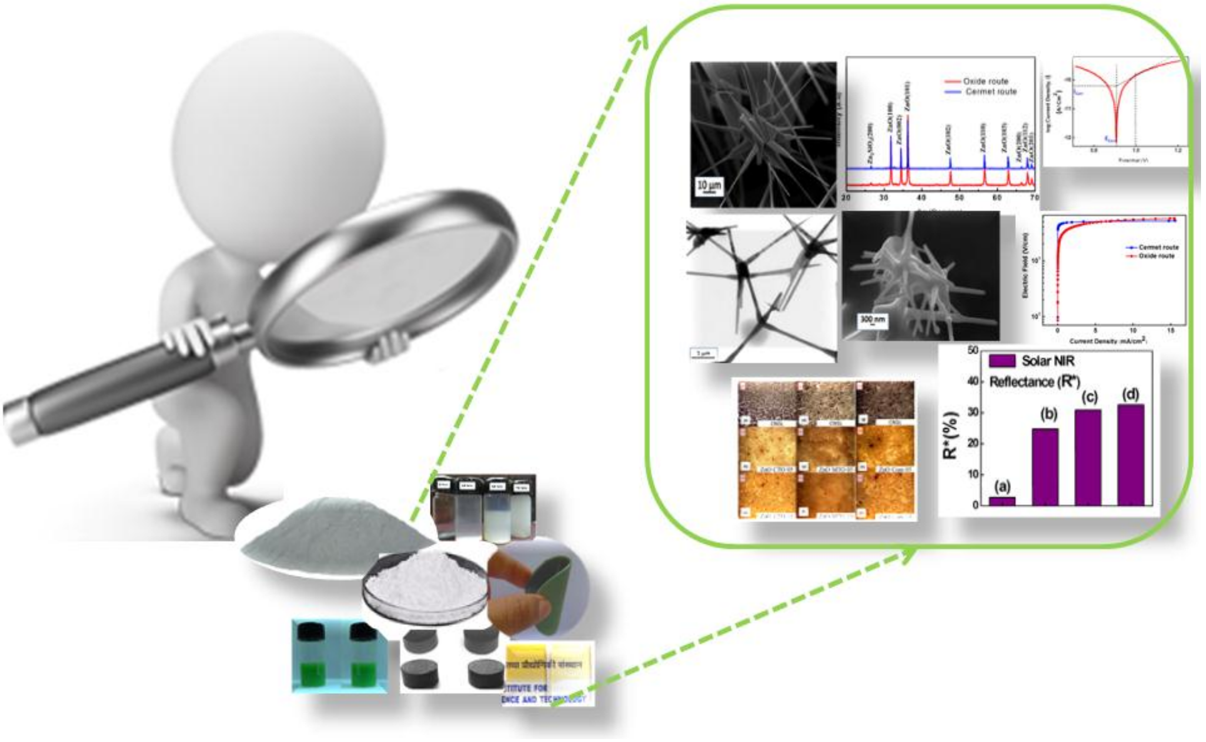

Chapter 2 described the various tools and techniques adopted for the characterizations of the product obtained at different stages of the research work. The specifications of the instruments used for the present work are provided at the end of each description.

Tools and Techniques for Material Characterizations

2.1 Introduction

The ever increasing demand for functional materials in various scientific and technological fields has fulfilled due to the in-depth knowledge of their properties with the help of various sophisticated tools and characterization technique. The rapid advancement in sophisticated tools and technique had made it possible the better and through understanding of physical and chemical properties of functional materials.

The current chapter provide a brief description of the tools and techniques adopted for the characterization and application studies of the material synthesized. Each instruments and technique described with the help of its basic principle. At the end of each description the specifications of the instruments used in the present research are also provided.

2.1.1 Powder X- Ray diffraction (XRD)

Powder X-ray diffraction (XRD) is a versatile, non-destructive analytical tool that reveals in depth information about the phases, crystallographic structure and texture of polycrystalline samples and other structural data like crystallinity, average grain size, chemical composition, and crystal defects. X-rays are form of electromagnetic radiation of wavelength ~ 1Å (10^{-10} m). X-rays are produced when high energy charged particles, like electrons collide with mater. X-ray diffraction occurs when it strikes the surface of crystalline material and interacted with its periodic structure [1].

When X-rays of fixed wavelength are bombarded on crystals, they get scattered according to their incidence direction. Depending upon the wavelength of X- rays and distance between atomic planes, at certain angles, the scattered X- rays reinforce each other to produce intense beam. X-ray diffraction is based on constructive interference of monochromatic X-rays when interacted with a crystalline sample. The incident rays interacted with the sample produces constructive interference when all conditions satisfy Bragg's Law,

$$n\lambda = 2d \sin\theta \tag{2.1}$$

where, λ is the wavelength of X-ray, n is the order of diffraction, θ is the angle of diffraction and d is the interplanar spacing. Thus the scattered waves interfere constructively when the path difference (2d sinθ) between two waves undergoing interference is equal to an integer multiple of the wavelength (n λ).

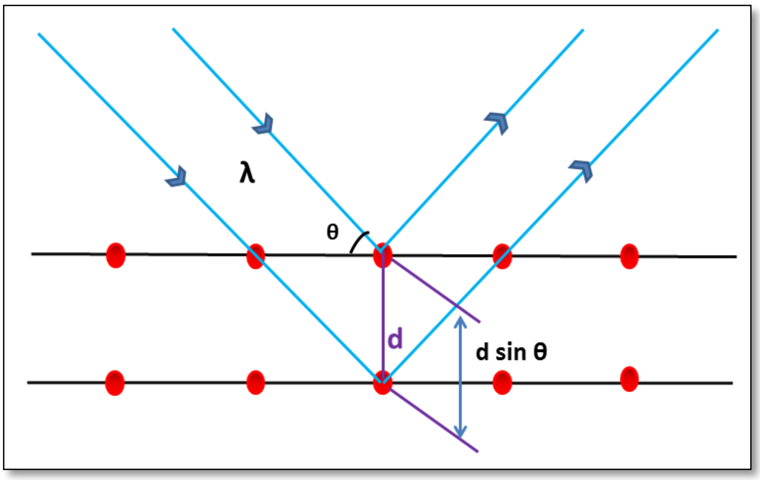

Figure 2.1: Schematic representation of the interaction of X-ray radiation with crystal planes to demonstrate Bragg's law.

Due to the random orientation of the material in the form of powder all the possible diffraction directions of the lattice should be attained by scanning the sample through a range of 2θ angles. Conversion of the diffraction peaks to d-spacing permits identification of the material because each material has a set of unique d-spacing. Typically, this is done by comparison of d-spacing with standard reference patterns called Joint Committee on Powder Diffraction Standards file (JCPDS). The crystallite size of the sample was calculated from the Scherrer Equation,

$$D = \frac{0.9\lambda}{\beta \cos\theta} \qquad (2.2)$$

where, D is the size of crystalline domain, K is the Scherrer constant generally taken as 0.9, λ is the wavelength of X-rays, β is the full width at half maximum in radians, and θ is the incident angle.

The lattice parameter of the samples was calculated from the X-ray diffraction data using the Equation 2.3 [2]

$$1/d^2 = 4/3[1/a^2] + 1/c^2 \qquad (2.3)$$

Where, d is the interplanar distance, a and c are the lattice parameters in nm (being hexagonal $c/a = (8/3)^{-1}$).

In this research for X–ray analysis of the sample the diffractometer unit used is PANalytical X'pert Pro, Model: PW 3040/60. It uses CuKα radiation (λ= 1.540566 Å) employing a proprietary detector, X'Celerator, and a monochromator at the side of diffracted beam. The X-ray beam is limited to a specified sample area by a programmable slit. The scans are performed in a tube current and at a voltage of 30 mA and 40 KV respectively. The finely powdered sample is filled in standard sample holder and result of analysis was recorded at room temperature.

2.1.2 Ultraviolet-visible spectroscopy

Ultraviolet-Visible spectroscopy (UV-Vis) is the absorption or reflectance spectroscopy in the ultra violet-visible region (wavelength = 200-800 nm) of the electromagnetic spectrum. It corresponds to electronic excitations between the energy levels that correspond to the molecular orbitals of the systems. In UV-Visible region of electromagnetic spectrum molecules containing non-bonding electrons or π-electrons can absorb the energy as ultraviolet or visible light. Then they undergo electronic transitions to higher anti-bonding molecular orbitals. UV-Vis spectroscopy is applied for characterizing the absorption, reflection and transmission of light by a variety of technologically important materials, such as coatings, pigments, filters, and windows.

It involves the measurement of the attenuation of a beam of light after it passes through a sample surface. Absorption measurements can be conducted at a single wavelength or over a long spectral range. The source of light used is a combination of halogen/tungsten, and deuterium lamps, which provides both visible and near ultraviolet radiation in the wavelength range 200-800 nm. It measures the light intensity (I) passing through a sample when the initial intensity (I_0) of light incident on the sample. Then the transmittance is defined by the ratio (I/I_0) and is expressed as a percentage (% T). UV-Vis spectroscopy obeys the Beer-Lambert Law, which states that when a beam of monochromatic light is passed through a solution containing absorbing substance, the rate of decrease in the intensity of radiation is proportional to the solution concentration and incident radiation. The Beer-Lambert law can be expressed as,

$$A = log \frac{I_0}{I} = \varepsilon cl \qquad (2.5)$$

Where, A is the absorbance, l is the optical path length in cm, c is the concentration of solution (mol dm^{-3}), and ε is the molar extinction, which is a constant depends on substance and wavelength. For UV-visible spectrometry the liquid sample is taken in a rectangular transparent cell called cuvette of 1 cm internal width.

In this research UV-visible absorption studies were carried out using UV-Vis spectrophotometer, UV 240 IPC, Shimadzu.

2.1.3 Particle size analysis- Dynamic light scattering (DLS)

Dynamic light scattering (DLS) [3, 4] also known as Photon Correlation Spectroscopy or Quasi-Elastic Light Scattering is a light scattering technique used to determine hydrodynamic particle diameters in colloidal solutions. Size of the particle can be determined by measuring the random fluctuations in the intensity of light scattered from a solution. The schematic of the DLS measurement setup is given in the Figure 2.2. To illuminates the sample cell laser light is used. The light collides with all the molecules in the solution and the light is diffracted by molecule in all directions. The light diffracted from the molecules in solution can interfere either constructively (light regions) or destructively (dark regions). This diffraction and interference of light is repeated at short time intervals and the patterns obtained are analysed by an autocorrelator which compares the light intensity at each spot over time. The signal of scattered light is collected with one of two detectors, either at a 90 ^{o} (right angle) or 173 ^{o} (back angle) scattering angle.

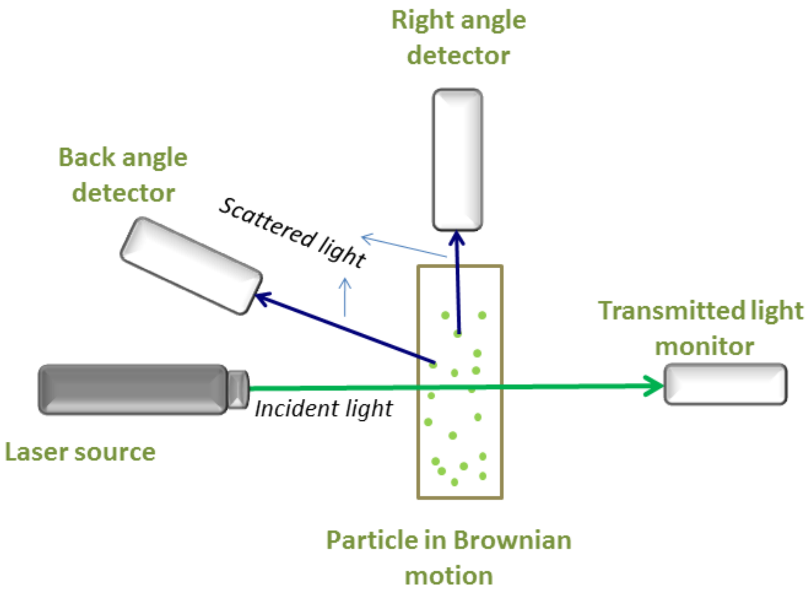

Figure 2.2: Schematic representation of particle size measurement in DLS analysis.

Small particles in suspension undergo random thermal motion known as Brownian motion. The Brownian motion of particles in suspension causes laser light to be scattered at different intensities and thereby imprint information about their motion. Analysis of the scattered light fluctuation thus yields information about the particles. Experimentally one quantifies intensity fluctuations by computing the intensity correlation function and whose analysis provides the translational diffusion coefficient of the particles (also known as diffusion constant). The random motion is modelled by the Stokes-Einstein equation, where the translational diffusion coefficient D_t is then related to the hydrodynamic diameter D_h of the particles,

$$D_h = \frac{K_B T}{3\Pi\eta\, D_t} \tag{2.4}$$

Where k_B is the Boltzmann-constant, T is the temperature and η the viscosity. Thus size and size distribution of the particle in a suspension are calculated from the diffusion coefficient in terms of hydrodynamic diameter.

In this research DLS measurement was performed with 3000H Malvern Zetasizer Instrument with He- Ne laser (λ = 633 nm). Initially the intensity autocorrelation function is recorded by the instrument and is then transformed into volume functions to get information regarding size of the particle.

2.1.4 Thermo Gravimetric Analysis

TGA is a type of thermal analysis which gives a detailed figure of changes in chemical and physical properties of material with increase in temperature [5]. In TGA weight alteration of material with respect to the changes in temperature is monitored. TGA is commonly used to determine residual solvent content, polymer degradation temperatures, absorbed moisture content, and to study the decomposition of both inorganic and organic materials. It is also used to evaluate the corrosion kinetics in high temperature oxidation. The sample is kept on a high-precision balance and subsequently heated according to a predefined temperature program. Varying atmospheres such as air, helium or argon can be used depending on the purpose of the measurement. The TGA instrument continuously weighs a sample as it is heated to the target temperature. With increase in the temperature, various components of the sample are decomposed and the percentage of weight of resulting mass change at any stage of analysis can be measured. Results are plotted with temperature along X-axis and weight % along Y-axis.

In this research the TGA analysis of the prepared samples carried out by Thermo Gravimetric Analyzer TG-50 Shimadzu in the temperature range 100-1000 ^{o}C at a heating rate 10 ^{o}C/min performed in air atmosphere. About 40-50 mg samples were weighed in a platinum pan. Aluminium oxide is taken in the reference pan.

2.1.5 Optical Microscopy

The optical microscope apply visible light and a lens system to magnify small object using normal light sensing cameras. In this research the optical images were taken using Stereomicroscope Leica DM 2500 P.

2.1.6 Scanning Electron Microscopy (SEM)

Scanning electron microscope images a sample by scanning it with a high-energy beam of electrons. It provides superior depth of focus and special resolution compared to optical microscopy [6]. The electrons interact with the atoms of the sample and produce signals that contain information about the sample's surface topography, morphology, composition and crystallographic information.

The signals produced from SEM include secondary electrons, backscattered electrons (BSE), characteristic X-rays, light (cathode-luminescence), specimen current and transmitted electrons. In all SEMs secondary electron detectors are common, but it is uncommon that a single machine having detectors for all possible signals. The signals produced from the interactions of the electron beam with atoms on or near the sample surface. In the standard detection mode, secondary electron imaging or SEI, the SEM can yield very high-resolution images of the surface of sample giving information about less than 1 to 5 nm in size. Due to the very narrow electron beam, SEM images have a higher depth of field yielding a characteristic 3-D appearance useful for understanding the structure of the surface sample. Back-scattered electrons (BSE) are beam of electrons that are reflected from the sample by elastic scattering. BSE are used in analytical SEM along with the characteristic X-rays derived spectra. Since the intensity of the BSE signal is related to the atomic number (Z) of the sample, BSE images can offer information about the distribution of elements present in the sample. Characteristic X-rays are emitted from the sample when the electron beam eliminates an inner shell electron from the sample, resulting a higher energy electron to fill the shell and release energy. These characteristic X-rays are used to identify the composition and measure the abundance of elements in the sample. SEM image gives information more about the surface rather than its interior. A simple schematic representation of the SEM can be seen in Figure 2.3 (a).

In this research, the microstructural analysis was done using ZEISS EVO 18 Special Edition SEM operated at 20 KV in SEI mode.

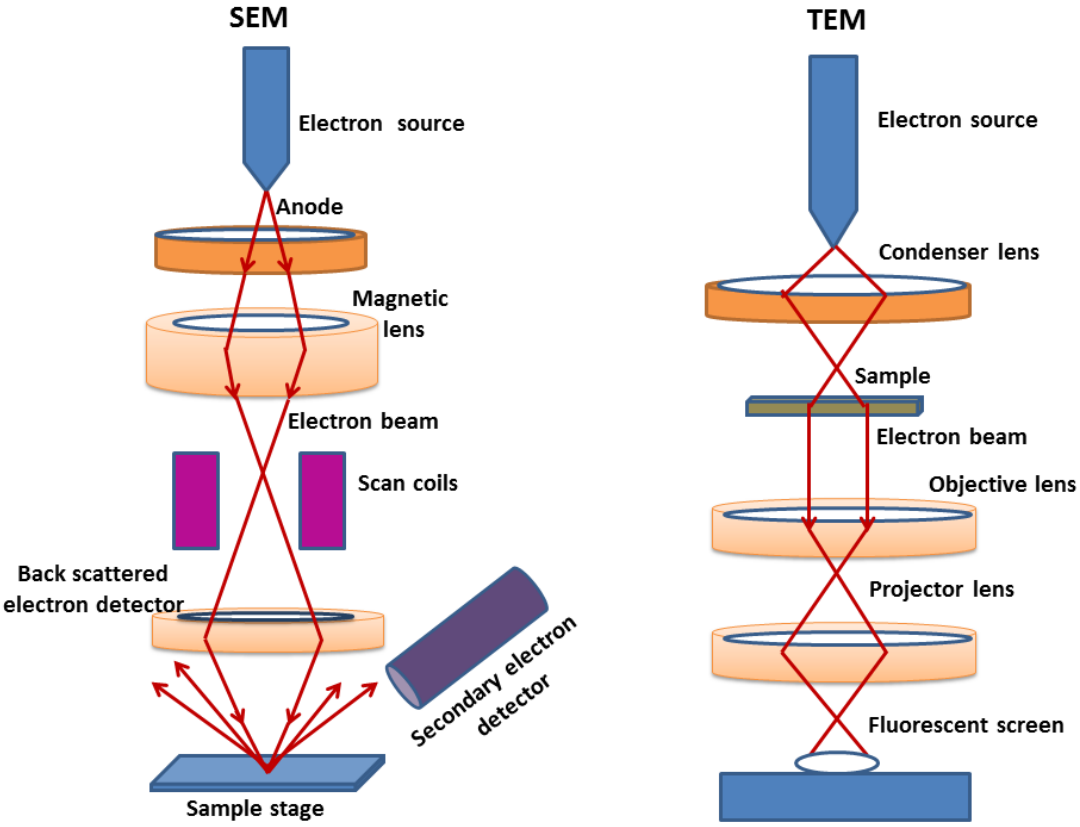

Figure 2.3: A schematic diagram of the (a) scanning electron microscope (SEM), and (b) Transmission electron microscope (TEM).

2.1.7 Transmission electron microscopy (TEM)

TEM is used for the microstructural characterization of the materials with very high spatial resolution (~1Å). Information regarding the crystal structure, morphology and defects, composition and crystal phases, and magnetic microstructure can be derived by a combination of electron-optical imaging, electron diffraction, and small probe capabilities. A beam of electrons is transmitted through a thin sample and the electrons are scattered in the specimen [7]. The transmitted electrons are focused on a fluorescent screen or CCD camera by electromagnetic coils and the image is formed. The image contrast originates from mass-thickness differences where thicker regions of the specimen absorb or scatter more electrons compared to thinner regions. A schematic diagram of the TEM can be seen in Figure 2.3 (b).

In this research transmission electron microscopic images were recorded using Transmission electron microscope (TEM) FEI Tecnai 30G2S-TWIN operating at an accelerating voltage of 300 KV.

2.1.8 Energy Dispersive X-ray Spectroscopy (EDX)

Energy Dispersive X-ray Spectroscopy is carried out in conjunction with SEM or TEM. X-rays with specific energies or wavelengths are produced when the sample is irradiated with a beam of electrons depending on the chemical composition of the area irradiated [8]. Analysis of emitted X–rays gives local chemical composition data. In SEM when the electron beam is scanned across the sample, X-rays are generated from the atoms and the ionized atom returned to its ground state. Then a large amount of energy is produced when the electron from outer shell of higher energy fills the empty inner shell. The released energy is equal to the potential energy difference between the two shells. This energy is characteristic for each atomic transition and will be emitted by the atom as an

X-ray photon, or absorbed, and emitted as an Auger electron. The energy possessed by emitted

X-ray photon is characteristic of the atom from which it escapes. The EDS system collects those X-rays and reveals the intensity *vs.* their energy. Further this qualitative EDX spectrum can then be analysed to produce either an area elemental analysis, displayed as a dot map or a linear elemental analysis, displayed as a line scan screening the distribution of diverse surface elements of the sample.

In this research EDX analysis was carried out using Energy Dispersive X-ray spectrometer EDX (Phoenix) which is attached with SEM. After collecting the spectrum by digital filtering algorithm the background is removed. The EDX pattern obtained is compared with standard values of material of known composition.

2.1.9 X-ray Photoelectron Spectroscopy (XPS)

XPS is one of the most widely accepted surface analysis technique due to its simplicity in use and data interpretation. In XPS analysis sample is irradiated with mono-energetic X-rays resulting in photoelectrons to be emitted from the surface of the sample [9]. The binding energy of the photoelectrons is determined by an electron energy analyser. The elemental identity, quantity and chemical state of an element are determined from intensity of a photoelectron peak and binding energy. XPS provides valuable information about thin film structures and surface layers which have application in catalysis, polymer surface modification, adhesion, corrosion, electronics packaging, semiconductor and dielectric materials, thin film coatings, and magnetic media used in a number of industries.

In this research the X-ray photoelectron spectroscopic studies were conducted in Surface Science Labs SSX-100, USA using monochromatic Al-Kα X-ray source (1486.6 eV) and the photoelectrons were processed and studied with the help of ESCA V2.1

software. The binding-energy values are calibrated with respect to the binding energy of C 1s at 284.6 eV.

2.1.10 X-ray Fluorescence (XRF)

XRF is a relatively non-destructive analysis which uses characteristic "secondary" X-rays from a material that has been excited by bombarding the sample with gamma rays or high-energy X-rays o for chemical and elemental analysis. XRF is based on the principle that excitation of individual atoms by an external energy source resulted in the emission of X-ray photons of a characteristic energy or wavelength. The elements present in the analyte may be identified and quantitated by counting the number of photons of each energy emitted from a sample [10]. When the materials are exposed to high energy short wavelength radiations like X-rays the component atoms may ionize. When the energy of the exposed radiation is greater than the ionization energy of the atom, ejection of one or more electron from the atom occurred. Thus the ejection of electron makes the electronic structure of atom unstable and electron from the higher orbital fall into lower orbital to occupy the hole left behind. Due to this relaxation process the atom undergoes fluorescence, or the emission of an X-ray photon having energy equal to the difference in energies of the initial and final states. Detecting this photon and measuring its energy enable us to characterize the elements present and specific electronic transition from which it originated.

2.1.11 Thermal conductivity

Thermal conductivity is the ability of a material to conduct heat. It can be defined as the rate at which the heat is transferred through the unit cross section area of the material by conduction [11]. The material with higher thermal conductivity is used as the heat sink and lower thermal conductivity material used as the insulating jackets. The thermal conductivity of a material depends on chemical composition, temperature and microstructure. Laser flash technique is used to measure the thermal conductivity of a variety of materials. This method is based on the measurement of temperature rise on one side of the sample due to the heating of other side of the material using short energy pulse produced from a light source in a vertical set up. Disc shaped polished samples of thickness 1 mm and diameter 12 mm were used for the thermal conductivity measurement. The thermal conductivity of the material with known density is given by the relation,

$$TC = \lambda \times Cp \times \rho \qquad (2.5)$$

λ is the thermal diffusivity of sample, Cp is the specific heat capacity of the material.

In this research, the thermal conductivity of the samples measured using thermal conductivity analyser (Flash Line TM2000, Anter Corporation, USA by laser flash technique.

2.1.12 Near-infrared reflectance (NIR) measurement

Near infrared radiation includes the wavelengths between 780 and 2500 nm of the electromagnetic spectrum. In NIR spectroscopy the specimen is irradiated with NIR source and both reflected and transmitted radiations are analysed [12]. Generally, total incident radiation = reflected radiation + absorbed radiation + transmitted radiation. Where the total reflectance is the sum of diffusive reflectance and specular reflectance. Depending upon the materials refractive index the incident beam is reflected, refracted and scattered [13]. The diffusive reflectance of the sample is measured in the wavelength range 380-780 nm with barium sulphate as reference. The NIR solar reflectance(R^*) in the wavelength region from 700 to 2500 nm was tabulated in accordance with the ASTM standard E891-87. The NIR solar reflectance is the irradiance weighed average of sample’s specular reflectance r (λ), and is given by the Equation,

$$R^* = \frac{\int_{700}^{2500} r(\lambda) i(\lambda) d(\lambda)}{\int_{700}^{2500} i(\lambda) d(\lambda)} \qquad (2.6)$$

r(λ) is the experimentally derived spectral reflectance in W. m^{-1}, i(λ) is the solar spectral irradiance in W.m^{-2}. nm^{-1} derived from ASTM standard E891-87.

In this research, NIR reflectance of the films were measured by a UV–vis–NIR spectro-photometer Shimadzu, UV-3600 with an integrating sphere attachment. The IR and NIR solar reflectance data measured in the wavelength range 700-2500 nm.

2.1.13 Corrosion Studies – Electrochemical impedance spectroscopy (EIS)

Since corrosion occurs *via* electrochemical reactions, electrochemical techniques are ideal for the study of the corrosion processes. EIS uses small periodic signals to perturb an electrode surface and measure an electrochemical response that can be analysed to gain information on corrosion mechanism and corrosion kinetics. In corrosion experiment a sinusoidal voltage signal 10-50 mV is applied to a corroding electrode interface and measure the resulting current signal occurring at the same excitation frequency. The voltage and current signals are related by the impedance in a form that is analogous to Ohm's law,

$$Z(\omega) = \frac{V(\omega)}{I(\omega)} \tag{2.7}$$

Where $Z(\omega)$ denotes the complex impedance. EIS measurements on corroding surfaces are usually made using two or three electrode cell configurations.

In electrochemical analysis, to model the metal in a corroding system a metal sample with a few square centimetres surface area is used. The metal sample is dipped in a solution which is ideal to the metal's environment in the application being studied. All the electrodes are immersed in the solution, and are connected to a potentiostat. A potentiostat is a device which alters the sample's potential in a controlled manner and measure the current which is a function of applied potential [14].

In this research electrochemical impedance and potentiodynamic polarization measurement were conducted with Electrochemical Analyser, CH instruments, Inc., Model no.608A with three electrode cell consisting of reference electrode- saturated calomel electrode (SCE), counter electrode- platinum mesh and sample as working electrode. 3.5% NaCl solution is used as the electrolyte and measurements were carried out at room temperature 26 ± 2 as per standard guidelines in ASTM G5-94. The area of the sample immersed in electrolyte is $1cm^2$ and immersed for 20-30 minutes to monitor open circuit potential (OCP). With respect to their OCP value the sample is scanned from cathodic to anodic region from -200 mV to +300 mV at a rate $1\ mV.s^{-1}$. From Tafel plot the corrosion current density (i_{corr}) and corrosion potential (E_{corr}) are calculated.

2.1.14 Current-Voltage characteristics - Electrometer

The current-voltage analysis (I-V characteristics) was performed using a high resistance meter/electrometer. The dense disc shaped samples were polished using metallographic grade emery paper. The polished sample was electroded using silver paste on both sides. At every 10 V the current passing through the cross section of the sample was measured. At the end graph is plotted with current density along X-axis and electric field along Y-axis. From the current-voltage curve the value of non-linear coefficient (α) was calculated using the Equation,

$$\alpha = \frac{\log J_2 - \log J_1}{\log E_2 - \log E_1} \tag{2.8}$$

Where, E_1 and E_2 are the electric field at current densities J_1 and J_2 respectively.

The breakdown field of the varistor is the electric field corresponding to $1\ mA.cm^{-2}$ current density. The leakage current (J_L) is the as the current at $0{\cdot}80 \times E_{1\ mA}$ (where, $E_{1\ mA}$ is the electric field at 1 mA current.

This research used electrometer Keithley 6517A India having a built in power up to 1000Vwith a current limit of about 1mA.

2.1.15 Dielectric measurement – LCR meter

The dielectric properties of the material from 500 Hz to 3 MHz were measured *via* the parallel plate capacitor method with the aid of an LCR meter. The parallel plate capacitor method involves sandwiching a thin sheet of material between two electrodes to form a capacitor [15]. This is done by uniformly coating thin layer of silver paste on both sides of the cylindrical specimen. LCR meter uses auto balancing bridge technique to measure the complex impedance from which the capacitance and loss tangent are calculated. The relative permittivity is calculated using the equation,

$$\mathrm{C} = \frac{\varepsilon_r \varepsilon_0 \mathrm{A}}{\mathrm{d}} \tag{2.9}$$

Where C is the capacitance, ε_r is the relative permittivity of the material, ε_0 is the permittivity of free space, A is the cross sectional area and d is the thickness of the sample.

In this research the dielectric characterization of the sample carried out by parallel plate capacitor method using a precision LCR metre Hioki 3532-50LCR HiTESTER, Nagano, Japan. Circular disc shaped samples of thickness 1mm and diameter 10 mm coated with silver paste was used for dielectric measurement.

2.1.16 Tensile measurement

Among the various tests used to evaluate mechanical properties of materials, tensile test in which the sample is pulled to failure in a relatively short period of time, is perhaps the most useful. In this test the sample is elongated at a constant rate and the load required to produce a given elongation is measured as a dependant variable. A stress-strain curve may be plotted from the results of a tension test which may reveal the toughness of the material.

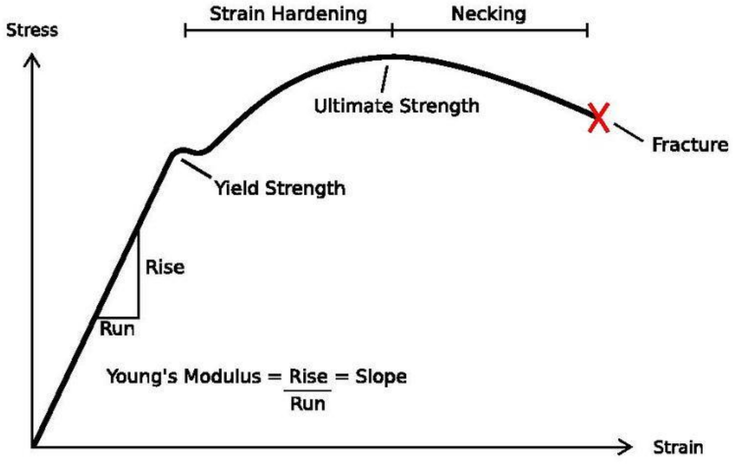

Figure 2.4: Stress-strain curve of mild steel.
(Reff. http://commons.wikimedia. org/wiki/File:Stress_Strain_Ductile_Material.pdf)

A typical stress-strain curve of mild steel is depicted in Figure 2.4. In the starting region of the graph the response of material is linear elastic. In this region material will retain its original state after the load is removed. The extent of deformation of the material in this region is measured by young's modulus. If the applied force is increased the material will reach at its yield point after which the material will experience plastic or permanent deformation.

In this research the tensile test of the film strips were carried out on rectangular shaped sample at room temperature (32 ^oC) according to ASTM standard D882 using tensile testing machine Tinious Olsen H5KS. Gauge length of the film strip used was 15 mm and load was applied on the specimen with a cross speed of 100 mm/min.

2.1.17 Vickers Hardness

Vickers microhardness tester consists of Vickers diamond pyramidal indenter having a square base and pyramidal angle of 136 ^{o}. The specimens are subjected to a particular load for a definite dwell time. Average values of five readings were reported as the microhardness of the samples. The average hardness of five readings was taken using average diagonal length of the residual indentation mark on the composite sample. Indentation image was displayed on the projected screen through objective lens.

Vickers hardness number (H_V) can be calculated by using Equation,

$$H_V = 1.8544 \, (F/d^2) \qquad (2.10)$$

where, F is load (kg) and d is the average diagonal length (mm).

In this research work, the microhardness of the composite was measured by Microhardness tester (SHIMADZU HMV) having pyramidal Vickers diamond indenter. A load of 25 gf was applied for a dwell time 14 s on finely polished samples. Five trials were carried out for each sample and average was taken.

References

[1] Guinier, A., Lorrain, P., Lorrain, D.S.M. and Gillis, J. "X-ray diffraction in crystals, imperfect crystals, and amorphous bodies." Physics Today 17 (1964): 70.

[2] Jayanthi, K., Chawla, S., Joshi, A.G., Khan, Z.H. and Kotnala, R.K. "Fabrication of luminescent, magnetic hollow core nanospheres and nanotubes of Cr-doped ZnO by inclusive coprecipitation method." *The Journal of Physical Chemistry C* 114.43 (2010): 18429-18434.

[3] Chu, B. "Dynamic light scattering." Soft matter characterization. Springer Netherlands, 2008. 335-372.

[4] Pecora, R. ed. *Dynamic light scattering: applications of photon correlation spectroscopy*. Springer Science & Business Media, 2013.

[5] Gaisford, S., Kett, V. and Haines, P. Principles of thermal analysis and calorimetry. Royal society of chemistry, 2016.

[6] Brundle, C.R., Evans, C.A. and Wilson, S. *Encyclopedia of materials characterization: surfaces, interfaces, thin films*. Gulf Professional Publishing, 1992.

[7] Buseck, P., Cowley, J. and Eyring, L. eds. *High-Resolution Transmission Electron Microscopy: And Associated Techniques*. Oxford University Press, 1989.

[8] Goldstein, J.I., Newbury, D.E., Michael, J.R., Ritchie, N.W., Scott, J.H.J. and Joy, D.C. *Scanning electron microscopy and X-ray microanalysis*. Springer, 2017.

[9] Pleul, D. and Simon, F. "X-ray photoelectron spectroscopy." *Polymer Surfaces and Interfaces*. Springer, Berlin, Heidelberg, 2008. 71-89.

[10] Shiraiwa, T. and Fujino, N. "Theoretical Calculation of Fluorescent X-Ray Intensities in Fluorescent X-Ray Spectrochemical Analysis." *Japanese Journal of Applied Physics* 5.10 (1966): 886.

[11] os Santos, W.N., Mummery, P. and Wallwork, A. "Thermal diffusivity of polymers by the laser flash technique." *Polymer testing* 24.5 (2005): 628-634.

[12] Nicolai, B.M., Beullens, K., Bobelyn, E., Peirs, A., Saeys, W., Theron, K.I. and Lammertyn, J. "Nondestructive measurement of fruit and vegetable quality by means of NIR spectroscopy: A review." *Postharvest biology and technology* 46.2 (2007): 99-118.

[13] Vishnu, V.S. and Reddy, M.L. "Near-infrared reflecting inorganic pigments based on molybdenum and praseodymium doped yttrium cerate: Synthesis, characterization and optical properties." *Solar Energy Materials and Solar Cells* 95.9 (2011): 2685-2692.

[14] Jayaraj, J., Raj, S.A., Srinivasan, A., Ananthakumar, S., Pillai, U.T.S., Dhaipule, N.G.K. and Mudali, U.K. "Composite magnesium phosphate coatings for improved corrosion resistance of magnesium AZ31 alloy." *Corrosion Science* 113 (2016): 104-115.

[15] Tereshchenko, O.V., Buesink, F.J.K. and Leferink, F.B.J. "An overview of the techniques for measuring the dielectric properties of materials." *General Assembly and Scientific Symposium, 2011 XXXth URSI*. IEEE, 2011.

CHAPTER 3

Aqueous Mechanical Oxidation of Zn-Dust:-A Novel Room Temperature Synthesis of Nano ZnO

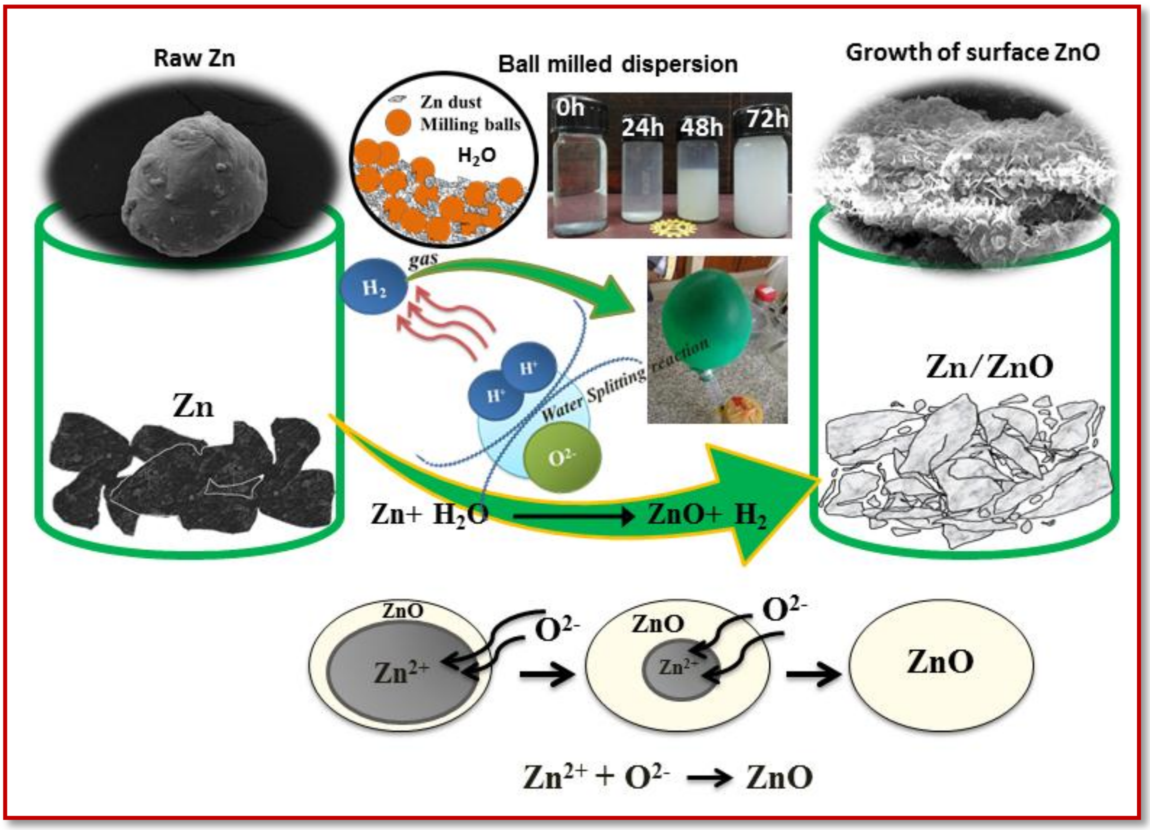

Chapter 3 is divided into two parts. The ***first part*** *describes a facile and sustainable technique namely 'aqueous mechanical-oxidation for the conversion of Zn-metal to nano ZnO powder at room temperature. Low cost Zn dust was just subjected to aqueous mechanical milling without any catalyst or thermal treatment. The process used only Zn dust and water as the main reagents. No other catalysts or organic materials are anyway involved at any stages of the production. Interestingly, the process produced* H_2 *gas as a by-product along with ZnO via water splitting reaction during the mechanical oxidation of Zn dust. In the* ***second part*** *of this chapter, an attempt was also made in order to validate the effects of surfactants on mechanical-oxidation for the synthesis of nano ZnO. Finally, the nano ZnO produced via mechanical oxidation with and without surfactants was explored for obtaining fine-grained sintered ZnO ceramics.*

A part of the work discussed in this chapter has been published in, ***ACS Sustainable Chemistry and Engineering*** *6, (2018) 143–154.*

3.1 Aqueous Mechanical Oxidation of Zn Dust

3.1.1Abstract

Room temperature processing of nano ZnO was successfully carried out *via* a novel approach called *aqueous mechanical oxidation* of raw metallic Zn dust. Micron sized metallic Zn dust (~45 µm, 99.9 %) was mechanically milled for different time period to have ZnO seed nuclei on its surface. The mill induced nucleation and growth of nano ZnO layer on the surface of Zn particles were observed at different stages of milling. Effect of milling on the growth of ZnO seed layer, particle size distribution, oxidation kinetics, phase purity, dispersion stability and UV absorption properties were systematically investigated and reported. Direct wet-milling of micron sized Zn dust (~45 µm) using ceramic milling media for 72 h, resulting in the production of bulk monocrystalline nano rods of ZnO with aspect ratio ~5.2 and hydrodynamic diameter of 315 nm. The voluminous H_2 gas was also produced *as* a by-product *via* catalyst-free water-splitting reaction during milling operation. In a nutshell, the present study throws light into an economic, zero - effluent, single-step and parallel processing route for two high value products, bulk nano ZnO and catalyst-free H_2 gas from an industrial by-product Zn dust.

3.1.2 Introduction

Among the different metal oxides, nano zinc oxide (ZnO) has earned enormous attention for its diverse applications [1-6]. ZnO is a multipurpose functional material with wide range of growth morphologies [7-9]. Variety of synthesis methods for the production of nano ZnO including the sol-gel process [10, 11], vapour deposition [12, 13], precipitation from micro emulsions [14, 15], hydrothermal synthesis [16-18], precipitation method [19-21], and mechanochemical processes [22-24] from laboratory scale to bulk industrial scale are often discussed. Commonly followed synthesis approaches for ZnO usually starts either from chemical precursors or from the ores of the metal itself [5, 25-27]. Although the vapour phase methods have advantages of high quality product and simple operation, they generally need expensive equipment and high processing temperature. Solution phase approaches are also promising due to its low cost, lower operating temperature and high quality product, but still the sedimentation and calcination leads to agglomeration of nanoparticle [14]. Therefore, it is highly desirable to have new synthesis methods to facilitate the nucleation and growth for the large scale production of ZnO nanoparticles [28-29].

Solid-state, top-down mechano-chemical approaches for the synthesis of functional nano materials are facile and low cost route for the large scale production of nanomaterials [23, 30, 31]. This includes mechanical activation of starting powder mixture prior to subsequent chemical reaction/heat treatment and is usually adopted by industries for the large scale synthesis of nano-materials owing to its simple unit-operations at the various processing stages [32-34]. Currently, mechano-synthesis is an established green-route for the production of various scientifically and commercially important nano-materials including nanocomposites, nano-quasicrystalline materials and nano-alloys [35-38]. Because of the '*zero-waste*' processing and elimination of harmful chemical effluents, mechanical methods are often associated with various chemical processing of nano-materials [35, 39]. High energy ball milling (HEBM) is a well-recognized technique for particle size reduction, triggering surface activation at atomic level and for even tailoring the chemistry of nano-materials [38, 40-43]. The localized regions having high temperature (< 1000 ^{o}C) along with high pressure upto several GPa are created during mechanical milling due to high impact energy generated from the high energy collision of ceramic milling-media [44]. This can induce nucleation, accelerated growth of exotic nanostructures and phase transformations [38, 45, 46]. In fact, the mechanical treatment of reactants induced sequential phase transformations which were found identical to that occurred during thermal treatments [47]. In the work by Bodaghi *et al.*, α-Al_2O_3 seeds formation was identified during the milling operation of metastable γ -Al_2O_3, which accelerated the transformation kinetics of γ- Al_2O_3 to α-Al_2O_3 during milling action [48]. Delogu *et al.* also identified the mechanically induced phase transformation of TiO_2 from anatase to TiO_2 (II) and finally to rutile during milling [49]. The capability of mechano-syntheses for triggering variety of complex oxide formation reactions was described by Zyryanov *et al.* [50].

Handful reports are also available on synthesis of nano metal oxide from their nano chemical precursors at ambient temperature conditions *via* mechano-synthesis route [51-53]. High energy milling assisted synthesis of nano metal oxides were reported to have unusual functional properties and high degree of surface and structural order compared to particles that obtained *via* ‘soft methods’, like chemical routes [54, 55]. Castro *et al.*, in their work on synthesising conducting and stable complex oxide Bi_2VO_5 endorsed the importance of the mechanical activation step [56]. The role of the mechanical milling as an activation step in obtaining soft PZT type piezoceramics was investigated by Miclea *et al.* [57]. Lately a work by Khayati *et al.* confirmed the formation of Cuprous (Cu_2O) nanoparticle induced during solid state milling of Copper in oxygen atmosphere [58]. However, till date no reports are there on using milling technique as a direct synthesis route for the bulk production of metal oxide nanoparticle *via* aqueous milling of metals.

The present chapter of the thesis describes an eco-friendly, aqueous, mechanical processing for the direct oxidation of Zn dust to ZnO nanoparticle by systematically varying the process conditions and operating parameters. The most opted techniques for the synthesis of ZnO from metallic Zn are thermal oxidation [59] and evaporation technique because of its simplicity, cost effectiveness and the reaction is catalyst free [60, 61]. However the poor control over synthesis process and evaporation losses of metallic Zn are still remains challenging [59, 62]. Reports are there on mechano-chemical methods for the synthesis of ZnO particles [46, 63, 64]. Some of them are already enlisted in the table in the Section 1.3.2.4. In a work done by Salah *et al.*, they reported the milling induced structural modifications of ZnO powders, which improved actively its inherent antibacterial property [65]. The same technique is used by Glushenkov *et al*. as a kind of activation prior to the sequence of annealing steps, for generating corrugated ZnO nanowires [66]. Reports indicate that the activity of nano ZnO has improved significantly by the mechanically induced crystalline imperfections [67, 68]. Recently, a work by Francavilla *et al.* described the enhanced photocatalytic degradation of phenol by employing ZnO obtained *via* dry-milling of chemical precursors and sacrificial templates polysaccharide and subsequent calcination step at 600 °C [69]. Thus, most of those approaches use the mechanical processing just as the activation of reactant mixture or as an initial treatment process prior to the subsequent calcination step. Also it has to be considered that the precursors used for most of mechano-chemical synthesises reported so far are the Zn salts along with a base. Thus numerous washing steps are necessary in almost all those works before calcination, to obtain the final ZnO nanoparticles [70]. Among the various reported works mentioned in the Table 1.4 and 1.5, none of them have reported the direct oxidation of metallic Zn to nano ZnO *via* aqueous mechanical oxidation of raw Zn dust.

Two-step water splitting of Zn/ZnO couple and subsequent production of hydrogen gas *via* Zn hydrolysis by heat from solar process were investigated and reported by many research groups in the previous years [71, 72]. As reported by Weibel *et al.* the high oxygen looping capacity per unit mass of Zn is responsible for the capability of Zn for the water splitting reaction [73]. Abanades *et al.* investigated the production of solar hydrogen by thermally reducing metal oxides using a solar reactor [74]. This approach is found to be effective for the production of solar fuels in addition to the material synthesis intended.

The present study employs only raw Zn dust and water as the major reagents for the synthesis of nano ZnO *via* aqueous mechanical oxidation and thereby totally eluded the environmental concerns which are usually required to be addressed while employing the chemical precursors. In addition to the transformation of the raw Zn dust to nano-ZnO the evolution of the valuable by-product hydrogen gas during the process was also identified. The selection of low cost starting material, the micron sized Zn dust obtained from secondary sulphide concentrates for this work itself highlights ‘waste to wealth’ engineering initiative and is reported for the first time.

3.1.3 Experimental Section

3.1.3.1 Materials

Zinc (Zn) dust (99.9 %) having particle size ~ 45 μm (Binani Zinc Pvt. Ltd., India) was used as the starting material. For the comparative study commercial ZnO (Sigma–Aldrich, Germany) was used. Aqueous milling was carried out in distilled water.

3.1.3.2 Mechanical Milling and Processing

A belt driven laboratory type ball mill operating with a rotor speed of 250 rpm was used to carry out the aqueous mechanical oxidation of raw Zn dust. Fixed amount of raw Zn dust (20 g) was charged into the milling bottles (propylene bottles (Tarsons, India)) with a mill space volume of 250 mL along with Zirconia balls (10 mm dia., Jyoti Ceramics Pvt. Ltd., India) and distilled water as the milling medium. The ball to powder mass ratio

(BPMR) was selected as 6:1. All the parameters of milling process were optimized after repeated trials and listed in the Table 3.1.

Table 3.1: Optimised milling process parameters.

Volume of mill chamber (mL)	250
Milling media	Zirconia balls (dia. 10mm, wt. ~3 g (each))
Mass of Zn dust loaded (g)	20
Liquid carrier, charged (mL)	Distilled water, 170
Speed of mill RPM (rev/min)	250
BPMR[1]	6:1
Milling period (h)	24,48,72

[1] *BPMR: Ball-to-powder mass ratio*

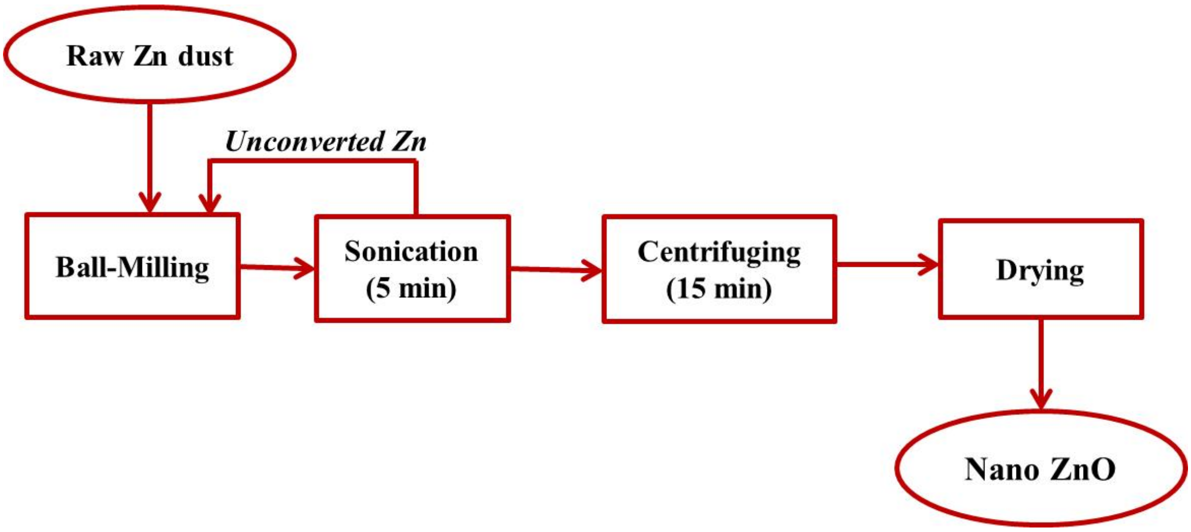

Figure 3.1: Processing route adopted for the aqueous mechanical oxidation of raw Zn dust.

The raw Zn dust was milled for different periods of time (24, 48, and 72 h) and the samples were marked as Zn 24, Zn 48, and Zn 72, respectively. In order to ‘peel off’ the surface ZnO layer formed on Zn particle, the milled slurry was then sonicated for a period of 5 min using an ultrasonic bath (GT Sonic, Ultra Instruments, India). After each individual experiments the unconverted fraction of Zn was transferred back to the milling chamber while the top dispersion formed were collected and centrifuged (TC 4100F, Eltek, India) to obtain the final product. The schematic representation of processing of raw Zn is illustrated in Figure 3.1.

3.1.3.3 Gas analysis: Gas Collection from the Mill Chamber

The gas generated during milling of Zn dust was collected and analyzed using standard gas chromatographic techniques. Extreme care was taken to collect the gas generated in the mill chamber. A pin hole was drilled on the chamber wall and to carry the gas to an air bag (TEDLAR® bags) a fuel hose with a pin nozzle arrangement was used. The gas collected was tested using the Gas Chromatographic (490 Micro GC, Agilent Technologies, UK) technique using GPA Standard 2145-09 (FPS). The gas collection setup used in the present study is shown in Figure 3.2.

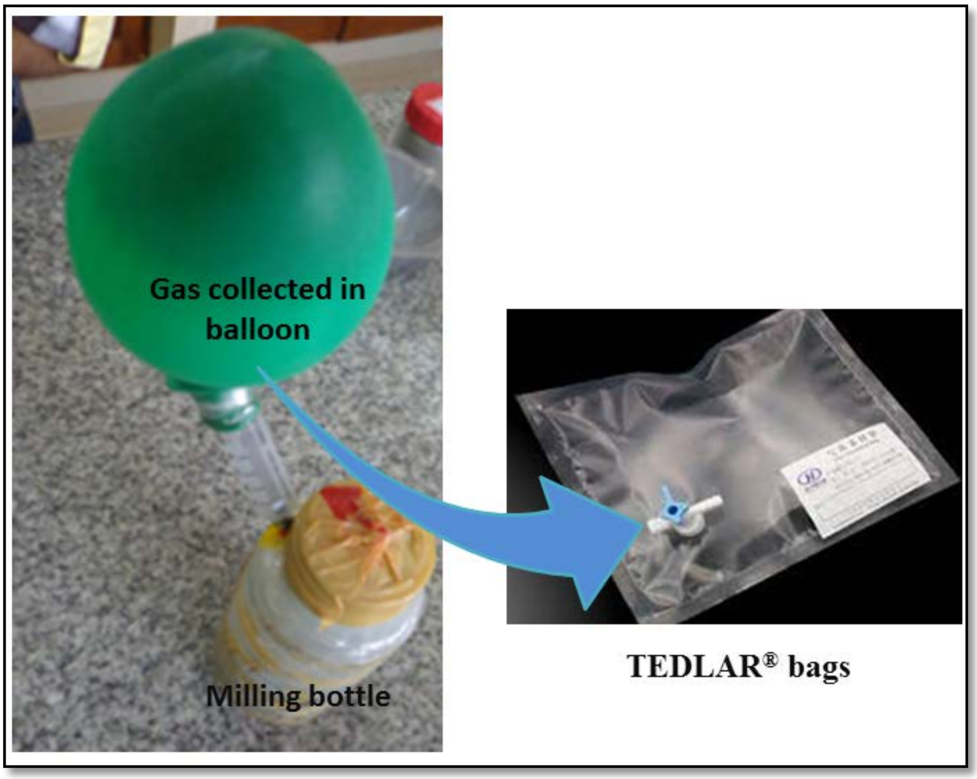

Figure 3.2: Gas collection setup from mill chamber.

3.1.4 Results and Discussion

3.1.4.1 Raw Zn Dust Microstructure and Properties.

Micron sized Zn dust (~45 μm), the raw material used for this study is a partially avoided by-product of smelt industry. The XRF analysis was conducted for raw Zn dust and results are presented in the Table 3.2. The raw Zn dust contains 99.96 % Zn and insignificant amount of Si and Cd only at ppm level.

Table 3.2. XRF analysis of Raw Zn dust.

Elements	Concentration
Al	0
Si	159.4 ppm
P	0
Cl	0
K	0
Co	0
Zn	99.96%
Cd	119.6 ppm
In	0

The SEM microstructure of the raw Zn dust used in the present study is shown in Figure 3.3 (a). It can be seen from the SEM image that, individual Zn particle is a dense, melt-solidified, micron sized particle having almost spherical shape (Figure 3.3 (b)). Figure 3.3 (c) shows the phase analysis of as received Zn dust. All the diffraction peaks presented in the obtained spectra are indexed to hexagonal Zn with lattice parameters of a = 2.665 Å and c = 4.947 Å (JCPDS card no. 04-0831). The diffraction peaks observed at 2θ values of 36.3, 39.07, 43.3, 54.3, 70.1 and 70.7 corresponds to the lattice planes (002), (100), (101), (102), (103) and (110) respectively.

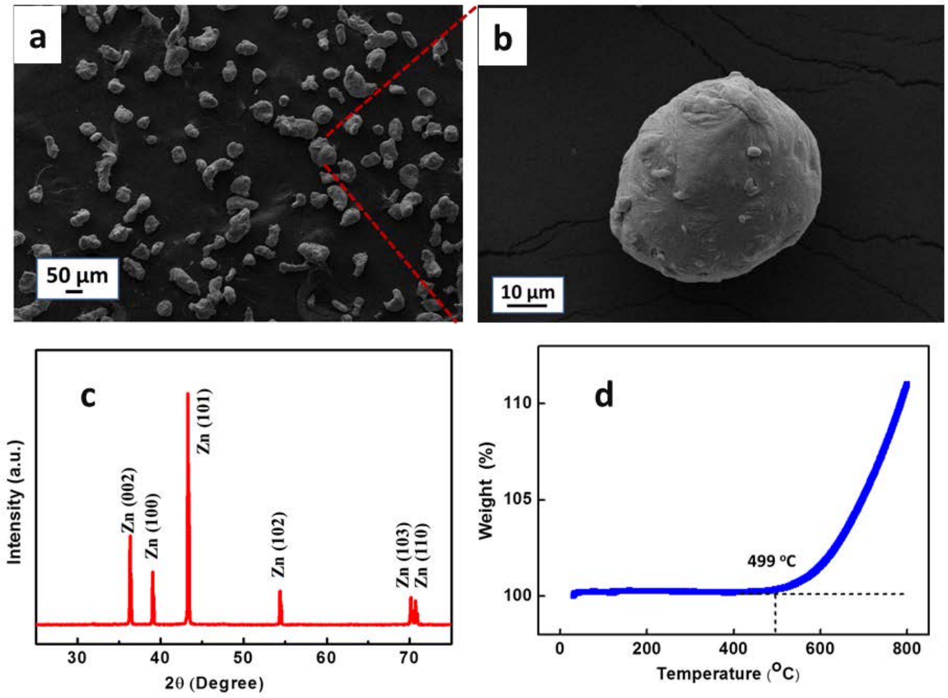

Figure 3.3: (a and b)SEM image of raw Zn dust at lower and higher magnification, (c) XRD and (d) TG analysis of raw Zn dust.

Other characteristics peaks corresponding to any of the impurity phases were not found, indicating that the raw Zn dust composed of pure Zn phase only, no other impurity were present. The decomposition profile of raw Zn dust is illustrated by TGA curve depicted in Figure 3.3 (d). Pure Zn dust has a theoretical melting point of 419 ^{o}C and a boiling point of 908 ^{o}C. With increase in temperature, oxidation of the Zn dust starts at around 499 ^{o}C causing a steep rise in the TGA curve.

3.1.4.2 Metal to Metal Oxide *via* Mechanical Milling

Milling induced surface growth of nano ZnO on Zn particle is apparently seen from the SEM images of milled Zn dust at different intervals of time shown in Figure 3.4 (a)-(c). During aqueous milling of Zn dust ZnO seed nuclei are formed due to the oxidation of surface Zn atoms caused by the interaction with atmospheric oxygen. Previous reports are there on the passivation of the Zn surface by an impermeable ZnO layer during different processing stages [46, 73]. The Figure 3.4 (a) clearly shows raw Zn dust particle with clean surface without any characteristic surface growths. After about 12 h of continuous milling, distinctive growth of nano ZnO was observed on the surface of Zn dust particles, as seen in the Figure 3.4 (b). This nano ZnO sprouting on the surface of Zn particles are induced from the mechanochemical interaction of Zn particles with the milling media and the environment.

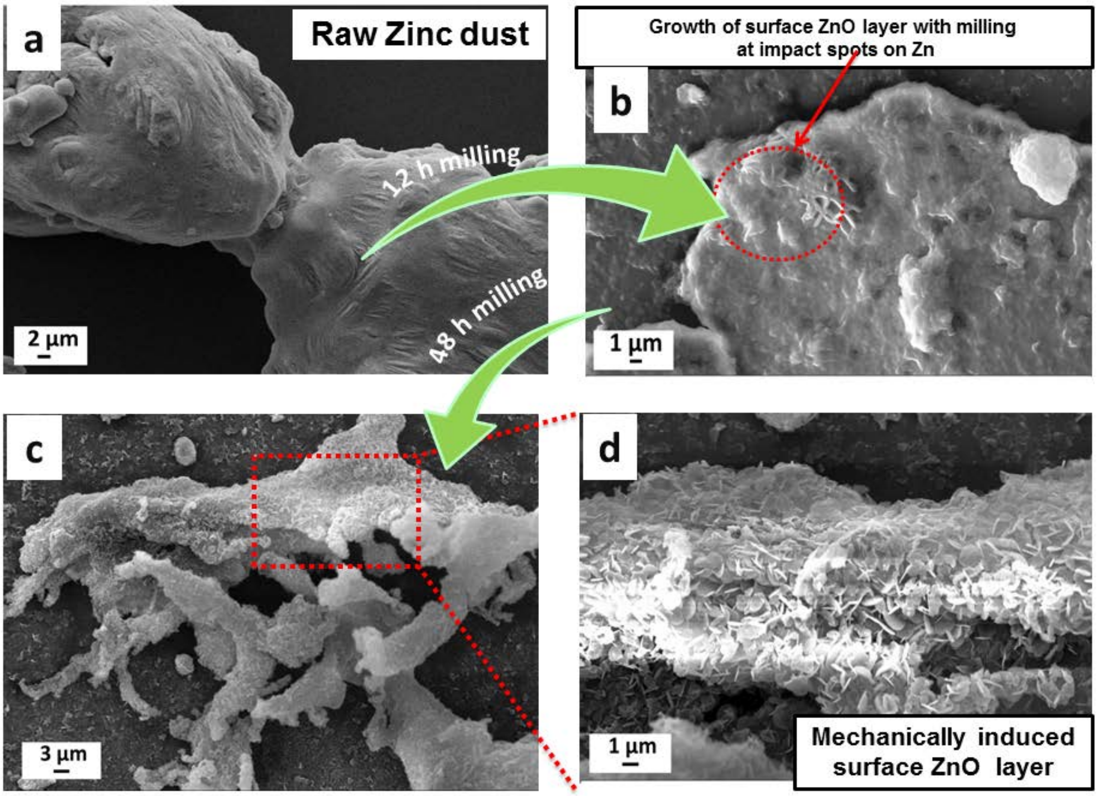

Figure 3.4: Surface growth of ZnO during milling of Zn dust. (a) Raw Zn dust, (b) growth of ZnO after 12 h milling, (c) Zn surface having flaky transitional phase after 48 h milling and (d) enlarged portion of (c) clearly showing growth of surface nano ZnO.

. Pineda *et al.* has previously reported the hydrolysis of metal precursors during mechanical milling [75]. Pacholski *et al*. reported the formation of single crystalline ZnO nanorods from spherical particles *via* oriented attachment (OA), a non-classical mechanism [76]. The proposed mechanism also suggests the existence of a 'pearl chain' like intermediate phase, finally resulting in the formation of rod shaped oxide nanoparticles.

The orient attachment mechanism was first proposed by Banfield *et al*. [77, 78]. The orient attachment model is based on the interactions that hold the assembled units together. The interactions between the components ranging from electrostatic forces to van de Waals forces act as the motive force for the orient attachment process. Yu *et al*. employed orient attachment mechanism to explain the growth of elongated quantum rods [79]. According to this mechanism the specific facet of individual nanoparticle formed at early growth stage of the process were attached together *via* weak interactions and resulted in the formation of elongated quantum rods. The mechanism of quantum rod formation is illustrated schematically in Figure 3.5. At the early growth stage individual isolated particles were formed and then the specific faces of particles were attached together (Figure 3.5 (a) and (b)) leading to the formation of elongated quantum rods (Figure 3.5 (c) and (d)). The mechanism was also employed in different works using reflux technique, where the length of the nanorods formed was controlled by reflux time [76].

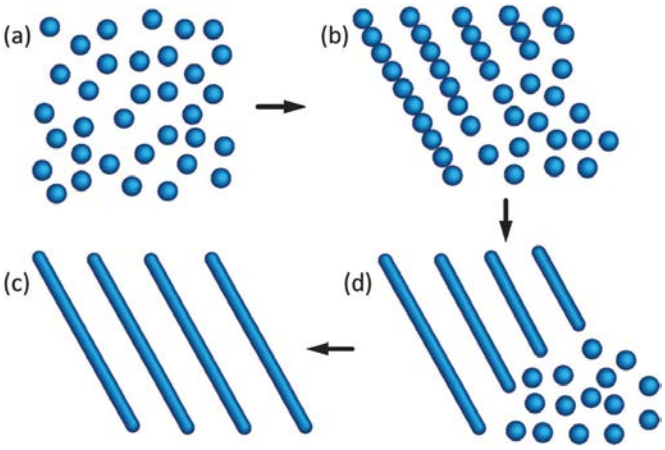

Figure 3.5: Schematic representation of quantum rod formation from spherical dots *via* orient attachment mechanism. (Reproduced with permission of American Chemical Society, https://pubs.acs.org/doi/abs/10.1021/ja044593f)

With extended milling for about 48 h, the growth of thin flaky layer was seen on the Zn surface Figure 3.4 (c). The growth of flaky surface nano ZnO is well clear from the SEM image at higher magnification (Figure 3.4 (d)). This can be considered as an oxide layer on Zn particle induced mechanically during milling due to the hydrolysis reaction at the interface [80]. With further milling these surface oxides formed get detached from the Zn particles and forms ZnO seeds in solution which grow into nanorods. Thus due to the mechanochemical interactions occurring at the mill chamber a direct conversion of the metal to metal oxide was perceived. In the present study ZnO yield from Zn *via* aqueous mechanical oxidation is calculated to be ~ 32 % after 72 h of milling.

The TGA curves of the milled Zn dust (72 h) displays a clear down (left) shift of ~100 ^{o}C in the onset oxidation temperature compared to unmilled Zn dust, indicating clearly the formation of ZnO seeds on the Zn dust due the mechanical action during milling [46] (Figure 3.6 (a)). The Figure 3.6 (b) depicts the TGA curves of the milled Zn dust for different time period (viz 24, 48, and72 h) and held at the maximum temperature (700 ^{o}C) for 1 h. The reduction in mass gain during the held period (1 h) at this extreme condition (700 ^{o}C) for the Zn 72 is quite evident from the corresponding TGA curve. This gradual reduction in mass gain from Zn 24 to Zn 72 clearly confirms the increased conversion rate of Zn to ZnO with increase in the milling period [46]. However, the evidences obtained from TG analysis and SEM are not enough to confirm the formation of ZnO during milling of Zn dust.

ZnO nanoparticles formation during mechanical milling was further confirmed from the XRD analysis of Zn dust milled for different time intervals. The Figure 3.7 shows the phase analysis of the powder collected from the dispersion obtained after sonication of the Zn dust milled for different time periods. The sprouting of peaks at 2θ values 31.91, 34.45, 36.28, 47.60, 56.64, 62.82°, and 67.93° after milling of 24 h confirms the formation of wurtzite phase ZnO crystal (JCPDS 36-1451) during milling [81].

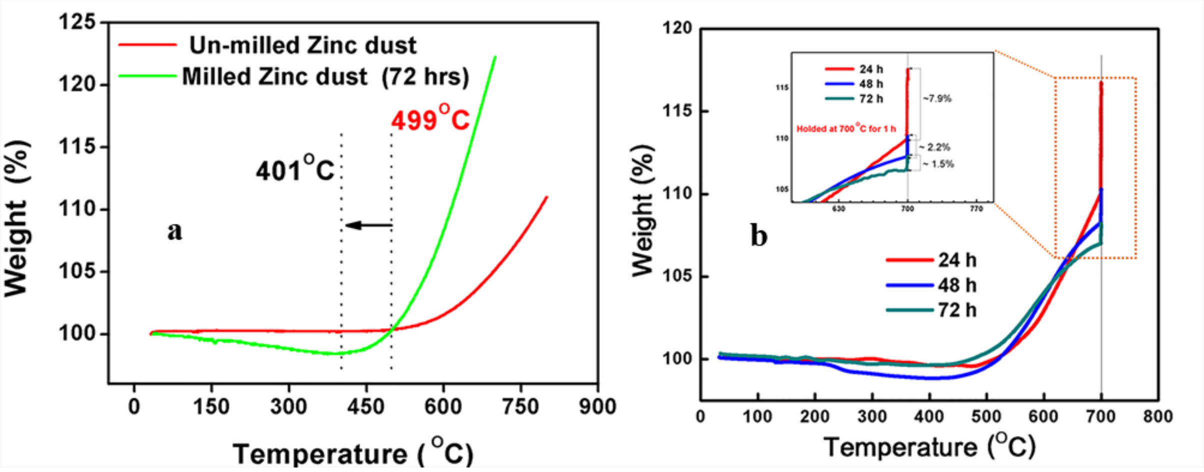

Figure 3.6: (a) TG analysis of unmilled and milled (72 h) Zn dust and (b) TG analysis of the Zn dust milled for different period of time and held at 700° C for of 1 h.

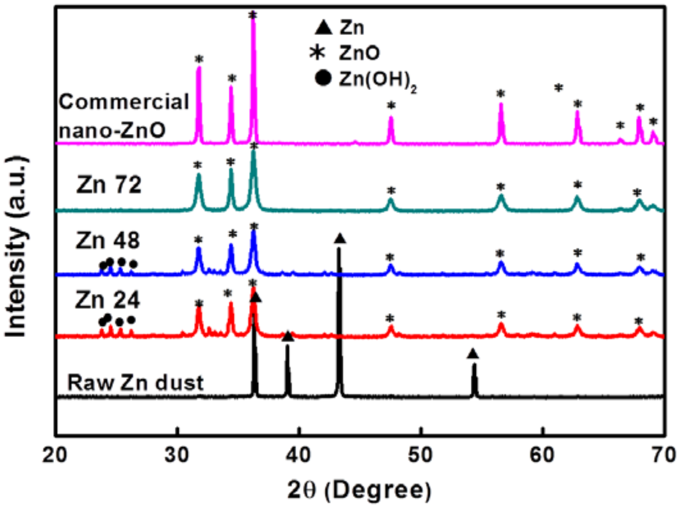

Figure 3.7: XRD pattern of Zn dust milled for different period of time and commercial ZnO (Sigma–Aldrich).

With the increase in milling time these peaks are found to become more prominent, as evidenced from the phase analysis. Some minor peaks in the region between 23°-27° are also present, which corresponds to the formation of hydroxide phase of Zn [26]. However, these peaks become less prominent with an increase in the milling time and after 72 h of milling, hydroxide peaks vanished completely and confirms the complete conversion of the hydroxide phase to the oxide phase. For comparative analysis the XRD patterns of commercial ZnO (Sigma–Aldrich) and of the raw Zn dust having characteristic peaks at 36.28^{o}, 39.07^{o}, 43.33^{o}, and 54.32^{o} are also given in the Figure 3.7.

During milling, the mechanical action triggered ZnO seeding and is apparently seen from the UV–vis spectra of the dispersion obtained at different time intervals of milling of Zn dust (viz 24, 48, 72 h) (Figure 3.8). The UV analysis shows strong absorption in the UV region with maximum absorption peak positioned at wavelength range 360–380 nm, which is the characteristic band edge absorption of ZnO. Thus the UV absorption spectrum supports and provides strong indication of ZnO seeding induced by milling.

The dispersions collected at different intervals of milling for the absorption studies are shown as inset in the Figure 3.8. The pictures clearly illustrate the stability of dispersion with increase in milling time. The more stable dispersions obtained with increase in milling time indicate the increased conversion of micron sized Zn dust to ZnO nanoparticles and also the increase in number of particles of nano ZnO formed during milling.

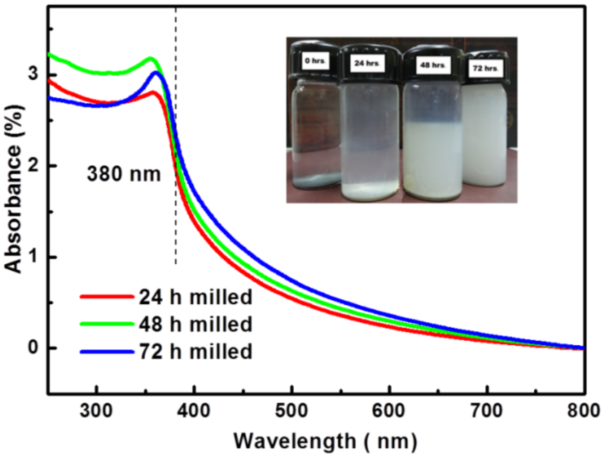

Figure 3.8: UV−vis spectroscopy of the samples obtained at different intervals of milling.

3.1.4.3 XPS analysis of Zn at Different Milling Intervals

To affirm the surface growth and chemical composition, corresponding XPS analyses were conducted for the samples. A low-resolution scan conducted over a wide energy range for unmilled and milled samples are shown in Figure 3.9(a). Presences of oxygen (O) and Zn along with some traces of carbon (C) were clearly seen in the spectrum. From this observation the formation of oxidic phases over the surface of the pure metal particle during milling was confirmed. The traces of C observed in the spectrum can come from the atmosphere. Although the C peaks are insignificant in the present study, the C 1s peak positioned at 284.6 eV is taken as the reference peak throughout the XPS analysis.

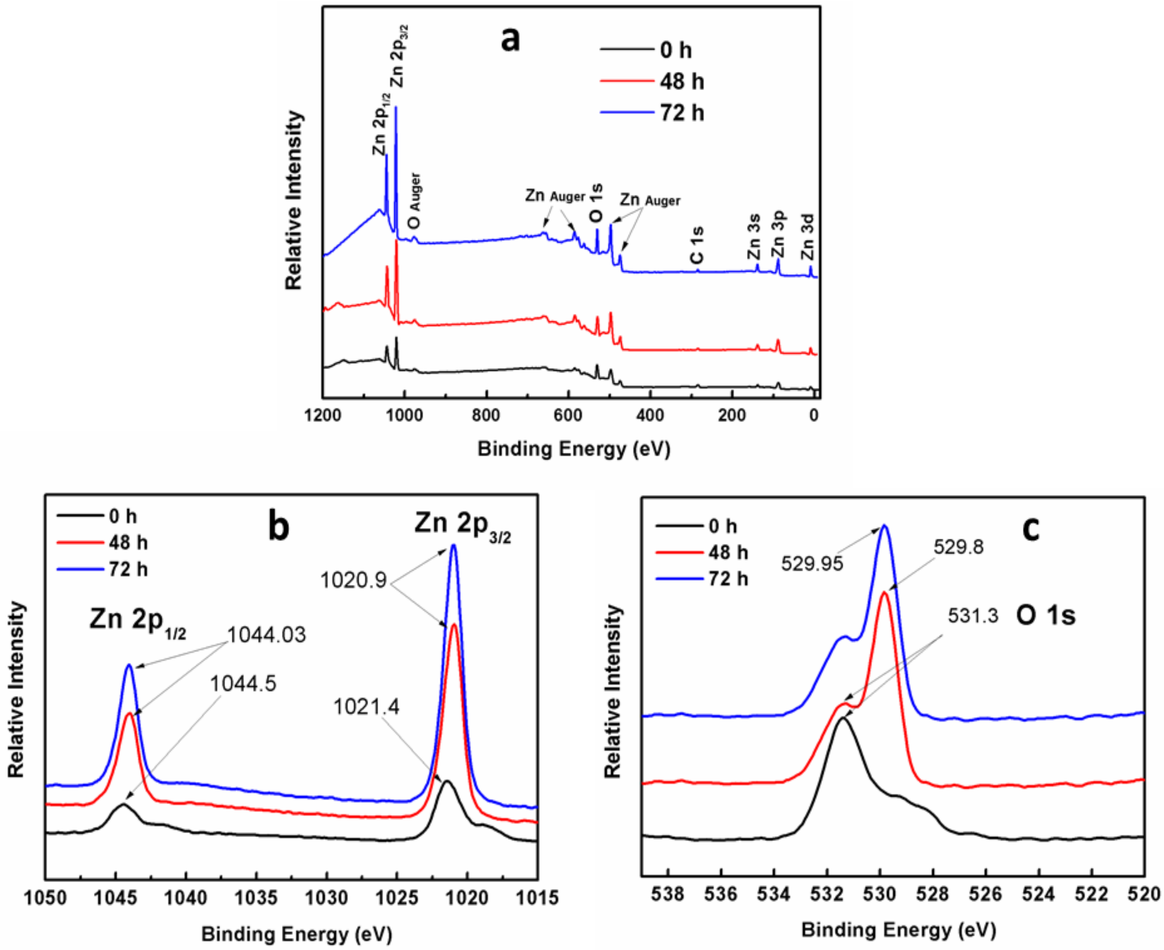

Figure 3.9: (a) Low-resolution wide scan on the unmilled and samples and High-resolution scan for (b) Zn 2p and (c) O 1s peaks on the unmilled and milled samples 0, 48, and 72 h.

The high resolution scans conducted for the peaks corresponds to Zn 2p and O 1s are shown respectively in Figure 3.9 (b) and (c). From the figure, for the 72 h milled sample the narrow scan results showed peaks at 1020.9 and 1044.03 eV corresponding to the Zn $2p_{3/2}$ and Zn $2p_{1/2}$ and can be assigned to the nano ZnO formed on surface of Zn particles [82-84]. For unmilled Zn also some characteristic peaks of Zn (2p) were seen at 1021.4 and 1044.5 eV positions. However, these peaks can be assigned to the Zn−OH bond formed when the Zn metal comes in contact with the water vapor present in the atmosphere [83, 84]. These peaks show a clear shift (right shift) with the milling of the Zn dust, as seen from the above-mentioned 72 h milled samples. This shift in the energy values can be well understood from the deconvoluted data given in Figure 3.10 (a)-(f). The loosely attached hydroxides of Zn on surface of Zn particle are gradually converted to the stable oxide phase during milling. This is due to the diffusion of the oxygen atoms into the Zn lattice [85-87]. This conversion is apparent after 48 h of milling of raw Zn dust, as the peaks of Zn 2p are seen at 1020.9 and 1044.03 eV positions (Figure 3.9 (b) and Figure 3.10 (e)).

The formation of both hydroxide and oxide phases on Zn particles was again confirmed from the narrow scan peaks of O 1s. From the Figure 3.9 (c), for the unmilled (0 h) sample the peak seen at 531.3 eV can be attributed to the oxygen in the hydroxide phase [82, 83, 85]. However, this peak position shifted to the 529.8 eV after 48 h of milling, indicating the conversion of the hydroxide phase to the oxide phase [83, 84]. A peak observed at 529.95 eV for the sample obtained after 72 h of milling, which clearly confirmed the formation of stable oxide [83, 84]. The shifts in the O 1s peaks are more clear from the deconvoluted data shown in Figure 3.10 (d)-(f). Thus, the XPS analysis of milled Zn for different time period obviously evidences the formation of nano ZnO by aqueous mechanical milling of micron-sized Zn dust particles. Thus, from the XRD, UV−vis spectroscopic result, TGA and XPS the formation of nano ZnO *via* aqueous mechanical milling of Zn dust was confirmed. Further studies were conducted with nano ZnO collected from the dispersion of the 72 h of milled sample, hereafter denoted to as aqueous mechano-synthesized ZnO.

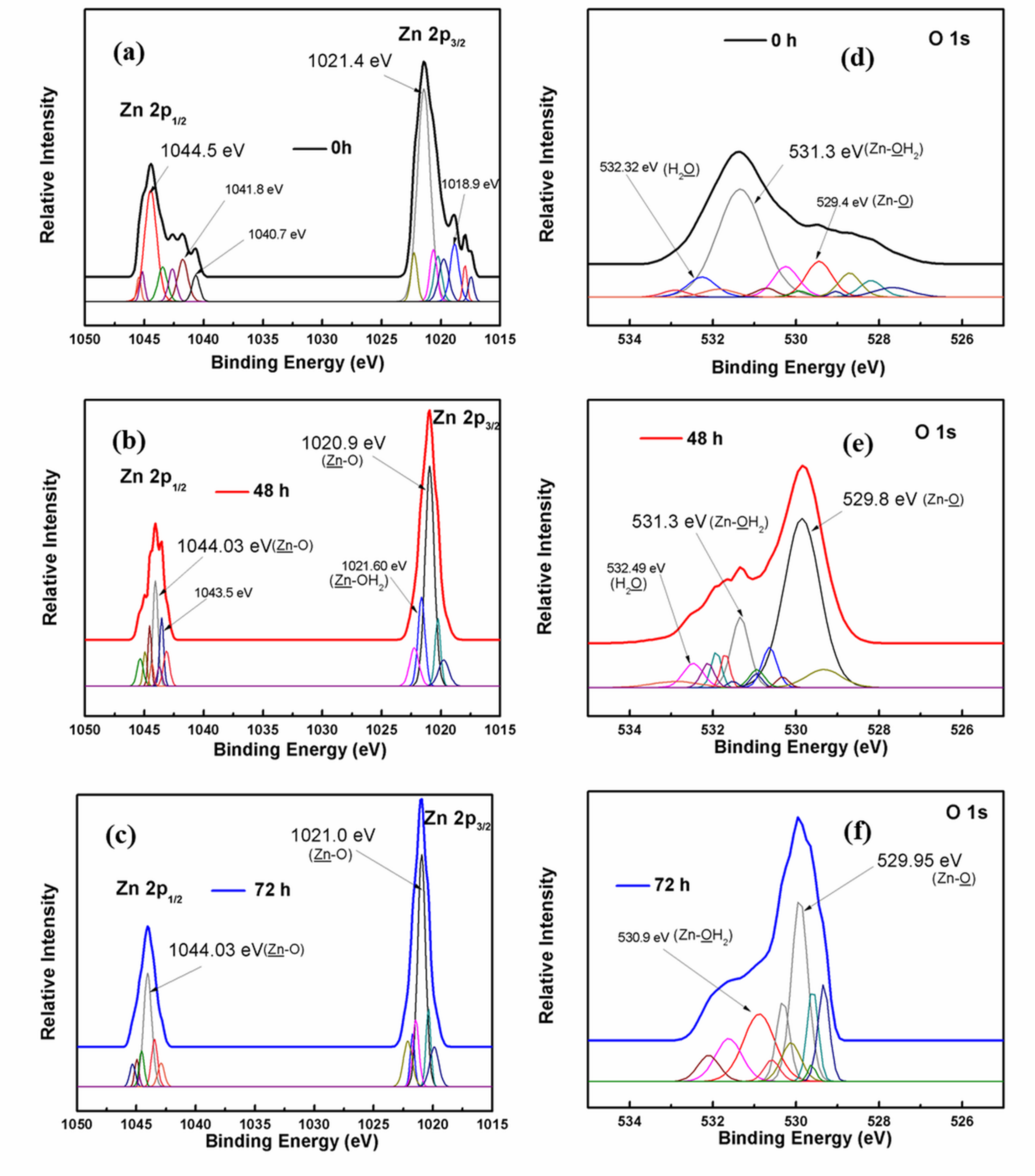

Figure 3.10: XPS, deconvoluted peaks of ((a)-(c)) Zn 2p and ((d)-(e)) O 1s from the analysis of zinc dust surfaces, after milling for different time intervals (*viz* 0h,48h and 72h).

3.1.4.4 Morphology of 'Aqueous Mechano-Synthesized ZnO'

The SEM micrograph of the aqueous mechano-synthesized nano ZnO obtained from the dispersion collected after 72 h of milling of raw Zn displays nearly rod shaped particles with aspect ratio of ~ 5.2, and length in the range 300-400 nm (Figure 3.11 (a)). Eventually the ZnO seed formed on the surface of the Zn dust during the milling grows into nanorods *via* oriented attachment (OA) mechanism.

The hydrodynamic diameter of the particles collected from the dispersion of raw Zn after 72 h milling was also measured using DLS measurement system and the average particle size observed was 315 nm (Figure 3.11 (b)), validating the result from the SEM analysis. However from the SEM image the particle appears to be highly agglomerated.

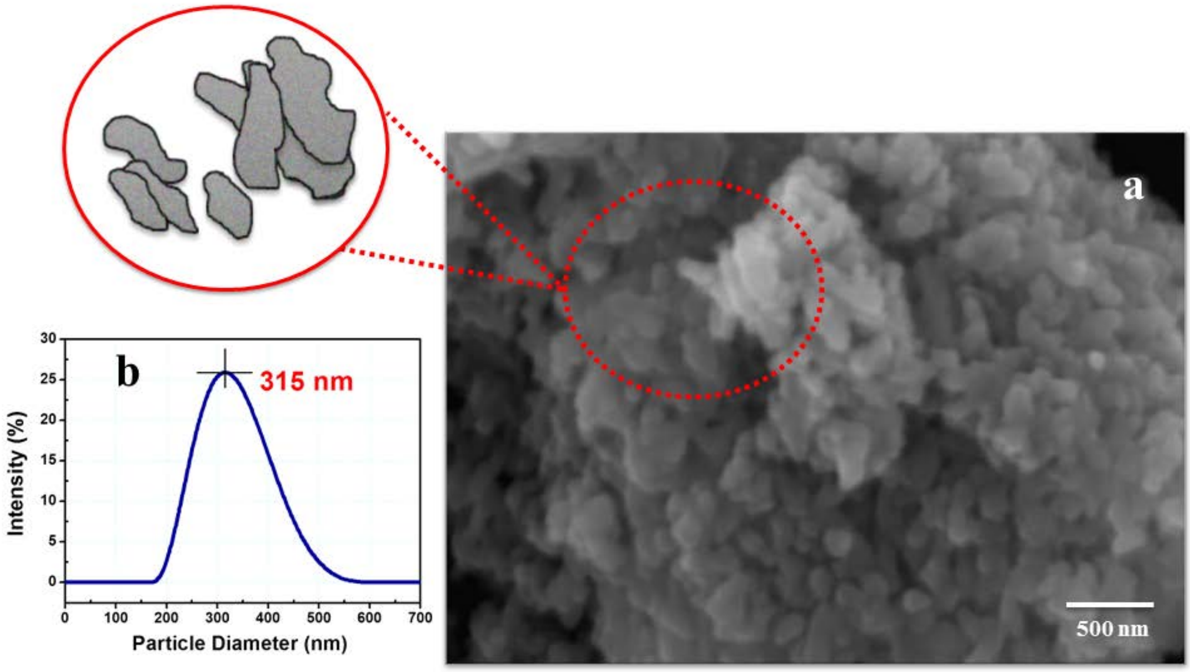

Figure 3.11: (a) SEM analysis on the synthesized ZnO; (b) average particle size measured.

To confirm the morphology of particle a higher magnification image was required. For that TEM analysis was conducted on the same samples and rod like morphology of particles were confirmed. In the TEM image the nanorods were found to be more evident and isolated. The size of the particles observed from TEM were found to be in the range 300-400 nm (Figure 3.12 (a) and (b)), which is in well agreement with the observations from the DLS and SEM analysis.

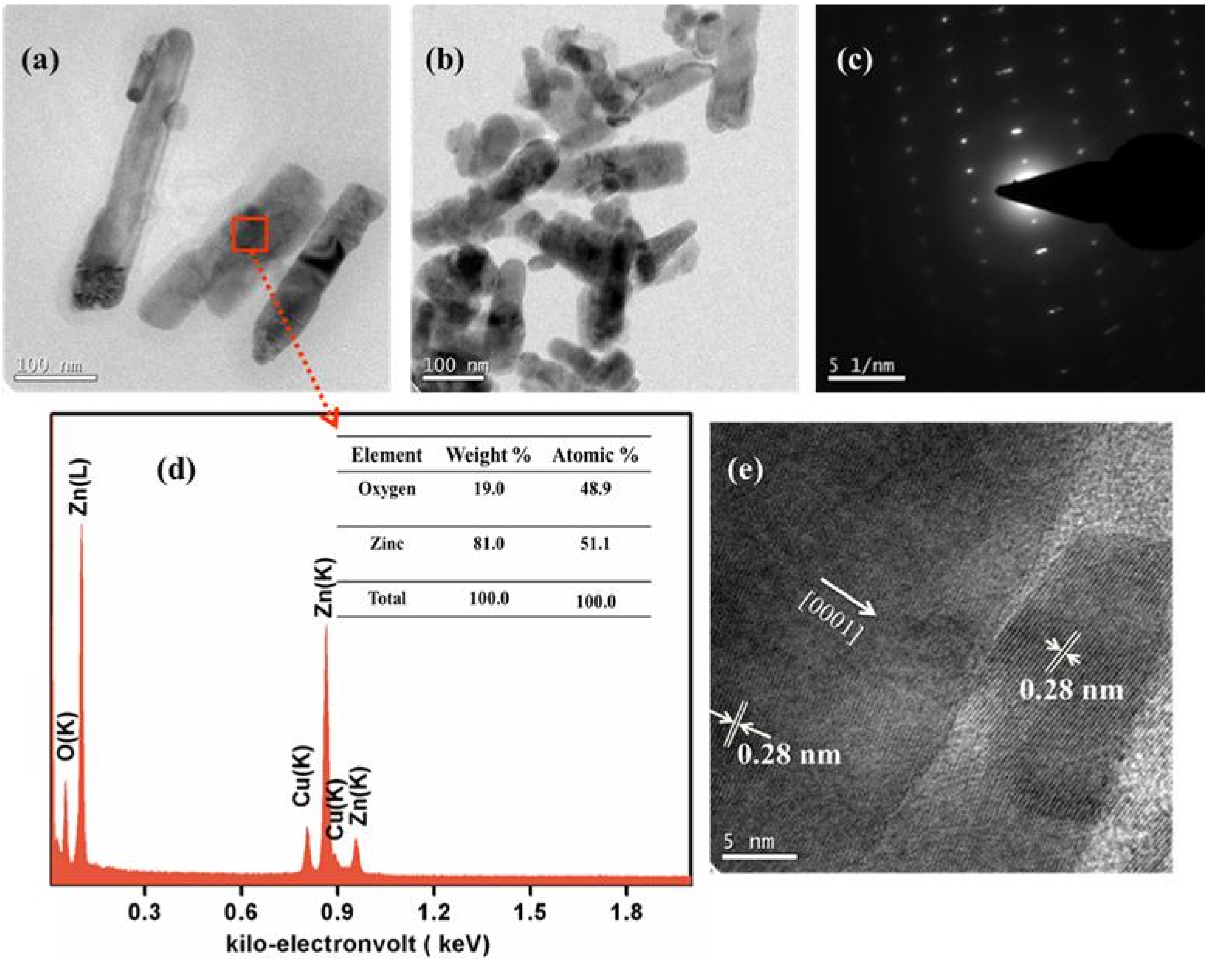

Figure 3.12: (a, b) TEM images of the synthesized ZnO, (c) SAED pattern, (d) EDX spectrum, and (e) HR-TEM images of the ZnO showing growth in (001) direction.

The corresponding SAED pattern confirms the highly crystalline nature of the particles obtained (Figure 3.12 (c)). It also confirmed the single crystalline nature for the ZnO synthesised [76, 89]. The monocrystalline characteristics of the product obtained was much predictable in the present case as the oriently attached (OA) particles were mostly identified to have mono-crystalline nature [76]. Thus the current observation further authenticates the claim of the occurrence of OA in the growth of nanorods of ZnO *via* aqueous mechanical oxidation.

The EDX analysis at selected region displays prominent peaks of zinc and oxygen supporting the formation of ZnO. In EDX spectra the peaks corresponding to copper (Cu) came from the Cu-membrane grid used for analysis (Figure 3.12 (d)). From the EDX the calculated elemental composition of the product also shows the equal contribution of Zn and oxygen in the measured area of the particle (inset in Figure 3.12 (d)). The high resolution TEM (HR-TEM) image taken at a selected area of the synthesized ZnO is also shown in the Figure 3.12 (e).

3.1.4.5 Gas analysis: Identification of the Gas Evolved

The gas evolved during the aqueous milling (after 72 h) of Zn dust, was collected and identified using standard gas chromatographic techniques. To identify the gas three sets of trails were carried out. The main gas detected was hydrogen. From the first set of trials carried out, almost equal percentage of hydrogen and oxygen along with traces of nitrogen were identified in the collected gases. This is due to the problem of flushing of the atmospheric gases into testing system. However, the mistake was identified and from the second trial onwards precautions were taken to avoid the flushing of atmospheric air into the measurement system. The second and third trial sets, confirmed that the gas produced during milling of Zn dust is hydrogen gas with a nominal percentage of >95 %. The results are presented in Figure 3.13. The bar chart of the nominal percentages of the different gases tested and the gas collected in a balloon from the mill chamber after 72 h of milling operation are shown in the inset of Figure 3.13.

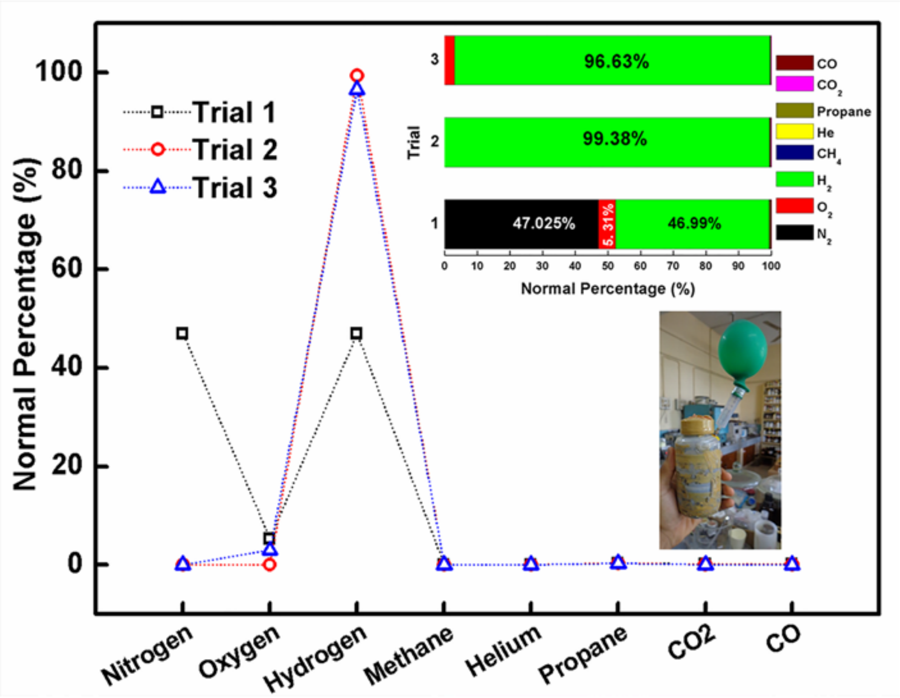

Figure 3.13: Gas analysis results (inset, bar chart showing the gas percentages and the photograph of the gas collected in a balloon from the mill chamber after 72 h of milling).

3.1.4.6 The Mechanism of Oxidation: 'Aqueous Mechano-Synthesized ZnO'

The mechanism of formation of ZnO *via* aqueous mechanical oxidation of Zn dust has to be understood to validate the process. Zn/ZnO redox reactions resuling in water splitting are well documented in previous reports [62, 72]. Small localised hotspots having high temperature and pressures were created by milling impacts triggered the reaction between Zn and water [44], which is exothermic in nature as reported in earlier works [62, 90]. This leads to thermolysis of water and generate hydrogen (H^+) and oxygen (O^{2-}) and leading to Zn hydrolysis [35, 62, 72]. The possibility for a gaseous phase reaction of Zn is eliminated in the present case by degasing the milling chamber before the milling operation starts. The water splitting reaction produced a continuous stream of oxygen ions (O^{2-}). These oxygen ions diffused into the Zn lattices resulting in the formation of ZnO [86, 87].

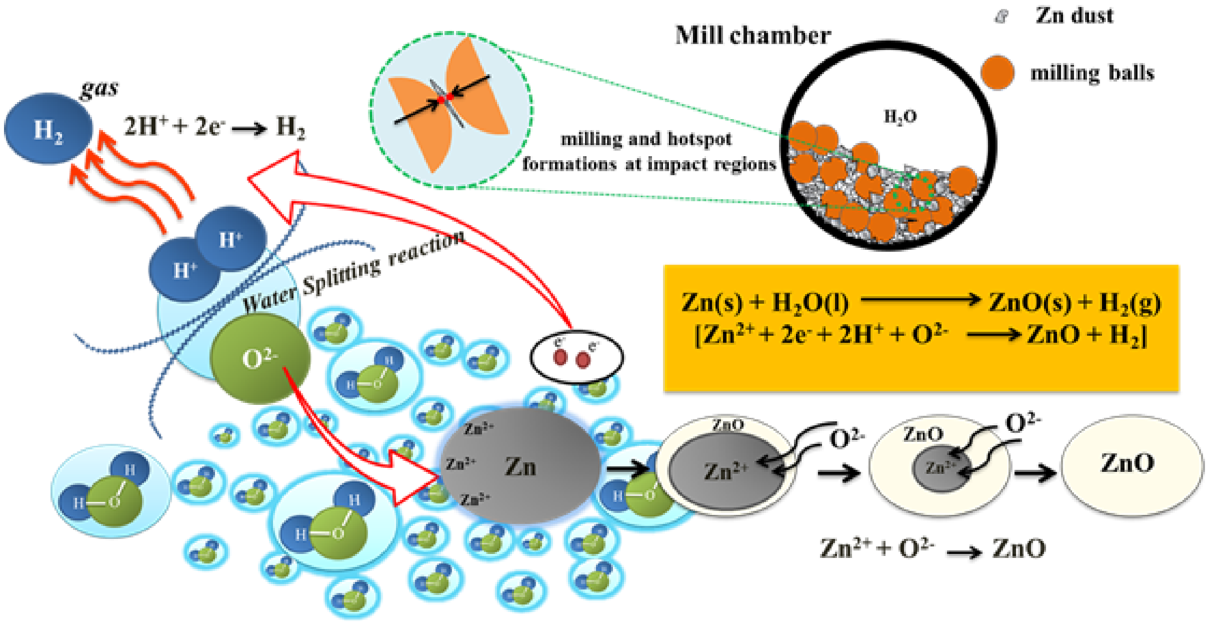

Figure 3.14: Schematic of the oxidation mechanism proposed for the mechanical conversion of Zn to ZnO.

The H^+ ions produced will finally enter the gaseous phase to generate hydrogen gas and was confirmed from the gas analysis conducted. The ZnO seeds developed on the surface of the Zn particle during milling grows into well-defined nanostructures with the progress of the process with time [46]. The ZnO seeds formed would act as a catalyst to produce the further conversion of Zn to ZnO together with the evolution of the H_2 gas [35, 73]. The crystallization and growth of well-defined nanorod of ZnO progresses through the oriented attachment (OA) mechanism, reported as a non-classical crystallization mechanism for ZnO by Verges *et al.* [91].

In addition to this, in due course of milling the passivation layer of nano ZnO on the Zn particle surface are also ‘skinned off ’ and the fresh Zn metal was exposed for further oxidation by which the whole particle are subjected to oxidation with increase in milling time. Thus, this is the mechanism possible for the formation ZnO during aqueous mechanical oxidation of Zn dust. The proposed mechanism of ZnO formation *via* aqueous mechanical oxidation of Zn dust is schematically represented in Figure 3.14.

3.1.5 Conclusions

Nanorods of ZnO with aspect ratio ~5.2 were successfully synthesized through a clean aqueous mechanical approach by employing simple ball milling. By carefully controlling the processing parameters, milling of micron sized Zn dust in distilled water was found to be capable for the large scale production of nano ZnO without any added chemical reagents or catalyst. Since in the present study, Zn metal (∼45 μm) is chosen as the starting material and water is the only active reactant needed for the synthesis, the process can be considered as a green synthesis route. For the production of nano ZnO the process parameters were well-optimized and the formations of ZnO nanorod were confirmed using various standard characterization techniques. The ZnO seeds formed on the Zn metal surface with milling were confirmed from the XRD results, and their further development into surface scales was observed from the morphological and XPS analysis milled samples. The production of the hydrogen gas along with ZnO during aqueous mechanical oxidation of Zn dust confirmed the water splitting reaction occurring simultaneously, which supplied actively O^{2-} for the oxide formation during milling. The formation of ZnO nanorod in the medium is supposed to occur by the oriented-attachment (OA) technique. Based on the experimental results a formation mechanism was also proposed for the production of ZnO nanorod and evolution of hydrogen gas during the aqueous mechanical oxidation of Zn dust. Thus noting all these points, the ‘Aqueous Mechanical oxidation’ technique described in this work has an upper hand over many of the other mechanochemical approaches so far discussed. This approach put forward a new economical, sustainable and environment friendly technique for the production of high quality nano ZnO and hydrogen gas with immense scale up opportunities.

3.2 Surfactant Assisted Aqueous Mechanical Oxidation of Zn Dust

3.2.1 Abstract

The aqueous mechanical oxidation of raw Zn was performed in presence of surfactants in order to reduce the cluster formation tendency of ZnO nanoparticle. Mechanical milling of raw Zn was carried out for 48 h in presence of surfactants cetyltrimethylammonium bromide (CTAB) and polyvinylpyrrolidone (PVP) (5 wt % and 10 wt %). The particle size of ZnO obtained was reduced to 154 and 184 nm for PVP and CTAB (10 wt %) assisted milled samples respectively from 382 nm for ZnO obtained without any surfactants. The ZnO nano particle obtained *via* PVP assisted milling showed uniform ultra-thin circular plate like morphology without any agglomeration. This effect also reflected in sintering behaviour of ZnO obtained *via* surfactant assisted milling. The sintering at 1200 ^{o}C of ZnO obtained *via* PVP assisted mechanical milling showed 99 % theoretical density with grain size in the range 1.5-2 µm.

3.2.2 Introduction

In the previous section ZnO nanorods have been successfully synthesized *via* aqueous mechanical oxidation of Zn dust. However, due to the cluster formation the average particle size of nano ZnO obtained continues to increase. This agglomeration behaviour of the product will reduce the quality of final product [92]. So it is necessary to restrain the particle from coarsening. To aid the dispersion of particle, stabilizers such as surfactants are used to provide ionic or steric barrier [93]. The aggregation behaviour of nanoparticle resulted from the attractive force between particles and can be controlled effectively by inducing an electrostatic double layer or by employing surfactant as a steric stabiliser [94]. The electrostatic double layer formation is a pH sensitive strategy in which the stabilisation of nanoparticle is induced by charge. In the synthesis of high quality nanostructures surfactant plays an important role by the manipulation of nanoparticle nucleation and growth. Surfactants are able to prevent aggregation, can control the size and shape of the nanoparticle, and can also make surface of nanoparticle hydrophobic/hydrophilic. Derjaguin-Landau-Verwey-Overbeek (DLVO) theory explained the agglomeration tendency and dispersion stability of nanoparticle in terms of van der Waals forces, electrostatic and steric interaction between the particles [94]. Surfactant molecules are chemisorbed on the surface of nanoparticle in the suspension during surfactant assisted stabilization and lead to steric stabilization and prevent particle from further aggregation due to steric hindrance effect [95, 96].

Nowadays, for the synthesis of various nanostructured materials from bulk solid materials surfactant aided high energy ball milling has been widely exploited [97, 98]. The synthesis of Sm_2Co_{17} nanoparticles by surfactant assisted ball milling from $SmCo_5$ precursors was reported by Zheng *et al*. where oleyl amine and oleic acid were used as a surfactant and a mixture of single and polycrystalline structures were obtained [99]. Islam *et al*. reported the synthesis of pure $CaCO_3$ nanoparticles with diameter 30 nm from cockle shells using dodecyl dimethyl betain (BS-12) as surfactant *via* simple and low cost milling approach [100]. Fe, Co and FeCo nanoplates and nanoparticles are synthesized by surfactant assisted ball milling carried out in organic solvents by Poudyal et *al.* [101,102]. Nano plates with thickness in the range of 20-200 nm and nanoparticles with diameter of 6 nm having super paramagnetic properties were obtained. The synthesis of nanoscale carbons from graphite *via* surfactant assisted ball milling for 10-30 h using Sodium dodecyl benzene sulphonate (SDBS)/ Sodium dodecyl sulphate (SDS) surfactants was reported by Nandhini *et al.* [103]. The size of the nanoparticles obtained was in the range of 80-500 nm. Wang et al. synthesized successfully hard magnetic Sm–Co nanoparticle *via* surfactant assisted ball milling where, oleyl amine (98 %) and oleic acid (90 %) were used as the surfactants. In the processing of nanoparticle the surfactant plays multifold roles and resulted in particles with an average size of 23 nm [104].

Cetyltrimethylammonium bromide (CTAB) [105], sodiumdodecyl sulfate (SDS) [106], polyvinylpyrrolidone (PVP) [107], tetraethylammonium bromide (TEAB) [108] and hexamine [109] are the commonly used surfactants for the synthesis of ZnO nano particle *via* chemical methods. The surface modification of ZnO nano particle can be performed either after synthesis, which is called post modification, or during the particle synthesis, called in-situ modification. *In situ* modification allows for the use of less amount of surfactant in addition to the advantages of controlling the morphology, particle size, and particle size distribution of the final product [95, 96].

During synthesis of ZnO *via* aqueous mechanical oxidation of Zn dust, the surfactants aid in achieving smaller particle size and dispersing the fine ZnO nano particles by providing steric and electrostatic force [110]. Once the ZnO particle is formed in the milled slurry these surfactants will adhere on the surface of ZnO particle and play a major role in governing the kinetics of nucleation, direction of crystal growth, particle size, morphology and porosity. In synthesis of ZnO, on the surface of ZnO surfactant plays two major roles: firstly, during nucleation it helps in reduction of the defects in nanocrystals and secondly, it attaches to the surface of nanoparticles so as to control the particles size. As a polar crystal, ZnO own a polar axis and due to the asymmetrical distribution of atoms (Zn and O) along its polar axis ZnO also possess a positive face and a negative face (polar surfaces) on the crystal structure. The positive face (0001) is occupied by Zn atoms and O atoms are distributed on the negative face $(000\bar{1})$. This polar nature and non-central symmetry of ZnO assisted the selective adhesion of surfactant molecule on the surface of ZnO particle formed during mechanical milling [111].

The effect of surfactants CTAB and PVP on the evolution of ZnO nanostructures during aqueous mechanical oxidation of Zn dust is investigated in the present section. Cetyltrimethylammonium bromide (CTAB) is a cationic surfactant and it will ionize into CTA^+ and Br^- when dissolved in ethanol or water [112]. Due to the polar nature of ZnO, by electrostatic attraction CTA+ and Br^- ions are selectively adsorbed on ZnO surface and can affect the morphology and size of ZnO nanoparticles formed. CTAB also can form micelles or reverse micelles, which also play a very important role in the morphology of the ZnO nanoparticles. Polyvinylpyrrolidone (PVP) is a non-ionic surfactant. Although it is non-ionic, the oxygen in PVP would be partially charged due to the presence of positively charged nitrogen in PVP [107]. Therefore compared to other non-ionic surfactants PVP would electrostatically adhere more strongly on the surface of ZnO [113].

In the present study the influence of surfactant CTAB and PVP on the growth, size and morphology of ZnO nano particle during ball milling were investigated. Further the effect of ZnO derived from Zn dust *via* mechanical milling with and without surfactant on the sintering behaviour of ZnO was also investigated.

3.2.3 Experimental Section

3.2.3.1 Materials

Zinc (Zn) dust (99.9 %) having an average particle size of 40-50 μm (Binani Zinc Pvt. Ltd., India) was used as the starting material. Polyvinylpyrrolidone (PVP, SD fine chem.), Cetyltrimethylammonium bromide (CTAB, S D fine chem.) were used as the surfactant during milling. The whole process was carried out in distilled water. Distilled ethanol was used for washing of the product.

3.2.3.2 Surfactant Assisted Aqueous Mechanical Oxidation of Zn

The milling of Zn dust was carried out in laboratory type belt driven ball mill operating with a rotor speed of 250 rpm for 48 h. PVP and CTAB are separately dissolved in 100 mL of distilled water under magnetic stirring. The amount of surfactant used was varied as 5 % and 10 % weight of the starting powders. 20 g of Zn dust was loaded into milling bottles propylene jars (Tarsons, India) having volume of 250 ml along with zirconia balls and surfactant added distilled water as the milling medium. The ball to powder mass ratio (BPMR) was fixed as 6:1. The samples are milled for 24, 48 and 72 h. After milling the slurry mixture obtained was washed with water and ethanol to remove the excess surfactant and dried at 60 °C in vacuum oven afterwards. Then all samples obtained were calcined at 450 °C for 1 h to obtain fine ZnO nanoparticles.

3.2.4 Result and Discussion

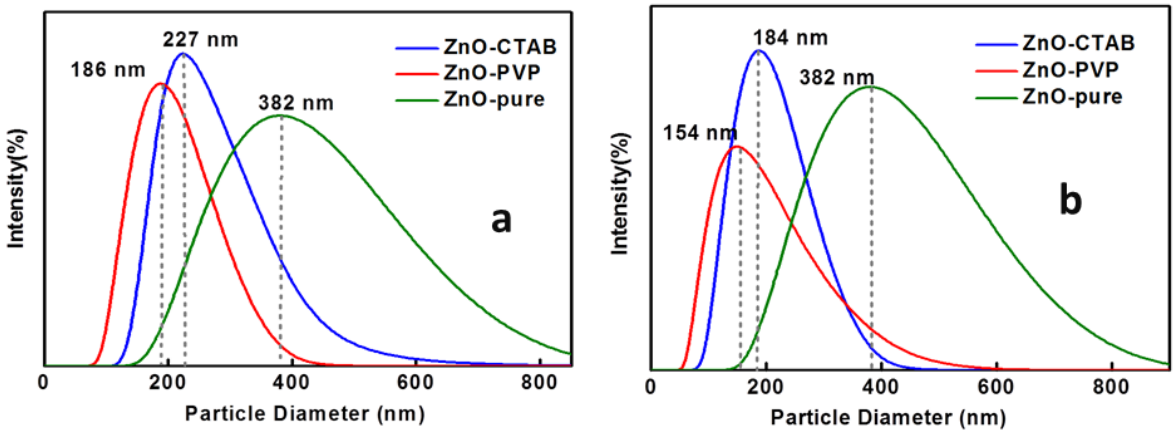

Figure 3.15: Particle size distribution of ZnO obtained *via* aqueous mechanical oxidation of Zn with and without surfactants: a) for 5 wt % and b) 10 wt % concentration of surfactants.

Systematic investigations were carried out on the effect of surfactant on the size and morphology of ZnO nanoparticle obtained *via* aqueous mechanical milling of Zn dust and the results indicate the critical role of surfactant on final product obtained *via* mechanical milling. From the particle size distribution curve (Figure 3.15 (a) and (b)) of ZnO particles obtained *via* surfactant (5 and 10 wt%) assisted milling it is observed that as the surfactant concentration increases from 5 to 10 wt % the size of ZnO particle decreased both in CTAB and PVP. For CTAB assisted synthesised sample the particle size reduced from 227 to 184 nm and for PVP assisted synthesized sample the particle size reduced from 186-154 nm. Thus for further studies 10 wt % of surfactant concentration was optimized and fixed. The size reduction was resulted from the increased micelles formation with increase in surfactant concentration. Thus at higher concentration of surfactant the number of micelles formed increases which has a pronounced effect on the particle growth. An increase beyond 10 wt % concentration of surfactant does not show any effect on particle size. This is due to the fact that the further increase in the surfactant concentration may increase the viscosity of solution and negatively affect the milling efficiency.

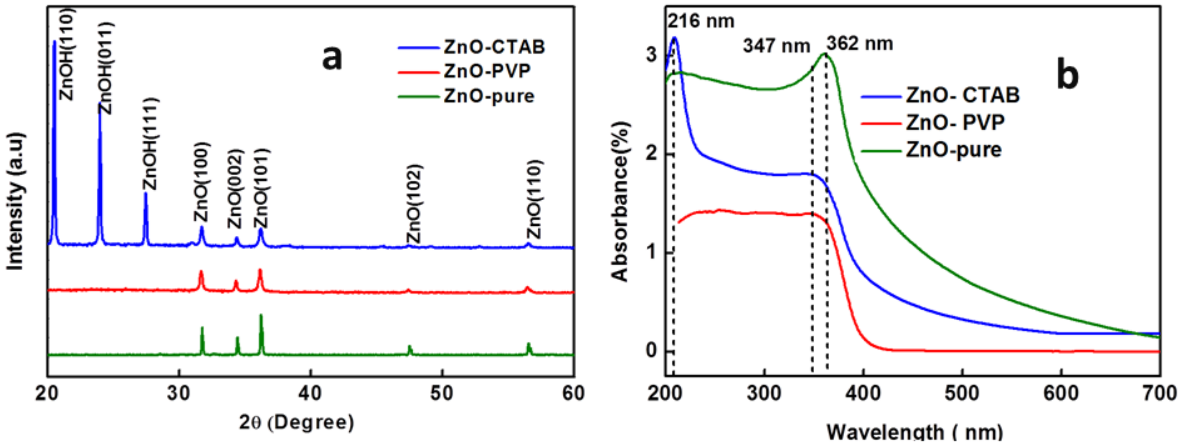

Figure 3.16: a) XRD analysis and b) UV spectra of ZnO obtained *via* aqueous mechanical oxidation of Zn dust with and without surfactant.

The phase analysis of the as obtained product after ball milling of Zn dust with and without surfactant have been studied based on their X-ray diffraction patterns obtained. The X-ray diffraction patterns of dispersion collected after surfactant assisted ball milling of Zn dust is presented in Figure 3.16 (a). The peaks obtained for all samples are sharper which indicates the crystalline nature of the product in all cases. The peaks at 2θ positions 31.91, 34.45, 36.28, 47.60, 56.64, 62.82, and 67.93° are well matched to the standard diffraction pattern of wurtzite ZnO (JCPDS 36-1451). In the case of CTAB assisted milling minor peaks are also seen in the region between 23°-27°, which corresponds to the hydroxide peaks of Zn [114]. For PVP assisted milled sample all diffraction peaks are consistent with the reported data and confirms the formation of ZnO with a wurtzite hexagonal phase (JCPDS 36-1451). The UV absorption spectra of dispersion collected after milling of Zn dust with and without surfactant are presented in Figure 3.16 (b). The Zn dust milled with and without PVP and CTAB showed absorption curve with intensive absorption in the range 200-380 nm with absorption edge in between 300-380 nm. For Zn dust milled without surfactant, the absorption peak is located at 362 nm. For Zn dust milled with surfactant CTAB and PVP, the absorption spectra showed peak at 358 and 347 nm respectively. Also Zn dust milled with CTAB showed an additional peak at 216 nm corresponding to band edge absorption of $Zn(OH)_2$. The blue shift in the UV absorption peak indicate reduction in particle size of the order ZnO-pure>ZnO-CTAB>ZnO-PVP.

In order to remove the traces of $Zn(OH)_2$ present, all samples were calcined at 450 °C for one hour. The phase analysis of the product after calcination at 450 °C is presented in Figure 3.17. After calcination at 450 °C, complete transformation all the phases to ZnO phase was observed for all samples. The sharpness of the peaks in all the three samples indicates high crystallinity of the calcined samples. The peak positions are in agreement with that of hexagonal wurtzite ZnO (JCPDS 36-1451). No characteristic peaks for other impurities were observed, which confirms that the product obtained after calcination was phase pure.

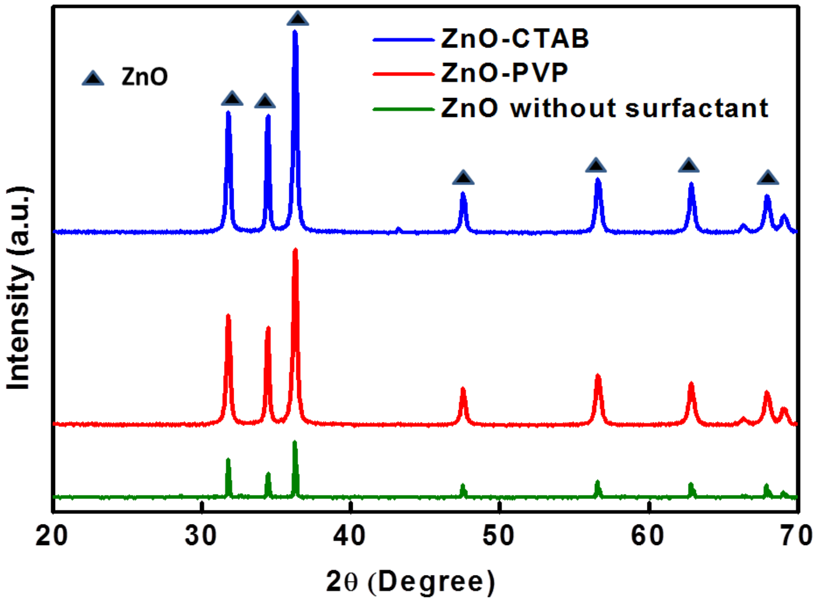

Figure 3.17: X-ray diffraction pattern of ZnO derived from Zn dust with and without surfactant *via* ball milling after calcination.

The morphological analysis of calcined ZnO obtained *via* aqueous mechanical oxidation with and without surfactant is presented in Figure 3.18 (a)-(c). The ZnO obtained without any surfactant shows highly agglomerated spherical cluster morphology (Figure 3.18 (a)). The presence of surfactants completely changed the growth direction and orientation of ZnO nanoparticle. The morphological change observed during surfactant assisted milling is due to change in surface tension of the reactant mixture. In presence of surfactant the energy required for the formation of ZnO was reduced. Also the stereo chemical and electrostatic effect influences the growth of ZnO and the erosion process of Zn. The ZnO obtained *via* CTAB (10 wt %) assisted milling of Zn dust is presented in Figure 3.18 (b). It is well clear that with the addition of CTAB the aggregation tendency of particle get reduced and particle morphology changed to ultra-thin circular plate like structure. For ZnO obtained *via* PVP assisted milling showed uniform ultra-thin circular plate like morphology without an agglomeration (Figure 3.18 (c)). The tendency for aggregation of nanoparticle is insignificant for PVP assisted milled sample. Thus PVP reveals to be the most suitable surfactant for the synthesis of ZnO particle with homogeneous size and shape *via* mechanical milling.

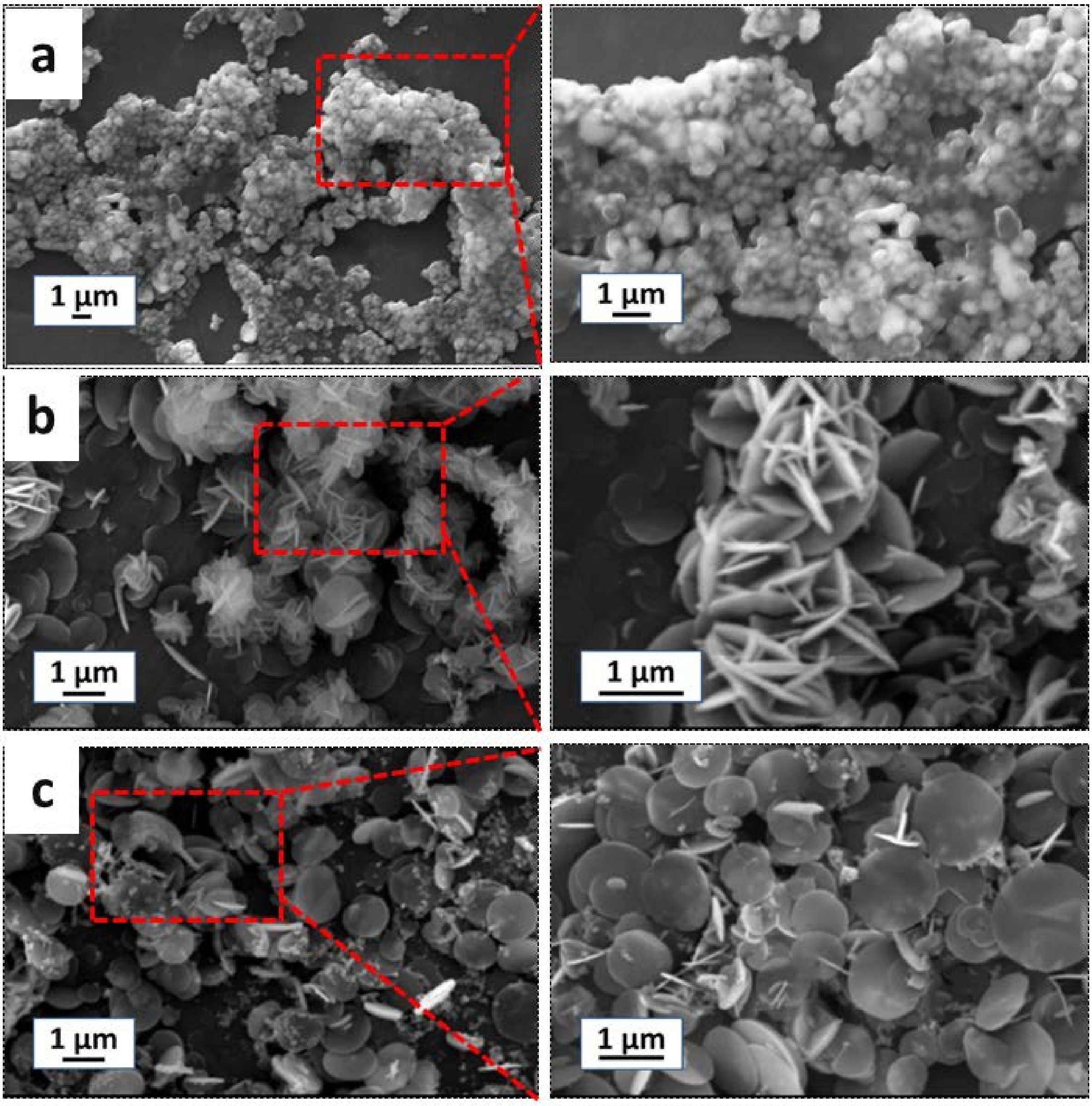

Figure 3.18: Morphology of ZnO nanoparticles obtained *via* aqueous mechanical oxidation a) without any surfactant, b) with CTAB and c) with PVP.

Large numbers of reports are there on PVP as a surface modifying agent for ZnO nanoparticle. PVP is an effective surface modifying agent for ZnO due to the strong interaction between PVP and surface of nanocrystals resulted from the effective coordination chemistry of N and O atom in the pyrollidone ring. The selective adsorption of PVP on different crystallographic planes plays a major role in the evolution of various ZnO morphologies. During PVP assisted aqueous mechanical oxidation of Zn it is believed that adsorption of PVP on various crystallographic planes of ZnO reduce the growth along polar axis of ZnO.

3.2.4.1 Sintering Behaviour of ZnO

ZnO powder was uni-axially pressed in the form of cylindrical discs having 10 mm diameter and 1 mm thickness at a pressure of 100 MPa using steel die.

The green densities of the ZnO samples obtained without and with surfactants are approximately in the range 62-68 %. The green density of commercial sample was 62.4 % and that of ZnO obtained *via* aqueous mechanical oxidation without any surfactant was 64 %. For ZnO obtained *via* aqueous mechanical oxidation with CTAB as surfactant, the green density obtained was 66.4 % and the maximum green density obtained was 67.8 % for ZnO produced *via* PVP assisted aqueous mechanical oxidation.

Sintering behaviour of ZnO obtained *via* aqueous mechanical milling with and without surfactant was studied by sintering at different temperature. For ZnO the complete densification close to theoretical density (5.61 g/cm^3) is usually accomplished by grain growth at temperature above 1200 ^{o}C. The sintering was performed in the temperature range 1000-1200 ^{o}C at a heating rate of 2 ^{o}C per minute. The variation of density with sintering temperature for ZnO obtained *via* aqueous mechanical oxidation with and without surfactant is compared with commercial ZnO.

The SEM microstructure in Figure 3.19 presents the microstructure of sintered disc of commercial ZnO, and ZnO obtained from aqueous mechanical oxidation of Zn with and without surfactant and densified at 1100 (Figure 3.19 (a)-(d)) and 1200 ^{o}C (Figure 3.19 (e)-(f)) respectively. At 1100 ^{o}C the presence of porosity indicate poor densification for all samples. When the sintering temperature was increased to 1200 ^{o}C the grain size and theoretical density increased rapidly for ZnO synthesized *via* aqueous mechanical oxidation with and without surfactant.

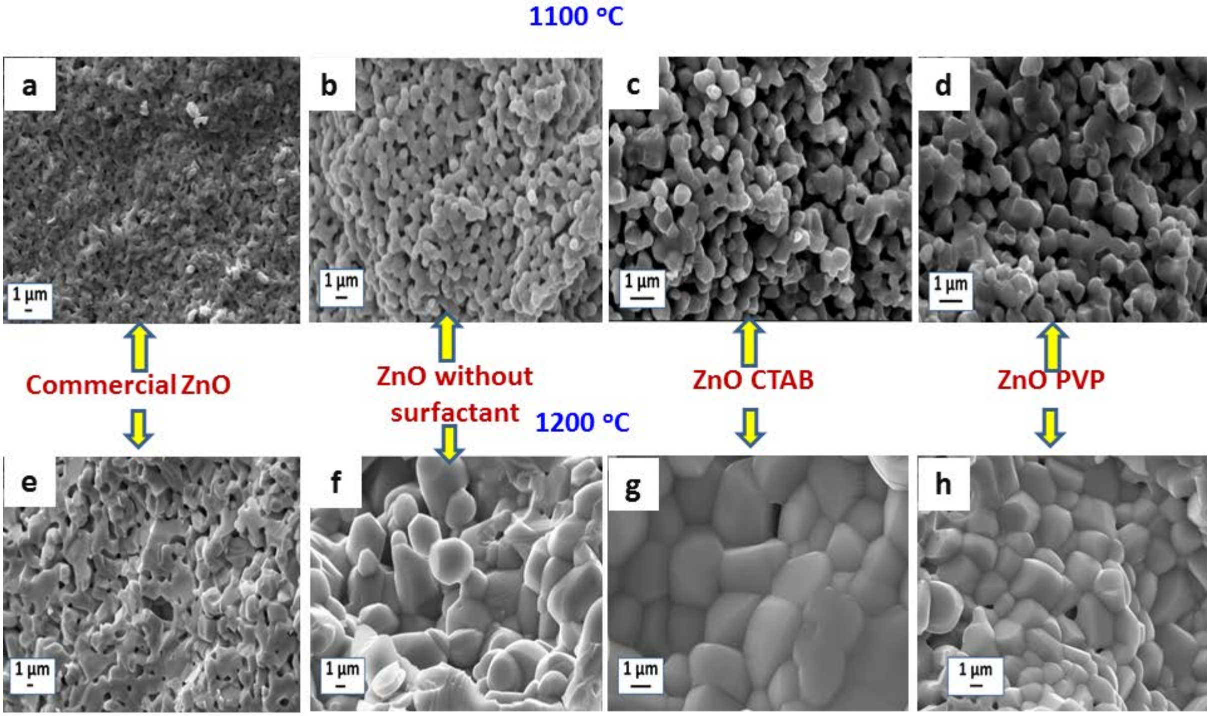

Figure 3.19: Microstructure of commercial ZnO and ZnO obtained *via* aqueous mechanical oxidation without any surfactant, with CTAB and with PVP (a), (b),(c),(d) and (e),(f),(g),(h) sintered at 1100 and 1200 ^{o}C respectively.

Variations of density and grain size with sintering temperature for ZnO obtained via aqueous mechanical oxidation with and without surfactant are presented in Figure 3.20 (a) and (b). It is evident from the bar diagram (Figure 3.20 (a)) that all the samples shows increasing trend in density with increase in sintering temperature. The theoretical density of ZnO is 5.61 g/cm^{3}. ZnO synthesised without any surfactant showed maximum density of 5.32 g/cm^3 at 1200 ^{o}C and further densification is possible by increasing sintering temperature. ZnO obtained *via* surfactant assisted aqueous mechanical oxidation showed 5.49 g/cm^3 and 5.59 g/cm^3 respectively for CTAB and PVP assisted milled sample. ZnO synthesised *via* surfactant assisted milling showed density above 97 % at 1100 ^{o}C. ZnO synthesised *via* PVP assisted milling showed 99 % density at 1200 ^{o}C. i.e., almost complete densification closer to theoretical density. No further increase in density with temperature was observed for this sample. The earlier densification for ZnO synthesized *via* PVP assisted milling can be attributed to the smaller particle size and thin plate like morphology which resulted in better compaction during sintering.

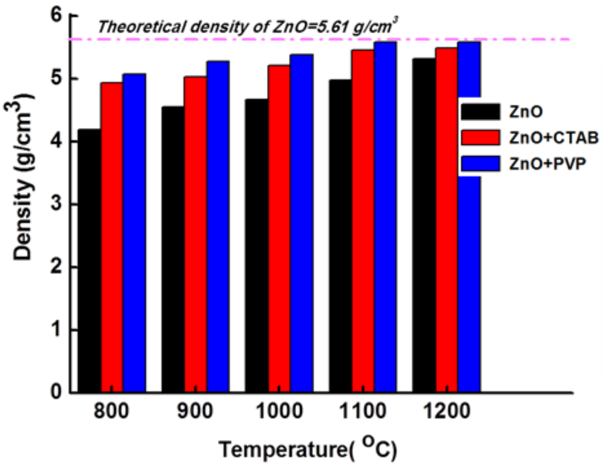

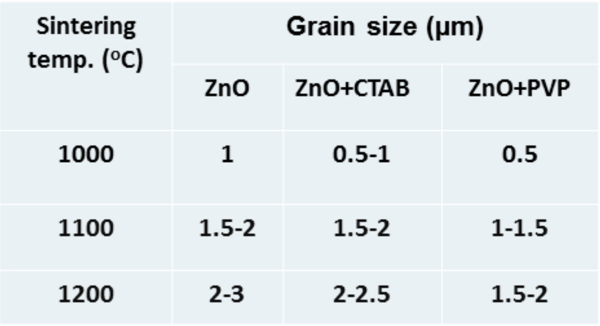

Sintering temp. (^{o}C)	Grain size (µm)		
	ZnO	ZnO+CTAB	ZnO+PVP
1000	1	0.5-1	0.5
1100	1.5-2	1.5-2	1-1.5
1200	2-3	2-2.5	1.5-2

Figure 3.20: a) Variation of density and b) grain size with increase in sintering temperature for ZnO synthesised via aqueous mechanical milling with and without surfactant.

The surfactant free sample showed average grain size 2.5 µm at 1200 ^{o}C. Sample modified with CTAB showed an average grain size 2.25 µm. The samples prepared with PVP have grown less with increase in sintering temperature and the average grain size determined was 1.75 µm at 1200 ^{o}C. For the commercial ZnO the sintering has just started at 1200 ^{o}C and the grain and grain boundaries are not clearly defined even at 1200

^{o}C. This can be attributed to the highly agglomerated particle resulting in slow sintering for commercial sample.

3.2.5 Conclusions

The effect of surfactants CTAB and PVP on the morphological evolution and size distribution of ZnO nanoparticle during aqueous mechanical oxidation of raw Zn was investigated. The sintering behaviour of ZnO obtained *via* aqueous mechanical oxidation of Zn dust with and without surfactant is compared with that of commercial ZnO. It is observed that for 10 wt % concentration of surfactant the particle size is reduced to 184 nm for CTAB assisted milled sample and 154 nm for PVP assisted milled sample compared to ZnO obtained without any surfactant with particle size 382 nm. Circular thin plate like morphology without any agglomeration was observed for nano ZnO obtained *via* PVP assisted milling. This can be attributed to the selective adsorption of PVP on various crystallographic planes of ZnO. In sintering studies also ZnO obtained *via* surfactant assisted aqueous mechanical oxidation showed enhancement in densification and grain growth inhibition. ZnO obtained *via* PVP assisted aqueous mechanical oxidation of Zn showed 99 % theoretical density and grain size in the range 1.5-2 µm sintered at 1200 ^{o}C. This can be attributed to the smaller particle size and thin plate like morphology of ZnO obtained *via* PVP assisted aqueous mechanical oxidation leads to better compaction during sintering.

References

[1] Kołodziejczak-Radzimska, Agnieszka, and Teofil Jesionowski. "Zinc oxide—from synthesis to application: a review." *Materials* 7.4 (2014): 2833-2881.

[2] Moezzi, Amir, Andrew M. McDonagh, and Michael B. Cortie. "Zinc oxide particles: Synthesis, properties and applications." *Chemical engineering journal* 185 (2012): 1-22.

[3] Sirelkhatim, Amna, et al. "Review on zinc oxide nanoparticles: antibacterial activity and toxicity mechanism." *Nano-Micro Letters* 7.3 (2015): 219-242.

[4] Arya, Sunil K., et al. "Recent advances in ZnO nanostructures and thin films for biosensor applications." *Analytica chimica acta* 737 (2012): 1-21.

[5] Espitia, Paula Judith Perez, et al. "Zinc oxide nanoparticles: synthesis, antimicrobial activity and food packaging applications." *Food and Bioprocess Technology* 5.5 (2012): 1447-1464.

[6] Djurišić, A. B., A. M. C. Ng, and X. Y. Chen. "ZnO nanostructures for optoelectronics: material properties and device applications." *Progress in quantum electronics* 34.4 (2010): 191-259.

[7] Wang, Zhong Lin. "Zinc oxide nanostructures: growth, properties and applications." *Journal of physics: condensed matter* 16.25 (2004): R829.

[8] Kar, Soumitra, and Swadeshmukul Santra. "ZnO nanotube arrays and nanotube-based paint-brush structures: a simple methodology of fabricating hierarchical nanostructures with self-assembled junctions and branches." *The Journal of Physical Chemistry C* 112.22 (2008): 8144-8146.

[9] Schmidt-Mende, Lukas, and Judith L. MacManus-Driscoll. "ZnO–nanostructures, defects, and devices." *Materials today*10.5 (2007): 40-48.

[10] Ristić, Mira, et al. "Sol–gel synthesis and characterization of nanocrystalline ZnO powders." *Journal of Alloys and Compounds* 397.1-2 (2005): L1-L4.

[11] Rani, Seema, et al. "Synthesis of nanocrystalline ZnO powder via sol–gel route for dye-sensitized solar cells." *Solar Energy Materials and Solar Cells* 92.12 (2008): 1639-1645.

[12] Wu, J-J., and S-C. Liu. "Low-temperature growth of well-aligned ZnO nanorods by chemical vapor deposition." *Advanced materials* 14.3 (2002): 215-218.

[13] Wang, R. C., Liu, C. P., Huang, J. L., and Chen, S. J. "ZnO hexagonal arrays of nanowires grown on nanorods." *Applied Physics Letters* 86.25 (2005): 251104.

[14] Wang, Y., Zhang, X., Wang, A., Li, X., Wang, G. and Zhao, L. "Synthesis of ZnO nanoparticles from microemulsions in a flow type microreactor." *Chemical Engineering Journal* 235 (2014): 191-197.

[15] Bumajdad, Ali, and Metwally Madkour. "In situ growth of ZnO nanoparticles in precursor-insensitive water-in-oil microemulsion as soft nanoreactors." *Nanoscale research letters* 10.1 (2015): 19.

[16] Baruah, Sunandan, and Joydeep Dutta. "Hydrothermal growth of ZnO nanostructures." *Science and Technology of Advanced Materials* 10.1 (2009): 013001.

[17] Shi, Weidong, Shuyan Song, and Hongjie Zhang. "Hydrothermal synthetic strategies of inorganic semiconducting nanostructures." *Chemical Society Reviews*42.13 (2013): 5714-5743.

[18] Wang, X., Zhang, Q., Wan, Q., Dai, G., Zhou, C., & Zou, B. "Controllable ZnO architectures by ethanolamine-assisted hydrothermal reaction for enhanced photocatalytic activity." *The Journal of Physical Chemistry C*115.6 (2011): 2769-2775.

[19] Chen, ChangChun, Ping Liu, and ChunHua Lu. "Synthesis and characterization of nano-sized ZnO powders by direct precipitation method." *Chemical Engineering Journal* 144.3 (2008): 509-513.

[20] Wang, Y., Zhang, C., Bi, S., & Luo, G. "Preparation of ZnO nanoparticles using the direct precipitation method in a membrane dispersion micro-structured reactor." *Powder Technology* 202.1-3 (2010): 130-136.

[21] Hong, R. Y., Li, J. H., Chen, L. L., Liu, D. Q., Li, H. Z., Zheng, Y., & Ding, J. "Synthesis, surface modification and photocatalytic property of ZnO nanoparticles." *Powder Technology* 189.3 (2009): 426-432.

[22] Xu, C., De, S., Balu, A. M., Ojeda, M., & Luque, R. "Mechanochemical synthesis of advanced nanomaterials for catalytic applications." *Chemical Communications* 51.31 (2015): 6698-6713.

[23] Yadav, Thakur Prasad, Ram Manohar Yadav, and Dinesh Pratap Singh. "Mechanical milling: a top down approach for the synthesis of nanomaterials and nanocomposites." *Nanoscience and Nanotechnology* 2.3 (2012): 22-48.

[24] Lu, Jun, Ka M. Ng, and Shihe Yang. "Efficient, one-step mechanochemical process for the synthesis of ZnO nanoparticles." *Industrial & engineering chemistry research*47.4 (2008): 1095-1101.

[25] Vaezi, M. R., and S. K. Sadrnezhaad. "Nanopowder synthesis of zinc oxide via solochemical processing." *Materials & design*28.2 (2007): 515-519.

[26] Demoisson, Frédéric, Romain Piolet, and Frédéric Bernard. "Hydrothermal synthesis of ZnO crystals from Zn (OH) 2 metastable phases at room to supercritical conditions." *Crystal Growth & Design* 14.11 (2014): 5388-5396.

[27] Allen, C., Kondos, P., Payant, S., Van Weert, G., & Van Sandwijk, A. "Production of zinc oxide from complex sulfide concentrates using chloride processing." U.S. Patent No. 6,395,242. 28 May 2002.

[28] Ao, W., Li, J., Yang, H., Zeng, X., & Ma, X. "Mechanochemical synthesis of zinc oxide nanocrystalline." *Powder Technology* 168.3 (2006): 148-151

[29] McCormick, Paul G., and Takuya Tsuzuki. "Recent developments in mechanochemical nanoparticle synthesis." *Materials Science Forum*. Vol. 386. Trans Tech Publications, 2002.

[30] Liu, X., Xu, T., Wu, X., Zhang, Z., Yu, J., Qiu, H., Hong, J.H., Jin, C.H., Li, J.X., Wang, X.R. and Sun, L.T. "Top–down fabrication of sub-nanometre

semiconducting nanoribbons derived from molybdenum disulfide sheets." *Nature communications* 4 (2013): 1776.

[31] Yu, H. D., Regulacio, M. D., Ye, E., & Han, M. Y. "Chemical routes to top-down nanofabrication." *Chemical Society Reviews* 42.14 (2013): 6006-6018.

[32] Suryanarayana, C., and Nasser Al-Aqeeli. "Mechanically alloyed nanocomposites." *Progress in Materials Science* 58.4 (2013): 383-502.

[33] Suryanarayana, C. "Synthesis of nanocomposites by mechanical alloying." *Journal of Alloys and Compounds* 509 (2011): S229-S234.

[34] Hela, Rudolf, and Denisa Orsáková. "The mechanical activation of fly ash." *Procedia Engineering* 65 (2013): 87-93.

[35] Baláž, P., Achimovičová, M., Baláž, M., Billik, P., Cherkezova-Zheleva, Z., Criado, J.M., Delogu, F., Dutková, E., Gaffet, E., Gotor, F.J. and Kumar, R. "Hallmarks of mechanochemistry: from nanoparticles to technology." *Chemical Society Reviews* 42.18 (2013): 7571-7637.

[36] Sánchez-De Jesús, F., Bolarín-Miró, A.M., Cortes-Escobedo, C.A., Valenzuela, R. and Ammar, S. "Mechanosynthesis, crystal structure and magnetic characterization of M-type SrFe12O19." *Ceramics International* 40.3 (2014): 4033-4038

[37] Düvel, A., Kuhn, A., Robben, L., Wilkening, M. and Heitjans, P. "Mechanosynthesis of solid electrolytes: preparation, characterization, and Li ion transport properties of garnet-type Al-doped Li7La3Zr2O12 crystallizing with cubic symmetry." *The Journal of Physical Chemistry C* 116.29 (2012): 15192-15202.

[38] Yadav, Thakur Prasad, Ram Manohar Yadav, and Dinesh Pratap Singh. "Mechanical milling: a top down approach for the synthesis of nanomaterials and nanocomposites." *Nanoscience and Nanotechnology* 2.3 (2012): 22-48.

[39] Huot, J., Ravnsbæk, D.B., Zhang, J., Cuevas, F., Latroche, M. and Jensen, T.R. "Mechanochemical synthesis of hydrogen storage materials." *Progress in Materials Science* 58.1 (2013): 30-75.

[40] Gil-González, E., Perejón, A., Sánchez-Jiménez, P.E., Hayward, M.A. and Pérez-Maqueda, L.A. "Preparation of ytterbium substituted BiFeO3 multiferroics by mechanical activation." *Journal of the European Ceramic Society* 37.3 (2017): 945-954.

[41] Shin, H., Lee, S., Jung, H.S. and Kim, J.B. "Effect of ball size and powder loading on the milling efficiency of a laboratory-scale wet ball mill." *Ceramics International* 39.8 (2013): 8963-8968.

[42] Burmeister, C.F. and Kwade, A. "Process engineering with planetary ball mills." *Chemical Society Reviews* 42.18 (2013): 7660-7667.

[43] Jung, H.J., Sohn, Y., Sung, H.G., Hyun, H.S. and Shin, W.G. "Physicochemical properties of ball milled boron particles: dry vs. wet ball milling process." *Powder Technology* 269 (2015): 548-553.

[44] Xing, T., Sunarso, J., Yang, W., Yin, Y., Glushenkov, A.M., Li, L.H., Howlett, P.C. and Chen, Y. "Ball milling: a green mechanochemical approach for synthesis of nitrogen doped carbon nanoparticles." *Nanoscale* 5.17 (2013): 7970-7976.

[45] Šepelák, V., Bégin-Colin, S. and Le Caër, G. "Transformations in oxides induced by high-energy ball-milling." *Dalton transactions* 41.39 (2012): 11927-11948.

[46] Balanand, S., Maria, M.J., Rajan, T.P.D., Mohamed, A.P. and Ananthakumar, S. "Bulk processing of ZnO nanostructures via microwave assisted oxidation of mechanically seeded Zn dust for functional paints and coatings." *Chemical Engineering Journal* 284 (2016): 657-667.

[47] Kostić, E., Kiss, Š., Bošković, S. and Zec, S. "Mechanical activation of the gamma to alpha transition in Al2O3." *Powder technology* 91.1 (1997): 49-54.

[48] Bodaghi, M. A., Mirhabibi, R., Zolfonun, H.,Tahriri, M., Karimi, M. "Investigation of phase transition of gamma-alumina to alpha-alumina via mechanical milling method." Phase ransitions 81.2008, 571−580.

[49] Delogu, F. "A mechanistic study of TiO2 anatase-to-rutile phase transformation under mechanical processing conditions." *Journal of Alloys and Compounds* 468.1-2 (2009): 22-27.

[50] Zyryanov, V. V. "Mechanochemical synthesis of complex oxides." *Russian chemical reviews* 77.2 (2008): 105-135.

[51] Tsuzuki, T., E. Pirault, and P. G. McCormick. "Mechanochemical synthesis of gadolinium oxide nanoparticles." *Nanostructured materials* 11.1 (1999): 125-131.

[52] Yang, H., Hu, Y., Zhang, X. and Qiu, G. "Mechanochemical synthesis of cobalt oxide nanoparticles." Materials Letters 58.3-4 (2004): 387-389.

[53] Ao, W., Li, J., Yang, H., Zeng, X. and Ma, X. "Mechanochemical synthesis of zinc oxide nanocrystalline." *Powder Technology* 168.3 (2006): 148-151.

[54] Karimzadeh, I., Aghazadeh, M., Ganjali, M.R., Doroudi, T. and Kolivand, P.H. "Preparation and characterization of iron oxide (Fe3O4) nanoparticles coated with polyvinylpyrrolidone/polyethylenimine through a facile one-pot deposition route." *Journal of Magnetism and Magnetic Materials* 433 (2017): 148-154.

[55] Chua, C.K. and Pumera, M. "Chemical reduction of graphene oxide: a synthetic chemistry viewpoint." *Chemical Society Reviews* 43.1 (2014): 291-312.

[56] Castro, A., Millan, P., Ricote, Â., Pardo, L. "Room temperature stabilisation of c-Bi2VO5.5 and synthesis of the new fluorite phase f- Bi2VO5 by a mechanochemical activation method." Journal of Material Chemistry. 10 (2000): 767−771.

[57] Miclea, C., Tanasoiu, C., Gheorghiu, A., Miclea, C.F. and Tanasoiu, V. "Synthesis and piezoelectric properties of nanocrystalline PZT-based ceramics prepared by high energy ball milling process." *Journal of materials science* 39.16-17 (2004): 5431-5434.

[58] Khayati, G.R., Nourafkan, E., Karimi, G. and Moradgholi, J. "Synthesis of cuprous oxide nanoparticles by mechanochemical oxidation of copper in high planetary energy ball mill." Advanced Powder Technology 24.1 (2013): 301-305.

[59] Yuan, L., Wang, C., Cai, R., Wang, Y. and Zhou, G. "Temperature-dependent growth mechanism and microstructure of ZnO nanostructures grown from the thermal oxidation of zinc." *Journal of Crystal Growth* 390 (2014): 101-108.

[60] Yao, B. D., Y. F. Chan, and N. Wang. "Formation of ZnO nanostructures by a simple way of thermal evaporation." *Applied Physics Letters* 81.4 (2002): 757-759.

[61] Ren, S., Bai, Y.F., Chen, J., Deng, S.Z., Xu, N.S., Wu, Q.B. and Yang, S. "Catalyst-free synthesis of ZnO nanowire arrays on zinc substrate by low temperature thermal oxidation." *Materials Letters* 61.3 (2007): 666-670.

[62] Lv, M., Zhou, J., Yang, W. and Cen, K. "Thermogravimetric analysis of the hydrolysis of zinc particles." *International journal of hydrogen energy* 35.7 (2010): 2617-2621.

[63] Maria, M.J., Balanand, S., Anas, S., Mohamed, A.P. and Ananthakumar, S. "Zn-dust derived ultrafine grained ZnO non-linear ceramic resistors via in-situ thermal oxidation of cermet reactant mixture." *Materials & Design* 92 (2016): 387-396.

[64] Moballegh, A., Shahverdi, H.R., Aghababazadeh, R. and Mirhabibi, A.R. "ZnO nanoparticles obtained by mechanochemical technique and the optical properties." *Surface Science* 601.13 (2007): 2850-2854.

[65] Salah, N., Habib, S.S., Khan, Z.H., Memic, A., Azam, A., Alarfaj, E., Zahed, N. and Al-Hamedi, S. "High-energy ball milling technique for ZnO nanoparticles as antibacterial material." *International journal of nanomedicine* 6 (2011): 863.

[66] Glushenkov, A.M., Zhang, H., Zou, J., Lu, G.Q. and Chen, Y. "Unusual corrugated nanowires of zinc oxide." *Journal of crystal growth* 310.13 (2008): 3139-3143.

[67] Jaimy, K.B., Safeena, V.P., Ghosh, S., Hebalkar, N.Y. and Warrier, K.G.K. "Photocatalytic activity enhancement in doped titanium dioxide by crystal defects." *Dalton Transactions* 41.16 (2012): 4824-4832.

[68] Uzunova-Bujnova, M., Dimitrov, D., Radev, D., Bojinova, A. and Todorovsky, D. "Effect of the mechanoactivation on the structure, sorption and photocatalytic properties of titanium dioxide." *Materials Chemistry and Physics* 110.2-3 (2008): 291-298.

[69] Francavilla, M., Pineda, A., Romero, A.A., Colmenares, J.C., Vargas, C., Monteleone, M. and Luque, R. "Efficient and simple reactive milling preparation of photocatalytically active porous ZnO nanostructures using biomass derived polysaccharides." *Green Chemistry* 16.5 (2014): 2876-2885.

[70] Shobeiri, S. A. Mousavi-Kamazani, M. Beshkar, F. “Facile mechanical milling synthesis of $NiCr_2O_4$ using novel organometallic precursors and investigation of its photocatalytic activity.” Journal of Materials Science: Materials in Electronics 28. (2017): 8108.

[71] Lv, M., Zhou, J., Yang, W. and Cen, K. "Thermogravimetric analysis of the hydrolysis of zinc particles." International journal of hydrogen energy 35.7 (2010): 2617-2621.

[72] Ernst, F.O., Steinfeld, A. and Pratsinis, S.E. "Hydrolysis rate of submicron Zn particles for solar H_2 synthesis." *international journal of hydrogen energy* 34.3 (2009): 1166-1175.

[73] Weibel, D., Jovanovic, Z.R., Gálvez, E. and Steinfeld, A. "Mechanism of Zn Particle Oxidation by H2O and CO2 in the Presence of ZnO." *Chemistry of Materials* 26.22 (2014): 6486-6495.

[74] Abanades, S., Charvin, P. and Flamant, G. "Design and simulation of a solar chemical reactor for the thermal reduction of metal oxides: case study of zinc oxide dissociation." *Chemical Engineering Science* 62.22 (2007): 6323-6333.

[75] Pineda, A., Balu, A.M., Campelo, J.M., Romero, A.A., Carmona, D., Balas, F., Santamaria, J. and Luque, R. "A dry milling approach for the synthesis of highly active nanoparticles supported on porous materials." *ChemSusChem* 4.11 (2011): 1561-1565.

[76] Pacholski, C., Kornowski, A. and Weller, H. "Self-assembly of ZnO: from nanodots to nanorods." *Angewandte Chemie International Edition* 41.7 (2002): 1188-1191.

[77] Penn, R.L. and Banfield, J.F. "Morphology development and crystal growth in nanocrystalline aggregates under hydrothermal conditions: Insights from titania." *Geochimica et cosmochimica acta* 63.10 (1999): 1549-1557.

[78] Banfield, J.F., Welch, S.A., Zhang, H., Ebert, T.T. and Penn, R.L. Aggregation-based crystal growth and microstructure development in natural iron oxyhydroxide biomineralization products." *Science* 289.5480 (2000): 751-754.

[79] Yu, J.H., Joo, J., Park, H.M., Baik, S.I., Kim, Y.W., Kim, S.C. and Hyeon, T. "Synthesis of quantum-sized cubic ZnS nanorods by the oriented attachment mechanism." *Journal of the American Chemical Society* 127.15 (2005): 5662-5670.

[80] Alinejad, B. and Mahmoodi, K. "A novel method for generating hydrogen by hydrolysis of highly activated aluminum nanoparticles in pure water." *International Journal of Hydrogen Energy* 34.19 (2009): 7934-7938.

[81] Liang, H.Q., Pan, L.Z. and Liu, Z.J. "Synthesis and photoluminescence properties of ZnO nanowires and nanorods by thermal oxidation of Zn precursors." *Materials Letters* 62.12-13 (2008): 1797-1800.

[82] Biesinger, M.C., Lau, L.W., Gerson, A.R. and Smart, R.S.C. "Resolving surface chemical states in XPS analysis of first row transition metals, oxides and hydroxides: Sc, Ti, V, Cu and Zn." *Applied Surface Science*257.3 (2010): 887-898.

[83] Nicholas, N.J., Franks, G.V. and Ducker, W.A. "The mechanism for hydrothermal growth of zinc oxide." *CrystEngComm* 14.4 (2012): 1232-1240.

[84] Wang, M., Jiang, L., Kim, E.J. and Hahn, S.H. "Electronic structure and optical properties of Zn (OH) 2: LDA+ U calculations and intense yellow luminescence." *RSC Advances* 5.106 (2015): 87496-87503.

[85] Tomlins, G.W., Routbort, J.L. and Mason, T.O. "Oxygen Diffusion in Single-Crystal Zinc Oxide." *Journal of the American Ceramic Society* 81.4 (1998): 869-876.

[86] Haneda, H., Sakaguchi, I., Watanabe, A., Ishigaki, T. and Tanaka, J. "Oxygen diffusion in single-and poly-crystalline zinc oxides." *Journal of Electroceramics* 4.1 (1999): 41-48.

[87] Erhart, P. and Albe, K. "Diffusion of zinc vacancies and interstitials in zinc oxide." *Applied physics letters* 88.20 (2006): 201918.

[88] Wasekar, N.P., Jyothirmayi, A., Hebalkar, N. and Sundararajan, G. "Influence of pulsed current on the aqueous corrosion resistance of electrodeposited zinc." *Surface and Coatings Technology* 272 (2015): 373-379.

[89] Ludi, Bettina, and Markus Niederberger. "Zinc oxide nanoparticles: chemical mechanisms and classical and non-classical crystallization." *Dalton Transactions* 42.35 (2013): 12554-12568.

[90] Xiao, L., Wu, S.Y. and Li, Y.R. "Advances in solar hydrogen production via two-step water-splitting thermochemical cycles based on metal redox reactions." *Renewable Energy* 41 (2012): 1-12.

[91] Vergés, M. Andrés, A. Mifsud, and C. J. Serna. "Formation of rod-like zinc oxide microcrystals in homogeneous solutions." *Journal of the Chemical Society, Faraday Transactions* 86.6 (1990): 959-963.

[92] Anand, K. and Varghese, S. "Role of surfactants on the stability of nano-zinc oxide dispersions." *Particulate Science and Technology* 35.1 (2017): 67-70.

[93] Shang, Y., Liu, H., Xia, J. and Xu, Z. "Fabrication and Characterization of Flower-Like ZnO by Gemini Surfactant-Assisted Hydrothermal Process." *Journal of dispersion science and technology* 26.5 (2005): 525-530.

[94] Pfeiffer, C., Rehbock, C., Hühn, D., Carrillo-Carrion, C., de Aberasturi, D.J., Merk, V., Barcikowski, S. and Parak, W.J. "Interaction of colloidal nanoparticles with their local environment: the (ionic) nanoenvironment around nanoparticles is different from bulk and determines the physico-chemical properties of the nanoparticles." Journal of The Royal Society Interface 11.96 (2014): 20130931.

[95] Pellegrino, T., Kudera, S., Liedl, T., Muñoz Javier, A., Manna, L. and Parak, W.J. "On the development of colloidal nanoparticles towards multifunctional structures and their possible use for biological applications." *small* 1.1 (2005): 48-63.

[96] Ha, T.T., Canh, T.D. and Tuyen, N.V. "A quick process for synthesis of ZnO nanoparticles with the aid of microwave irradiation." ISRN Nanotechnology 2013 (2013).

[97] Zuo, W.L., Zhao, X., Xiong, J.F., Zhang, M., Zhao, T.Y., Hu, F.X., Sun, J.R. and Shen, B.G. "Strong textured SmCo 5 nanoflakes with ultrahigh coercivity prepared by multistep (three steps) surfactant-assisted ball milling." *Scientific reports* 5 (2015): 13117.

[98] Ullah, M., Ali, M. and Hamid, S.B.A. "SURFACTANT-ASSISTED BALL MILLING: A NOVEL ROUTE TO NOVEL MATERIALS WITH CONTROLLED NANOSTRUCTURE-A REVIEW." *Reviews on Advanced Materials Science* 37 (2014).

[99] Zheng, L., Cui, B. and Hadjipanayis, G.C. "Effect of different surfactants on the formation and morphology of SmCo5 nanoflakes." *Acta Materialia* 59.17 (2011): 6772-6782.

[100] Islam, K.N., Bakar, M.Z.B.A., Ali, M.E., Hussein, M.Z.B., Noordin, M.M., Loqman, M.Y., Miah, G., Wahid, H. and Hashim, U. "A novel method for the

synthesis of calcium carbonate (aragonite) nanoparticles from cockle shells." *Powder technology* 235 (2013): 70-75.

[101] Poudyal, N., Chaubey, G.S., Nandwana, V., Rong, C.B., Yano, K. and Liu, J.P. "Synthesis of FePt nanorods and nanowires by a facile method." *Nanotechnology* 19.35 (2008): 355601.

[102] Poudyal, N., Rong, C.B. and Liu, J.P. "Morphological and magnetic characterization of Fe, Co, and FeCo nanoplates and nanoparticles prepared by surfactants-assisted ball milling." *Journal of Applied Physics* 109.7 (2011): 07B526.

[103] Nandhini, R., Mini, P.A., Avinash, B., Nair, S.V. and Subramanian, K.R.V. "Supercapacitor electrodes using nanoscale activated carbon from graphite by ball milling." *Materials Letters* 87 (2012): 165-168.

[104] Wang, Y., Li, Y., Rong, C. and Liu, J.P. "Sm–Co hard magnetic nanoparticles prepared by surfactant-assisted ball milling." *Nanotechnology*18.46 (2007): 465701

[105] Sun, X.M., Chen, X., Deng, Z.X. and Li, Y.D. "A CTAB-assisted hydrothermal orientation growth of ZnO nanorods." *Materials Chemistry and Physics*78.1 (2003): 99-104.

[106] Ramimoghadam, D., Hussein, M.Z.B. and Taufiq-Yap, Y.H. "The effect of sodium dodecyl sulfate (SDS) and cetyltrimethylammonium bromide (CTAB) on the properties of ZnO synthesized by hydrothermal method." *International journal of molecular sciences* 13.10 (2012): 13275-13293.

[107] Wang, C., Shen, E., Wang, E., Gao, L., Kang, Z., Tian, C., Lan, Y. and Zhang, C. "Controllable synthesis of ZnO nanocrystals via a surfactant-assisted alcohol thermal process at a low temperature." *Materials Letters* 59.23 (2005): 2867-2871.

[108] Estévez-Hernández, O., Santiago-Jacinto, P. and Reguera, E. "Easy preparative route for ZnO nanoparticles using tetrabutylammonium bromide assisted ultrasonic irradiation." *Materials Focus* 2.6 (2013): 438-442.

[109] Sugunan, A., Warad, H.C., Boman, M. and Dutta, J. "Zinc oxide nanowires in chemical bath on seeded substrates: role of hexamine." *Journal of Sol-Gel Science and Technology* 39.1 (2006): 49-56.

[110] Chen, C.N., Chen, Y.L. and Tseng, W.J. "Surfactant-assisted de-agglomeration of graphite nanoparticles by wet ball mixing." *Journal of materials processing technology* 190.1-3 (2007): 61-64.

[111] Cho, S., Jung, S.H. and Lee, K.H. "Morphology-controlled growth of ZnO nanostructures using microwave irradiation: from basic to complex structures." *The Journal of Physical Chemistry C* 112.33 (2008): 12769-12776.

[112] Wang, Y.X., Sun, J., Fan, X. and Yu, X. "A CTAB-assisted hydrothermal and solvothermal synthesis of ZnO nanopowders." *Ceramics International* 37.8 (2011): 3431-3436.

[113] Panigrahy, B., Aslam, M., Misra, D.S. and Bahadur, D. "Polymer-mediated shape-selective synthesis of ZnO nanostructures using a single-step aqueous approach." CrystEngComm 11.9 (2009): 1920-1925.

[114] Demoisson, F., Piolet, R. and Bernard, F. "Hydrothermal synthesis of ZnO crystals from Zn (OH) 2 metastable phases at room to supercritical conditions." *Crystal Growth & Design* 14.11 (2014): 5388-5396.

CHAPTER 4

Bulk Processing of ZnO Nanostructures *via* Thermal Oxidation of Mechanically Seeded Zn Dust for Functional Paints and Coatings

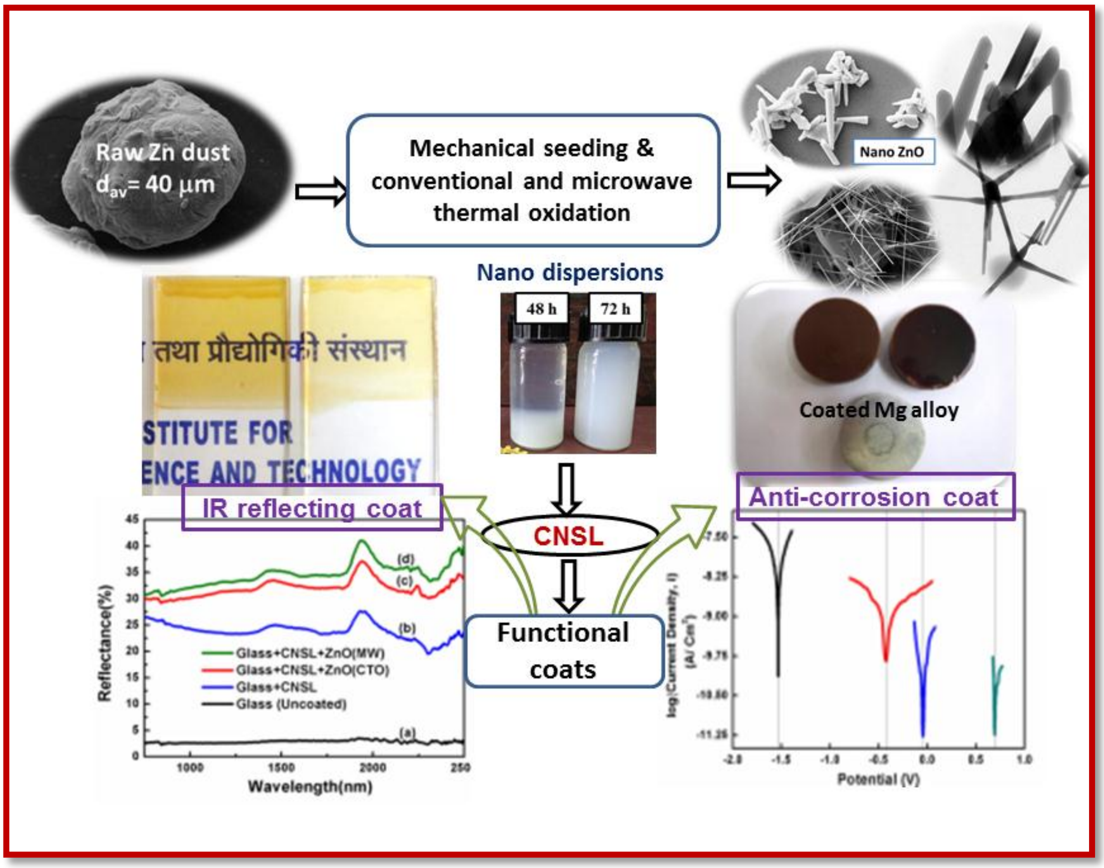

Chapter 4 comprises three parts. ***First part*** *describes the microstructural transformation of Zn dust during mechanical milling and evolution of ZnO nanostructures from mechanically activated Zn dust via conventional thermal oxidation (CTO). The* ***second part*** *of this chapter describes the production of ZnO nanostructure from mechanically activated Zn dust via microwave assisted thermal oxidation (MTO). The mechanical activation of as received Zn dust induced the growth of thin nano ZnO seed layer on the surface of individual Zn particle and this accelerated further oxidation process. The Structure, ball milling time, type of heating-and heating temperature correlation has been arrived at further from the results obtained. A paint formulation was made by dispersing the ZnO obtained in a naturally occurring organic resin Cashew nut shell liquid (CNSL).The Industrial application of nano ZnO obtained via thermal oxidation was tested for paint and coating applications and is described in* ***third part*** *of this chapter.*

The work reported in this chapter has been published in**,**

- ***Chemical Engineering Journal*** *284, (2016) 657–667*
- ***Materials and Design*** *92 (2016) 387–396*

4.1 Transformation of Mechanically Seeded Zn-Dust into Nano ZnO *via* Conventional Thermal Oxidation (CTO)

4.1.1Abstract

The morphological evolution of Zn dust during mechanical activation was analysed at different intervals of milling. Subsequently the effect of temperature on the growth of nano ZnO morphologies *via* conventional thermal oxidation (CTO) of mechanically activated Zn dust was investigated in the temperature range 700-1000 ^{o}C. The growth of diverse nano ZnO morphologies was observed at different temperatures. Temperature dependant evolution of nano ZnO morphologies including nano wire, nanoblade, tetrapod, and multipod from mechanically activated Zn was systematically analysed using XRD, SEM and TEM. From the microstructural analyses, the growths of well-defined ZnO nanowires of several tens of micrometre length and multipods with legs having several micrometre lengths were confirmed at 1000 ^{o}C, which finds futuristic applications in solar cells and sensors. The insight of the growth mechanisms of oxide nanostructures from present analysis may have practical implications for the fine control of the morphology, crystallinity, shape and aspect ratio of ZnO nanostructures. Thus the present study significantly highlights the possibility of designing various nano ZnO morphologies by simply tuning the temperature of thermal oxidation and milling parameters.

4.1.2 Introduction

Recently, the research on synthesis strategies of various nano ZnO morphologies is fuelled and fanned by its prospects in various fields like electronics [1-5], solar cells [6-8], optoelectronics [9], sensors [10, 11], biomedical [12,13] etc. The techniques such as sol gel [14], hydrothermal [15, 16], solochemical processing [17], pulsed laser and chemical vapour deposition [18-21], template assisted method [22, 23], vapour phase evaporation [24, 25] *etc.* are already attempted for the synthesis of nano ZnO from chemical precursors and the varied morphologies *viz.* nanowires [24, 25], nanorods [20], nanobelt, nanowhiskers [27, 28] and nanoblades [29] were produced. But, the complex and stringent multi-step synthesis procedures and the less reproducibility problems inhibited the above synthesis methods for the large scale industrial applications. Also some of the methods often confront difficulties of catalyst/template removal and follow tedious processing [30, 31].

An increased demand exists in scientific and industrial field for developing size and shape controlled bulk ZnO powders and its nanostructures from its cheapest metallic alternative metallic Zn [32, 33]. Compared to other synthesis routes for ZnO nanostructure fabrication involving complex and multistep processing, thermal oxidations of metallic source is simple, cost effective and possess large scale growth capabilities [34]. The direct oxidation of Zn dust is a non-catalytic approach for the nano ZnO production. It is beneficial in a way that one can grow unique size and shape controlled nanostructures without much processing difficulties [35]. In this process, the tailoring of nanostructure is possible by simply tuning the oxidation temperature and time of heating [36]. Many reports are available on the direct heating of metallic Zn source under oxygen gas flow which resulted in the formation of ZnO nanostructures with rich variety of morphologies [37]. Very recently Zhang *et al*. described the properties of bidirectional ZnO nanowire *via* thermal oxidation of metallic Zn foil fabricated in the same study [38]. Yuan *et al*. reported a detailed study on microstructure and growth morphologies of nano ZnO obtained *via* thermal oxidation of high purity Zn foils at different temperatures (200-1200 ^{o}C) with oxygen as reactant gas [36]. Evolution of bicrystalline nanowire, single crystalline morphology and tetrapod were observed at temperatures below melting point, between melting point and boiling point, and above the boiling point of Zn respectively.

Large scale synthesis of ZnO bicrystalline nanowire arrays on Si substrate with different growth direction other than [0001] direction *via* thermal oxidation of metallic Zn thin film was reported by Zhao *et al*. [39]. The synthesis of nano ZnO by the oxidation of metallic Zn particle prepared through an arc-discharge technique in air was reported by Wang *et al.* at different temperatures and time [34]. Low temperature synthesis of ZnO nanotube *via* thermal oxidation of Zn nanowire was studied and reported by Lu *et al.* [40]. Khan and Kordesch attempted the synthesis of ZnO nanowires by annealing metallic Zn nanowire made by heating ZnO and graphite mixture [41]. Dang *et al*. synthesized ZnO nanowire with an average diameter 40 nm by directly heating Zn powder in oxygen atmosphere [42]. In all the above mentioned research the use of metallic Zn in the form of foils, nano wire and nano particle prepared *via* different chemical routes have been used. Also the processing was carried out in the presence of an external gas supply and the substrate is necessary for the growth of size and shape controlled nanostructures. However, none of the studies explains the sequential evolution of ZnO nanostructures by direct thermal oxidation of Zn dust which is a widely available low cost and partially avoided industrial by-product. Till date not even a single report is there other than the work from the same group on the direct thermal oxidation of metallic Zn dust obtained from the industrial waste.

The thermal oxidation of mechanically activated Zn dust is highly economic and environmental friendly process for the production of diverse morphologies of nano ZnO. Material activation is a multistage approach to activate the reactant species and at each stage chemical, physical and energy parameters of material changes [43]. The observed changes to the solid state properties include structural deformation, along with the energy accumulation and active centre creation on the newly formed surfaces [44]. Various approaches have been developed till date, for the activation of reactant species [45].

Mechanical activation *via* ball milling is a simple low cost method for modifying physico-chemical properties of reactant materials which results in the development of specific assemblies that can induce and accelerate solid state reactions [44]. Unique material modification *via* mechanical milling is a widely discussed and accepted approach owing to its advantages like increased reactivity at lower reaction time with higher product yield and quality [46, 47]. Reduction in particle size and structural changes of parent species during mechanical milling are the driving forces for structural and morphological metastability of reactant material [47, 48]. Mechanical milling process also triggers surface oxidation of metallic Zn particle thereby initiating seed layer formation at an atomic scale which is a quite attractive pre-treatment procedure for the raw Zn dust prior to the subsequent thermal oxidation steps [49].

The present work is devoted to study the effect of material modification *via* mechanical milling prior to the thermal oxidation of raw Zn dust and to investigate the temperature dependant growth of ZnO nanostructures *via* conventional thermal oxidation.

4.1.3 Experimental Section

4.1.3.1 Raw Material Activation

Table 4.1: Ball milling parameters chosen for the milling of raw Zn dust.

Vessel volume (cm^3)	250
Powder charged (g)	15
BPMR[a]	4.5:1
Zirconia Ball diameter (mm)	10
Milling medium (liquid carrier)	Distilled water
Milling atmosphere	Air
Rotar speed (rev/min)[b]	250
Milling time (h)	12-72

[a] BPMR– Ball to Powder Mass ratio

[b] Rotar speed measured using Tachometer in revolutions per minute(rev/min)

15 g of raw metallic Zn dust (99.9% Binani Zn Pvt. Ltd. India) having average particle size 45 μm was charged into milling chamber along with deionised water and zirconia balls. The milled product after different period of milling time (12, 24, 48, 60 and 72 h) was collected and separated by centrifugal filtration. It was then dried overnight at 60 °C. The milling parameters and processing conditions for the current study are listed in Table 4.1.

4.1.3.2 Thermal Oxidation of Mechanically Activated Zn dust

Table 4.2: Processing details for conventional thermal oxidation (CTO).

Processing route	**Processing Parameters**
Conventional thermal oxidation (CTO)	Milling time (h), Holding temperature (^{o}C), Holding time (h)
	24, 900, 2
	24, 1000, 2
	48, 800, 2
	48, 900, 2
	48, 1000, 2
	72 700, 2
	72, 800, 2
	72, 900, 2
	72, 1000, 2

The thermal oxidation of mechanically activated Zn was carried out in a muffle furnace under air atmosphere in the temperatures range 700–1000 °C. The processing details adopted for conventional thermal oxidation is given in Table 4.2. The milled Zn dust were spread in the form of uniform bed of thickness about ~ 2 mm in a rectangular alumina boat with dimension 15 mm × 8 mm × 10 mm and was loaded into the furnace.

The sample was heated to the temperature desired at a rate of 10 °C min^{-1} and was soaked at that temperature for 2 h. After oxidation process, the furnace was normally cooled down to room temperature. Finally, the samples oxidised at different temperatures were collected and analysed. In the case of CTO, operating temperature and mechanical activation time were the two constraints chosen.

4.1.4 Result and discussion

4.1.4.1 Mechanical activation of Zn dust *via* milling

Kinetically active reactant mixture was produced *via* mechanical activation of raw Zn dust *via* ball milling prior to the subsequent thermal oxidation. Decreased particle size and defective lattice structure resulted from mechanical activation of Zn dust can accelerate chemical and phase transformations at lower temperatures [44]. Metallic Zn possess hexagonal close packed (HCP) crystal structure with high axial ratio [c/a = 1.856] and having low hardness (2.5 in Mohs scale). The application of mechanical force during milling produces shearing due to the reduction in number of slip systems in the crystal [50].

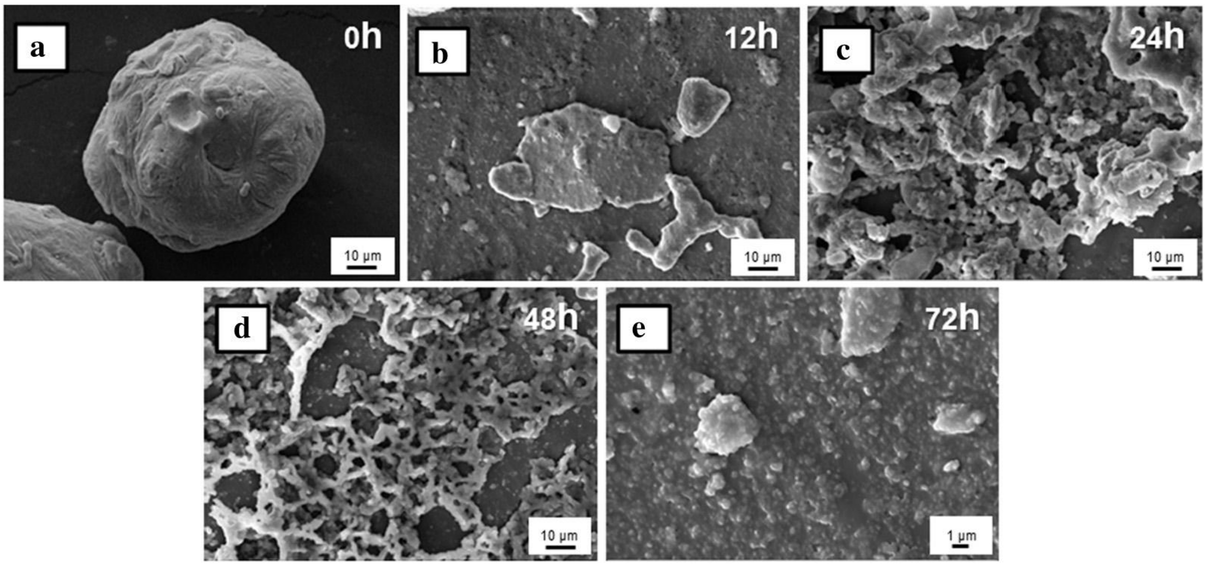

Figure 4.1: SEM microstructure of raw Zn dust (a) unmilled, (b) 12 h milled, (c) 24 h milled, (d) 48 h milled and (e) 72 h milled.

The impact of ball milling on the size, morphology and surface of the micron sized raw Zn dust at various time interval of milling are shown in Figure 4.1 (a)-(e). The raw Zn dust is a dense spherical particle (Figure 4.1 (a)). Continuous milling leads to drastic and sequential microstructural transitions of inherently soft Zn particle. During milling, the Zn particle experiences a ductile to brittle transition prompting the shearing and tearing of the particle and finally leading to the powdering of bulk metallic Zn, which is clearly understood from the corresponding SEM images. From the Figure 4.1 (b) it is clearly understood that12 h of milling has produced flaky and physically elongated Zn discs, which clearly indicates the shearing of particle induced by high impact energy during milling. These elongated Zn flakes structurally fragmented into weakly bonded structures of size <5 μm after 24 h of milling (Figure 4.1 (c)). The brittle fracture is well clear and the particle cleavage growth is more noticeable and wide spread at this stage. From Figure 4.1 (d) it can be perceived that, 48 h of milling has resulted in further outspreading of the cleavage growth, leading to the development of a physically weak porous frame work, which indicates its easiness to get powdered within next few hours of milling operation. It is evident from Figure 4.1 (e) that 72 h of milling results in fine powdered particles having a physical size <2 μm.

The sequential fracturing of the metallic Zn dust at different intervals of ball milling is further observed at 24, 48 and 72 h of milling under optical microscope to demonstrate the mechanism proposed. Figure 4.2 shows the optical microscopic images of the Zn dust at various stages of fracturing.

Initially, during milling, the Zn dust undergoes extensive plastic deformation. At this stage, shearing and particle elongation are clearly visible. Further milling leads to ductile to brittle transition of polycrystalline Zn. The basal cleavage crack usually occurs at the (0001) plane for HCP crystalline metallic Zn [50].

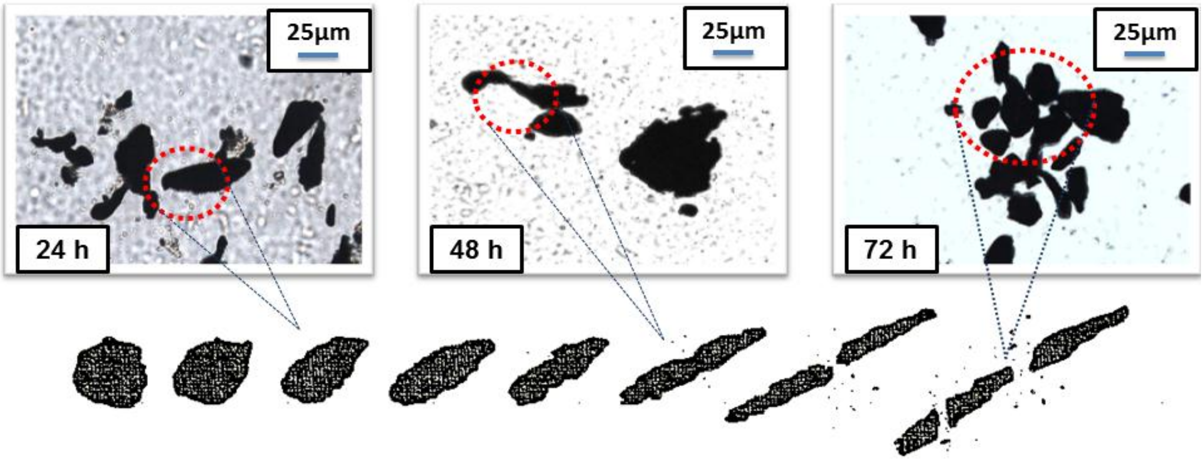

Figure 4.2: Schematic demonstration of the cleavage growth and fracturing of particle occurring at different time intervals of milling (supported with optical images at different time intervals).

The high impact energy produced due to the interaction of powder and milling media creates micro cracks during shearing. Upon continuous shearing, the micro-cracks produce mechanically weak zones where the necking takes place. The cleavage cracks produced at different areas of the particle finally leads to fracturing of metal. In addition to the afore mentioned mechanism other failure mechanisms like kinking, twinning and limited slips also produce metal cleavage and results in the fracture of bulk metal particle.

The milling of raw Zn dust in aqueous medium leads to the oxidation of surface Zn atoms and produces surface ZnO seed layer on every Zn particle as mentioned in Chapter 3 under the Section 3.1.4.2. The development of ZnO seed nuclei on the surface of Zn particle is evident from the corresponding XRD pattern of Zn dust at different intervals of milling (Figure 4.3). The X-ray diffraction peaks obtained at the 2θ positions 36.28, 39.07, 43.33, 54.32, 70.35 and 70.72 corresponds to the lattice planes (002), (100), (101), (102), (103), and (110) of pure Zn metal (JCPDS PDF #00-004- 0831) with HCP crystal structure.

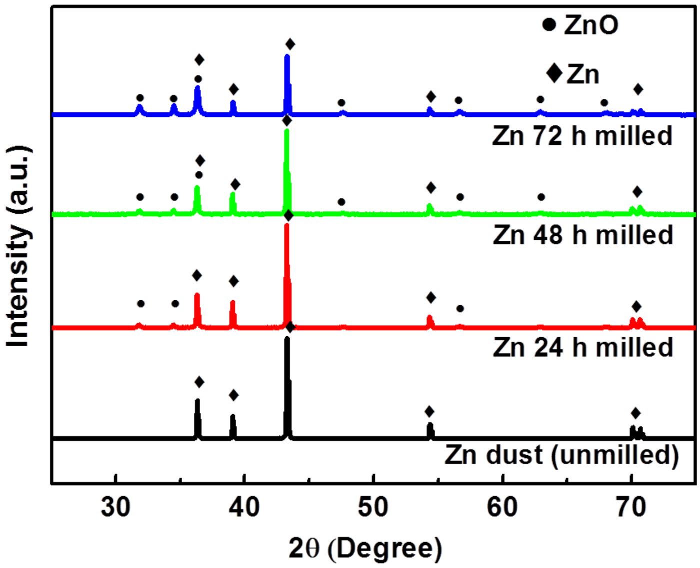

Figure 4.3: XRD patterns of Zn dust milled for different period of time.

In XRD pattern of raw Zn dust these are the prominent peaks and no characteristics peak of any impurities were observed. Milling this Zn dust for about 24 h, ensued the sprouting of ZnO nuclei on the surface of Zn particle and for the corresponding sample the XRD peaks obtained at positions 31.91, 34.45, 36.28, 47.60, 56.64, 62.82, and 67.93 ^{o} corresponds to the (100), (002), (101), (102), (110), (103) and (112) lattice planes of wurtzite phase ZnO (JCPDS no: 36-1451). With increase in the milling time from 24 h to 48 h, these ZnO peaks became more prominent confirming the claim of increased ZnO seeding with milling. After 72 h of milling, all the major ZnO peaks became clear and distinct along with peaks of Zn indicating the increased ZnO seeding due to the faster growth of surface ZnO with increase in milling time. The subsequent drop in intensity of peaks corresponding to Zn with milling time is also a clear evidence for the conversion of surface Zn atoms to ZnO seeds with milling.

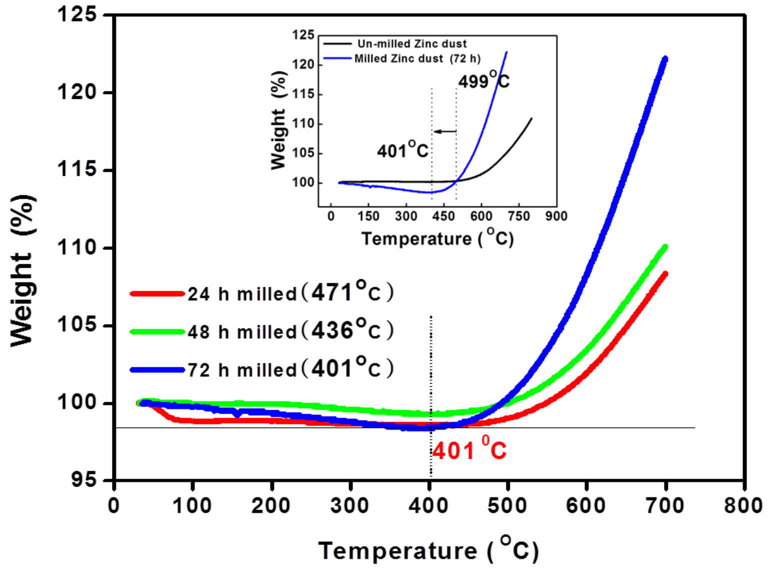

Figure 4.4: TG analysis of the samples obtained at different intervals of milling.

The TGA curve obtained for the sample milled for different time period is shown in Figure 4.4. The temperature dependant weight change also support ZnO seeding induced during ball milling. The theoretical melting point and boiling point of pure Zn dust are 419 °C and 908 °C respectively. The seeding of zinc oxy hydroxide is induced on the surface of Zn particle during aqueous milling of Zn dust. From the TGA curve, for 24 h milled Zn dust, a minor weight loss is observed in the range 51 to 142 °C. This weight loss is attributed to the decomposition of zinc oxy hydroxide formed during milling by the hydrolysis reaction in aqueous media. Previous reports are there on the formation of $Zn(OH)_2$ during milling which have very low decomposition temperature in around 130 °C [51]. This weight loss in TGA curve in the temperature range 51 to 142 °C is clearly seen for Zn dust milled for 24 h. However, the same weight loss is not visible in the TGA curves of the Zn dust milled for longer time intervals 48 and 72 h. The conversion of these hydroxides to more stable oxides readily takes place with the increase in milling time, due to the high milling impact energy as per the reactions 4.1 and 4.2 given below.

$$Zn(s) + H_2O\,(l) \longrightarrow Zn\,(OH)_2\,(s) + H_2\,(g) \qquad (4.1)$$

$$Zn(OH)_2(s) \longrightarrow ZnO(s) + H_2O(l) \qquad (4.2)$$

Further increase in temperature leads to the oxidation of the Zn dust causing a sharp rise in the TGA curve in the temperature range 400-470 ^{o}C. A gradual shift in the onset oxidation temperature with the increase in the milling time is evident from the TGA curves. The onset oxidation temperature drops by 35 ^{o}C from 471 ^{o}C to 436 ^{o}C when the milling time is increased from 24 h to 48 h. As the milling time increased to 72 h the oxidation onset temperature reduced by 35 ^{o}C from 436 ^{o}C to 401 ^{o}C. Thus from the TG analysis a reduction of ~ 100 ^{o}C in the onset oxidation temperature induced by milling was confirmed (Inset TGA curves in Figure 4.4). This reduction in the onset oxidation temperature was resulted from the increase in the specific surface area of the zinc dust due to the reduction in particle size during milling. Along with the size effect, the oxidation kinetics of Zn dust also accelerated by the formation of the atomic level ZnO surface seed-layer during milling.

The particle size distribution analysis (DLS) of the ZnO seed suspension collected at different milling period is presented in Figure 4.5 (a). The SEM microstructure of raw Zn particle is given as inset in Figure 4.5 (a). When the measurement was taken, the pH of the particle suspension was measured to be in the range 8.7–9.15. After 24 h of milling, the particle size of ZnO seed-clusters in the suspension showed an average value of about 537 nm which was then decreased to 217 nm when the milling duration was increased from 24 to 72 h. Using Debye– Scherrer relation, the crystallite size of the ZnO seed particles obtained from the milled dispersion was calculated and those values also showed an identical trend. The crystallite size of the ZnO seed particle obtained decreased from 52.78 nm for 24 h milled samples to 42.22 nm for 48 h milled samples and again decreased to 35.18 nm for 72 h milled sample. The SEM image of the ZnO seeds formed after 72 h milling is shown in Figure 4.5 (b) and the corresponding TEM image is shown as the inset in Figure 4.5 (b). From the TEM image, the cluster sizes of the seeds formed were measured to be ~ 135 nm. The variation of size of the seed particle in aqueous suspension obtained after different milling time is depicted in Figure 4.5 (c). The seed particles formed during milling gradually disperse in aqueous medium and tend to form primary ZnO seed-clusters and agglomerates in the absence of any surfactants or capping agents.

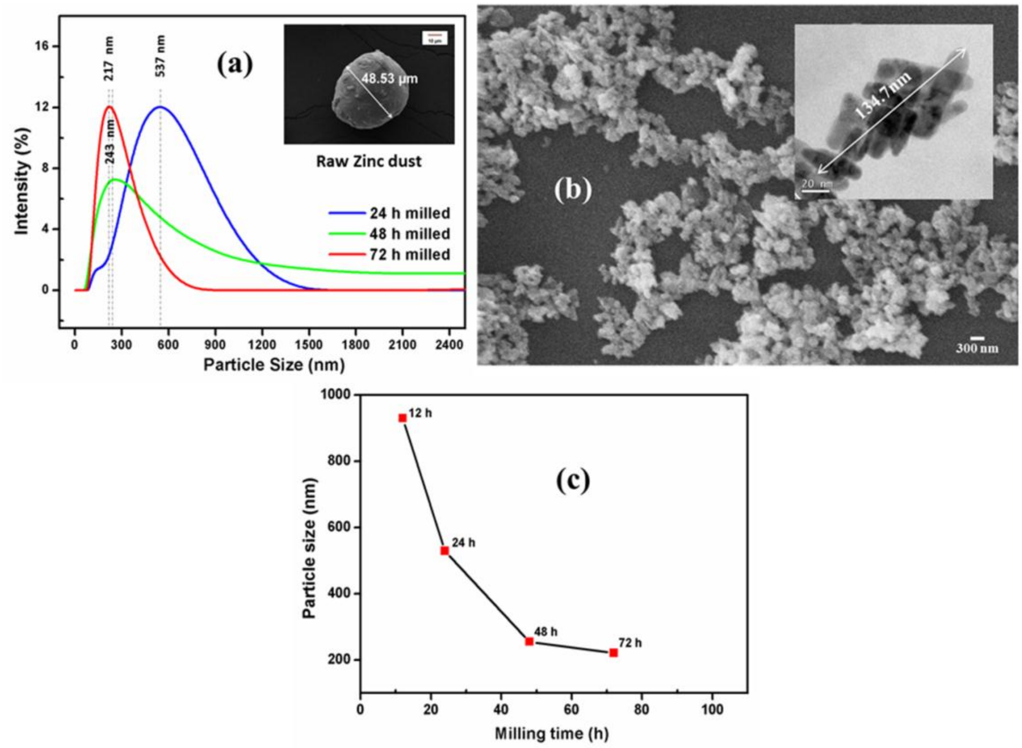

Figure 4.5: a) Size distribution (DLS) of ZnO seeds formed during milling for different time periods, SEM image of raw dust particle having an average particle size of 48.53 µm (Inset). (b) SEM image of ZnO seed particle formed during milling after 72 h and corresponding TEM image (Inset). (c) ZnO seed cluster size (nm) with milling time.

Thus the XRD, TGA, TEM and DLS analyses confirmed the formation of nano ZnO seeds during the milling operation, which in effect accelerates the thermal oxidation of Zn dust into nano crystalline ZnO without the assistance of any catalysts.

4.1.4.2 Conventional Thermal Oxidation (CTO) of mechanically activated Zn dust

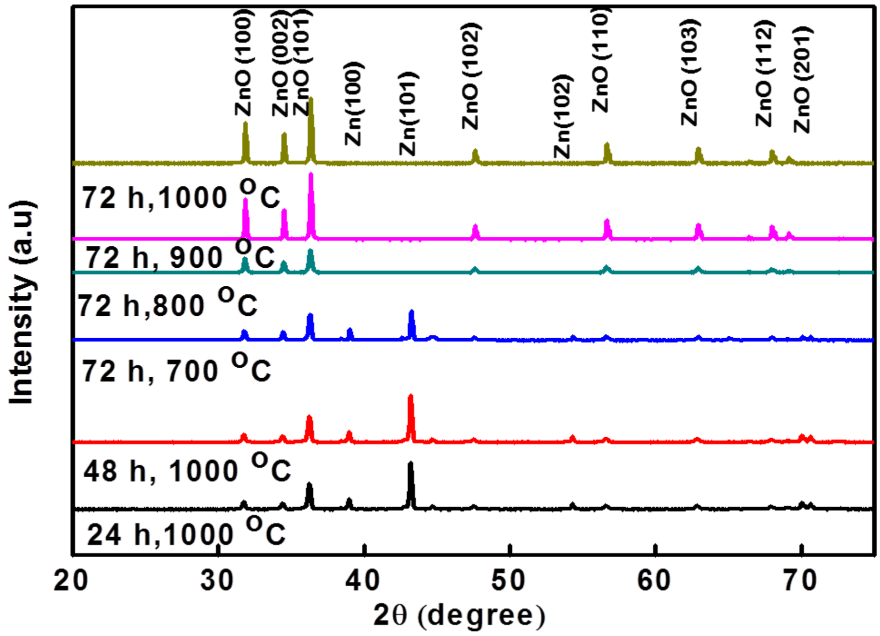

Figure 4.6: The X- ray diffraction pattern of ZnO obtained at different temperature *via* conventional thermal oxidation of mechanically activated Zn dust.

Several oxidation constraints (given in the Table 4.2) were tried in the CTO route. Out of which in few cases only complete oxidation of the Zn dust was achieved. The phase analysis of the final product obtained *via* CTO of mechanically seeded Zn dust at different temperatures has been carried out using the X-ray diffraction analysis. Figure 4.6 displays the X-diffraction pattern of the final product obtained at randomly selected conditions *via* CTO of mechanically seeded Zn dust. In all cases peaks are quite sharper, indicating the crystalline nature of product obtained at different conditions. The X-ray diffraction pattern obtained for 24 h and 48 h milled sample thermally oxidised at 1000 ^{o}C showed diffraction peaks corresponding to both Zn and ZnO. The immature peaks of ZnO indicate incomplete conversion of Zn to ZnO. The three diffraction peaks of Zn corresponding to (100), (101) and (102) planes at 39.01, 43.31 and 54.32^{o} respectively, are consistent with reported data of crystalline hexagonal close packed phase (JCPDS#

00-004-0831). All other eight peaks corresponding to (100), (002), (101), (102), (110), (103), (112) and (201) planes at 31.76, 34.62, 36.34, 47.65, 56.81, 62.97, 67.90 and 69.27 ^{o} respectively are of ZnO wurtzite structure. All peaks are well indexed to JCPDS file no. 36-1451. From 800 ^{o}C onwards for 72 h milled samples, CTO results in complete conversion of Zn to ZnO and all the peaks observed are consistent with crystalline hexagonal close packed wurtzite ZnO and no characteristic peaks corresponding to any sort of impurities were observed, indicating the complete conversion of metallic Zn to crystalline nano ZnO during thermal oxidation.

The values of a and c for ZnO obtained at different temperature are presented in Table 4.3. In all cases the values of a and c are in good accord with reported values (a = 3.24 Å and c = 5.21Å) [52]. The measured c/a ratio 1.62 showed good agreement with the value 1.605 for an ideal close packed hexagonal structure according to the standard JCPDS data 36-1451.

Table 4.3: Lattice constants a, b, and c corresponding to the (101) crystal plane for ZnO synthesized through CTO.

Samples	Processing conditions	Lattice parameter a = b (Å)	Lattice parameter c(Å)
a	CTO (800 ^{o}C)	3.23	5.28
b	CTO (900 ^{o}C)	3.24	5.27
c	CTO (1000 ^{o}C)	3.23	5.28

UV-visible absorption studies of nano ZnO obtained *via* CTO at different temperatures was carried out by ultrasonically dispersing the powder in water and the spectra are shown in Figure 4.7. The room-temperature absorption spectra exhibit excitonic absorption peak at 353, 348 and 346 nm for ZnO nano particle obtained at 800, 900 and 1000 ^{o}C respectively. This corresponds to the band edge absorption of ZnO.

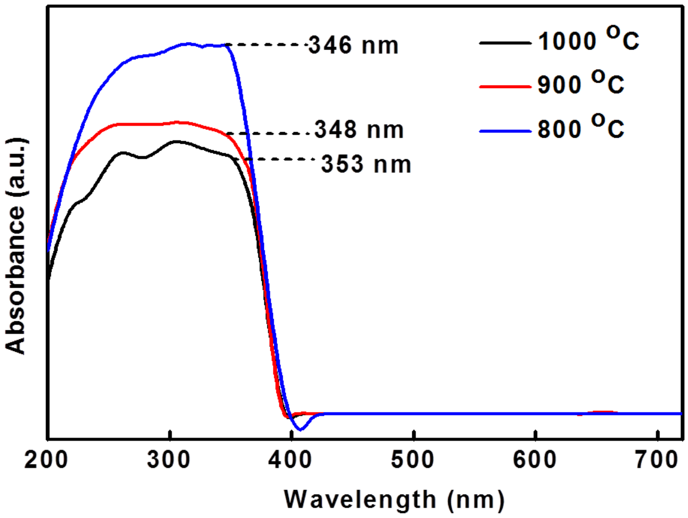

Figure 4.7: UV-visible absorption spectra of nano ZnO obtained *via* CTO at different temperature.

The temperature dependant growth of ZnO nanostructure *via* CTO of mechanically activated Zn is analysed using SEM analysis. After thermal oxidation at 600 °C the microstructure of the sample ball milled for 72 h is shown in Figure 4.8 (a). The surface of Zinc becomes roughened with the growth of taper shaped nanowire of ZnO with an average diameter 350 nm and length of several micrometres and the corresponding magnified image is given as inset of Figure 4.8(a). The EDX spectra and corresponding elemental constituents are also given in Figure 4.8 (b). In the resent case wt % of Zn and O is not matched with standard values of ZnO. The weight % of Zn is much higher than that of O which indicates the incomplete conversion of Zn to ZnO. The microstructures of the end product obtained after CTO of 72 h milled Zn at 700, 800 and 900 °C and the corresponding magnified images are given in Figure 4.9 (a), (b) and (c) respectively. Theoretically Zn melts at 450 °C. For effective thermal oxidation of Zn, a temperature greater than its melting point is needed. The XRD pattern (Figure 4.6) clearly reveals the presence of unconverted Zn along with ZnO formed in the final product obtained after thermal oxidation at 700 ^{o}C.

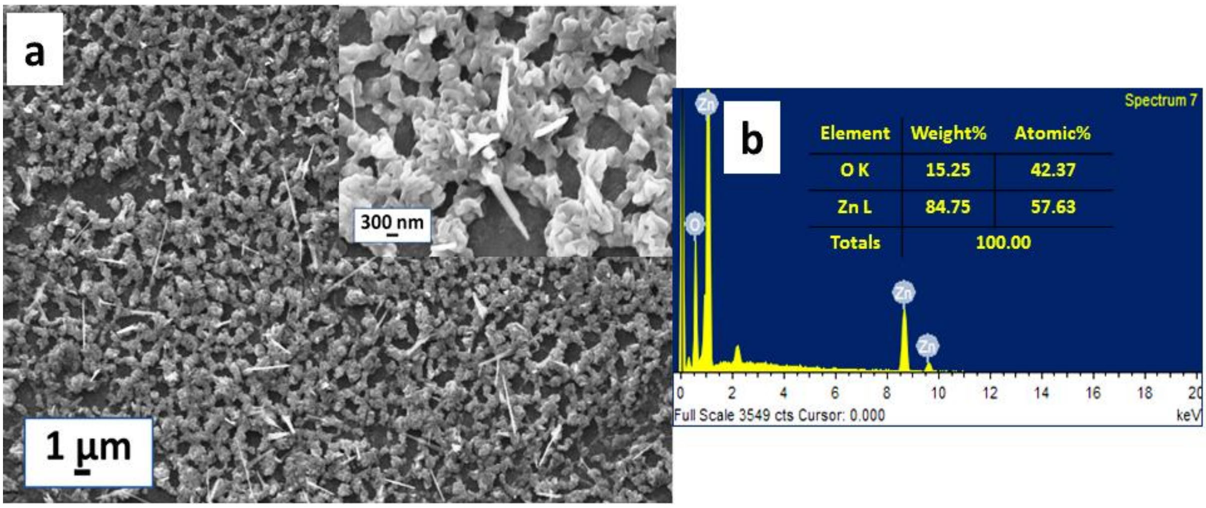

Figure 4.8: (a) Formation of nanowire on the surface of Zn at temperature 600 ^{o}C and corresponding magnified image of nanowire formed given in inset and (b) corresponding EDX spectra.

The barely visible ZnO formation on Zn surface suggest that a very few surface Zn atoms are oxidised to ZnO at temperatures up to 700 ^{o}C. At 700 °C, the mechanically deformed Zn flakes undergo oxidation to produce rod shaped structures with highly roughened surface with thick deposit of nano ZnO of much higher surface density on Zn flakes (Figure 4.9 (a)). The further increase in temperatures resulted in complete conversion of Zn to ZnO and growth of well-defined ZnO nanostructures. ZnO is a well-recognized flux for forming liquid phase in the temperature range 800–850 °C [53]. After CTO at 800 °C, liquid phase aided diffused growth of ZnO crystals were perceived and complete oxidation of Zn dust to nano ZnO was obtained (Figure 4.9 (b)).

At 900 °C, the SEM micrograph (Figure 4.9 (c)) clearly shows the growth of assorted ZnO morphologies including tetrapods, nanoblades and nanoneedles. In CTO anisotropic growth of nano ZnO morphologies was observed due to slow heating and variation in oxygen concentration at different regions of the furnace. At temperatures near the boiling temperature of Zn a super-heating phenomenon can be expected [34]. At this temperature region both liquid–solid and vapour-solid growth mechanisms can be assigned for the growth of nano ZnO. [34].

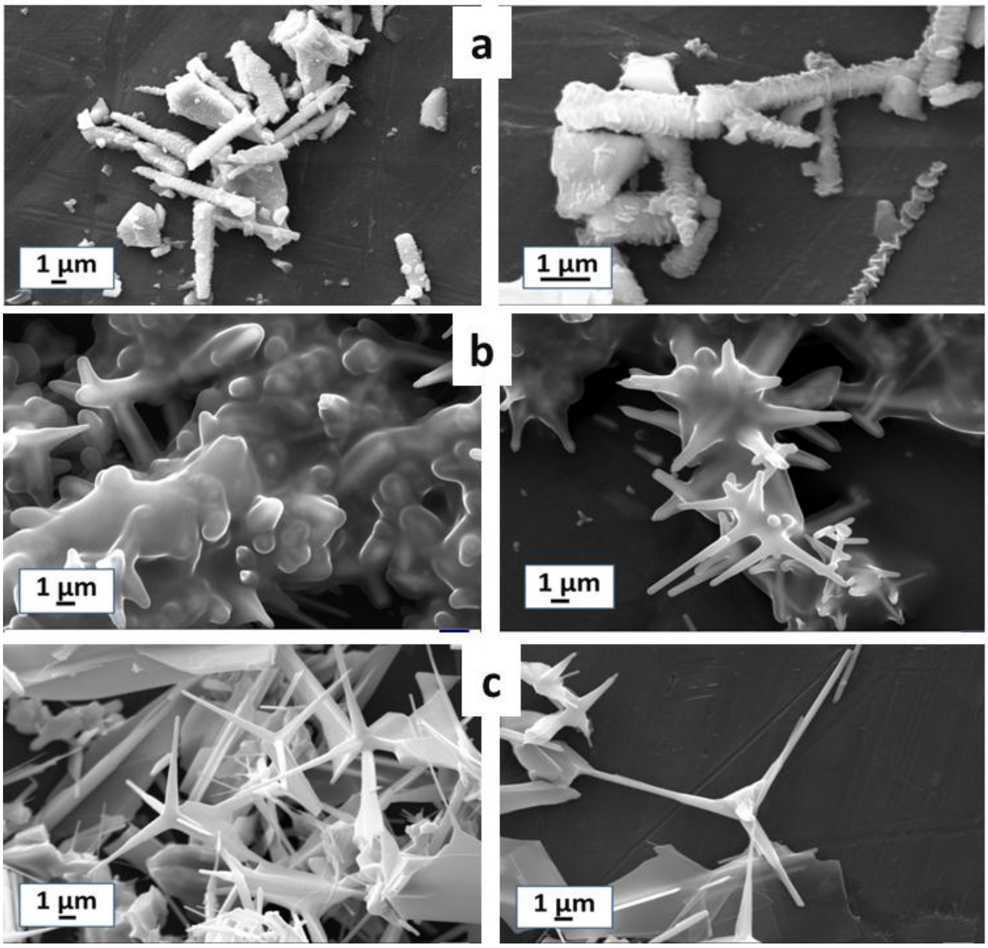

Figure 4.9: ZnO nanostructures obtained *via* CTO of mechanically activated Zn dust at (a) 700 °C, (b) 800 °C and (c) 900 °C.

At high temperature the oxidation of Zn at atomic level usually takes place. Under super heating conditions, the formation of melt in the core as well as formation of thick oxide-bed on the surface may simultaneously take place. The thin vapour layer of zinc produced at higher temperatures, may directly react with the atmospheric oxygen and results in growth of various ZnO nanostructures.

The molar volume difference between Zn and ZnO generates a compressive stress (stress relaxation mechanism) at the Zn–ZnO interface after the formation of ZnO layer over Zn particle during milling [36]. During CTO the stress gradient present across ZnO layer over Zn particle drives out the Zn cation, resulting in the growth of various ZnO nanostructures. Depending on the stress gradient formation, the growth of nanocrystals accelerated at multiple directions and resulted in the formation of multipod like morphology from single seed nuclei.

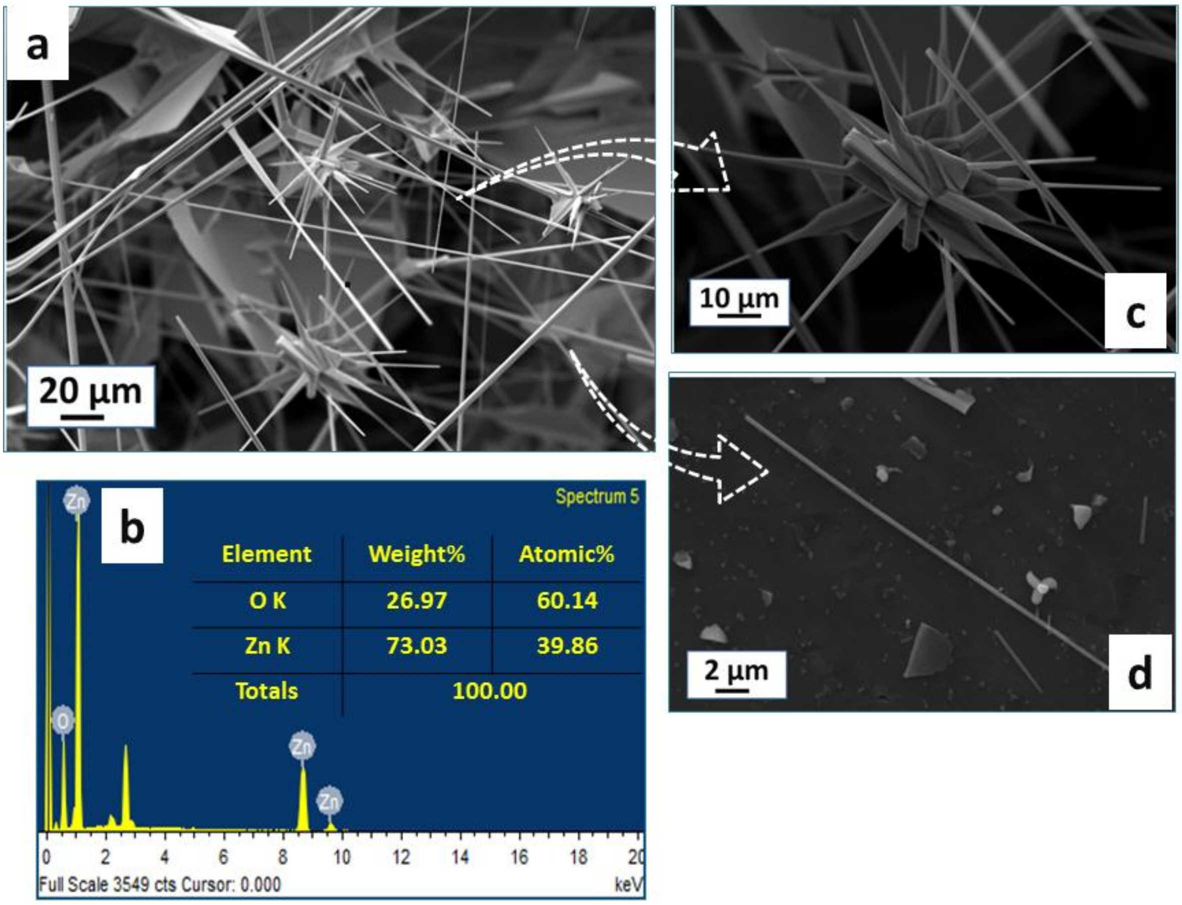

Element	Weight%	Atomic%
O K	26.97	60.14
Zn K	73.03	39.86
Totals	100.00	

Figure 4.10: (a) SEM microstructure of ZnO nanostructures formed at *via* CTO at 1000 °C, (b) corresponding EDX spectra, magnified images of (c) multipods and (d) nanowire formed at 1000 °C.

Above the boiling temperature of Zn, at 1000 °C the vapour–solid growth resulted in the formation of ZnO multipods having long legs of several micrometre lengths and long nanowire of several tens of micrometre lengths as shown in Figure 4.10 (a).The corresponding EDS analysis and elemental composition is presented in Figure 4.10 (b).

The images of nanowire and multipod at higher magnification are given in Figure 4.10 (c) and (d) respectively. Thus at temperature above the boiling point, growth of ZnO is accelerated in multiple directions and large 3D oriented growth of nanostructures like multipods from the central axis of the seed nuclei were observed.

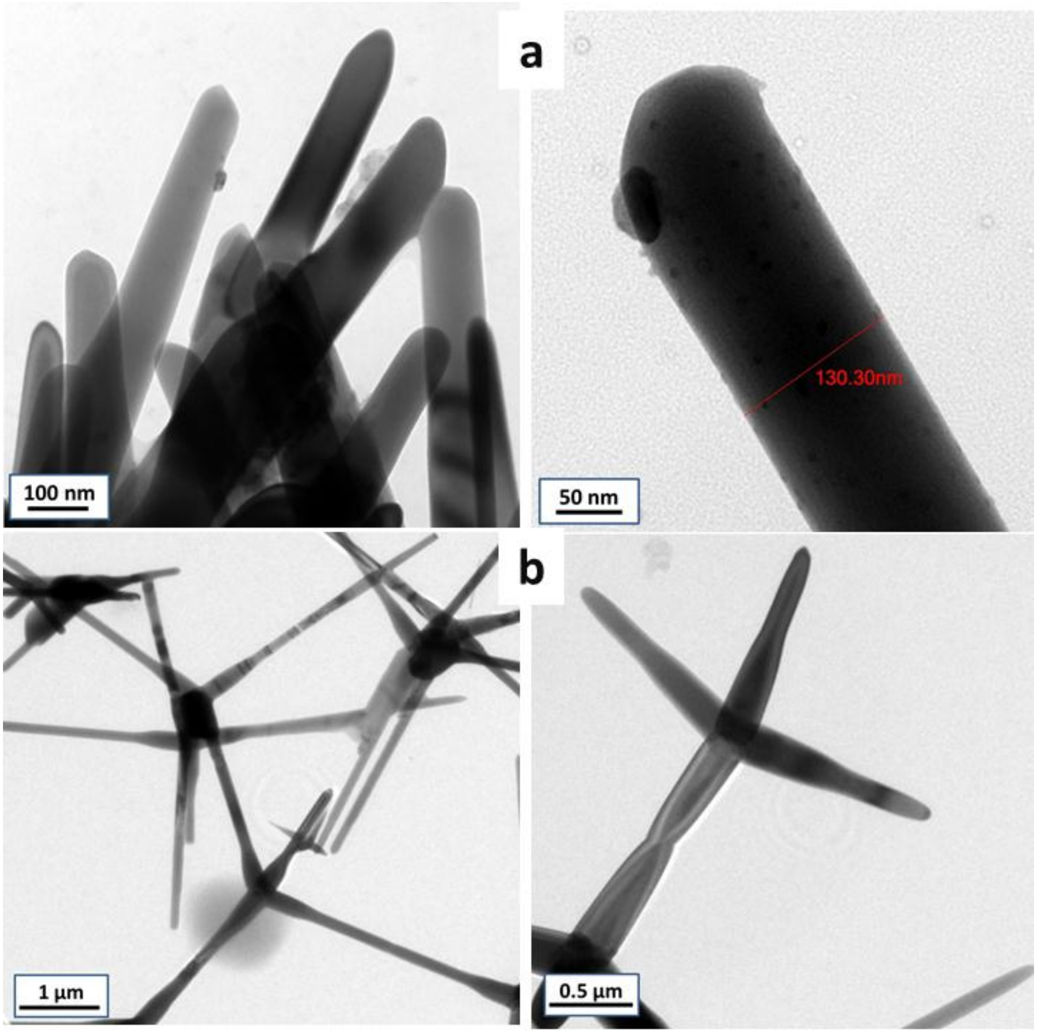

Figure 4.11: TEM images of ZnO nano structures obtained *via* CTO at (a) 800 and (b) 900 °C and the corresponding higher magnification image.

The temperature dependent ZnO nanostructure growths were again confirmed from the TEM analysis (Figure 4.11 (a) and (b)) of the product obtained at different CTO temperature. In the CTO temperature range 800–1000 °C, series of morphologies including nanorod, nanowire, nanoblade, tetrapod and multipod were obtained. TEM analysis confirms the growth of ZnO nanorod with several nanometre lengths and a diameter of 100 nm at 800 °C (Figure 4.11(a)). At high temperature (900 °C), the rod morphology of ZnO particle obtained is changed to tetrapod structures with the leg length 5 μm and diameter of few tens of nanometres. From the TEM analysis also the growth of multipods with a large number of legs along with several micro meter length nanowire at 1000 °C was confirmed (Figure 4.12 (a)). The higher magnification images of leg of multipod and nanowire are also shown in Figure 4.12 (b) and (c). The SEAD pattern given in Figure 4.12 (d) reveals high crystallinity of the sample obtained. The corresponding EDS analysis is shown in Figure 4.12 (e) and the elemental constitution is same as that of standard ZnO. All the morphologies obtained in TEM analysis are in well agreement with the corresponding SEM microstructure.

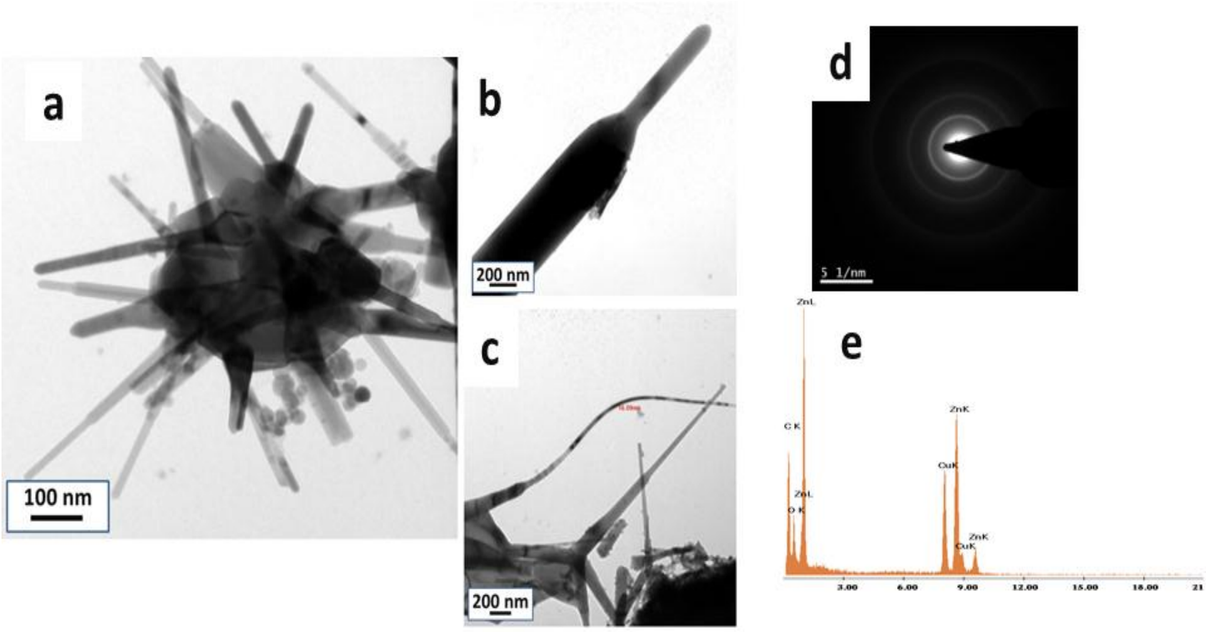

Figure 4.12: TEM images of (a) multipods, (b) single leg of multipod, (c) long nanowire, corresponding (d) SAED pattern and (e) EDS spectra of ZnO obtained *via* CTO at 1000 °C.

From SEM and TEM images it is clear that, the Zn dust derived ZnO has notable merits when compared to ZnO obtained *via* any other well-explored chemical routes [15, 54, 55]. Above all, the formation of such stable, long nano wires of ZnO obtained *via*

CTO at 1000 ^{o}C is not observed with simple chemical routes unless surfactants, structure-directing agents or template are employed. Among the various chemical methods reported, surfactant aided hydrothermal route is found to be capable for the well-controlled evolution of nanowires of ZnO [15].

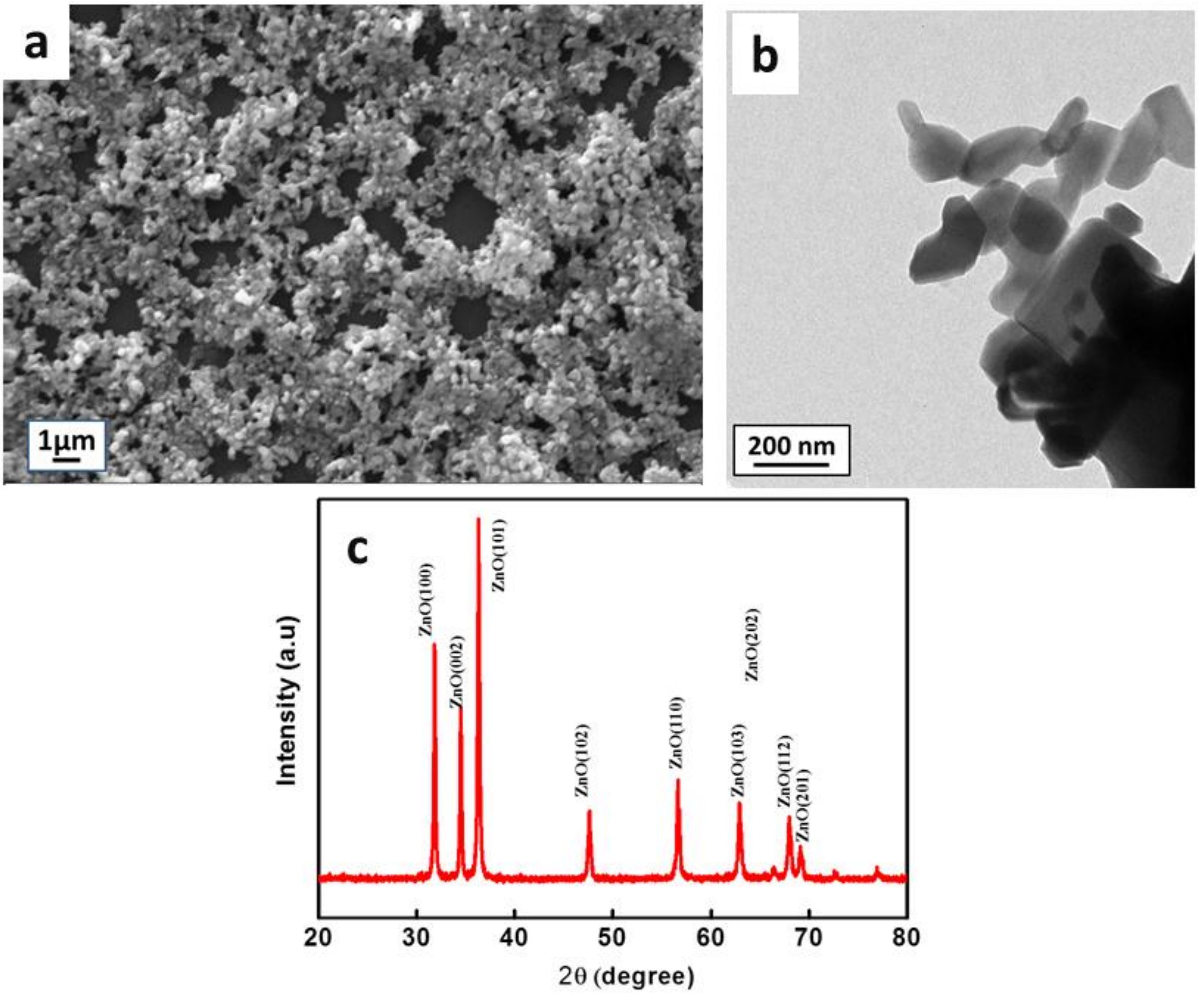

Figure 4.13. (a) SEM image, (b) TEM morphology and (c) XRD analysis of commercial ZnO.

According to the previous reports, the growth axis of ZnO nanostructures was controlled by the highly polar surfaces of ZnO. The basal plane is the common polar surface [56]. The presence of the polar surfaces with high energy and the non-centre symmetric structure characteristics of ZnO resulted in the c-axis oriented growth of ZnO nanostructures. In ZnO the oppositely charged ions create positively charged Zn-(001)

and negatively charged O-(001) surfaces [56-58]. As a result, the surface energy divergence and spontaneous polarizations along the c-axis form nanostructures with respect to the various crystal plane kinetics. In addition to the highly polar surfaces, the ZnO also possess other non-polar surfaces such as (010) with lower energy compared to highly polar surface (001). The difference in the relative surface energies of the facets of crystal decides the favoured growth of the nanostructure in a given reaction condition [59, 60].

For comparison, phase analysis and microstructure of commercial ZnO was also taken and the results are presented in Figure 4.13 (a), (b) and (c). The SEM and TEM micrographs of the commercial ZnO samples showed agglomerated nearly spherical ZnO particles having a size of 400–500 nm. The corresponding X-ray analysis showed characteristic diffraction peaks of hexagonal wurtzite ZnO only.

4.1.5 Conclusions

In this exploratory study, the role of mechanical activation of raw Zn dust on thermal oxidation *via* CTO route was systematically investigated for obtaining morphologically tuned ZnO nanostructures. The size reduction and formation of atomic level ZnO seed layer during mechanical activation of raw Zn dust accelerate the oxidation kinetics of Zn during thermal oxidation. The sequential evolution of ZnO nanostructures from mechanically activated metallic Zn dust was studied in the temperature range 600–1000 °C and the growth of various morphologies such as, nanorod, nanowire, tetrapod, nanoblade and multipods were reported. ZnO nanowire having lengths of several tens of micrometres were obtained at 1000 °C, which is a promising candidate for futuristic applications in sensors and solar cells. Thus the present investigations on CTO of mechanically activated Zn dust develop a new, cost effective and catalyst free technique for synthesising various nano grade ZnO morphologies.

4.2 Transformation of mechanically seeded Zn-dust into nano ZnO *via* Microwave Assisted Thermal Oxidation (MTO)

4.2.1 Abstract

The effect of microwave energy on the evolution of nano ZnO morphologies *via* microwave assisted thermal oxidation (MTO) of mechanically activated Zn is analysed systematically by varying microwave power and irradiation time. Initially, micron sized metallic zinc dust (99.9 %, D_{avg} 45 µm) was mechanically milled to have zinc oxide seed nuclei on its surface. Then the mechanically activated Zn dust is subjected to microwave energy in a domestic oven at different power for various time periods. Under microwave heating complete conversion of Zn dust into nano ZnO is accomplished within 15 min irradiation time. Further in the oxidation part, it can be seen that the MTO results in significant advancement in the particle morphology. In contrast to assorted morphology in conventional thermal oxidation, the microwave assisted route results in single morphology at a particular microwave irradiation condition. ZnO nanorod, tetrapod and multipods were successfully synthesised in bulk from mechanically activated Zn under microwave irradiation at a power 600-750 W for 10-15 minute through this facile route. Thus the present study strongly recommends microwave assisted thermal oxidation as a technologically important process for the bulk production of nano ZnO.

4.2.2 Introduction

New synthesis techniques for the economical and ‘zero-waste’ production of nano ZnO with good product yield and speckled morphologies having enriched properties are still emerging [36, 44, 61]. In the Section 4.1 the direct conversion of Zn dust *via* CTO was studied in the temperature range 600-1000 ^{o}C. Though direct oxidation of Zn dust has proven to be simple and clean, Zn to ZnO conversion by conventional thermal treatment processes need longer reaction time and high processing temperatures. Application of microwave energy for thermal oxidation is simple and rapid technique that can be exploited for the bulk production of nano ZnO from Zn dust [62].

As a better alternative source for thermal oxidation, microwave (MW) energy emerges as a high performance and powerful tool to process high quality materials and in most cases to improve the solid materials performance characteristics [63, 64]. Depending upon the dielectric characteristics of the material, microwave at a frequency of 2.45 GHz induces volumetric heating *via* molecular interactions with the material [62]. Thus, the microwave assisted heating is different from conventional heating processes where the heat transfer occurred by the mechanisms of conduction, convection and radiation processes [64, 65]. In conventional methods, heating starts from the material's surface followed by the heat moving inward. Thus a temperature gradient exists from the surface to the core of the particle [66]. On contrary, microwave heating generates heat within the material and then spreads to the entire volume [66] .The microwave heating is advantageous due to the reduction in energy consumption and processing time, enhanced diffusion processes, very rapid heating and lower environmental hazards [67]. Large numbers of reports are there on the use of microwave energy in solution chemistry for the nucleation and growth of nano inorganic oxides for laboratory scale production [68, 69]. Microwave-assisted synthesis has been labelled as an environment friendly processing route for producing high quality nanostructures [70]. Microwave assisted hydrothermal route was adopted by Zou *et al.* for fabricating submicron (200–500 nm) nano-heterostructures of Cu/Cu_2O with improved photo degradation efficiencies (92.1 %) and enhanced absorption ratios [71]. The development of mono-dispersed spherical ZnO clusters (sizes ranging from 50 to 274 nm) was reported by Hu *et al.* by a fast microwave-polyol based technique [72]. Using microwave assisted technique Wu *et al.*, successfully synthesized nano crystallites of SnO_2 particles with high purity and size < 30 nm [73]. Phuruangrat et al. synthesised hexagonal ZnO nano flowers with spear shaped nano rods (aspect ratio in the range 40–80) in them *via* microwave irradiation (180 W/20 min) of the aqueous reactant mixture [74]. Similarly, by employing microwave irradiation (10 min) Krishnakumar *et al.* attained ZnO nanostructures with flower shaped morphology without using any surfactants or ionic liquids [66]. However, no reports are there till date on microwave assisted direct thermal oxidation of micron sized metallic Zn dust, which is addressed in the present section.

In the present work, microwave assisted direct thermal oxidation (MTO) of mechanically activated Zn dust was carried out using a domestic microwave oven (with maximum power rating – 750 W, 2.45 Hz). Thus the present section report a novel and fast synthesis route for production of nano ZnO from raw Zn dust with a potential for industrial scale up which is energy efficient, simple, environmental friendly and cost effective.

4.2.3 Experimental Section

4.2.3.1 Microwave Assisted Thermal Oxidation of Zn Dust

The milling parameters and conditions employed in MTO were same as that for CTO (Table 4.1, section 4.1.3). The mechanically activated Zn dust was again hand milled using mortar and pestle for 15 min with graphite powder (10 wt %). Zn dust-graphite mixture readily interacts with microwaves and produces volumetric heat at a rapid rate [62, 75]. A rise in thermal conductivity of the reactant mixture is also observed, supporting the faster heat absorption and thus reducing the reaction time for oxidation. The graphite added will no way affect the quality of final oxide formed since it will burn out during the heating process.

The mechanically activated Zn dust (milled for different time period) was spread into uniform thin bed of thickness ~2 µm in a rectangular alumina boat having dimension 15 mm X 8 mm X 10 mm. The crucible with reactant powder was loaded into Teflon-lined domestic microwave oven (Samsung; Power 1100 W and 2.45 GHz) for the MTO. The maximum irradiated microwave power in the form of pulse was 750 W. The two constraints selected in the case of MTO are irradiation time and microwave power. Table 4.4 lists the details of the oxidation constraints and conditions.

Table 4.4: Processing details for MTO.

Processing route	**Processing conditions**		
Microwave assisted oxidation (MTO)	Milling time (h), Irradiation power (W), Irradiation time (min)		
	24,	450,	15
	24,	600,	10
	24,	600,	15
	24,	750,	10
	24,	750,	15
	48,	450,	15
	48,	600,	10
	48,	600,	15
	48,	750,	10
	48,	750,	15
	72,	450,	15
	72,	600,	10
	72,	600,	15
	72,	750,	10
	72,	750,	15

4.2.4 Result and Discussion

In the microwave route, the Zn dust milled for various time intervals 24-72 h was microwave irradiated for 10-15 min at the power of 450-750 W. In MTO the direct conversion of electromagnetic energy to thermal energy results in fast and uniform volumetric heating of the surface activated Zn within a short interval of time [63]. Figure 4.15 shows the XRD patters of selected samples of Zn dusts after MTO. The XRD analysis conducted on randomly selected samples showed immature ZnO peaks indicating the incomplete oxidation of Zn. In few cases only the complete oxidation of the Zn dust was attained.

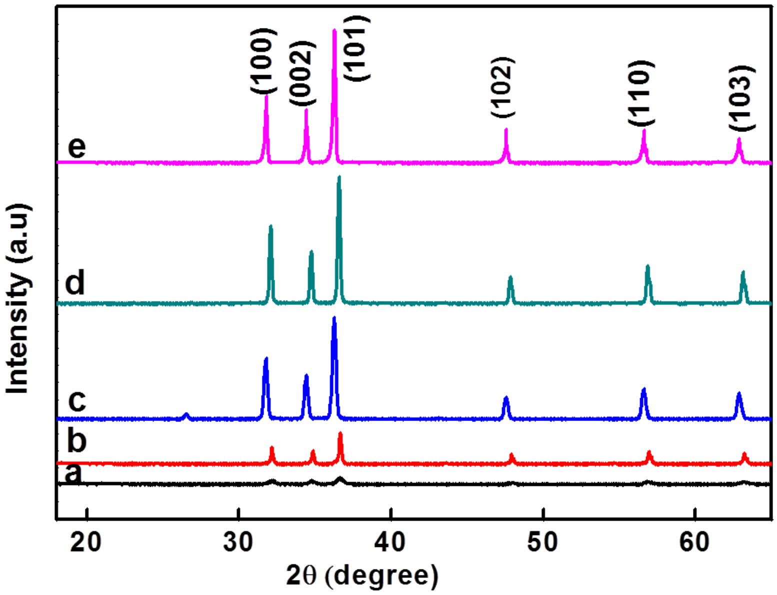

Figure 4.14: The XRD pattern of ZnO obtained at different MTO conditions (a) 450 W/15 min, (b) 600 W/10 min (c) 600 W/15 min, (d) 750 W/10 min and (e) 750 W/15 min.

The phase analysis of the completely oxidized Zn dust after mechanical activation (72 h milling) by MTO ((a), (b, (c), (d) and (e) of 450 W/15 min, 600 W/10 min, 600 W/15,750 W/10 min and 750 W/15 min respectively) are shown in Figure 4.14. The XRD spectra of these samples confirmed the presence of phase pure hexagonal wurtzite ZnO and no peaks are there corresponding to any sort of impurity phases, indicating a complete oxidation of Zn dust to nano crystalline ZnO at given conditions.

Table 4.5: Lattice parameters obtained at different MTO conditions.

Samples	Processing conditions	Lattice parameter a = b (Å)	Lattice parameter c (Å)
a	Microwave assisted oxidation (750 W/15 min)	3.21	5.24
b	Microwave assisted oxidation (750 W/10 min)	3.24	5.29

In MTO, it is noteworthy to mention that the complete oxidation of mechanically activated Zn is achieved within 15 min reaction time which reveals the competitiveness of the process in terms of speed and energy consumption. The crystalline quality of the nano ZnO obtained *via* MTO is not affected by rapid heating that occurs in microwave fields, which is confirmed from the lattice parameters of ZnO obtained. The typical lattice parameter values of ZnO are, a = 3.24 Å and c = 5.21 Å respectively [52]. Table 4.5 lists the lattice parameter values of the nano ZnO processed *via* MTO route. These values of ZnO well-matched with the standard values a = 3.24 Å and c = 5.21 Å indicating the advantage of the current processing technique. Thus the Zn dust derived nano ZnO possess wurtzite crystal structure and hexagonal unit cells with c/a = 1.633 [76]. The increase in the power and time of microwave irradiation further enhances the crystalline nature of the nano ZnO compared to CTO route which is confirmed from the XRD analysis.

Figure 4.15 shows the SEM microstructures of nano ZnO obtained from MTO techniques at different microwave power and irradiation time. ZnO prepared *via* MTO route at microwave power 600 W for 15 min showed nano-rod morphology where the diameter varies in the sub-micron scale and the length in micrometer range as evident from Figure 4.15 (a). At microwave heating condition of 750 W for 10 min the obtained ZnO showed tetrapod morphology with leg diameter 250 nm and length in sub-micron scale as seen from Figure 4.15 (b). Finally at microwave power of 750 W for 15 min irradiation the ZnO obtained showed multipod morphology with leg diameter 200 nm (Figure 4.15 (c)).

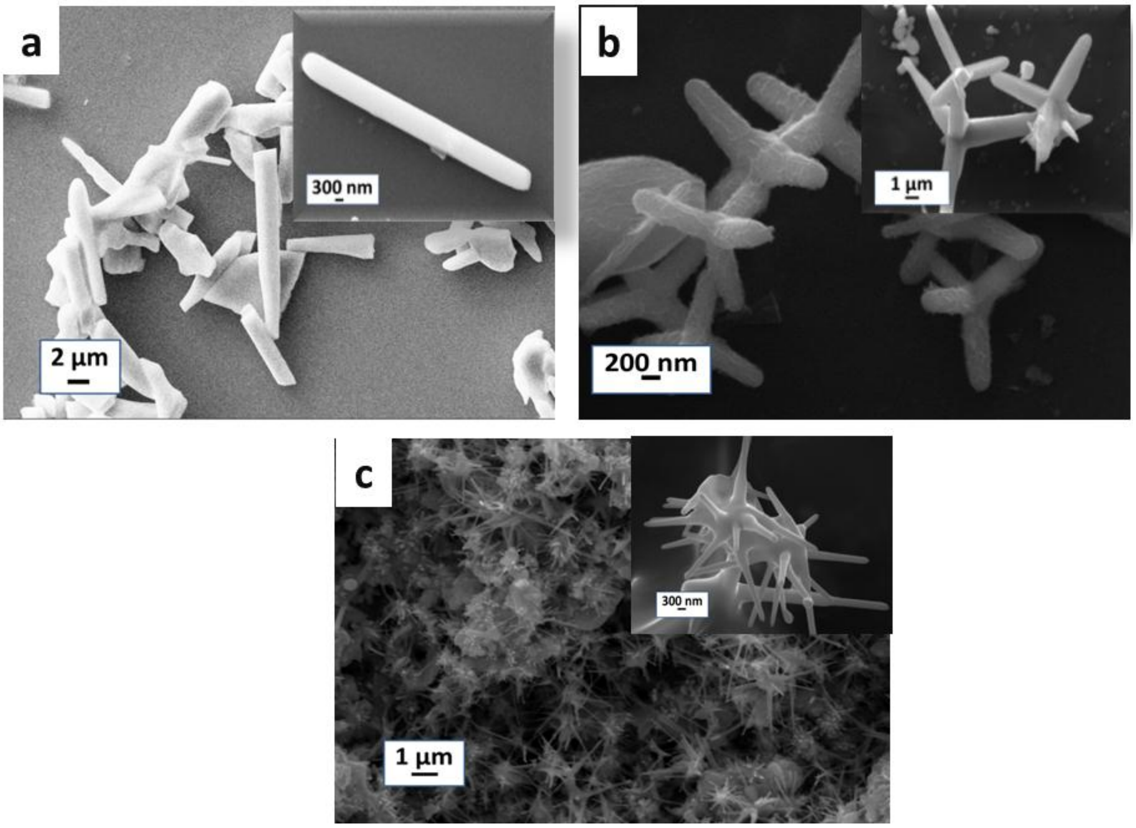

Figure 4.15: The SEM images of nano ZnO obtained *via* MTO at (a) 600 W/15 min, (b) 750 W/10 min and (c) 750 W/15 min.

The TEM images of product obtained at different heating conditions in MTO (Figure 4.16 (a-c)) also confirms the observation from SEM analysis. This morphological variation and evolution of single morphology of nano *Z*nO at a particular reaction condition v*ia* MTO route resulted from the rapid seed-assisted nucleation and growth under microwave irradiation. The reduction in surface energy due to the action of microwave energy on the bulk Zn caused unidirectional as well as multi directional growth [77] and leads to the formation of highly crystalline nano-structures, like nano rods, tetrapods and multipods in the present case. Compared to the CTO, the reversible homogeneous temperature gradients and fast build-up of heat in MTO cause directionally uniform growth of the nano ZnO morphologies at a particular experimental condition.

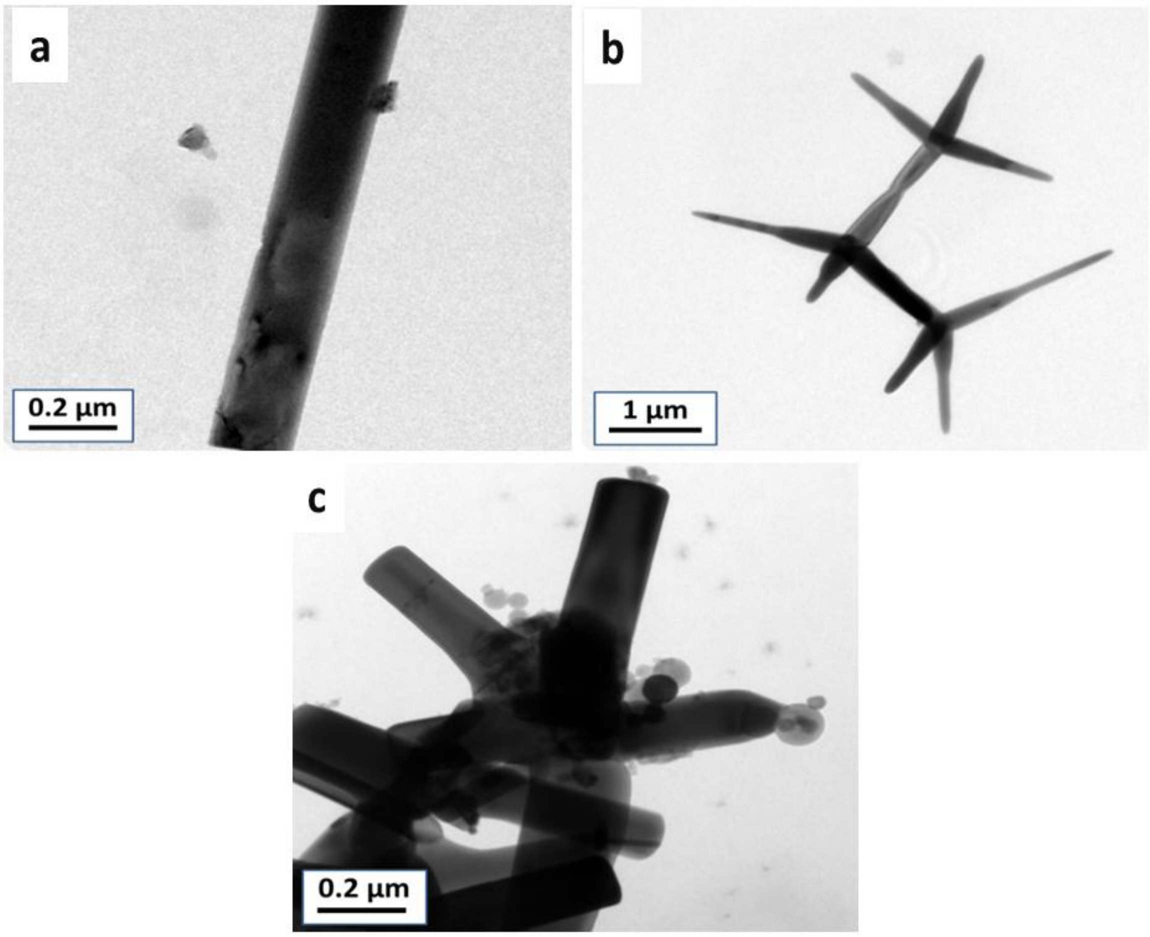

Figure 4.16: The TEM images of nano ZnO obtained via MTO at (a) 600 W/15 min, (b) 750 W/10 min and (c) 750 W/15 min.

4.2.5 Conclusions

Synthesis of nano ZnO through MTO was optimized and complete conversion of Zn dust into nano ZnO is accomplished within 15 min reaction time, under microwave heating. Further in the oxidation part, it can be seen that the microwave assisted oxidation shows significant advancement in the particle morphology. In microwave route, at a particular experimental condition the product showed single morphology compared to assorted morphology in CTO. The evolution of ZnO nanorods, tetrapod and multipod were observed *via* microwave assisted thermal oxidation conditions of 600 W/15 min, 750 W/10 min and 750 W/15 min respectively. The directionally uniform growth of the nano

ZnO morphologies at given experimental conditions have resulted from the rapid heat build-up and existence of reversible temperature gradient. Thus the present study focused on developing a novel, cost effective, clean and catalyst free approach for synthesising ZnO nanostructures from raw Zn dust.

Comparative study of ZnO produced *via* Conventional thermal oxidation and microwave assisted thermal oxidation

Nano ZnO synthesis *via* both conventional thermal oxidation and microwave assisted route was optimized. In CTO the complete conversion of Zn to ZnO have been observed for milled Zn dust thermal oxidised at 800 ^{o} C/2 h. The sequential evolution of ZnO nanostructures from metallic Zn dust was studied from 700–1000 °C and the growth of assorted morphologies were observed at a particular experimental condition. The observed morphologies include nanowire, nano blade, tetrapod and multipod. In microwave assisted oxidation, complete conversion of Zn dust into nano ZnO is accomplished within 15 min reaction time. The microwave power varies in the range 450-750 W for 10-15 minutes. Compared to the assorted morphology for conventional thermal oxidation, the microwave assisted route showed single morphology at a particular experimental condition and ZnO rods, tetrapod and multipod can be successfully synthesized by the microwave assisted oxidation at conditions 600 W/15 min, 750 W/10 min and 750 W/15 min respectively of mechanically modified (ball-milled for 72 h) raw Zn dust.

4.3 NIR reflective and anti-corrosive Nano ZnO coatings:- Application study of CTO and MTO derived ZnO products

4.3.1 Abstract

Nano ZnO obtained *via* thermal oxidation of Zn dust through both CTO and MTO are systematically characterized and studied with the motive to design functional paints and coatings. A paint formulation was prepared by blending the as synthesized nano ZnO v*ia* both CTO and MTO with cashew nut shell liquid (CNSL), a natural organic resin and surface coatings were made over metal and glass substrates. Further the ZnO–CNSL coatings were studied for optical transparency, NIR reflectance, and hydrophobic characteristics. The effective corrosion resistance of the coatings has been validated with highly corrosive Mg- AZ31 alloy substrates which are a future vital material for automobile applications. The ZnO–CNSL coatings developed showed about 33% enhancement in NIR shielding and about 156% enhancement in corrosion resistance with respect to their uncoated counterparts. Thus the current study contributes a technologically competent product, nano ZnO derived from Zn dust *via* thermal oxidation for paint and coating industry.

4.3.2 Introduction

Surfaces are coated with paint in-order to protect them against chemical, mechanical and weather-related attacks [78]. To meet the ever-growing demands on modern coatings, the paint industry steadily strives to enhance their products properties. Out of various attempts, introduction of nano particles into paint formulation enhances the efficiency and provide new functionalities to coatings [79]. Nano additives including alumina [80], zinc oxide [81], iron oxide [82], titania [83] and silica [84] offer superior technical characteristics to solvent borne and waterborne coatings. Being inorganic those particulate remains stable and non-migratory within the applied coating media and potentially supply enhanced durability and integrity to coatings. Among the various nano particulates nano ZnO offers better UV resistance, corrosion protection and antimicrobial protection for the coatings developed [85, 86].

Typically a coating formulation contains a resin, pigment and other optional additives [87]. Until now various resins derived from petroleum based stocks have been explored in coating industry *viz*, alkyd, epoxy, polyurethane, acrylic, phenolic, silicate and polyester [88]. But their uses are overshadowed by ecological and economical aspects such as high depletion rate, health hazards, toxicity and high cost [89]. Considering the above mentioned issues of new generation coating industry, the maximum utilization of naturally occurring bio-based materials are encouraged [88, 89]. Until now a number of bio-based materials like starch, cellulose, sugar, sucrose, plant and animal oils, lignin *etc.* have been explored in the coating industry [90].

Development of new products from renewable resources has received much attention in the current industrial community due to concerns over depletion of fossil resources and environmental issues [89]. Among various renewable resources reported, cardanol is a kind of easily available, widely used and inexpensive agricultural by-product extracted from cashew nut shell liquid [88, 91]. With the highly reactive phenolic hydroxyl group and unsaturated long alkyl chain, cardanol is considered as a flexible platform for various chemical modifications [92]. CNSL and its derivatives have been widely studied in various fields including bio composites, coatings, antioxidants and curing agents [91, 94, 95].

CNSL is a by-product of cashew nut industry. Cashew nut shell liquid (CNSL) - a cheaply available organic base, is an effective substitute for petroleum derived material due to its reactive functionalities, cost effectiveness, availability and sustainability. It is a naturally available substituted phenol which can undergo various chemical reactions. It enjoys considerable cost benefits and renewability which can replace petroleum products with equivalent or better results. The use of renewable natural sources has become an interesting area of research, especially when the purpose is to recycle the huge amount of agro-industrial wastes like CNSL, through environmentally sustainable routes. In nature, CNSL occurs in the soft honeycomb of cashew nut as a greenish-yellow viscous liquid. Phenolic compounds with long-chain substitution at the meta position are the main constituents of CNSL. CNSL consist of approximately 70 % anacardic acid, 18 % cardol, and 5% cardanol, with the remainder being less polar substances and other phenols [96].

The present section describes the industrial applications of nano ZnO derived from mechanically activated Zn *via* thermal oxidation (both MTO and CTO) for multifunctional paint coatings with NIR reflectance and corrosion resistance. In the current study CNSL was selected as a paint medium. Paint formulation was made by blending nano ZnO in CNSL medium. The enhanced NIR reflectance and anti-corrosion properties imparted by nano ZnO dispersed in CNSL were investigated with the motive to fabricate low cost high performance coatings for various functional applications.

4.3.3 Experimental Section

4.3.3.1 Materials and Methods

Cashew Nut Shell Liquid (CNSL, Vijayalaxmi Cashew company Pvt. Ltd., Kerala), a cheaply and widely available organic base was selected as the medium for paint formulation. The synthesized nano ZnO *via* thermal oxidation (both CTO and MTO route) was uniformly dispersed in CNSL using ultrasonication and mechanical stirring. The loading of ZnO was varied as 5 and 10 wt %. Another variant for this study is the type of ZnO used *i.e.*, commercial ZnO, ZnO obtained *via* conventional thermal oxidation

(ZnO-CTO) and ZnO obtained *via* microwave assisted thermal oxidation (ZnO-MTO). The paint formulation formed was then coated on glass substrates using a computer controlled dip-coating technique (KSV instruments, Netherlands) and on the surface AZ31 Mg alloy using brush.

The as cast Mg AZ31alloy was used for corrosion testing. The samples for testing were machined to cylindrical blocks (4 mm D×1mm H). The face of cylindrical block to be coated was polished with emery paper (#1600) and polished surface was further cleaned and degreased using acetone and ethanol respectively.

4.3.4 Result and Discussion

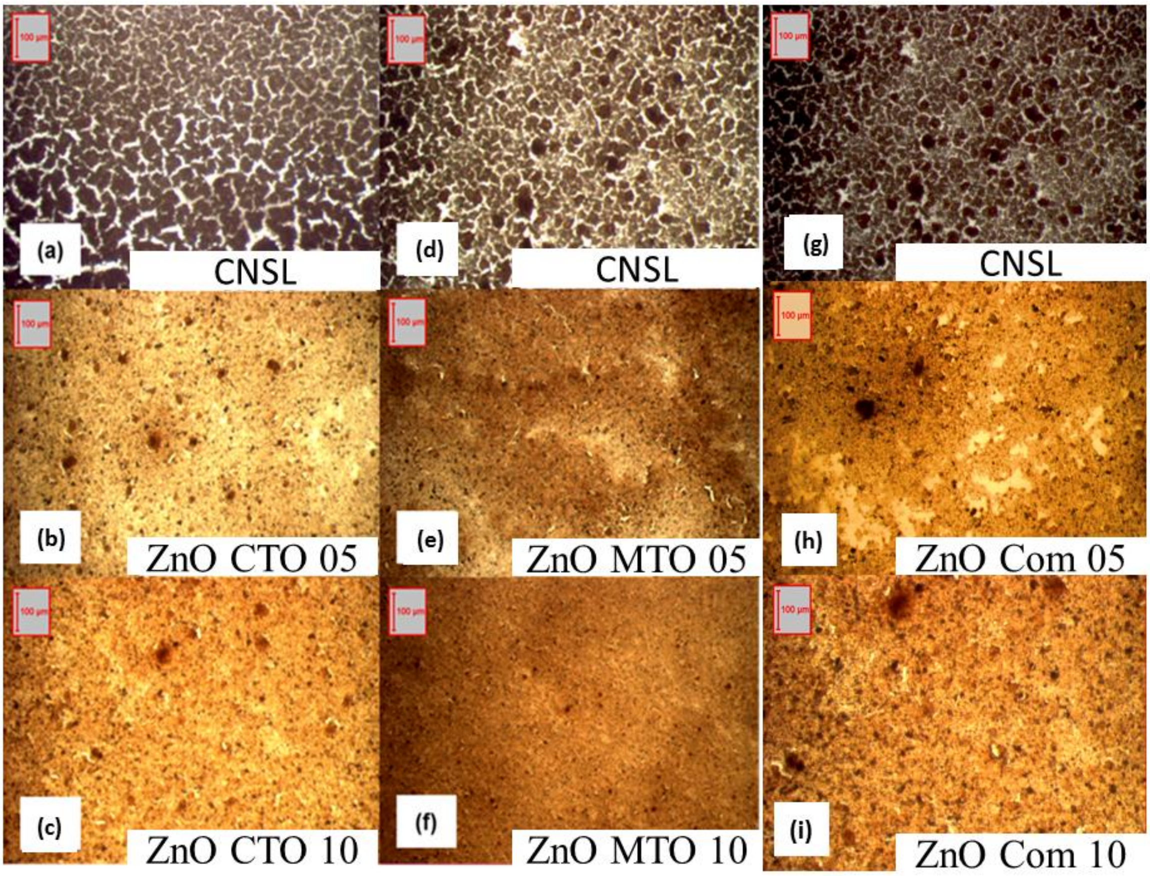

Figure 4.17: Optical images of ZnO-CNSL coatings made over glass. (a), (d) and (g) pure CNSL, (b), (e) and (h) CNSL with 5 wt % CTO, MTO and commercial ZnO respectively and (c), (f) and (i) CNSL with 10 wt % CTO, MTO and commercial ZnO respectively.

The applicability of ZnO nanoparticles derived from Zn dust for producing multifunctional coatings were tested. Blends for coating were prepared with CNSL resin as the matrix (medium of coating) and Zn dust derived nano ZnO powder as the filler (pigment for coating).

The optical examination of the coatings loaded with 5 and 10 wt % of ZnO obtained *via* thermal oxidation (both CTO and MTO) and from commercial source was done for the identification of microstructural defects and the results are presented in Figure 4.17 (a)-(i).

The surface texture obtained *via* optical imaging of the neat CNSL coating was compared with the CNSL base loaded with nano ZnO synthesized *via* CTO and MTO routes. It is clearly seen from the optical images that for pure CNSL coatings, many deep level drying-cracks are present and possible detachment of the coating layer from the substrate was observed (Figure 4.17 (a), (d) and (g)). However, the optical images well conveyed that the addition of nano ZnO into CNSL base has visibly reduced this problem and has formed uniform coatings with less cracks. It is also presumed from the optical images that with ZnO loading the problem of detachment of coating from the substrate has been reduced (Figure 4.17 (b), (e), (h), (c), (f) and (i)). For all samples coating quality is found to be increasing with increase in loading. The coating of CNSL base loaded nano ZnO synthesized through MTO, ZnO (MTO) 10 (Figure 4.17(f)) has formed the best coating. This might be contributed by the typical morphology of the ZnO which roots an effective knitting effect producing excellent and crack free coatings, when compared to the coatings of CNSL and CNSL incorporated with ZnO prepared through CTO (Figure 4. 17 (c)). Thus for further application studies the percentage of loading of synthesized ZnO for coatings was fixed as 10 wt%.

The brown tinted transparent coating of CNSL loaded with different ZnO is shown in Figure 4.18 (a). The XRD analysis (Figure 4.18 (b)) of the coatings obtained confirmed the amorphous characteristics of CNSL resin. When CNSL base was loaded with nano ZnO, the coatings showed the characteristic crystalline peaks of ZnO. The peaks corresponding to (100), (002), (101), (102), (110), (103), (112) and (201) planes well matched with JCPDS file of hexagonal wurtzite ZnO (JCPDS file no. 36-1451). It is also clearly seen that the XRD peaks are more prominent in the case of coatings having ZnO (MTO) 10 compared to those with ZnO (CTO) 10 and ZnO (Com) 10. This can be attributed to the better crystalline purity of ZnO obtained *via* MTO route [97].

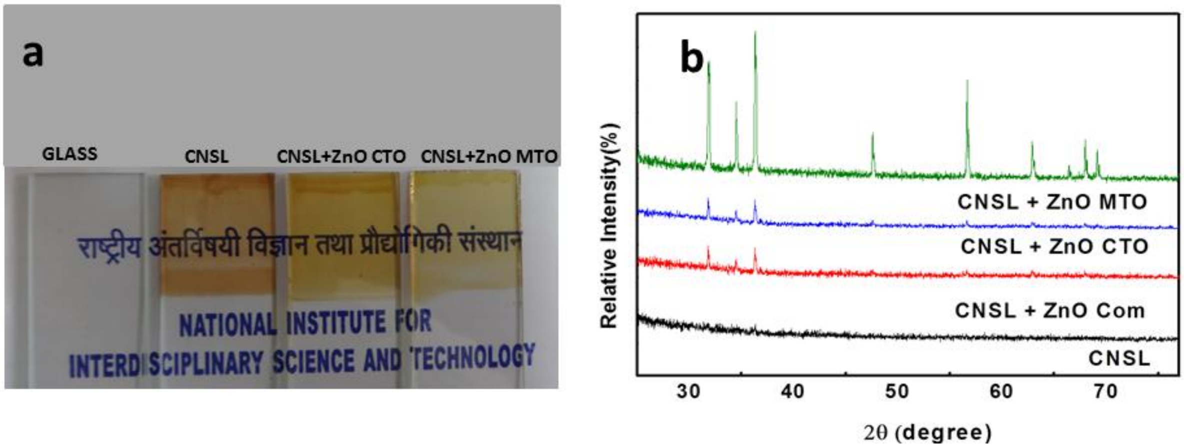

Figure 4.18. (a) Brown tinted transparent CNSL-ZnO coating obtained on glass plate and (b) XRD analysis of CNSL-ZnO coating.

For the CNSL and CNSL + ZnO coatings the water contact angle measured was compared with the uncoated surface. The Contact Angle measurements of the coatings was done by using a Tensiometer (Dataphysics-DCAT 11, Germany) *via* 'Wilhelmy balance method'. The coated surfaces found to have significant hydrophobic characteristics. For bare glass the contact angle value obtained was 34^{o}, showing the highly hydrophilic nature of the glass surface. When the glass is coated with CNSL resin, the contact angle has been increased to 91°, indicating the significant hydrophobic character imparted by the cardonol present in CNSL. It is already reported that chemically unmodified cardonol inherently possess long-hydrophobic hydrocarbon chains with a slightly polar phenolic ring, and hence offering good water repellent nature [98]. As evidenced in the optical images, during drying crack growth in pure CNSL based coatings increases the roughness of the coated surface, which leads to the reduction in its water repellent characteristics [99]. However, as the coating still maintains its hydrophobicity and the effect of drying cracks seems to be negligible.

Marginal drop in the contact angle values was observed as 78 °, 86 ° and 85 ° for MTO, CTO and commercial derived ZnO with the addition of ZnO into the CNSL matrix, , respectively. The nanostructured ZnO is known to possess high hydrophilic character in the absence of any surface modifying agents such as silane, [100]. Also, with filler addition the number of reactive hydrophobic groups in the CNSL base gets reduced [98]. These two factors together contribute to an insignificant reduction in the contact angle values for ZnO loaded CNSL coatings. However, even if all the factors affect the contact angle value, the change in the contact angle value is not much significant, and still the coatings retains its hydrophobic character with ZnO loading.

To investigate the effect of various morphology of ZnO on hydrophobic nature of coatings, the contact angle measurement of coating incorporated with ZnO obtained *via* MTO of Zn at different MW power was conducted. It is observed that when the morphology changed from rod —› tetrapod —› multipod with change in microwave power and irradiation time, the contact angle increased from 76—›82—›86 respectively.

4.3.4.1 IR Shielding Characteristics

Around 52% of ultraviolet radiation received by the earth surface is in the near infrared region (700–2300 nm) of the electromagnetic spectrum [101]. Absorption of radiation in this wavelength range will eventually result in heat gain in many materials. To reduce the absorption of these radiations NIR reflective colorants are used [102]. Bulk ZnO is known to have NIR reflection property [103]. Herein the NIR shielding characteristics of ZnO synthesised *via* thermal oxidation dispersed in CNSL medium was checked. The NIR reflectance of Zn dust derived ZnO dispersed in CNSL and coated on glass substrate are presented in Figure 4.20 (a). From Figure 4.19 (a) it is evident that the CNSL and CNSL + ZnO coatings developed showed good optical transparency with the possibility for getting transparent brown tinted functional coatings.

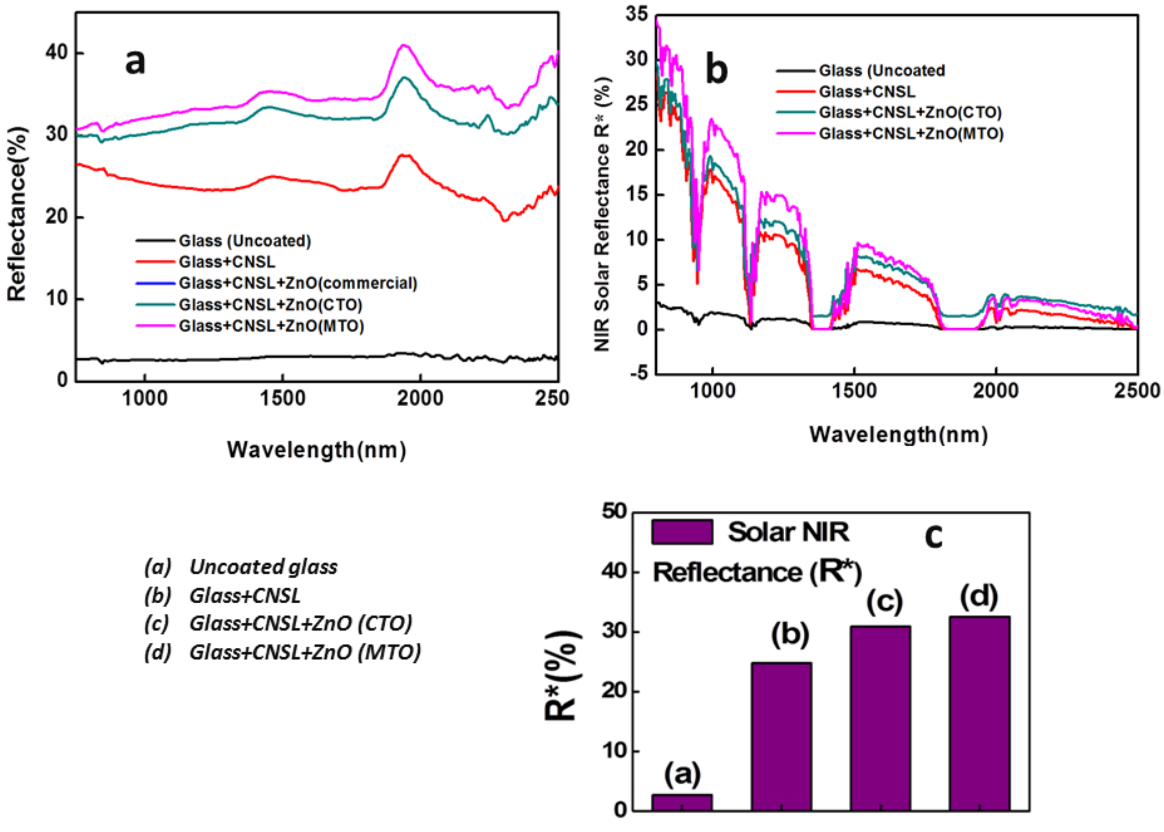

Figure 4.19: (a) NIR reflectance spectra of different coatings made, (b) NIR solar reflectance (R*) of different coatings made on glass and (c) the bar chart showing R* value of different coatings.

The efficiency of NIR reflectance of these CNSL based transparent ZnO coatings were evaluated and compared with uncoated glass surfaces and pure CNSL coatings. The

NIR reflectance properties of CNSL coatings prepared with and without the addition of nano ZnO is shown in Figure 4.19 (a). From the data obtained bare glass showed poor NIR reflectance (below 3 %) but when it was applied with CNSL coatings, it gained significant NIR reflecting property. The CNSL coatings containing nano ZnO resulted in about 35% enhancements in NIR reflectance. It also has to be noted that, among the different samples prepared, the CNSL coatings incorporated with MTO derived nano ZnO has showed better NIR reflecting characteristics. The Solar NIR reflectance of coatings is also improved (Figure 4.19 (b, c)) with the incorporation of the as-synthesized nano ZnO in the organic base CNSL.

To investigate the effect of morphology of ZnO synthesised *via* MTO on NIR reflectance the above process is repeated with ZnO obtained *via* MTO at different power and time. It is observed that NIR reflectance found to be increasing 35-32-30 % with change in morphology to rod⟶ tetrapod ⟶ multipod. Compared to other CNSL coating loaded with ZnO, CNSL MW 600 (10) and CNSL MW 750 (15), CNSL MW 750 (10) showed less NIR reflectance. This can be explained as follows. The decreased reflectance property of nano ZnO (MTO) loaded CNSL was related to size and shape of nano ZnO. Only ZnO in the whisker family shows a special tetrapod shape and single crystalline property. In a study Wu *et al.* reported that in the wavelength range 800 to 2525 nm, compared to nanoparticles the nanowhiskers reflected less infrared light. The dependence of the infrared light absorption on the morphology of nanoparticle was attributed to the surface effects and lattice distortion. The coefficient of absorption of the nanowhiskers is proportional to the imaginary number of the dielectric function, which has dependence on lattice distortion of nanoparticle [104]. The feet of the nanowhiskers possessed a constant surface tension, but moving towards the tip the diameter of the leg got smaller and smaller. The surface tension caused increased stress towards the pinpoint, which leads to lattice distortion along the leg. Because of the varying degree of lattice distortion at different parts of the legs, the imaginary number increased to a higher value over a wide range wavelength of light. Therefore, the nanowhiskers intensely absorbed more infrared light compared to the nanoparticles. Along with this, surface states also have been identified as another possible reason for the increased light-absorption by the ZnO Nano whiskers [104].

4.3.4.2 Corrosion Resistance Study

The electro chemical corrosion resistance of CNSL coatings incorporated with nano ZnO dispersed were evaluated by coating it on AZ31 Mg alloy which is susceptible to corrosion. Potentiodynamic polarisation curves for different CNSL coating were plotted after immersing in NaCl solution (3.5 %) at room temperature conditions.

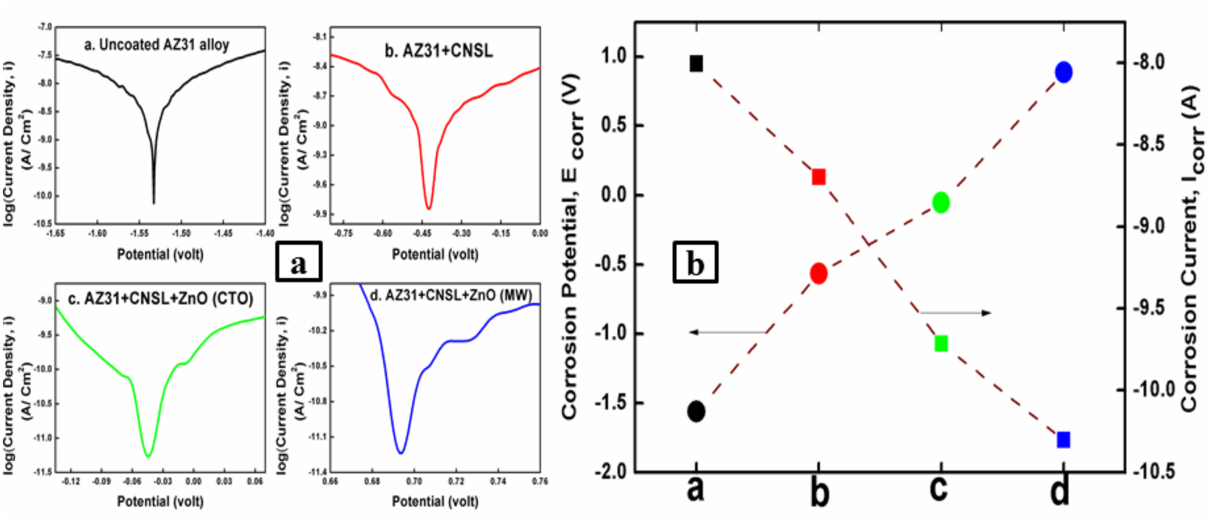

Figure 4.20: Tafel Plots of the different coatings made over Mg- AZ31 alloy. (b) Variation of the Corrosion Potential (E_{corr}) and Corrosion Current (I_{corr}) for the different coatings.

Figure 4.20 (a) shows the respective Tafel plots of the bare surface and surface coated with CNSL and nano ZnO dispersed CNSL (10 wt %). The corrosion parameters of coated alloy, corrosion potential (E_{corr}), corrosion current (I_{corr}) and corrosion rate (CR) were evaluated from the obtained polarization curves/Tafel curves and is represented in Figure 4.20 (b) [105]. The calculation of corrosion current from the Tafel plot is illustrated with the help of Figure 4.21. To determine i_{corr}, a slope was drawn in the cathodic region at +100 mV from the meeting point of anodic and cathodic curves (E_{corr}) of the Tafel plot [105].The corrosion current of the point at which the horizontal line drawn from the E_{corr} intersect with the slope line was considered as i_{corr}.

The Mg alloy coated with both pure CNSL and nano ZnO dispersed CNSL showed significant enhancement in performance than the uncoated surface. It can be seen that there is a shift from the negative to the positive values for the corrosion potential (E_{corr}); indicating the improved corrosion resistance efficiency of the ZnO/CNSL coatings over the bare alloy.

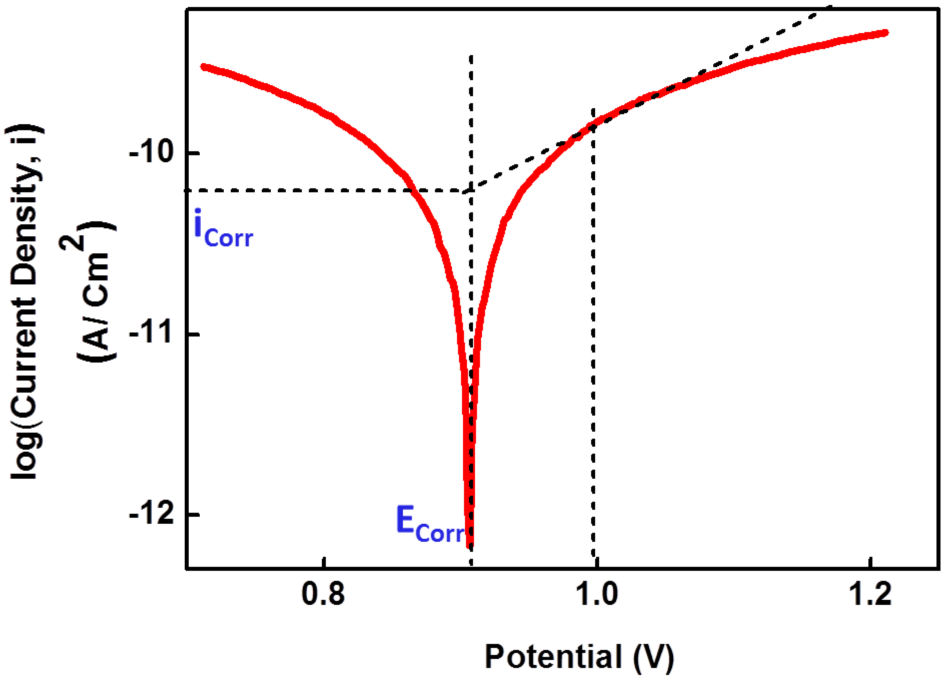

Figure 4.21: Illustration of calculation of corrosion current from Tafel plot.

The E_{corr} value increased from -1.56 V for bare alloy to -0.567—›-0.0553—› 0.887 for the surface coatings prepared with CNSL, CNSL + ZnO (CTO) 10 and CNSL + ZnO (MTO) 10. The phenolic character and the long alklyl side chain imparted corrosion resistance property to CNSL [50]. Moreover, the addition of nano ZnO (MTO) to CNSL base effectively by-passed the current conduction path. This is possible by the better knitting of the particles derived *via* MTO route when compared to its CTO counterpart. The reduction in the corrosion current (I_{corr}) value (as shown in Fig. 4.21 (b) also confirms the corrosion resistance imparted by ZnO/CNSL coatings. The corrosion current value obtained was -8.004 A for the bare alloy surface, for and for CNSL + ZnO (MW) 10 coated surface which gradually reduced to -10.3 A. Thus it can be concluded that, CNSL based coatings incorporated with nano ZnO are the potential candidates to develop an efficient protective outer crust for corrosion prone alloys.

4.3.5 Conclusions

A functional paint was prepared by dispersing nano ZnO obtained *via* thermal oxidation (both MTO and CTO) of mechanically activated Zn dust in naturally occurring organic resin CNSL. The coating developed on glass plate showed significant improvement in the NIR reflectance with the possibility of obtaining brown tinted transparent coating. For uncoated glass substrate a measured NIR reflectance value of <3 % is improved to 24 % for CNSL + ZnO (CTO) 10 coatings which was again enhanced to 33 % for CNSL + ZnO (MW) 10. The corrosion studies of the coating developed on Mg-AZ31 alloy were conducted *via* an electrochemical route and showed remarkable improvement in the corrosion resistance compared to bare alloy, which was imparted by the coatings on the bare Mg alloy. About 156 % improvement in the corrosion resistance was observed for alloy coated with CNSL + ZnO (MW) 10, compared to uncoated surface. Thus the present section opens up a new platform for developing ZnO-CNSL coatings with enhanced corrosion resistance and IR-shielding property.

References

[1] Vidor, F.F., Meyers, T. and Hilleringmann, U. Thorsten Meyers, and Ulrich Hilleringmann. "Inverter circuits using ZnO nanoparticle based thin-film transistors for flexible electronic applications." *Nanomaterials*6.9 (2016): 154.

[2] Subramanian, V., Bakhishev, T., Redinger, D. and Volkman, S.K. "Solution-processed zinc oxide transistors for low-cost electronics applications." *Journal of Display Technology* 5.12 (2009): 525-530.

[3] Pillai, S.C., Kelly, J.M., Ramesh, R. and McCormack, D.E. "Advances in the synthesis of ZnO nanomaterials for varistor devices." *Journal of Materials Chemistry C* 1.20 (2013): 3268-3281

[4] Song, W., Kwon, S.Y., Myung, S., Jung, M.W., Kim, S.J., Min, B.K., Kang, M.A., Kim, S.H., Lim, J. and An, K.S."High-mobility ambipolar ZnO-graphene hybrid thin film transistors." Scientific reports 4 (2014): 4064.

[5] Alivov, Y.I., Look, D.C., Ataev, B.M., Chukichev, M.V., Mamedov, V.V., Zinenko, V.I., gafonov, Y.A. and Pustovit, A.N. "Fabrication of ZnO-based metal–insulator–semiconductor diodes by ion implantation." Solid-State Electronics 48.12 (2004): 2343-2346.

[6] Hames, Y., Alpaslan, Z., Kösemen, A., San, S.E. and Yerli, Y. "Electrochemically grown ZnO nanorods for hybrid solar cell applications." *Solar Energy* 84.3 (2010): 426-431.

[7] Ko, S.H., Lee, D., Kang, H.W., Nam, K.H., Yeo, J.Y., Hong, S.J., Grigoropoulos, C.P. and Sung, H.J. "Nanoforest of hydrothermally grown hierarchical ZnO nanowires for a high efficiency dye-sensitized solar cell." *Nano letters* 11.2 (2011): 666-671.

[8] Wang, Z.A., Chu, J.B., Zhu, H.B., Sun, Z., Chen, Y.W. and Huang, S.M. "Growth of ZnO: Al films by RF sputtering at room temperature for solar cell applications." *Solid-State Electronics* 53.11 (2009): 1149-1153.

[9] Djurišić, A.B., Ng, A.M.C. and Chen, X.Y. "ZnO nanostructures for optoelectronics: material properties and device applications." Progress in quantum electronics 34.4 (2010): 191-259.

[10] Biasotto, G., Ranieri, M.G.A., Foschini, C.R., Simões, A.Z., Longo, E. and Zaghete, M.A, "Gas sensor applications of zinc oxide thin film grown by the polymeric precursor method." *Ceramics International* 40.9 (2014): 14991-14996.

[11] Dong, X., Cao, Y., Wang, J., Chan-Park, M.B., Wang, L., Huang, W. and Chen, P. "Hybrid structure of zinc oxide nanorods and three dimensional graphene foam for supercapacitor and electrochemical sensor applications." *RSC Advances* 2.10 (2012): 4364-4369.

[12] Zhang, Y., R Nayak, T., Hong, H. and Cai, W. "Biomedical applications of zinc oxide nanomaterials." *Current molecular medicine* 13.10 (2013): 1633-1645.

[13] Hanley, C., Layne, J., Punnoose, A., Reddy, K.M., Coombs, I., Coombs, A., Feris, K. and Wingett, D. "Preferential killing of cancer cells and activated human T cells using ZnO nanoparticles." *Nanotechnology* 19.29 (2008): 295103.

[14] Ristić, Mira, et al. "Sol–gel synthesis and characterization of nanocrystalline ZnO powders." Journal of Alloys and Compounds 397.1-2 (2005): L1-L4.

[15] Baruah, Sunandan, and Joydeep Dutta. "Hydrothermal growth of ZnO nanostructures." Science and Technology of Advanced Materials 10.1 (2009): 013001.

[16] Shi, Weidong, Shuyan Song, and Hongjie Zhang. "Hydrothermal synthetic strategies of inorganic semiconducting nanostructures." Chemical Society Reviews42.13 (2013): 5714-5743.

[17] Gusatti, M., do Rosário, J.D.A., de Campos, C.E.M., Kunhen, N.C., de Carvalho, E.U., Riella, H.G. and Bernardin, A.M. "Production and characterization of ZnO nanocrystals obtained by solochemical processing at different temperatures." *Journal of nanoscience and nanotechnology* 10.7 (2010): 4348-4351.

[18] Villanueva, Y.Y., Liu, D.R. and Cheng, P.T. "Pulsed laser deposition of zinc oxide." Thin Solid Films 501.1-2 (2006): 366-369.

[19] Sun, Y., Fuge, G.M. and Ashfold, M.N. "Growth of aligned ZnO nanorod arrays by catalyst-free pulsed laser deposition methods." *Chemical Physics Letters* 396.1-3 (2004): 21-26.

[20] Wu, J-J., and S-C. Liu. "Low-temperature growth of well-aligned ZnO nanorods by chemical vapor deposition." Advanced materials 14.3 (2002): 215-218.

[21] Chang, P.C., Fan, Z., Wang, D., Tseng, W.Y., Chiou, W.A., Hong, J. and Lu, J.G. "ZnO nanowires synthesized by vapor trapping CVD method." *Chemistry of materials* 16.24 (2004): 5133-5137.

[22] Fan, H.J., Lee, W., Hauschild, R., Alexe, M., Le Rhun, G., Scholz, R., Dadgar, A., Nielsch, K., Kalt, H., Krost, A. and Zacharias, M. "Template-Assisted Large-Scale Ordered Arrays of ZnO Pillars for Optical and Piezoelectric Applications." *Small* 2.4 (2006): 561-568.

[23] Xu, S., Wei, Y., Kirkham, M., Liu, J., Mai, W., Davidovic, D., Snyder, R.L. and Wang, Z.L. "Patterned growth of vertically aligned ZnO nanowire arrays on inorganic substrates at low temperature without catalyst." *Journal of the American Chemical Society*130.45 (2008): 14958-14959.

[24] Huang, M.H., Wu, Y., Feick, H., Tran, N., Weber, E. and Yang, P. "Catalytic growth of zinc oxide nanowires by vapor transport." *Advanced Materials* 13.2 (2001): 113-116.

[25] Yu, D., Trad, T., McLeskey, J.T., Craciun, V. and Taylor, C.R. "ZnO nanowires synthesized by vapor phase transport deposition on transparent oxide substrates." Nanoscale research letters 5.8 (2010): 1333.

[26] L Hu, H., Huang, X., Deng, C., Chen, X. and Qian, Y, "Hydrothermal synthesis of ZnO nanowires and nanobelts on a large scale." *Materials Chemistry and Physics* 106.1 (2007): 58-62

[27] Ma, X.Y. and Zhang, W.D. "Effects of flower-like ZnO nanowhiskers on the mechanical, thermal and antibacterial properties of waterborne polyurethane." *Polymer Degradation and Stability* 94.7 (2009): 1103-1109.

[28] Shi, X., Cao, M., Zhao, Y., Song, W. and Rong, J. "Preparation and properties of ZnO nano-whiskers." *Science in China Series E: Technological Sciences*51.9 (2008): 1433-1438.

[29] Suh, H.W., Kim, G.Y., Jung, Y.S., Choi, W.K. and Byun, D. "Growth and properties of ZnO nanoblade and nanoflower prepared by ultrasonic pyrolysis." *Journal of applied physics* 97.4 (2005): 044305.

[30] Singla, M.L. and Kumar, M. "Optical characterization of ZnO nanoparticles capped with various surfactants." *Journal of Luminescence* 129.5 (2009): 434-438.

[31] Sun, X.M., Chen, X., Deng, Z.X. and Li, Y.D, "A CTAB-assisted hydrothermal orientation growth of ZnO nanorods." *Materials Chemistry and Physics*78.1 (2003): 99-104.

[32] Balanand, S., Maria, M.J., Rajan, T.P.D., Mohamed, A.P. and Ananthakumar, S. "Bulk processing of ZnO nanostructures via microwave assisted oxidation of mechanically seeded Zn dust for functional paints and coatings." *Chemical Engineering Journal* 284 (2016): 657-667.

[33] Balanand, S., Babitha, K.B., Jeen Maria, M., Mohamed, A.A.P. and Ananthakumar, S. "Aqueous Mechanical Oxidation of Zn Dust: An Inventive Technique for Bulk Production of ZnO Nanorods." *ACS Sustainable Chemistry & Engineering* 6.1 (2017): 143-154.

[34] Wang, Z.H., Geng, D.Y., Han, Z. and Zhang, Z.D. "Characterization and optical properties of ZnO nanoparticles obtained by oxidation of Zn nanoparticles." *Materials Letters* 63.29 (2009): 2533-2535.

[35] Xu, C.H., Lui, H.F. and Surya, C. "Synthetics of ZnO nanostructures by thermal oxidation in water vapor containing environments." *Materials letters* 65.1 (2011): 27-30

[36] Yuan, L., Wang, C., Cai, R., Wang, Y. and Zhou, G. "Temperature-dependent growth mechanism and microstructure of ZnO nanostructures grown from the thermal oxidation of zinc." *Journal of Crystal Growth* 390 (2014): 101-108.

[37] Escobedo-Morales, A., Aranda-García, R.J., Chigo-Anota, E., Pérez-Centeno, A., Méndez-Blas, A. and Arana-Toro, C.G. "ZnO Micro-and Nanostructures Obtained by Thermal Oxidation: Microstructure, Morphogenesis, Optical, and Photoluminescence Properties." *Crystals* 6.10 (2016): 135.

[38] Wu, Z.W., Tyan, S.L., Chen, H.H., Wu, C.L., Lee, C.R. and Mo, T.S. "Photoluminescence and electrical properties of bidirectional ZnO nanowires on Zn foils *via* a thermal oxidation method." *RSC Advances* 7.10 (2017): 5807-5812.

[39] Zhao, C.X., Li, Y.F., Zhou, J., Li, L.Y., Deng, S.Z., Xu, N.S. and Chen, J. "Large-scale synthesis of bicrystalline ZnO nanowire arrays by thermal oxidation of zinc film: growth mechanism and high-performance field emission." *Crystal Growth & Design* 13.7 (2013): 2897-2905.

[40] Lu, H.B., Li, H., Liao, L., Tian, Y., Shuai, M., Li, J.C., Hu, M.F., Fu, Q. and Zhu, B.P. "Low-temperature synthesis and photocatalytic properties of ZnO nanotubes by thermal oxidation of Zn nanowires." *Nanotechnology* 19.4 (2008): 045605.

[41] Khan, A. and Kordesch, M.E. "Large-scale fabrication of metallic Zn nanowires by thermal evaporation." *Physica E: Low-dimensional Systems and Nanostructures*33.1 (2006): 88-91.

[42] Dang, H.Y., Wang, J. and Fan, S.S. "The synthesis of metal oxide nanowires by directly heating metal samples in appropriate oxygen atmospheres." Nanotechnology 14.7 (2003): 738.

[43] Suryanarayana, C. "Mechanical alloying and milling." *Progress in materials science* 46.1-2 (2001): 1-184.

[44] Xing, T., Sunarso, J., Yang, W., Yin, Y., Glushenkov, A.M., Li, L.H., Howlett, P.C. and Chen, Y. "Ball milling: a green mechanochemical approach for synthesis of nitrogen doped carbon nanoparticles." Nanoscale 5.17 (2013): 7970-7976.

[45] Li, X., Chen, Z., Chen, X., Zhang, Y. "Effects of mechanical activation methods on thermo-oxidation behaviors of pyrite." *Journal of Wuhan University of Technology-Mater. Sci. Ed.* 30.5 (2015): 974-980.

[46] Giri, P.K., Bhattacharyya, S., Singh, D.K., Kesavamoorthy, R., Panigrahi, B.K. and Nair, K.G.M. "Correlation between microstructure and optical properties of ZnO nanoparticles synthesized by ball milling." *Journal of Applied Physics* 102.9 (2007): 093515.

[47] Burmeister, C.F. and Kwade, A. "Process engineering with planetary ball mills." *Chemical Society Reviews* 42.18 (2013): 7660-7667.

[48] Yadav, T.P., Yadav, R.M. and Singh, D.P. "Mechanical milling: a top down approach for the synthesis of nanomaterials and nanocomposites." *Nanoscience and Nanotechnology* 2.3 (2012): 22-48

[49] Šepelák, V., Bégin-Colin, S. and Le Caër, G. "Transformations in oxides induced by high-energy ball-milling." *Dalton transactions* 41.39 (2012): 11927-11948.

[50] Hughes, G.M., Smith, G.E., Flewitt, P.E. and Crocker, A.G. "The brittle fracture of polycrystalline zinc." *Proceedings of the Royal Society of London A: Mathematical, Physical and Engineering Sciences*. Vol. 463. No. 2085. The Royal Society, 2007.

[51] Ma, X. and Zachariah, M.R. "Size-resolved kinetics of Zn nanocrystal hydrolysis for hydrogen generation." *international journal of hydrogen energy* 35.6 (2010): 2268-2277.

[52] Vinodkumar, R., Lethy, K.J., Arunkumar, P.R., Krishnan, R.R., Pillai, N.V., Pillai, V.M. and Philip, R. "Effect of cadmium oxide incorporation on the microstructural and optical properties of pulsed laser deposited nanostructured zinc oxide thin films." *Materials Chemistry and Physics* 121.3 (2010): 406-413.

[53] Zhou, H.F., Wang, H., Zhou, D., Pang, L.X. and Yao, X. "Effect of ZnO and B2O3 on the sintering temperature and microwave dielectric properties of LiNb0. 6Ti0. 5O3 ceramics." *Materials Chemistry and Physics* 109.2-3 (2008): 510-514.

[54] Choi, J., Ji, H., Tambunan, O.T., Hwang, I.S., Woo, H.S., Lee, J.H., Lee, B.W., Liu, C., Rhee, S.J., Jung, C.U. and Kim, G.T. "Brush-shaped ZnO heteronanorods

synthesized using thermal-assisted pulsed laser deposition." *ACS applied materials & interfaces* 3.12 (2011): 4682-4688.

[55] Podrezova, L.V., Porro, S., Cauda, V., Fontana, M. and Cicero, G. "Comparison between ZnO nanowires grown by chemical vapor deposition and hydrothermal synthesis." *Applied Physics A* 113.3 (2013): 623-632.

[56] Wang, Z.L. "Zinc oxide nanostructures: growth, properties and applications." *Journal of physics: condensed matter* 16.25 (2004): R829.

[57] Kong, X.Y. and Wang, Z.L. "Spontaneous polarization-induced nanohelixes, nanosprings, and nanorings of piezoelectric nanobelts." *Nano Letters* 3.12 (2003): 1625-1631.

[58] Padmanabhan, S.C., Ledwith, D., Pillai, S.C., McCormack, D.E. and Kelly, J.M. "Microwave-assisted synthesis of ZnO micro-javelins." *Journal of Materials Chemistry* 19.48 (2009): 9250-9259.

[59] Rečnik, A., Daneu, N. and Bernik, S. "Nucleation and growth of basal-plane inversion boundaries in ZnO." *Journal of the European Ceramic Society* 27.4 (2007): 1999-2008.

[60] Xu, S. and Wang, Z.L. "One-dimensional ZnO nanostructures: solution growth and functional properties." *Nano Research* 4.11 (2011): 1013-1098.

[61] Maciel, A.V., da Nova Mussel, W. and Pasa, V.M.D. "A novel synthesis of nanostructured ZnO via thermal oxidation of Zn nanowires obtained by a green route." *Materials Sciences and Applications* 1.05 (2010): 279.

[62] Zhu, Y.J. and Chen, F. "Microwave-assisted preparation of inorganic nanostructures in liquid phase." *Chemical reviews* 114.12 (2014): 6462-6555.

[63] Oghbaei, M. and Mirzaee, O. "Microwave versus conventional sintering: A review of fundamentals, advantages and applications." *Journal of Alloys and Compounds* 494.1-2 (2010): 175-189.

[64] Pickles, C.A. "Microwaves in extractive metallurgy: Part 2–A review of applications." Minerals Engineering 22.13 (2009): 1112-1118.

[65] Kang, M. and Kim, H.S. "Microwave-assisted facile and ultrafast growth of ZnO nanostructures and proposition of alternative microwave-assisted methods to address growth stoppage." *Scientific reports* 6 (2016): 24870.

[66] Krishnakumar, T., Jayaprakash, R., Pinna, N., Singh, V.N., Mehta, B.R. and Phani, A.R. "Microwave-assisted synthesis and characterization of flower shaped zinc oxide nanostructures." *Materials Letters* 63.2 (2009): 242-245.

[67] Agrawal, D. "Latest global developments in microwave materials processing." *Materials Research Innovations* 14.1 (2010): 3-8.

[68] Wu, L., Wu, Y. and Wei, L.Ü. "Preparation of ZnO Nanorods and optical characterizations." *Physica E: Low-dimensional Systems and Nanostructures* 28.1 (2005): 76-82.

[69] Wang, W.W., Zhu, Y.J. and Ruan, M.L. "Microwave-assisted synthesis and magnetic property of magnetite and hematite nanoparticles." *Journal of Nanoparticle Research* 9.3 (2007): 419-426.

[70] Mahmoud, M.M., Link, G. and Thumm, M. "The role of the native oxide shell on the microwave sintering of copper metal powder compacts." *Journal of Alloys and Compounds* 627 (2015): 231-237.

[71] Zou, X., Fan, H., Tian, Y., Zhang, M. and Yan, X. "Microwave-assisted hydrothermal synthesis of Cu/Cu_2O hollow spheres with enhanced photocatalytic and gas sensing activities at room temperature." *Dalton Transactions* 44.17 (2015): 7811-7821.

[72] Hu, X., Gong, J., Zhang, L. and Yu, J.C "Continuous Size Tuning of Monodisperse ZnO Colloidal Nanocrystal Clusters by a Microwave-Polyol Process and Their Application for Humidity Sensing." *Advanced Materials* 20.24 (2008): 4845-4850.

[73] Wu, D.S., Han, C.Y., Wang, S.Y., Wu, N.L. and Rusakova, I.A. "Microwave-assisted solution synthesis of SnO nanocrystallites." *Materials Letters* 53.3 (2002): 155-159.

[74] Phuruangrat, A., Thongtem, T. and Thongtem, S. "Microwave-assisted synthesis of ZnO nanostructure flowers." *Materials Letters* 63.13-14 (2009): 1224-1226.

[75] Fan, Y., Yang, H., Li, M. and Zou, G. "Evaluation of the microwave absorption property of flake graphite." *Materials Chemistry and Physics*115.2-3 (2009): 696-698.

[76] Morkoç, H. and Özgür, Ü. *Zinc oxide: fundamentals, materials and device technology*. John Wiley & Sons, 2008.

[77] Zhang, L. and Zhu, Y.J. "ZnO micro-and nano-structures: microwave-assisted solvothermal synthesis, morphology control and photocatalytic properties." *Applied Physics A* 97.4 (2009): 847.

[78] Dhoke, S.K., Khanna, A.S. and Sinha, T.J.M. "Effect of nano-ZnO particles on the corrosion behavior of alkyd-based waterborne coatings." *Progress in Organic Coatings* 64.4 (2009): 371-382.

[79] Dhoke, S.K. and Khanna, A.S. "Effect of nano-F_e2O_3 particles on the corrosion behavior of alkyd based waterborne coatings." *Corrosion Science* 51.1 (2009): 6-20.

[80] Brickweg, L.J., Floryancic, B.R., Sapper, E.D. and Fernando, R.H. "Shear-induced 1-D alignment of alumina nanoparticles in coatings." *Journal of Coatings Technology and Research* 4.1 (2007): 107-110.

[81] Rashvand, M. and Ranjbar, Z. "Effect of nano-ZnO particles on the corrosion resistance of polyurethane-based waterborne coatings immersed in sodium chloride solution via EIS technique." Progress in Organic Coatings 76.10 (2013): 1413-1417.

[82] Wang, Q., Jang, M. and Chen, Y.F. "Effects of nanosized iron oxide with different morphology on nanomechanical properties of nanocomposite coating." Key Engineering Materials. Vol. 336. Trans Tech Publications, 2007.

[83] Allen, N.S., Edge, M., Ortega, A., Sandoval, G., Liauw, C.M., Verran, J., Stratton, J. and McIntyre, R.B. "Degradation and stabilisation of polymers and coatings: nano versus pigmentary titania particles." Polymer degradation and stability 85.3 (2004): 927-946.

[84] Zhou, S., Wu, L., Sun, J. and Shen, W. "The change of the properties of acrylic-based polyurethane via addition of nano-silica." *Progress in Organic Coatings* 45.1 (2002): 33-42.

[85] Soumya, S., Kumar, S.N., Mohamed, A.P. and Ananthakumar, S. "Silanated nano ZnO hybrid embedded PMMA polymer coatings on cotton fabrics for near-IR reflective, antifungal cool-textiles." New Journal of Chemistry 40.8 (2016): 7210-7221.

[86] Soumya, S., Mohamed, A.P., Mohan, K. and Ananthakumar, S. "Enhanced near-infrared reflectance and functional characteristics of Al-doped ZnO nano-pigments embedded PMMA coatings." *Solar Energy Materials and Solar Cells* 143 (2015): 335-346.

[87] Yong, H.E., Krishnamoorthy, K., Hyun, K.T. and Kim, S.J. "Preparation of ZnO nanopaint for marine antifouling applications." *Journal of Industrial and Engineering Chemistry* 29 (2015): 39-42.

[88] Balgude, D. and Sabnis, A.S. "CNSL: an environment friendly alternative for the modern coating industry." *Journal of Coatings Technology and Research* 11.2 (2014): 169-183.

[89] Kathalewar, M. and Sabnis, A. "Epoxy resin from cardanol as partial replacement of bisphenol-A-based epoxy for coating application." *Journal of Coatings Technology and Research* 11.4 (2014): 601-618.

[90] Balgude, D., Konge, K. and Sabnis, A. "Synthesis and characterization of sol–gel derived CNSL based hybrid anti-corrosive coatings." *Journal of sol-gel science and technology* 69.1 (2014): 155-165.

[91] Kathalewar, M., Sabnis, A. and D'Melo, D. "Polyurethane coatings prepared from CNSL based polyols: Synthesis, characterization and properties." *Progress in Organic Coatings* 77.3 (2014): 616-626.

[92] Lubi, M.C. and Thachil, E.T. "Cashew nut shell liquid (CNSL)-a versatile monomer for polymer synthesis." *Designed Monomers and polymers* 3.2 (2000): 123-153.

[93] NAYAK, P.L. "Natural oil-based polymers: opportunities and challenges." *Journal of Macromolecular Science, Part C: Polymer Reviews* 40.1 (2000): 1-21.

[94] Wang, X., Zhou, S., Guo, W.W., Wang, P.L., Xing, W., Song, L. and Hu, Y. "Renewable cardanol-based phosphate as a flame retardant toughening agent for epoxy resins." *ACS Sustainable Chemistry & Engineering* 5.4 (2017): 3409-3416.

[95] dos Santos, T.D.J.A., Araújo, B.Q., Citó, A.M.D.G.L., da Silva, J., Saffi, J., Richter, M.F. and Ferraz, A.D.B.F. "Antioxidant properties and chemical composition of technical Cashew Nut Shell Liquid (tCNSL)." *Food Chemistry* 126.3 (2011): 1044-1048.

[96] Tyman, J.H.P., Wilczynski, D. and Kashani, M.A., 1978, "Compositional studies on technical cashew nutshell liquid (CNSL) by chromatography and mass spectroscopy." *Journal of the American Oil Chemists' Society* 55.9 (1978): 663-668.

[97] Liang, H.Q., Pan, L.Z. and Liu, Z.J. "Synthesis and photoluminescence properties of ZnO nanowires and nanorods by thermal oxidation of Zn precursors." *Materials Letters* 62.12-13 (2008): 1797-1800.

[98] Balachandran, V.S., Jadhav, S.R., Vemula, P.K. and John, G. Balachandran, Vijai Shankar, et al. "Recent advances in cardanol chemistry in a nutshell: from a nut to nanomaterials." *Chemical Society Reviews* 42.2 (2013): 427-438.

[99] Zhao, M.H., Chen, X.P. and Wang, Q. "Wetting failure of hydrophilic surfaces promoted by surface roughness." *Scientific reports* 4 (2014): 5376.

[100] Moezzi, A., McDonagh, A.M. and Cortie, M.B. "Zinc oxide particles: Synthesis, properties and applications." *Chemical engineering journal* 185 (2012): 1-22.

[101] Viswanathan, B. *Energy sources: fundamentals of chemical conversion processes and applications*. Newnes, 2016.

[102] Soumya, S., Mohamed, A.P., Paul, L., Mohan, K. and Ananthakumar, "Near IR reflectance characteristics of PMMA/ZnO nanocomposites for solar thermal control interface films." Solar Energy Materials and Solar Cells 125 (2014): 102-112.

[103] Soumya, S., Kumar, S.N., Mohamed, A.P. and Ananthakumar, S. "Silanated nano ZnO hybrid embedded PMMA polymer coatings on cotton fabrics for near-IR reflective, antifungal cool-textiles." New Journal of Chemistry 40.8 (2016): 7210-7221.

[104] Wu, R. and Xie, C. "Formation of tetrapod ZnO nanowhiskers and its optical properties." *Materials Research Bulletin* 39.4-5 (2004): 637-645.

[105] Jayaraj, J., Raj, S.A., Srinivasan, A., Ananthakumar, S., Pillai, U.T.S., Dhaipule, N.G.K. and Mudali, U.K. "Composite magnesium phosphate coatings for improved corrosion resistance of magnesium AZ31 alloy." *Corrosion Science* 113 (2016): 104-11.

CHAPTER 5

Design of Zn/ZnO Cermet Fillers from Zn-dust: A Metal/Semiconductor Interface Effect on Epoxy Composites for Thermally Conducting High-*k* Dielectrics

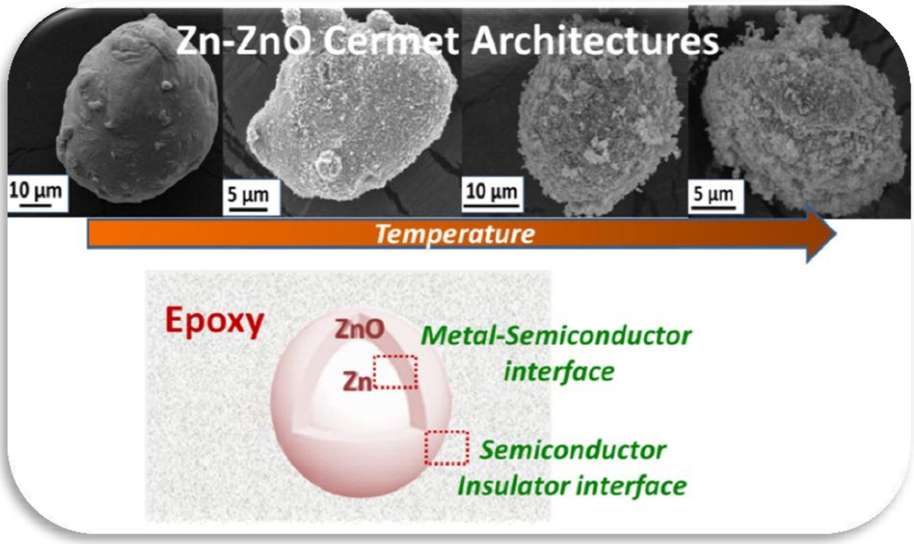

Chapter 5 is devoted to describe the fabrication of a new type of Functional filler Zn/ZnO cermet architecture for thermally conducting high-k epoxy dielectrics. Zn/ZnO metal-semiconductor cermet particles were designed via simple heat treatment of raw Zn dust under air. The obtained Zn/ZnO cermet particles were incorporated into epoxy polymer to enhance the dielectric properties and thermal conductivity of pure epoxy via interface design. The enhanced dielectric property of epoxy-cermet composite is attributed to the duplex interfacial polarization induced in epoxy matrix by cermet particle.

Design of Zn/ZnO Cermet Fillers from Zn-dust: A Metal/ Semiconductor Interface Effect on Epoxy Composites for Thermally Conducting High-*k* Dielectrics

5.1 Abstract

The fabrication of Zn/ZnO metal-semiconductor cermet architecture *via* a simple heat treatment of raw Zn dust was investigated at different calcination temperature and time under air atmosphere. Raw Zn dust was calcined in the temperature range 450-600 ^{o}C for 1-3 h. The obtained Zn/ZnO cermet particles were incorporated into epoxy matrix to obtain high dielectric permittivity materials with enhanced thermal conductivity *via* interface design. The effect of ceramic-metal content of cermet particle on properties of epoxy was analysed by incorporating cermet particle obtained at different calcination condition in the epoxy matrix. The epoxy-cermet composites were fabricated by a simple solution casting method. The enhanced dielectric constant of epoxy-cermet composites has resulted from the duplex interfacial polarization induced by metal-semiconductor interface and semiconductor-insulator interface. Initially epoxy-cermet composite was fabricated by loading 30 wt % of cermet filler obtained at different calcination conditions. Out of them, the cermet particle obtained at the calcination condition of 500 ^{o}C/ 3 h was showed best dielectric properties and was optimised for further studies. Further the effect of particle loading on properties of epoxy-cermet composite was investigated by varying the loading (10-30 wt %) of Zn/ZnO cermet particle obtained at 500 ^{o}C/ 3h. For different filler loading the dielectric constant was varied in the range 16-102 while keeping dielectric loss and conductivity within an acceptable limit. The thermal conductivity of epoxy cermet composite has also enhance to1.152 W m^{-1}.K^{-1} for epoxy

loaded with 30 wt % cermet particle (Zn/ZnO @ 500 ^{o}C/ 3h). Thus the dielectric and thermal properties of epoxy composites were tailored by interface design of epoxy composite by adjusting metal to semiconductor ratio of cermet particle.

5.2 Introduction

For the fabrication of smaller, faster and higher performance passive elements such as capacitor, resistor and inductor in integrated circuits material having good thermal conductivity, high dielectric constant but low loss and low processing temperature are required [1-3]. Polymer based dielectric materials filled particles having high dielectric permittivity are potential candidates for many electronic devices and electric power systems [3]. Polymers possess advantages like mechanical flexibility, easy processing and low cost [2]. However, organic polymeric materials often possess low dielectric constant in the range of 2–10 compared with inorganic counterparts. Thus it is required to substantially raise the dielectric permittivity of polymers without sacrificing their excellent mechanical properties [3, 5, 6]. Recently, new strategies, including polymer composites and synthesis of new polymers, have been developed to improve the dielectric permittivity of polymers. The most common one is composite approach by selective incorporation of filler particle with desired property in polymers. The most adaptable approach to develop polymer dielectrics with high dielectric constant is to introduce high-k ceramic particle or conducting particle such as metal in to polymer matrix [8-14]. This approach is inspired by the fact that the combination of high-*k* ceramic particle in a high dielectric strength polymer of good compatibility could generate high-*k* dielectric materials with tunable properties [2, 15]. Filler particles with high thermal conductivity and good dielectric properties have been of interest to design polymer composites with large energy storing capacity and good heat dissipation behaviour [14, 15]. These fillers includes ceramics, metals, carbon based materials and organic fillers such as conducting polymers and semi conductive oligomers [8, 16-19].

Large numbers of reports are there on conducting filler/polymer composite approach for designing high-*k* composite which is based on percolation theory, in which high-*k* values are expected when the concentration of filler particle reached percolation threshold value. Ning *et al.* reported the fabrication of high-*k* composite with low loss by incorporating multi-walled carbon nanotubes in polyvinyl alcohol [18]. The silver addition to carbon black/epoxy composite resulted in high-k, low loss dielectric composite as reported by Lu *et al*. [20]. Min *et al*. developed graphite nanoplate–epoxy composites with good dielectric properties and thermal conductivity *via* typical interface design [15]. The main limitation of this approach is that the higher loading of conducting filler particle may destroy the mechanical properties of polymer. Also higher loading of filler particle in polymer matrix may results in high dielectric loss and conductivity of composites [22-24].

Ferroelectric ceramic/polymer composite was reported for obtaining high-k composite by adopting ceramic fillers such as $Pb(Zr,Ti)O_3$ (PZT), $Pb(Mg_{0.33}\ Nb_{0.77})O_3$-$PbTiO_3$ (PMNT), and $BaTiO_3$ (BT) [25-28]. However these composite are facing some difficulties. Firstly, the electromechanical effect exhibited by these fillers limit the reliability of the device. Secondly the dielectric property of this material has a strong dependence on temperature. Additionally most of them are lead based material, which is not environmental friendly [2].

Recently, the designing of polymer-filler interface has emerged as an effective approach for developing polymer composites with enhanced dielectric properties [15]. Large number of efforts has been devoted towards the effective interfacial control of polymer composites by designing filler particle [28-32]. Core-shell approach is a well acknowledged interface design of filler particle for obtaining high-k polymer composite with low loss [33]. The core–shell structure is assumed to make use of the enhancement effect of constituents and provide the polymer composites with outstanding properties [34]. It is beneficial to explore the synergy between core and shell materials of core-shell particle to achieve desired properties for polymer matrix composites. However, the previously reported core-shell fillers such as GNPs@Al_2O_3 [35], CNTs@SiO_2 [36], Ag@C [15], GNPs@TiO_2 [37], CNTs@TiO_2 [38] are usually fabricated *via* complicated chemical synthesis with high production cost. Another interface design in polymer composite was done by surface functionalization of filler particle in which the dielectric loss was controlled by introducing a surfactant layer on the surface of filler particle [39, 40]. This approach also has some drawbacks like high production cost, need for addition washing step after synthesis *etc.*

Epoxy is a widely used thermosetting plastic in advanced electronic industry. Among the thermoset materials, epoxy resins shows special characteristics such as low shrinkage during curing, absence of by-products or volatiles after curing, curing over a wide temperature range and possible to control the degree of cross-linking [41, 43]. However the low dielectric constant and extremely low thermal conductivity (0.18 $W.m^{-1}.K^{-1}$) of epoxy resin impedes them to use as high-*k* dielectric material [43].

The present study focused on the design of a cermet type metal – semiconductor architecture of Zn and ZnO as filler for epoxy matrix to impart good thermal and dielectric properties. Cermet is a mixture of ceramic and metallic part which combines the properties of both ceramic and metallic constituent [44]. This study is believed to open up a deeper insight into dependence of composite properties on the ceramic to metal ratio of cermet particle.

5.3 Experimental Section

5.3.1 Materials

Zn dust (99.9 %) was supplied by Binani Zinc Pvt. Ltd., Epoxy resin (Araldite CY 225, DGEBA) and aromatic anhydride (Aradur HY 925) hardener was procured from Huntsman Resins, Switzerland.

5.3.2 Fabrication of Zn-ZnO Cermet Particles

As received raw Zn dust is sieved to have uniform particle size ~10 µm. The Zn dust was spread in the form of thin bed of thickness 2 mm in alumina boat of dimension 15 mm x 8mm x 10 mm. Then it was heated in air atmosphere at 450-600 °C for 1-3 h in a closed muffle furnace. The Zn-ZnO cermet particles were obtained by the formation of ZnO seed layer on the surface of Zn particle.

5.3.3 Fabrication of Epoxy-Cermet Composite

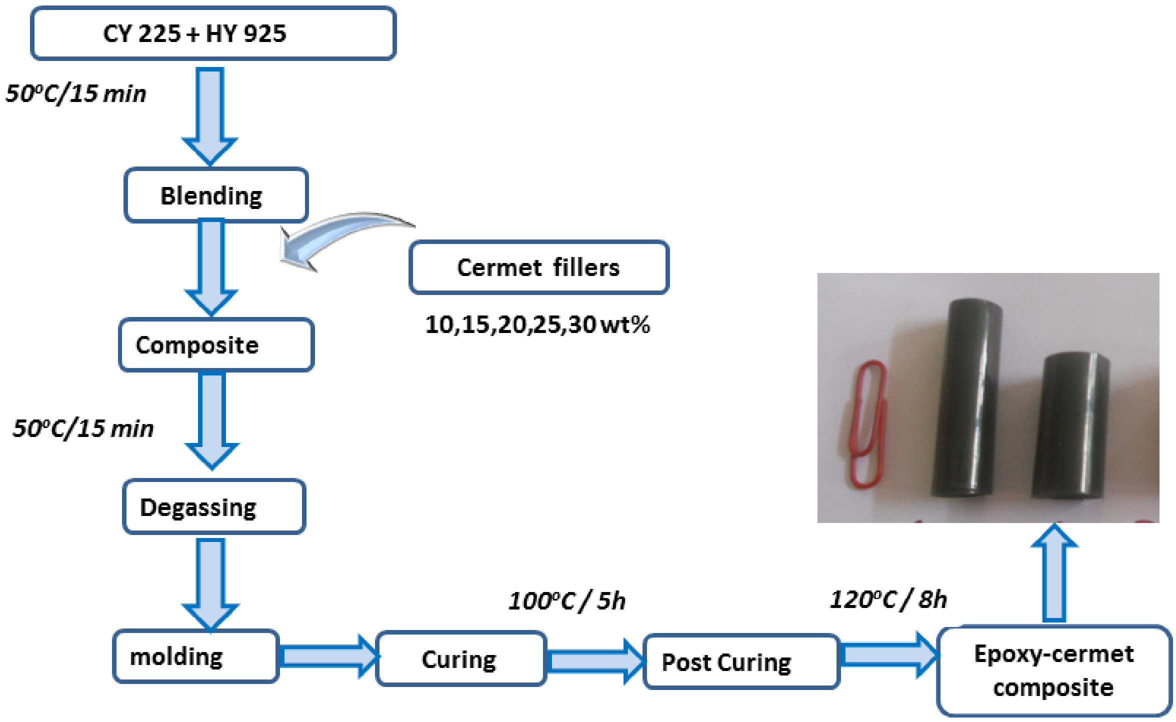

Figure 5.1: The processing of epoxy-cermet composites and epoxy-cermet composite fabricated in this study (inset).

The processing steps followed for the fabrication of epoxy cermet composite is shown in the flow sheet in Figure 5.1. The required amount of epoxy (100 parts) and hardener (80 parts) were weighed in a stainless steel container and mechanically stirred at mild temperature of not above 50 ^{o}C to reduce the viscosity. After 15 min. stirring the cermet fillers were added and maintained at a stirring speed of 750 rpm. The melt mixing was continued until homogeneous epoxy cermet composite was obtained. In order to remove the trapped air bubbles an intermediate degassing was done. The casting of epoxy cermet composite was done in a metallic mould which is preheated at 150 ^{o}C in order to avoid the settling of the filler. Then the casted composite was cured at 100 °C for 5 h and post curing was done at 130 °C for 8 h.

5.4 Result and discussion

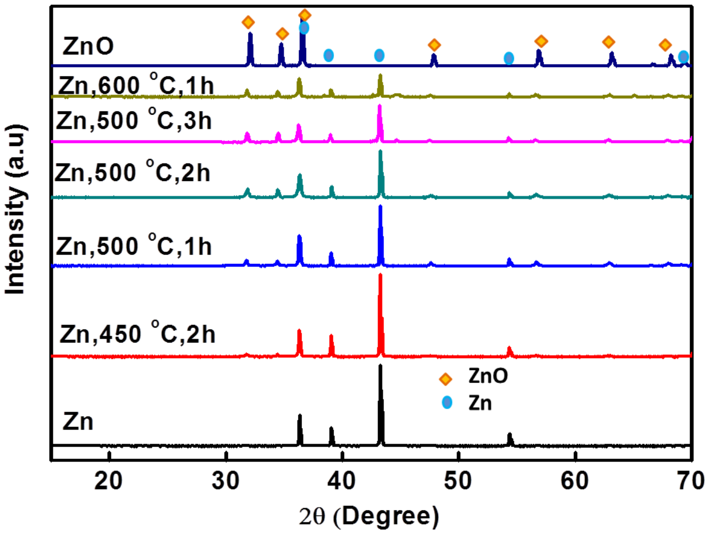

Figure 5.2: The phase analysis of Zn-ZnO cermet particle obtained at different calcination conditions.

Zn-ZnO cermet fillers were fabricated by simple calcination of raw Zn dust (sieved to have particle size <10 µm) in air atmosphere and ZnO seed layer was formed on the surface of Zn particle. Figure 5.2 shows the XRD pattern of Zn-ZnO cermet particle calcined at different conditions. For comparison XRD pattern of raw Zn and ZnO is also given. The peaks at different 2θ values can be indexed to Zn metal (JCPDS PDF #00-004-0831) and ZnO ((JCPDS no: 36-1451). The diffraction peaks are sharp which indicates high crystallinity of the product. All peaks correspond to either ZnO or pure Zn metal. No characteristic peak of other impurity phase was observed. The diffraction peaks obtained at the 2θ positions 36.28, 39.07, 43.33, 54.32 and 70.35 corresponds to the lattice planes (002), (100), (101), (102) and (103) of pure Zn metal and the peaks at 2θ positions 31.91, 34.45, 36.28, 47.60, 56.64, 62.82, and 67.93 corresponds to the (100), (002), (101), (102), (110), (103) and (112) lattice planes of hexagonal wurtzite phase ZnO. The normalized intensities of XRD peaks showed that with increase in calcination condition, the peaks corresponding to ZnO become prominent and peaks corresponding to Zn phase diminished. This indicates the increased ZnO content in the cermet structure with increase in calcination temperature.

The variation of mass fraction (W_{ZnO}) of ZnO and relative thickness ($h_{r(ZnO)}$) of ZnO layer formed on the surface of Zn particle are displayed in Figure 5.3. The mass fraction of ZnO is calculated by direct comparison method from XRD analysis [45]; the corresponding Equations are given below.

$$W_{ZnO} = \frac{\frac{I_{ZnO}}{(I_{ZnO})_0}\mu_{m(Zn)}}{\frac{I_{ZnO}}{(I_{ZnO})_0}(\mu_{m(Zn)} - \mu_{m(ZnO)}) + \mu_{m(ZnO)}} \tag{5.1}$$

where I_{ZnO} and $(I_{ZnO})_0$ are the intensities of the same line for ZnO formed at different heating conditions and pure ZnO respectively. $\mu_{m(Zn)}$ and $\mu_{m(ZnO)}$ are the mass absorption coefficient of Zn and ZnO respectively.

The relative thickness $h_{r(ZnO)}$ is given by the equation $(r_2-r_1)/r_1$ and is obtained by the Equation,

$$\frac{m_{Zn}}{m_{ZnO}} = \frac{r_1^3 \rho_{Zn}}{(r_2^3 - r_1^3)\rho_{ZnO}} \pi r^2 \tag{5.2}$$

where m_{Zn} and m_{ZnO} are the weight of Zn content and weight of ZnO content respectively. ρ_{Zn} and ρ_{ZnO} are the densities of Zn and ZnO. r_1 and r_2 are the radius of Zn and Zn-ZnO cermet structure respectively.

$$h_{r(ZnO)} = \frac{r_2 - r_1}{r_1} = \left(\frac{m_{ZnO}\rho_{Zn} + m_{Zn}\rho_{ZnO}}{m_{Zn}\rho_{ZnO}}\right)^{\frac{1}{3}} - 1 \qquad (5.3)$$

The mass fraction and relative thickness of ZnO was calculated using the equations 5.1 and 5.2. It is well clear that with increase in the calcination temperature both mass fraction and relative thickness of ZnO in cermet architecture were increased. It is also evident from the appearance of raw Zn dust and Zn calcined at different conditions in the corresponding SEM images displayed in Figure 5.4 (a) and (b).

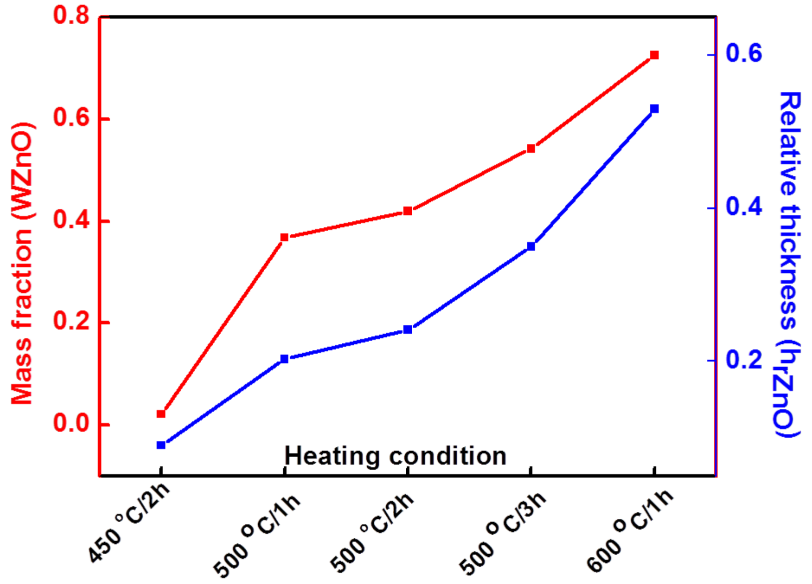

Figure 5.3: The variation of ZnO shell mass fraction (W_{ZnO}) and relative thickness ($h_{r(ZnO)}$) at different calcination conditions

.

The raw Zn particles are nearly spherical in shape and with smooth surface having average particle size ~ 10 µm. With increase in calcination condition the growth of ZnO layer on the surface Zn particle was observed. The shape of Zn-ZnO cermet particle become irregular and the surface roughness increased due to the volume expansion during oxidation [46]. Beyond calcination condition at 500 °C/ 3h, at 600 °C/ 1h the detachment of ZnO from the surface of cermet particle was observed. Thus the concept of cermet particle is no longer valid after the calcination condition 500 °C/ 3h.

The SEM microstructure of polished surface of epoxy-cermet composite (30 wt %) incorporated with cermet particle obtained at different calcination conditions is shown in Figure 5.5. The extend of interfacial interaction between epoxy and cermet particle obtained at different calcination conditions is well clear from the corresponding SEM images. Epoxy loaded with raw Zn (Figure 5.5 (a)) showed loose binding between filler particle and polymer matrix.

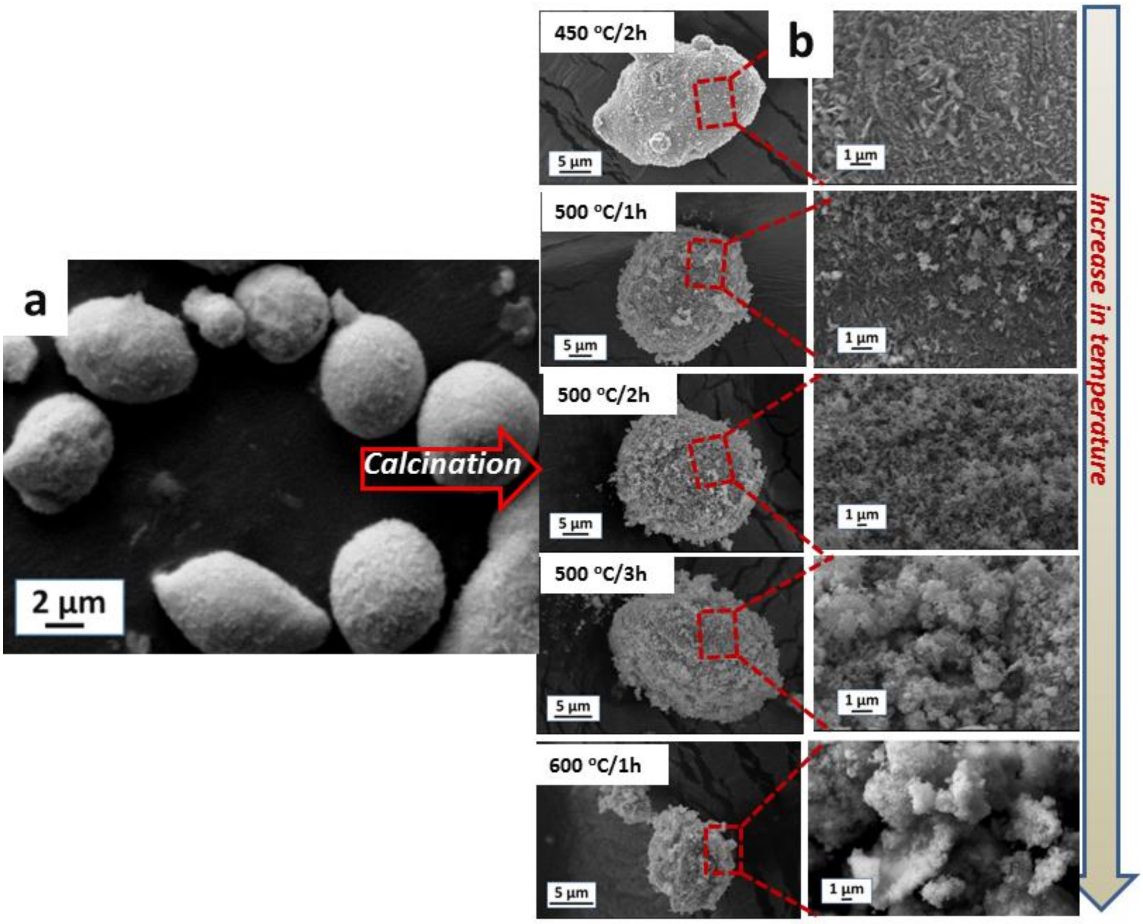

Figure 5.4: SEM images of (a) raw Zn dust and (b) Zn-ZnO cermet architecture obtained at different calcination conditions.

As the cermet particle obtained at different calcination conditions are incorporated to the epoxy matrix, the filler particles are embedded within the polymer matrix and tightly binded with polymer matrix. During the curing of epoxy cermet composite, strong interfacial adhesion was believed to occur between the ZnO on the surface of cermet particle and epoxy molecular chain. Compared to raw Zn particle ZnO on the surface of cermet particle showed good interaction with polymer matrix. Thus cermet particles are homogeneously dispersed in epoxy matrix which is beneficial for increasing the dielectric constant and decreasing the conductivity and dielectric loss of the resulting composite.

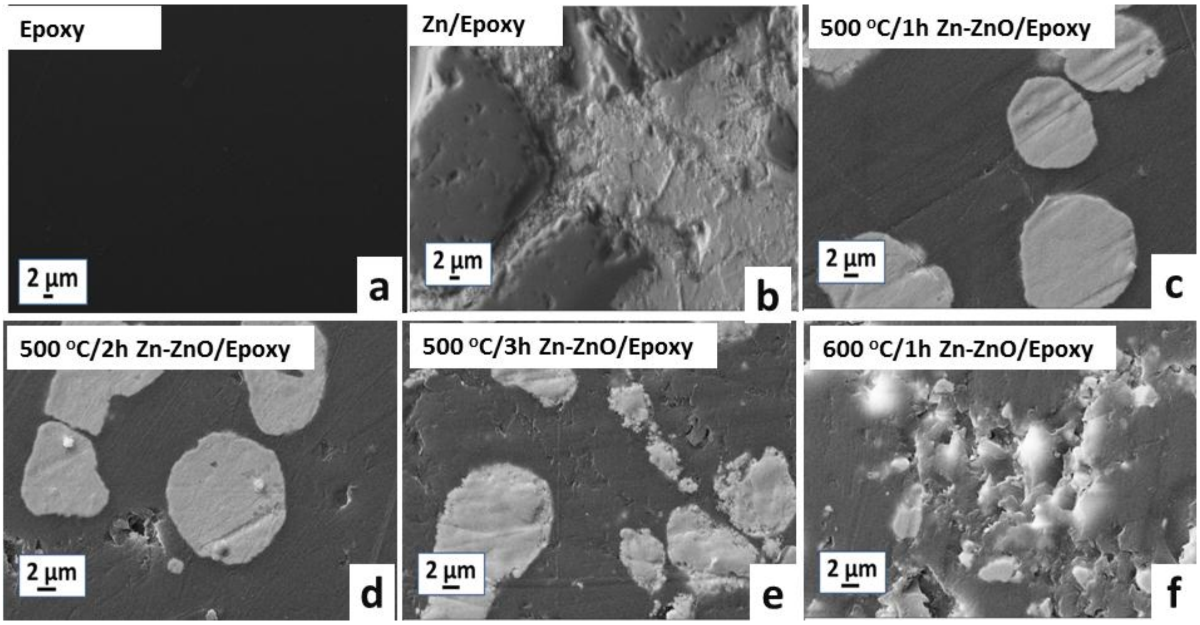

Figure 5.5: SEM images of (a) pure epoxy, (b) Zn-epoxy composites and (c)-(f) epoxy composite incorporated with cermet particle obtained at different calcination conditions.

The thermo gravimetric analysis (TGA) curves of pristine epoxy and epoxy cermet composites with different loading of cermet particle obtained at calcination condition 500 ^{o}C for 3h are shown in Figure 5.6. Both pristine epoxy and epoxy composite showed almost similar decomposition profile and the decomposition of polymer takes place in two stages.

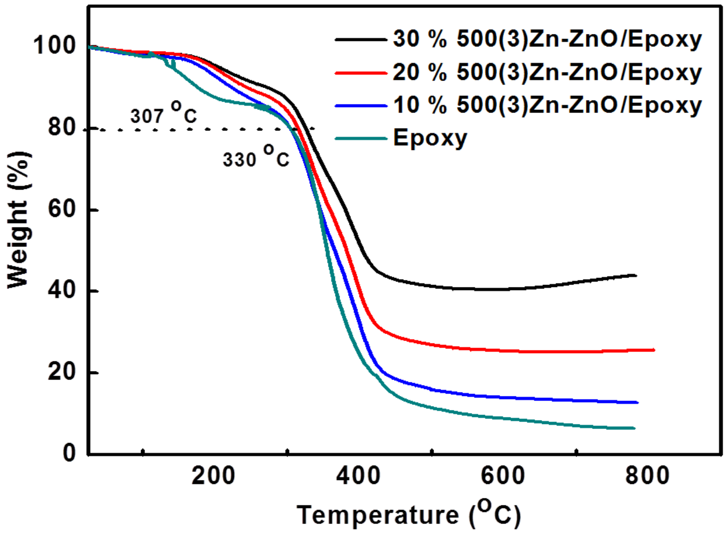

Figure 5.6: TGA analysis of epoxy composite with different wt % loading of cermet particle obtained at calcination condition 500 °C for 3h.

The thermal stability of epoxy-cermet composite is slightly increased as compared to pristine epoxy. With the addition of cermet particle the temperature corresponding to 20 % weight loss is increased by about 23 °C for 30 % cermet particle loaded sample. This can be attributed to the good interfacial adhesion of cermet particle with epoxy matrix.

In order to confirm the fact that cermet architecture is maintained in epoxy-cermet composite also, the EDX analysis was conducted at different areas of epoxy-cermet composites. The SEM image of epoxy composite loaded with Zn-ZnO cermet particle obtained at calcination condition 500 °C/3h and corresponding EDS spectrum at different areas are given in Figure 5.7 (a), (b) and (c) respectively. The EDX spectrum 3 corresponds to the central area of cermet particle dispersed in epoxy matrix. As seen from the EDX spectra Zn constitute about 99 % of the central area. This indicates that the central area is maintained as Zn. The EDX spectrum 2 corresponds to the outer region of cermet particle which is in contact with epoxy matrix. As evident from EDX spectra that area contain both Zn (85 wt %) and O (15 wt %). This indicates that the ZnO layer on Zn particle is maintained in composite also.

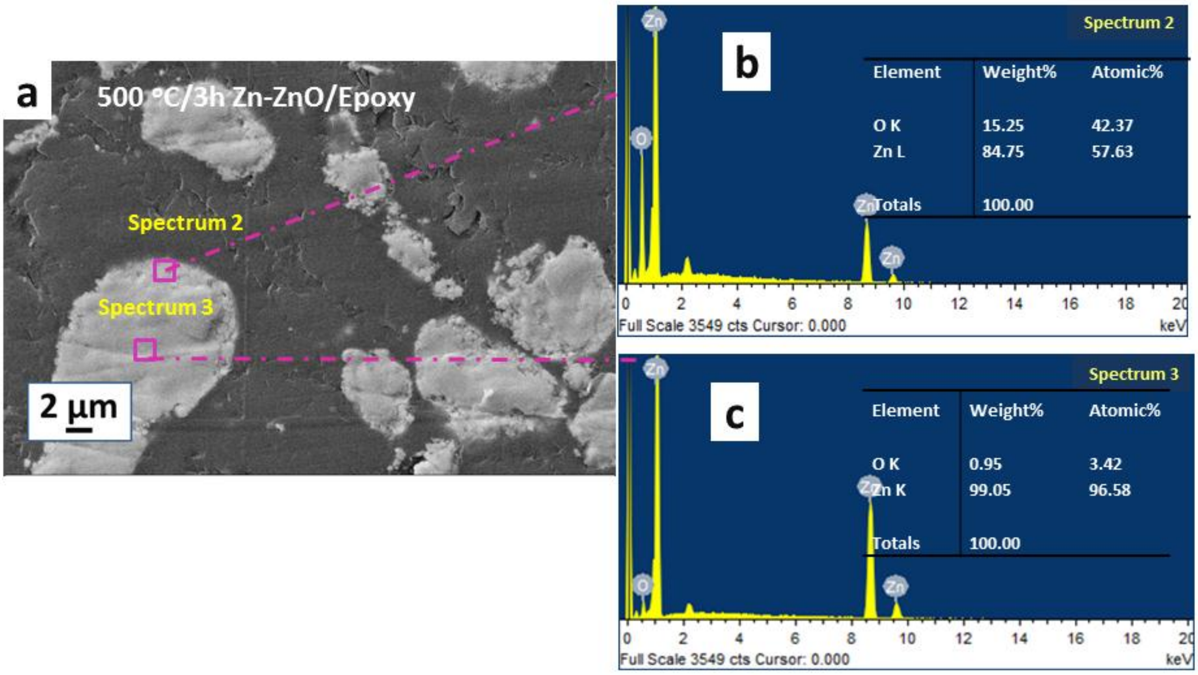

Element	Weight%	Atomic%
O K	15.25	42.37
Zn L	84.75	57.63
Totals	100.00	

Element	Weight%	Atomic%
O K	0.95	3.42
Zn K	99.05	96.58
Totals	100.00	

Figure 5.7: (a) SEM image of epoxy loaded with 30 wt % cermet particle, (b) and (c) EDS spectra obtained at different points respectively at the periphery and centre of cermet particle dispersed in polymer matrix.

5.4.1 Dielectric Properties of Epoxy-Cermet Composites

The effect of calcination conditions and frequency on dielectric properties of epoxy-cermet composite is investigated for epoxy-cermet composite loaded with 30% cermet particle obtained at different calcination conditions. The variation of dielectric permittivity with frequency for epoxy-cermet composite loaded with cermet particle obtained at different calcination conditions is given in Figure 5.8 (a). From the figure it is clearly seen that all epoxy cermet composite showed obviously higher dielectric constant compared to epoxy-raw Zn composite. At frequency 1 KHz, the dielectric permittivity obtained for Zn/epoxy composite was 28 and reached to 102 for epoxy composite loaded with cermet particle obtained at calcination condition 500 °C/ 3h. As the calcination condition is increased to 600 °C/ 1h, the dielectric permittivity decreased to 89.

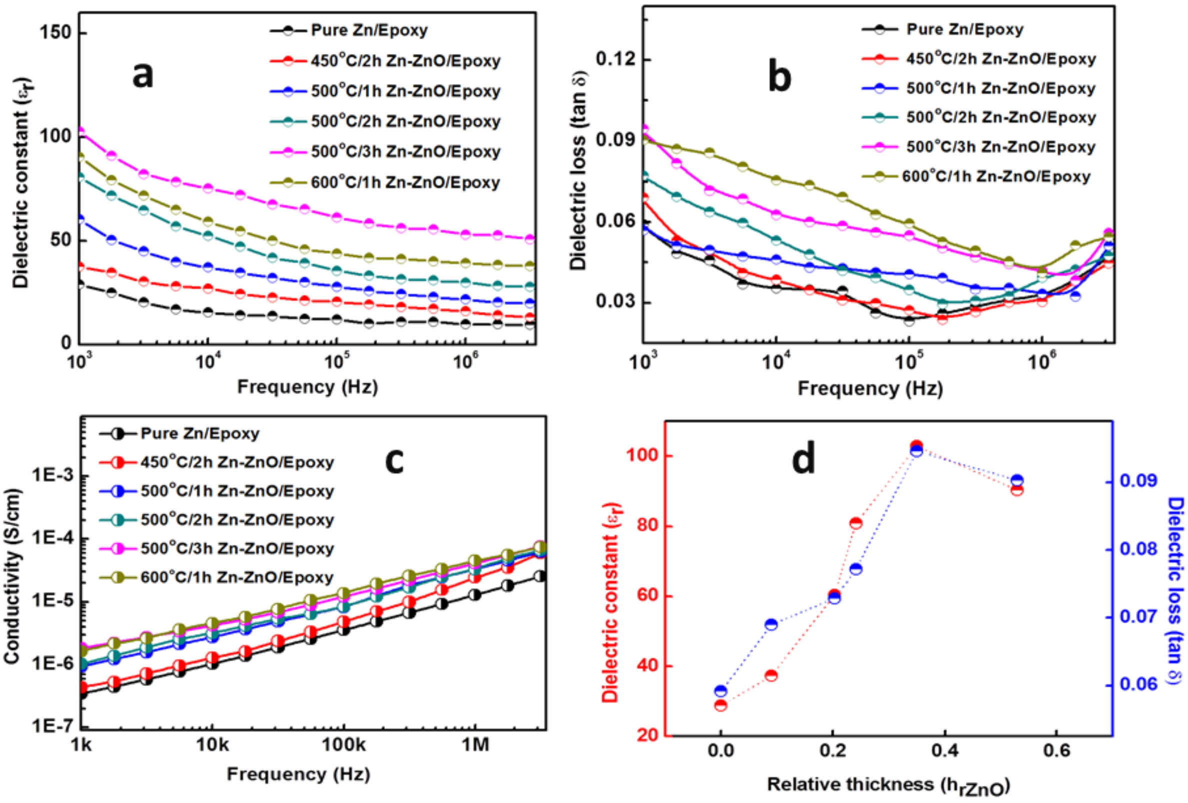

Figure 5.8: The frequency dependant variation of (a) Dielectric permittivity, (b) dielectric loss and (c) conductivity of epoxy with 30 wt % Zn-ZnO as a function of calcination conditions and (d) the variation of dielectric constant and dielectric loss with increase in relative thickness of ZnO formed.

The higher dielectric constant epoxy cermet composite is attributed to the induced duplex interfacial polarization [46, 47] due to metal (Zn)-semiconductor(ZnO) interface and semiconductor(ZnO)-insulator(epoxy) interface as shown in Figure 5.9. Moreover on each Zn particle, a natural insulating self-passivation layer is present and this leads to weak interfacial polarization compared to epoxy cermet composite.

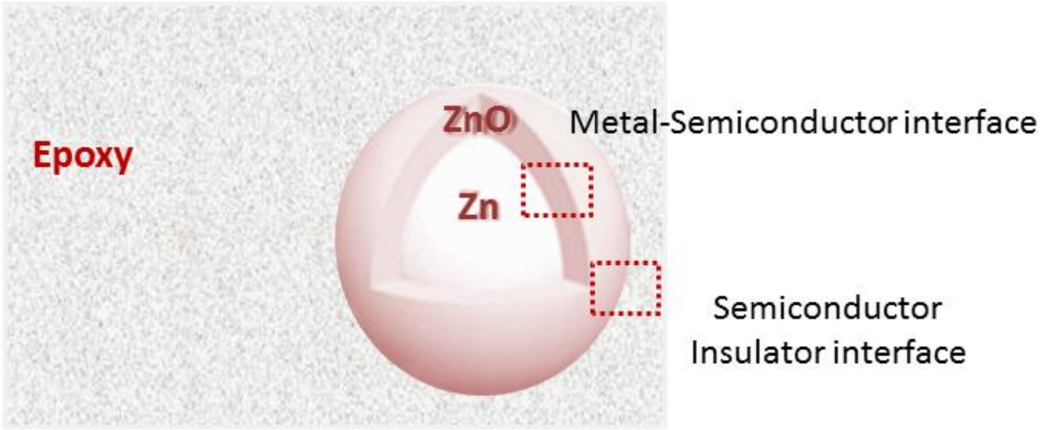

Figure 5.9: Duplex interfacial polarization induced in epoxy cermet composite.

For epoxy cermet composite the dielectric constant is increased with increase in calcination temperature and time. This can be attributed to the increased ZnO content in cermet particle which is favourable for enhancing the interfacial polarization and endows the composite with higher dielectric permittivity. The interfacial area is increased with increase in ZnO content in cermet particle due to the volume expansion during oxidation. However beyond the calcination condition of 500 ^{o}C/ 3h, the dielectric permittivity started to decrease clearly. Generally, when the relative thickness of ($h_{r\ (ZnO)}$) of ZnO has reached ∞, at any content of cermet filler, the dielectric constant was decreased. This can be attributed to the weakened metal semiconductor interfacial polarization due to the decrease in metal semiconductor interfacial area or even due to the disappearance of metal part in the cermet structure.

As far as the dielectric loss is considered the epoxy-cermet composite showed higher conductivity and dielectric loss compared to epoxy-Zn composite (Figure 5.8 (b)). The conductivity of ZnO on cermet particle is higher than that of insulating self-passivation layer on Zn particle. At low frequencies, the dielectric loss of polymer composite with semiconducting or conducting fillers depend on filler conductivity as they can provide lots of free charge carriers. In the present case, the outer layer cermet particle is semiconducting ZnO which results in higher dielectric loss for epoxy cermet composite compared to epoxy Zn composite. With increase in relative thickness of ZnO layer, the dielectric loss was further increased due to the increased number of free charge carriers with increase in ZnO content in cermet particle. Furthermore the dielectric loss of all epoxy-cermet composite was maintained within an acceptable limit due to the presence of semiconducting ZnO outer layer on cermet particle which could prevent the transfer of charge carriers between adjacent conducting Zn particles.

The variation of conductivity of epoxy-cermet composite loaded with 30 % cermet filler obtained at different calcination conditions is given in Figure 5.8 (c). It is evident from the figure that the conductivities of all samples linearly increased with increase in frequency, which indicates the typical insulating behaviour of resulting composite. Due to the presence of semiconducting ZnO layer on Zn particle, the percolation threshold shifted to higher loading and is not observed in the present case. The variation of dielectric constant and dielectric loss with increase in relative thickness of ZnO is represented in Figure 5.8 (d). It is well clear from the figure that beyond a certain relative thickness value $h_{rZnO} = 0.35$ (at 500 ^oC/ 3h) dielectric loss showed a decreasing trend. This is due to the disappearance of semiconductor-metal interface resulted from the detachment of surface ZnO formed from the metallic Zn.

Among the six samples prepared in the current study, epoxy incorporated with cermet particle calcined at 500 ^oC/ 3h manifested best dielectric properties due to the highest dielectric constant coupled with low dielectric loss. The loading of filler particle beyond 30 wt % will reduce the processability and mechanical properties of the composite. Hence in the present study the maximum loading was selected as 30 wt%. In order to study the effect of loading of cermet particle in polymer matrix the loading of cermet particle was (500 ^oC/ 3 h) varied from 10-30 wt %. It is obvious that dielectric constant has increased with increase in filler loading. It is observed that at all loadings the dielectric constant gradually decreased with increase in frequency. This is due to the fact that at higher frequencies the interfacial polarization and orientation polarization cannot follow the external electric field.

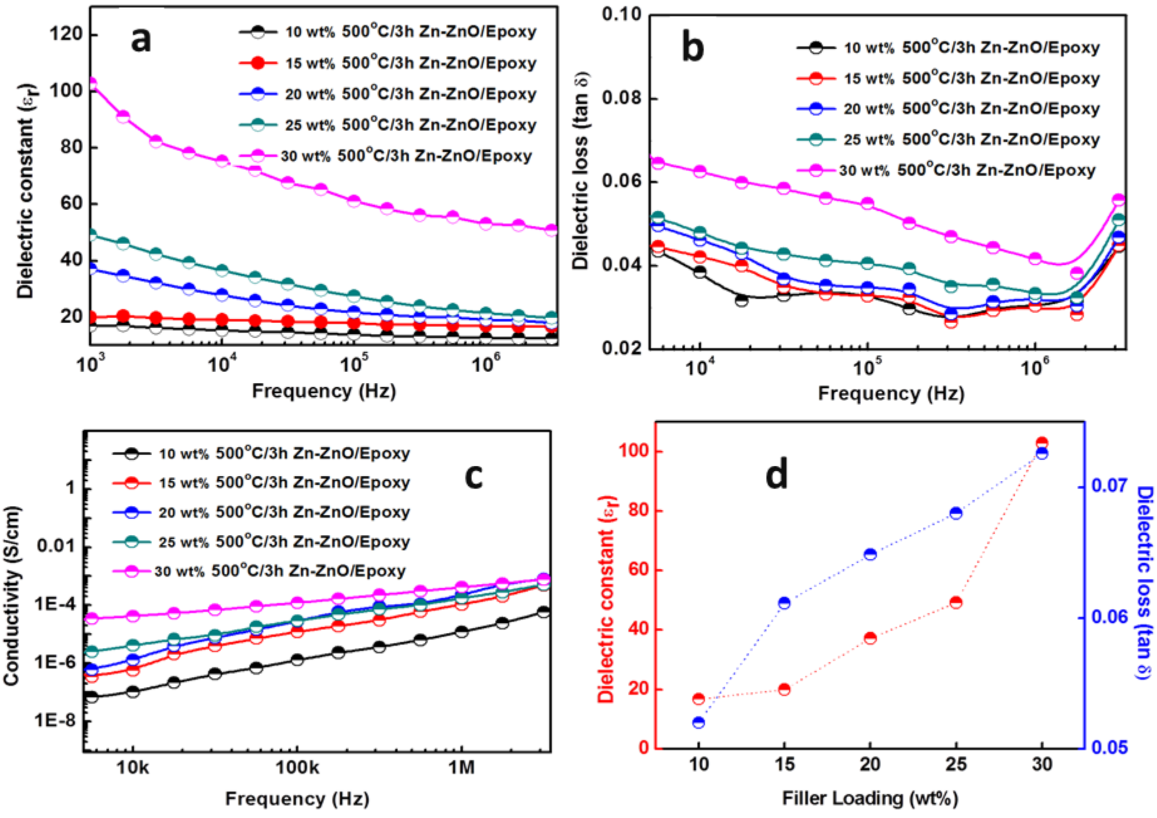

Figure 5.10: Frequency dependence of (a) Dielectric permittivity, (b) dielectric loss, and (c) conductivity of epoxy composite with various loading of cermet particle obtained at calcination condition 500 ^{o}C/3h and (d) variation of dielectric constant and dielectric loss with variation of filler loading.

At higher frequencies only atomic polarization is there to contribute to the dielectric permittivity of the material. The net polarization of a dielectric material is the sum of electronic polarization, atomic polarization, orientation polarization and interfacial polarization. There exist a minimum reorientation time for each type of polarization. The reciprocal of this reorientation time gives relaxation frequency of that particular polarization. If the frequency of applied field is greater than the relaxation frequency of a particular polarization then that particular polarization can no more contribute to total polarization of a material.

Figure 5.10 (b) shows the variation of dielectric loss with increase in loading of filler. The dielectric loss for all composition is maintained within an acceptable limit due to the presence of semiconducting ZnO on the surface of Zn particle which serves as a barrier layer between the adjacent Zn particles to prevent transfer of free charge carriers.

The conductivity of all composites showed typical insulating characteristics (Figure 5.10 (c)). The variation of dielectric constant and dielectric loss with filler loading is represented in Figure 5.10 (d). With increase in loading the dielectric constant showed an increasing trend resulted from the increased interfacial area formed at higher loading which resulted in increased polarization.

5.4.2 Thermal Conductivity of Composites

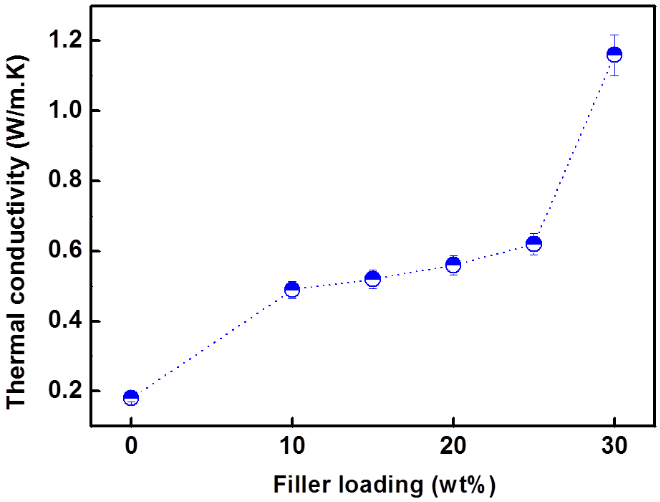

Figure 5.11: The variation of thermal conductivity of epoxy composite with different loading of cermet particles.

The variation of thermal conductivity of epoxy composite with different loading of cermet particles is shown in Figure 5.11. The thermal conductivities of epoxy-cermet composite strongly depend on filler loading because the heat propagation in Zn-ZnO cermet particle occurred by diffusion of phonons and the formation of well-connected network of filler particle at higher loading in polymer matrix leads to effective heat dissipation.

The higher filler loading obviously resulted in higher thermal conductivity for epoxy composite. This can be attributed to the good dispersion of filler particle in polymer matrix and with the addition of cermet particle the thermal conductivity of pure epoxy increased from 0.18 $W.m^{-1}\cdot K^{-1}$ to 1.152 $W\ m^{-1}\cdot\ K^{-1}$ *i.e*, about 6.3 fold improvement for epoxy cermet composite loaded with 30 wt % cermet particle. Better dispersion of cermet particle in polymer matrix and good interfacial adhesion between filler and polymer matrix lead to easy phonon transport, resulting in higher thermal conductivity for epoxy-cermet composite.

5.5 Conclusions

Zn-ZnO cermet particle were prepared by a simple calcination of raw Zn dust in air atmosphere. The metal to semiconductor ratio of cermet particle can be tuned by changing the calcination conditions and has great impact on dielectric properties of epoxy cermet composites. The Zn-ZnO cermet particle incorporated epoxy composite showed higher dielectric constant compared to epoxy-Zn counterpart. This can be ascribed to duplex interfacial polarization induced by metal-semiconductor and semiconductor-insulator interfaces present in epoxy-cermet composite. As far as the dielectric loss is concerned epoxy composite containing Zn-ZnO cermet particles showed slightly higher dielectric loss than the composite prepared with Zn particles. This is due to the higher conductivity of semiconducting ZnO layer on cermet particle compared to the insulating self-passivation layer on the Zn particle. Among the different compositions prepared epoxy composite incorporated with cermet particle (30 wt %) obtained at 500 ^{o}C/ 3h leads to highest dielectric constant (102) and acceptable dielectric loss (0.09). The thermal conductivity of epoxy composite is also improved with the addition of cermet particle. High thermal conductivity of 1.152 W. m^{-1}. K^{-1} was obtained for epoxy loaded with 30 wt % cermet particle (500 ^{o}C/ 3h). This is due to the excellent interfacial adhesion of cermet particle with polymer matrix. Thus the interface design in epoxy-cermet composite by controlling the metal to ceramic ratio of cermet particle introduce a new strategy for developing epoxy composite with good dielectric properties which can be applied in embedded passive components and other related electronic devices.

References

[1] Zhu, L. "Exploring strategies for high dielectric constant and low loss polymer dielectrics." *The journal of physical chemistry letters* 5.21 (2014): 3677-3687.

[2] Arbatti, M., Shan, X. and Cheng, Z.Y. "Ceramic–polymer composites with high dielectric constant." *Advanced Materials* 19.10 (2007): 1369-1372.

[3] Dang, Z.M., Yuan, J.K., Zha, J.W., Zhou, T., Li, S.T. and Hu, G.H. "Fundamentals, processes and applications of high-permittivity polymer–matrix composites." *Progress in Materials Science* 57.4 (2012): 660-723.

[4] Dang, Z.M., Zheng, M.S. and Zha, J.W. "1D/2D Carbon Nanomaterial-Polymer Dielectric Composites with High Permittivity for Power Energy Storage Applications." *Small* 12.13 (2016): 1688-1701

[5] Huo, X., Li, W., Zhu, J., Li, L., Li, Y., Luo, L. and Zhu, Y. "Composite based on Fe_3O_4@ BaTiO3 particles and polyvinylidene fluoride with excellent dielectric properties and high energy density." *The Journal of Physical Chemistry C* 119.46 (2015): 25786-25791.

[6] Zhang, Z., Gu, Y., Wang, S., Li, Q., Li, M. and Zhang, Z. "Enhanced dielectric and mechanical properties in chlorine-doped continuous CNT sheet reinforced sandwich polyvinylidene fluoride film." *Carbon* 107 (2016): 405-414.

[7] Zhang, Z., Gu, Y., Wang, S., Li, Q., Li, M. and Zhang, Z. "Enhanced dielectric and mechanical properties in chlorine-doped continuous CNT sheet reinforced sandwich polyvinylidene fluoride film." *Carbon* 107 (2016): 405-414.

[8] Huang, X., Jiang, P. and Xie, L. "Ferroelectric polymer/silver nanocomposites with high dielectric constant and high thermal conductivity." *Applied Physics Letters* 95.24 (2009): 242901.

[9] da Silva, A.B., Arjmand, M., Sundararaj, U. and Bretas, R.E.S. "Novel composites of copper nanowire/PVDF with superior dielectric properties." *Polymer*55.1 (2014): 226-234.

[10] Xing, C., Wang, Y., Huang, X., Li, Y. and Li, J. "Poly (vinylidene fluoride) nanocomposites with simultaneous organic nanodomains and inorganic nanoparticles." *Macromolecules* 49.3 (2016): 1026-1035.

[11] Zhao, X., Zhao, J., Cao, J.P., Wang, X., Chen, M. and Dang, Z.M. "Tuning the dielectric properties of polystyrene/poly (vinylidene fluoride) blends by selectively localizing carbon black nanoparticles." *The Journal of Physical Chemistry B* 117.8 (2013): 2505-2515.

[12] Yang, K., Huang, X., Fang, L., He, J. and Jiang. "Fluoro-polymer functionalized graphene for flexible ferroelectric polymer-based high-k nanocomposites with suppressed dielectric loss and low percolation threshold." *Nanoscale* 6.24 (2014): 14740-14753.

[13] Wang, D., Bao, Y., Zha, J.W., Zhao, J., Dang, Z.M. and Hu, G.H. "Improved dielectric properties of nanocomposites based on poly (vinylidene fluoride) and poly (vinyl alcohol)-functionalized graphene." *ACS applied materials & interfaces* 4.11 (2012): 6273-6279.

[14] Xiao, Y.J., Wang, W.Y., Lin, T., Chen, X.J., Zhang, Y.T., Yang, J.H., Wang, Y. and Zhou, Z.W. "Largely enhanced thermal conductivity and high dielectric constant of poly (vinylidene fluoride)/boron nitride composites achieved by adding a few carbon nanotubes." *The Journal of Physical Chemistry C* 120.12 (2016): 6344-6355.

[15] Min, C., Yu, D., Cao, J., Wang, G. and Feng, L. "A graphite nanoplatelet/epoxy composite with high dielectric constant and high thermal conductivity." *Carbon* 55 (2013): 116-125.

[16] Bai, Y., Cheng, Z.Y., Bharti, V., Xu, H.S. and Zhang, Q.M. "High-dielectric-constant ceramic-powder polymer composites." *Applied Physics Letters* 76.25 (2000): 3804-3806.

[17] Zhou, Y., Han, S.T., Xu, Z.X., Yang, X.B., Ng, H.P., Huang, L.B. and Roy, V.A.L. "Functional high-k nanocomposite dielectrics for flexible transistors and inverters with excellent mechanical properties." *Journal of Materials Chemistry* 22.28 (2012): 14246-14253.

[18] Ning, N., Bai, X., Yang, D., Zhang, L., Lu, Y., Nishi, T. and Tian, M. "Dramatically improved dielectric properties of polymer composites by controlling the alignment of carbon nanotubes in matrix." *RSC Advances* 4.9 (2014): 4543-4551.

[19] Kuo, D.H., Chang, C.C., Su, T.Y., Wang, W.K. and Lin, B.Y. "Dielectric behaviours of multi-doped $BaTiO_3$/epoxy composites." *Journal of the European Ceramic Society* 21.9 (2001): 1171-1177.

[20] Lu, J., Moon, K.S., Xu, J. and Wong, C.P. "Synthesis and dielectric properties of novel high-K polymer composites containing in-situ formed silver nanoparticles for embedded capacitor applications." *Journal of Materials Chemistry* 16.16 (2006): 1543-1548

[21] Feng, Y., Li, W.L., Wang, J.P., Yin, J.H. and Fei, W.D. "Core–shell structured BaTiO 3@ carbon hybrid particles for polymer composites with enhanced dielectric performance." Journal of Materials Chemistry A 3.40 (2015): 20313-20321.

[22] Zhang, Y., Wang, Y., Deng, Y., Li, M. and Bai, J. "High dielectric constant and low loss in polymer composites filled by self-passivated zinc particles." *Materials Letters* 72 (2012): 9-11.

[23] Qi, L., Lee, B.I., Chen, S., Samuels, W.D. and Exarhos, G.J. "High-Dielectric-Constant Silver–Epoxy Composites as Embedded Dielectrics." *Advanced Materials*17.14 (2005): 1777-1781.

[24] Shen, Y., Lin, Y., Li, M. and Nan, C.W. "High dielectric performance of polymer composite films induced by a percolating interparticle barrier layer." *Advanced Materials* 19.10 (2007): 1418-1422.

[25] Kobayashi, Y., Tanase, T., Tabata, T., Miwa, T. and Konno, M. "Fabrication and dielectric properties of the BaTiO3–polymer nano-composite thin films." *Journal of the European Ceramic Society* 28.1 (2008): 117-122

[26] Zak, A.K., Gan, W.C., Majid, W.A., Darroudi, M. and Velayutham, T.S. "Experimental and theoretical dielectric studies of PVDF/PZT nanocomposite thin films." *Ceramics International* 37.5 (2011): 1653-1660.

[27] Chan, H.L.W., Cheung, M.C. and Choy, C.L. "Study on BaTiO3/P (VDF-TrFE) 0–3 composites." *Ferroelectrics* 224.1 (1999): 113-120.

[28] Bai, Y., Cheng, Z.Y., Bharti, V., Xu, H.S. and Zhang, Q.M. "High-dielectric-constant ceramic-powder polymer composites." *Applied Physics Letters* 76.25 (2000): 3804-3806.

[29] Tanaka, T., Kozako, M., Fuse, N. and Ohki, Y. "Proposal of a multi-core model for polymer nanocomposite dielectrics." IEEE transactions on dielectrics and electrical insulation 12.4 (2005): 669-681.

[30] Tanaka, T. "Dielectric nanocomposites with insulating properties." *IEEE Transactions on Dielectrics and Electrical Insulation* 12.5 (2005): 914-928.

[31] Min, C. and Demei Y. "Simultaneously improved toughness and dielectric properties of epoxy/graphite nanosheet composites." *Polymer Engineering & Science* 50.9 (2010): 1734-1742.

[32] Wan, W., Yu, D., He, J., Xie, Y., Huang, L. and Guo, X. "Simultaneously improved toughness and dielectric properties of epoxy/core-shell particle blends." *Journal of applied polymer science* 107.2 (2008): 1020-1028

[33] Feng, Y., Li, W.L., Wang, J.P., Yin, J.H. and Fei, W.D. "Core–shell structured BaTiO 3@ carbon hybrid particles for polymer composites with enhanced dielectric performance." *Journal of Materials Chemistry A* 3.40 (2015): 20313-20321.

[34] Huang, L., Zhu, P., Li, G., Lu, D.D., Sun, R. and Wong, C. "Core–shell SiO 2@ RGO hybrids for epoxy composites with low percolation threshold and enhanced thermo-mechanical properties." *Journal of Materials Chemistry A* 2.43 (2014): 18246-18255.

[35] Qian, R., Yu, J., Wu, C., Zhai, X. and Jiang, P. "Alumina-coated graphene sheet hybrids for electrically insulating polymer composites with high thermal conductivity." *RSC Advances* 3.38 (2013): 17373-17379.

[36] Cui, W., Du, F., Zhao, J., Zhang, W., Yang, Y., Xie, X. and Mai, Y.W. "Improving thermal conductivity while retaining high electrical resistivity of epoxy composites by incorporating silica-coated multi-walled carbon nanotubes." Carbon 49.2 (2011): 495-500.

[37] Wu, C., Huang, X., Xie, L., Wu, X., Yu, J. and Jiang, P. "Morphology-controllable graphene–TiO $_2$ nanorod hybrid nanostructures for polymer composites with high dielectric performance." *Journal of Materials Chemistry*21.44 (2011): 17729-17736.

[38] Wu C., Huang X.Y. and Jiang P.K. “TiO2-nanorod decorated carbon nanotubes for high-permittovity and low-dilelctric-loss polystyrene composites.” 72 (2012): 521–527.

[39] Tuncer, E., Rondinone, A.J., Woodward, J., Sauers, I., James, D.R. and Ellis, A.R. "Cobalt iron-oxide nanoparticle modified poly (methyl methacrylate) nanodielectrics." *Applied Physics A*94.4 (2009): 843-852.

[40] Barber, P., Balasubramanian, S., Anguchamy, Y., Gong, S., Wibowo, A., Gao, H., Ploehn, H.J. and Zur Loye, H.C. "Polymer composite and nanocomposite dielectric materials for pulse power energy storage." *Materials*2.4 (2009): 1697-1733.

[41] Zhu, J., Wei, S., Ryu, J., Sun, L., Luo, Z. and Guo, Z. "Magnetic epoxy resin nanocomposites reinforced with core− shell structured Fe@ FeO nanoparticles: fabrication and property analysis." *ACS Applied Materials & Interfaces* 2.7 (2010): 2100-2107.

[42] Fu, Y.X., He, Z.X., Mo, D.C. and Lu, S.S. "Thermal conductivity enhancement with different fillers for epoxy resin adhesives." *Applied Thermal Engineering* 66.1-2 (2014): 493-498.

[43] Vaisakh, S.S., Hassanzadeh, M., Metz, R., Ramakrishnan, S., Chappelle, D., Sudha, J.D. and Ananthakumar, S. "Effect of nano/micro-mixed ceramic fillers on the dielectric and thermal properties of epoxy polymer composites." *Polymers for Advanced Technologies*25.2 (2014): 240-248.

[44] Antonov, M. and Hussainova, I. "Thermophysical properties and thermal shock resistance of chromium carbide based cermets." *Proc. Estonian Acad. Sci. Eng* 12.4 (2006): 358-367.

[45] Cullity, B. D. and Stock, S. R. Elements of X-Ray Diffraction, 3rd ed.; Prentice Hall: Upper Saddle River, NJ, 2001.

[46] Zhang, Y., Wang, Y., Deng, Y., Li, M. and Bai, J. "Enhanced dielectric properties of ferroelectric polymer composites induced by metal-semiconductor Zn-ZnO Core–shell structure." *ACS applied materials & interfaces* 4.1 (2012): 65-68

[47] Zhou, W., Dong, L., Sui, X., Wang, Z., Zuo, J., Cai, H. and Chen, Q. "High dielectric permittivity and low loss in PVDF filled by core-shell Zn@ ZnO particles." *Journal of Polymer Research* 23.3 (2016): 45

CHAPTER 6

Application studies of Zn/ZnO Cermet Reactant Mixture for the development of Ultrafine Grained ZnO Varistors and Multi-Functional Micro-Varistor Fillers for PVC Composites

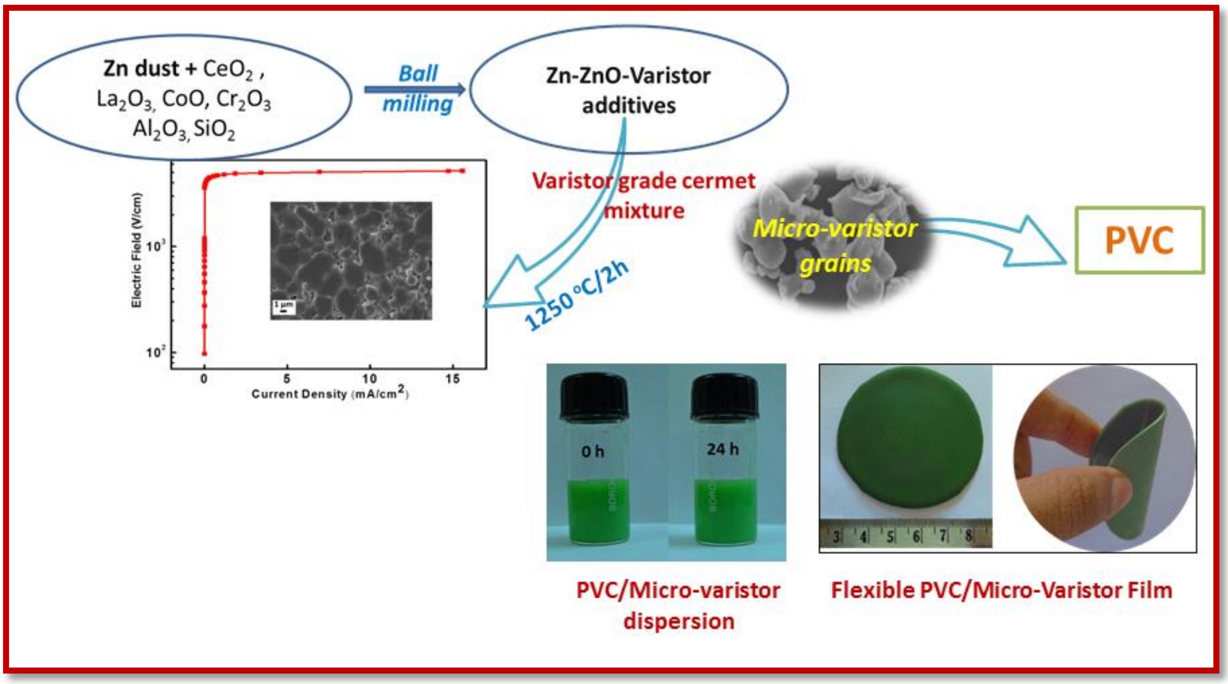

Chapter 6 is divided into two parts. The ***first part*** *describes the fabrication of high performance ZnO-rare earth varistors derived from raw Zn dust via cermet route. The blending of varistor precursor mixture was carried out by mechanical milling. The cermet mixture obtained was calcined and sintered at different temperatures to obtain dense fine grained ZnO varistors. The advantages of using Zn metal on microstructure, grain size distribution and non-linear current-voltage characteristics of ZnO varistors sintered in the temperature range 1100-1300 °C were investigated. The* ***second part*** *of this chapter describes the use of Zn dust derived microvaristors as a multifunctional filler for Poly(vinyl chloride) (PVC) matrix. The PVC/microvaristor composites were fabricated by simple solution casting method. The effect of microvaristor filler particle on the dielectric properties, thermal stability, UV resistance and mechanical behaviour of PVC composites were analysed.*

The work reported in this chapter has been published in**,**

- ***Materials and Design*** 92 (2016) 387–396
- ***Journal of Applied Polymer Science*** 135 (2018) 46031-46041.

6.1 Fabrication of Ultrafine Grained ZnO Non-linear Ceramic Resistors from Zn Dust *via* Cermet Route

6.1.1 Abstract

Cermet route was explored to fabricate high performance ZnO based varistors from raw Zn dust. The processing of ceramic–metal composite (cermet) varistor powder was done by blending micron sized (< 10 µm) metallic Zn dust with rare earth oxides (CeO_2 and La_2O_3) and other varistor forming minor additives (Cr_2O_3, CoO, SiO_2, Al_2O_3 and MnO_2) *via* mechanical milling. The toxic Bi_2O_3 and Sb_2O_3 additives for conventional ZnO varistors were avoided in the present study. The cermet varistor mixture after calcination was uniaxially pressed into cylindrical pellets and sintered in the temperature range 1100-1300 ^{o}C to obtain fine grained ZnO varistors. A comparative study of characteristics of varistor was also performed by preparing ZnO varistors from commercial ZnO under the same processing conditions. At 1250 °C, Zn dust derived cermet composition showed 99 % theoretical density, average sintered grain size ~ 1.5 µm, breakdown voltage $V_b = 477$ V mm^{-1} and non-linear coefficient $\alpha = 38$ compared to its commercial counterpart. Thus this exploratory research clearly promote Zn dust as a potential source for developing functional grade electroceramics such as high performance ZnO varistors.

6.1.2 Introduction

Varistors are electroceramic devices widely used for over voltage protection in different areas of electronics and communication technology [1-6]. Varistors possess extremely nonlinear current-voltage characteristics at ambient temperature and keep a relatively small voltage change across its terminals when a disproportionate large surge current flow through it [7]. The conventional solid state processing of varistor has plenty of drawbacks [3, 8]. The major limitations of the current varistor processing are inhomogeneous distribution of varistor additives [8], evaporation of minor dopants [9, 10], and secondary spinel and pyrochlore phases formation [10, 11]. All of the drawbacks mentioned above resulted in an undesirable grain growth in ZnO (15–20 μm) ceramics which limits the energy handling capabilities of varistors [12]. Extensive research has been carried out on low, high and variable voltage ZnO varistors which covers additive distributions, grain size control *via* novel synthesis routes, optimization of sintering conditions, tuning of grain boundary properties, and varistor degradation analysis leading to the enhancement of nonlinear properties and the breakdown voltage [12-16].

The remarkable progress in the size controlled production of devices like smart mobile phones, tablet computers and other electronic devices with improved performance and miniaturization has demanded for ever smaller high performance zinc oxide varistors [1, 2, 17]. To date large number of investigations have been carried out to enrich the performance of varistors and those attempts includes, 1) modification in selection and optimization of minor and major varistor additives in order to tailor and design the microstructure and derive better electronic properties [18], 2) enhancement of the compositional homogeneity by the modification in processing techniques [19-21], 3) new sintering methods and adjustment of processing parameters in order to lower the sintering temperature, 4) reduction or complete removal of the volatilization additive elements in varistor composition and so forth [21-23].

Since the performance of varistor is directly related to the number of grain boundaries between electrodes, it is possible to improve the varistor properties by controlling the microstructure through limiting the grain growth [3]. Therefore, efforts have been made to develop ultra-fine grained ZnO varistors by tailoring the grain size, through different synthesis techniques like sol–gel [24], precipitation [25], and combustion [26] methods. Westin and co-workers have reported sol-gel method for the fabrication of varistors which resulted in varistors with breakdown voltage 249 V mm^{-1} and α=37 [27]. Cheng *et al.* prepared high performance sol-gel based Al_2O_3-doped ZnO varistors in which the breakdown voltage increased from 720 V. mm^{-1} to 1160 V. mm^{-1} as the amount of Al_2O_3 increased from 0.0 wt % to 0.40 wt % [14]. Pillai *et al.* tried a novel mixed precursor method for the production of ZnO varistor powder which showed a high breakdown voltage of about 941 V. mm^{-1} and non-linear coefficient α = 33 at a sintering temperature of 1050 ^{o}C/ 2 h [2]. Haile *et al.* synthesised ZnO varistor *via* precipitation route and sintered at 1200 ^{o}C. Satisfactory electric behaviour with breakdown voltage 180 V mm^{-1} and non-linear coefficient α = 44 was recorded [28]. Core shell type varistor powder was synthesised by Pillai *et al*. Sintering was carried out at 1050 ^{o}C and resulting varistor showed breakdown voltage 850 V mm^{-1} and non-linear coefficient α = 33 [12].

In general ZnO varistors are categorised into two groups in terms of varistor forming additives, ZnO-Bi_2O_3 system and ZnO-Pr_6O_{11} system doped with rare earth dopants [29-32]. Presently most of the commercial varistors are based on ZnO-Bi_2O_3 system. ZnO-Bi_2O_3 based conventional ceramic varistor system has a few shortcomings due to the high reactivity and volatility of Bi_2O_3 during liquid phase sintering. Bi_2O_3 can readily react with metals used in the fabrication of multilayer chip varistors, and thus it will destroy the multilayer structure of varistors. Also it is reported that Bi_2O_3 will form an additional insulating spinel phase, which does not contribute anything to the electrical conduction [33]. Therefore, in order to overcome the above mentioned problems ZnO varistors doped with rare-earth as major additives instead of Bi_2O_3 and Sb_2O_3 along with other minor additives have been actively investigated for advanced varistors.

It is reported that rare earth elements can enhance the performance of ZnO- based varistor and show similar properties to Bi_2O_3, which form a layer of inter-granular material and supply ions to the ZnO grain boundaries to form potential barriers at the grain boundaries [30, 34, 35]. The influence of different rare earth oxides such as Sm_2O_3 [36], Er_2O_3 [37], Sc_2O_3 [38], Y_2O_3 [39], Nd_2O_3 [40], CeO_2 [41] and La_2O_3 [34] on the microstructure and electrical properties of the ZnO varistor ceramics have been investigated by many research groups. Rare earth varistor additives can significantly enhance the varistor characteristics like non-linear coefficient, leakage current, and breakdown voltage by selecting optimum rare earth element [40]. Shichimiya *et al*. investigated the effect of various rare earth elements on the break down voltage of ZnO varistors. An increase of 1-1.5 times was observed in the breakdown voltage for certain amount of rare earths [42]. Nahm *et al*. studied the effect of La_2O_3 on the breakdown voltage of ZnO varistors. Break down voltage of 777 V. mm^{-1} was obtained for 1 mol % La_2O_3 addition after sintering at 1230 ^oC [34]. During high temperature sintering, rare earth oxides tend to segregate ZnO grain boundary inhibiting the ZnO grain growth by pinning ZnO grains, and thereby increasing the breakdown strength [40]. Rare earth doping also can enhance the non-linear performance of ZnO varistors. Addition of 0.5 mol % La_2O_3 to ZnO varistor composition resulted in a non-linear coefficient value of 81 after sintering at 1300 ^oC. 4 mol % Y_2O_3 additions resulted in a non-linear coefficient value of 87 for ZnO varistor sintered at 1300 ^oC [43]. Lei *et al.* reported the addition of 0.9 mol % CeO_2 resulting in a non-linear coefficient 30 for ZnO varistor sintered at 1175 ^oC [44]. Thus by adding rare earth oxides by certain amount the grain boundary properties including interface state density, donor concentration, and barrier height can be tailored so that the non-linear coefficient enhanced [45]. Out of various rare earth oxides investigated for varistor performance enhancement La_2O_3 and CeO_2 are easily available and less expensive [46]. The present study used La_2O_3 and CeO_2 instead of Bi_2O_3 and Sb_2O_3 in conventional varistor system.

The present study used ball milled mixture of Zn dust and major varistor additives La_2O_3 and CeO_2 along with other minor additives as the precursor for the fabrication of ZnO varistors. The minor additives used in the present varistor composition include SiO_2, Cr_2O_3, Al_2O_3, CoO and MnO and are selected from the earlier reports on enhancement of varistor properties. SiO_2 form a liquid phase during sintering and plays an important role in controlling the sintering mechanism and increases the power handling capability and energy absorption of the varistor [47]. MnO and CoO enhances the nonlinear properties. Al_2O_3 increases the ZnO grain conductivity [2]. Cr_2O_3 has been stated to yield better varistor properties *via* reduction in grain size (larger volume of grain boundary) [2, 3].

As mentioned in the Section 3.1.4.2 milled Zn contains both ZnO seed particle and metallic Zn and it can be considered as a ‘cermet’ source which is a mixture of ceramic and metal. Thus the current study proposed a facile approach for the fabrication of rare earth doped ZnO varistor from an industrial by product Zn dust for the first time.

6.1.3 Experimental Section

6.1.3.1 Materials

Zinc dust (Binani Zinc Pvt. Ltd. India, 99.9%, <10 µm) and zinc oxide (Sigma Aldrich 99.0%) were used as two different precursors for the fabrication of ZnO varistors. Cerium nitrate (Sigma Aldrich, 99 %), Lanthanum nitrate (Alfa Acer, 99.99 %), Silicon dioxide (Sigma Aldrich, 99.5%), Chromium nitrate (Sigma Aldrich, 99 %), Aluminium nitrate (Merck, 95 %), Cobalt nitrate (Sigma Aldrich, 99%) and Manganese acetate (Sigma Aldrich, 98 %) were used as the varistor additives along with ZnO source for the fabrication of varistors.

6.1.3.2 ZnO Varistor Fabrication from cermet mixture

The schematic representation of processing of ZnO varistor from cermet source is shown in Figure 6.1. Varistor composition constituting, 97.1 mol % ZnO (9.39 g) + 0.5 mol %

CeO_2 (0.10 g) + 0.5 mol % La_2O_3 (0.19 g) + 0.2 mol % Al_2O_3 (0.02 g) + 0.5 mol % Cr_2O_3 (0.09 g) + 0.5 mol % SiO_2 (0.03 g) + 0.5 mol % CoO (0.15 g) + 0.2 mol % MnO_2 (0.03 g), was initially prepared. The precursor mixture was then charged into polypropylene milling bottle (250 cm^3 chamber volume), along with Zirconia balls (dia. ~10 mm.) in ethanol medium and milled for 24 h using a belt driven ball mill (250 rpm). The collected milled slurry was then dried overnight, at a temperature of 60 °C in a vacuum oven. The dried cermet mixture was then calcined at 600 °C for the decomposition of the volatile components.

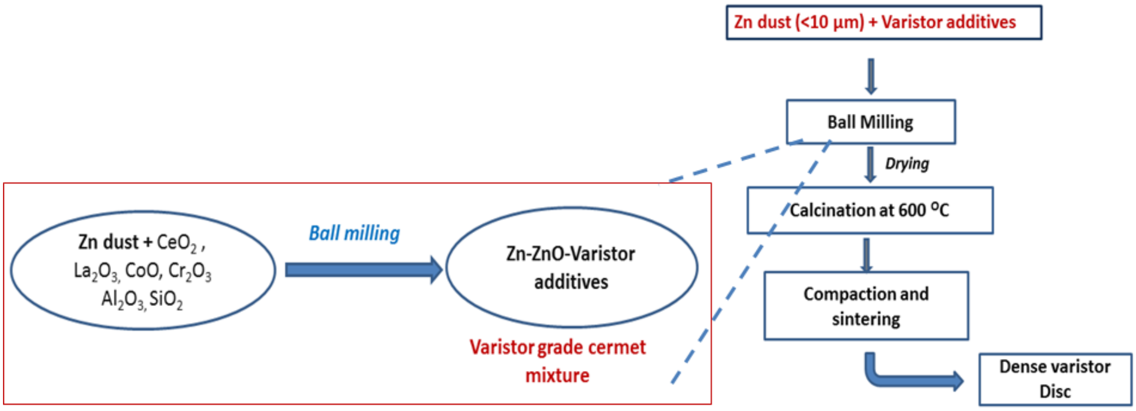

Figure 6.1: Schematic representation of the processing of ZnO varistors from cermet source.

Then the varistor grade powder was pressed in the form of cylindrical discs having 10 mm diameter and 1 mm thickness at a pressure of 100 MPa. 1 mL PVA (Polyvinyl alcohol, 0.5 %) was added into the cermet powder as the binder material before pressing. The varistor discs were sintered at 1100, 1200, 1250 and 1300 °C in air for 2 h. Sintering was performed at a heating rate of 3 °C min^{-1} under air atmosphere. To ensure the removal of organic binder, at 600 °C, the sample was hold for 20 min. At the target temperature, a holding time of 2 h was given to the sample to facilitate the maximum densification. Both sides of the sintered varistor discs were lapped with SiC paper and finely polished to a mirror finish surface using 3 μm diamond suspensions. The samples were etched at a temperature of 1000 °C prior to the microstructural analysis. The varistor discs were also processed from commercial ZnO powder (Aldrich chemicals, 99.0 %) with same composition under identical conditions. ZnO varistor processed from the metallic Zn dust *via* cermet route was compared with that processed from commercial. For convenience, the former is named as ‘cermet route’ and the latter as ‘oxide route’. Both samples were characterized for the particle size, phase analysis, densification, microstructural and non-linear features.

6.1.4 Result and Discussion

Cermet can be considered as a composite material consisting of both ceramic and metallic constituents [48]. During milling, Zn dust gets partially oxidised to ZnO and the resulting mixture contains both metal (Zn) and ceramic (ZnO) components. Hence the term ‘cermet’ has become relevant in the present study. The cermet composition of varistor precursor after milling of Zn dust and other varistor additives was confirmed from the XRD spectra of milled powder as shown in Figure 6.2. The XRD spectra showed the peaks corresponding to both Zn and ZnO and thus confirmed the presence of both metal and ceramic components in the varistor precursor mixture. Thus the term ‘cermet precursor’ becomes suitable in the present study.

XRD analysis of varistor mixture processed by cermet route and oxide route calcined at identical conditions is presented in Figure 6.3 (a). Both the samples showed well resolved characteristic peaks of crystalline ZnO. The major peaks observed can be assigned to (100), (002), (101), (102) (110), (103), (200), (112) and (201) planes of wurtzite ZnO (JCPDS file No. 36- 1451) and a minor peak corresponding to zinc silicate (Zn_2SiO_4) ((200) plane) was also identified. Kutty *et al*. reported the presence of this minor peak corresponding to zinc silicate (Zn_2SiO_4), which is formed by the addition of SiO_2 to the varistor composition [47].

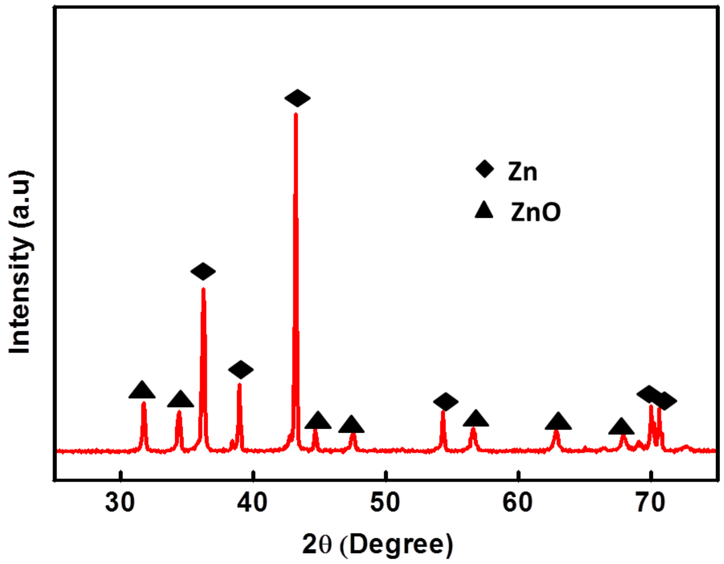

Figure 6.2: XRD analysis of varistor grade cermet powder obtained *via* mechanical milling of Zn dust along with varistor additives.

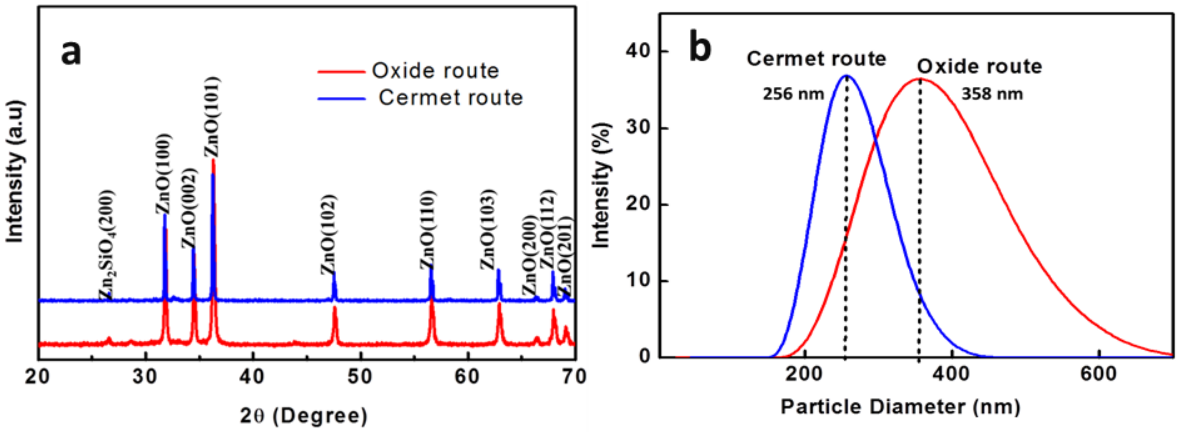

Figure 6.3: (a) Phase analysis and (b) particle size distribution curve of varistor powder processed *via* cermet route and oxide route.

The particle size distribution of varistor powder derived *via* cermet route and oxide route is shown in Figure 6.3 (b). From the size analysis the cermet route derived varistor particle showed an average particle size of 256 nm with narrow size distribution while those derived from oxide route showed an average particle size of 358 nm with broad size distribution.

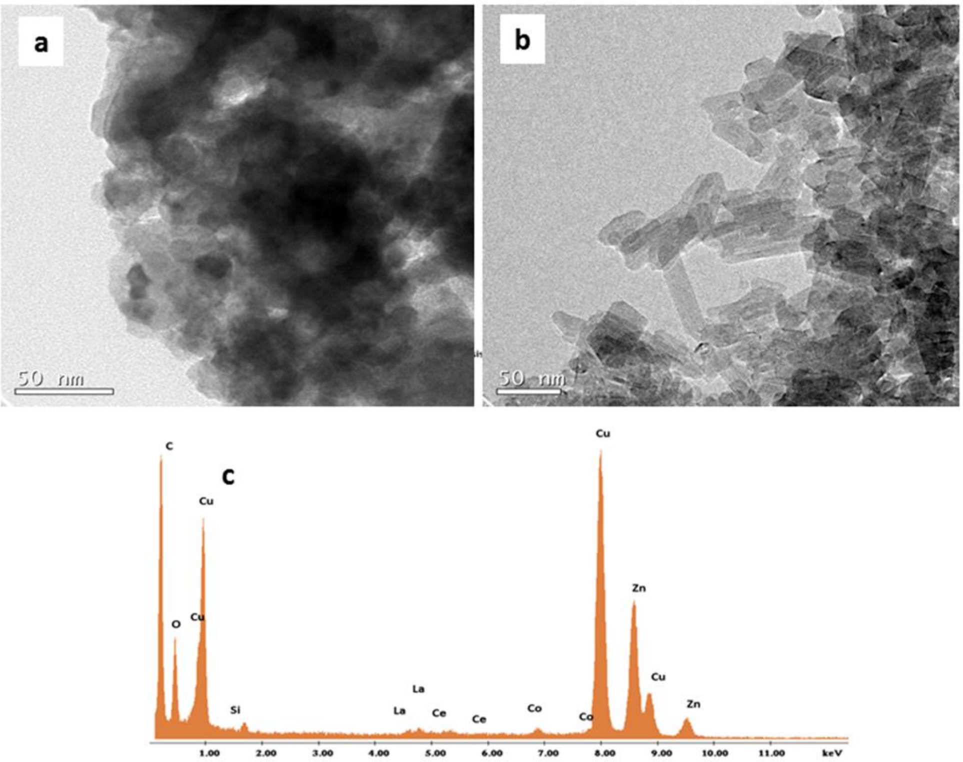

Figure 6.4: TEM images of varistor powder derived *via* (a) oxide route, (b) cermet route and (c) elemental analysis (EDS) of cermet route derived varistor powder.

TEM images of varistor powder obtained *via* oxide route and cermet route are shown in Figure 6.4 (a) and (b) respectively. The TEM analysis revealed large agglomerates of spherical particles (Figure 6.4 (a)) for the oxide route and mixed morphologies of nanorod and spherical particle for the cermet route (Figure 6.4 (b)) derived samples. The rod shaped and nearly spherical morphologies obtained for cermet route derived varistor powder may have multiple advantages including enhanced compaction of particles during pressing, production of oriented-ZnO grains upon sintering and lowering of activation energy during sintering for cermet route derived varistor sample. The uniform distribution of varistor forming additives was also expected for the cermet route derived varistor samples. The corresponding EDX analysis, presented in Figure 6.4 (c), gave clear evidence for the presence of all additive elements in the cermet derived varistor samples**.**

The density profile for the varistor derived from cermet and oxide route are shown in Figure 6.5. The varistor powder derived *via* cermet route contains nano sized rod shaped particles and nearly spherical particle (Figure 6.4 (b)). This resulted in better compaction during pressing and enhanced sintering density compared to its oxide route counterpart. An increase in relative density of varistor from 5.36 to 5.60 g. cm^{-3} was observed for cermet route derived sample, whereas in oxide route, the sintered density has increased from 4.92 to 5.56 g. cm^{-3} in the temperature range 1100-1300 °C.

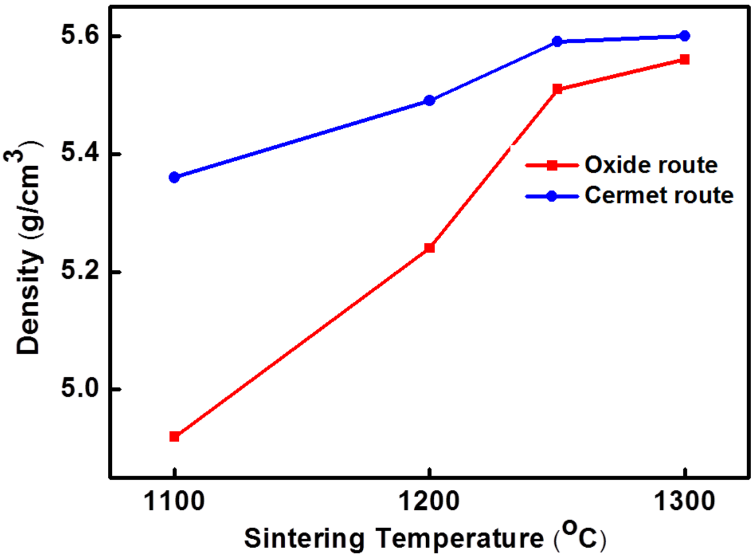

Figure 6.5: Variation of density of varistor samples obtained *via* cermet and oxide route at different sintering temperature.

Thus the earlier densification of ZnO varistor derived from cermet source compared to that derived from commercial source is confirmed. The cermet route derived varistors densified close to its theoretical density at 1250 °C and produced more number of extremely fine grains with better compositional homogeneity compared to oxide route derived varistor sample.

6.1.4.1 Microstructure of varistors

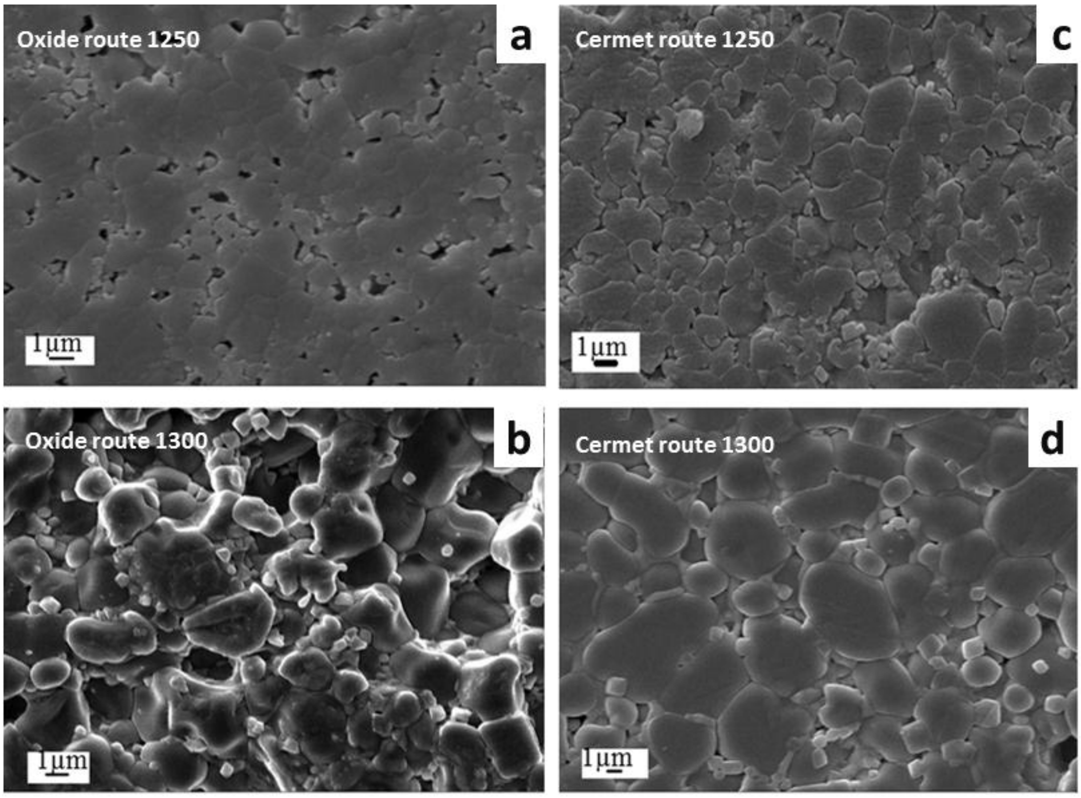

Figure 6.6: SEM images of varistor derived via (a) oxide route @1250 ^{o}C, (b) oxide route @ 1300 ^{o}C, (c) cermet route @1250 ^{o}C and (d) cermet route @ 1300 ^{o}C.

Figure 6.6 (a)–(d) depicts the SEM microstructures of surface of polished and etched varistor processed *via* oxide and cermet routes sintered at different temperatures. The oxide route derived varistor ceramics (Figure 6.6 (a)) showed porous microstructure with grain coalescence and isolated ZnO grains at 1250 °C. The corresponding cermet route derived varistor microstructure (Figure 6.6 (c)) appeared to be far superior compared to those processed from oxide route. The microstructure revealed elongated grains with an average grain size in the range of 1–2 μm. During sintering, grains are formed by diffusion process between particles. In varistor microstructure, grain boundaries were formed when two identical grains joined together. This grain boundary material constitutes the same semiconducting material as that of grain. However at grain boundary, defects and dopants are present due to the segregation of various additives during sintering.

The basis of varistor action is voltage dependant electron transport across charged grain boundaries [49, 50]. The varistor I–V characteristics are controlled by the electrostatic barrier existing at the grain boundaries [50]. The rare earth oxides in the varistor composition controlled the grain growth by segregating and pinning the grain boundaries [23]. Thus the fine grained varistors derived from cermet route can have more active grain boundaries per unit volume, which significantly contribute to the varistor properties.

Further increase in sintering temperature beyond 1250 ^{o}C resulted in grain growth in both oxide and cermet route derived samples (Figure 6.6 (b) and (d)). The higher growth rate was observed for oxide route derived sample. From the above observations, the use of Zn dust as the starting material for varistor fabrication seems to be promising because Zn metal preferably forms low-melting phase at lower sintering temperatures and facilitates mass transfer of different varistor additive atoms in the varistor microstructure to modify the ZnO grain and grain boundary. Addition of rare earth elements, mainly CeO_2 and La_2O_3 further helps in controlling the grain size by restricting the grain growth. The oxide additives like La_2O_3 with +3 valences are promising candidates for controlling the non-linear properties of varistors [11]. In the past years, large numbers of researches have been carried out to improve the microstructural characteristics of ZnO varistors. Varistor fabricated from nano ZnO (prepared by solid state pyrolysis reaction) combined with various oxide additives showed larger number of grain boundaries per unit area with comparatively higher breakdown voltage (656 V. mm^{-1}) [19]. However, due to higher surface area of the synthesized nano powders, grain boundary phase engineering and grain size control becomes more challenging in actual industrial fabrication conditions. In addition to that, varistors derived from nano precursors sometimes end up with high leakage current that make it inadequate for high energy varistors.

6.1.4.2 Non-linear characteristics

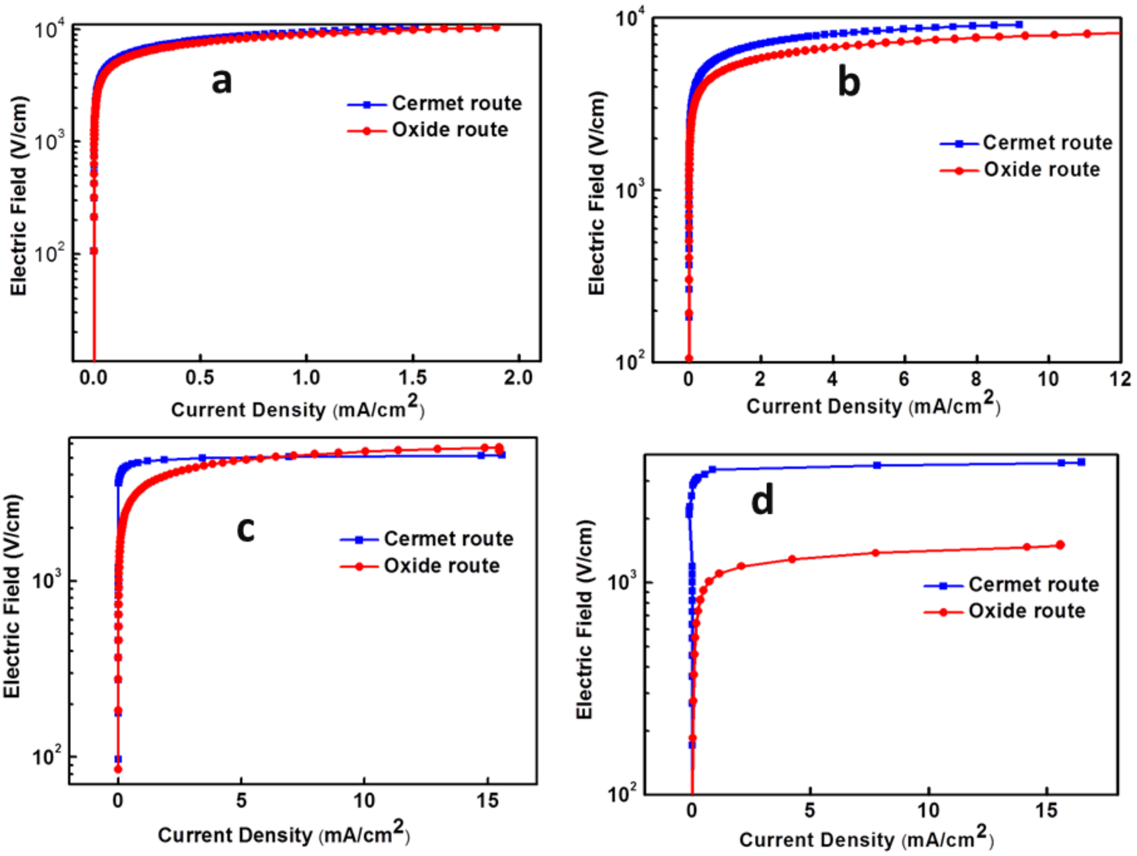

Figure 6.7: E-J characteristics of ZnO varistors processed *via* cermet route and oxide route sintered at temperatures (a) 1100, (b) 1200, (c) 1250 and (d) 1300 ^{o}C.

The comparison of non-linear electric field *vs* current density (E–J) characteristics of cermet derived ZnO varistors with its oxide route counterpart are presented in Figure 6.7 (a)-(d). Like typical E-J characteristics of varistors, the samples in the present study also show high and low resistivity regions resembling a diode. The non-linear property of varistors is determined by the sharpness of the knee separating these two regions [17]. In this work, the nonlinearity of varistors prepared *via* different routes was investigated for the samples sintered in the temperature range 1100 to 1300 °C. At all the sintering temperatures, cermet route derived varistors showed similar but improved non-linear properties compared to its oxide route counterpart. Among the samples sintered at 1100 °C, the cermet derived varistor showed a break down voltage (V_b) of 7529 V cm^{-1}, whereas the oxide route derived varistor showed a V_b of 7182 V cm^{-1}.

This value gradually decreased for both the samples when the sintering temperature was increased to 1300 °C. At 1300 °C, the cermet route resistors showed V_b value of 3421 V cm^{-1} while the ZnO derived varistors showed V_b value of 1105 V cm^{-1}. The beneficial properties of varistor microstructure in cermet route derived samples are clearly visible from the higher break down voltage compared to oxide route derived sample at all the sintering temperatures. According to the Equation (6.1), the break down voltage is directly proportional to number of grains/unit volume. Hence the decrease in breakdown voltage at higher sintering temperature is due to the increase in grain size and associated decrease in number of grains**.**

$$E_{1\,mA} = \frac{V_{gb}}{d} \qquad (6.1)$$

where, 'V_{gb}' is the breakdown voltage per grain boundary and 'd' is the average grain size.

The varistor parameters calculated for oxide and cermet routes derived samples at different sintering temperatures are summarised in Table 6.1. Although, a lower sintering temperature (1100 and 1200 °C) produced varistors with high breakdown voltage, the nonlinearity coefficient was relatively low for both the systems due to the reduced densification of varistors at lower sintering temperatures. Therefore a sintering temperature of above 1200 °C is highly recommended for varistors for obtaining better performance. Out of the eight samples prepared at different experimental conditions the cermet route derived varistors sintered at 1250 °C showed better E–J characteristics and markedly improved nonlinear properties, with $V_b = 4778$ V cm^{-1}, $\alpha = 38$ and $J_L = 0.01$ μA cm^{-2}.

Table 6.1: Comparison of electrical characteristics of varistors derived *via* oxide route and cermet route.

Sintering temperature (°C)	d (μm)		Density (ρ) (g/cm^3)		E $_{1mA}$ (V/cm)		α		J_L (μA/cm^2)	
	C - route	O - route	C - route	O - route	C - route	O - route	C - route	O - route	C - route	O - route
1100	-	-	5.36	4.92	7529	7182	-	-	0.46	0.52
1200	1-1.5	1-2	5.49	5.24	5873	5050	12	5	0.21	0.45
1250	1-2	2-3.5	5.58	5.51	4778	3494	38	6	0.01	0.30
1300	2-3.5	3-5	5.6	5.56	3421	1105	46	9	0.002	0.01

C – route: Cermet route, O – route: Oxide route

6.1.4.3 Dielectric Characteristics of varistors

Figure 6.8 (a) shows the dielectric characteristics of varistors derived from both cermet and oxide routes. At a selected frequency of 10 kHz, the dielectric constant linearly increases with sintering temperature and a two fold increase in dielectric constant was observed for samples sintered at temperatures above 1200 °C. The increase in sintering temperature reduced the dielectric loss. This can be attributed to the decreased leakage current at higher sintering temperature due to improved densification of the samples. At 10 kHz, the dielectric constant of varistors derived from cermet route showed an increase from 15–616 while the same is only 14–299 for the oxide route derived varistors with the increase in sintering temperature.

Thus, out of different sintered polycrystalline varistor ceramics prepared *via* cermet and oxide route, the varistors produced *via* cermet route showed good dielectric properties compared to oxide route derived one processed at under similar conditions.

This can again be explained with the support of the grain size effect on dielectric properties as per the Equation 6.2,

$$\varepsilon_{APP} = E_g\left(\frac{d}{t}\right) \qquad (6.2)$$

where, ‘E_g’ is the dielectric constant of ZnO, ‘d’ is the average grain size and ‘t’ is the depletion layer width.

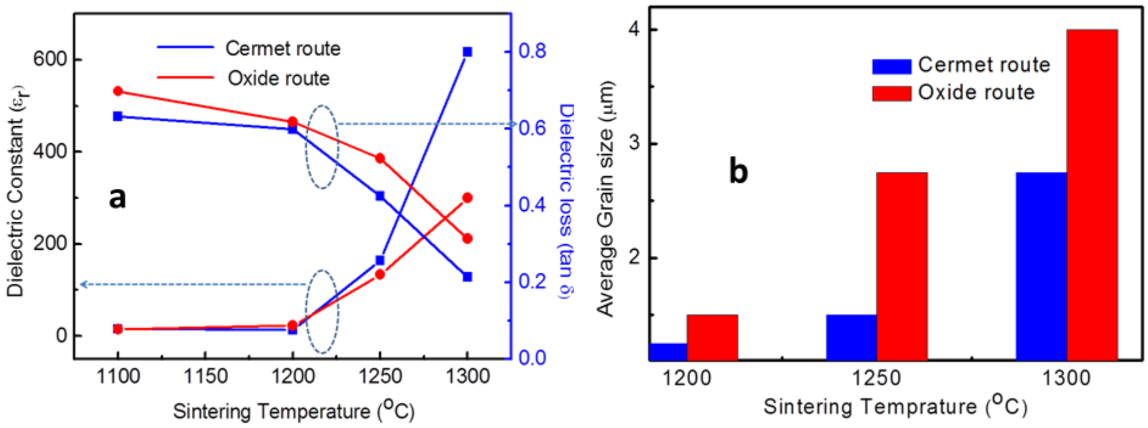

Figure 6.8: a) Variation of dielectric properties and (b) grain size with sintering temperature for cermet route and oxide route derived varistors.

At higher sintering temperatures, the increase in grain size reduced the width of depletion layer resulting in an increase in dielectric constant. The average grain size of both cermet and oxide route derived varistors at different sintering temperature are shown in Figure 6.8 (b). Thus, from the dielectric and sintering studies, it can be well presumed that, the porosity and grain size are the key factors deciding the varistor performance. The porous, macro sized varistor grains obtained for oxide route derived varistors resulted in poor dielectric and varistor properties, when compared to the dense, fine grained varistor derived from the cermet route.

Thus, the cermet route derived samples were found to be superior to oxide route derived samples in all respects. The adaptation of Zn dust as the starting material for the

ZnO varistors permits ample opportunities for framing highly economical and low cost field limiting materials for various applications.

6.1.5 Conclusions

ZnO varistors were successfully fabricated from Zn dust with rare-earth oxides La_2O_3 and CeO_2 as the major additives and other minor additives. The properties of Zn dust derived varistors were studied and the results were compared with the commercial ZnO derived varistor counterparts. The varistor derived from Zn dust source exhibited promising microstructural properties, sintering benefits and non-linear properties. The advantages like low grain-size, good non-linear characteristics and low leakage current were systematically reported for the cermet derived varistors when compared to the commercial counterpart. The cermet route derived varistors produced dense, nano-micro mixed and fine-grained varistor microstructures. The best varistor performance was obtained for the cermet route derived sample sintered at 1250 ^{o}C/2 h which showed better E–J characteristics and markedly enhanced nonlinear properties, *viz.* V_b = 4778 V cm^{-1}, $\alpha = 38$ and J_L = 0.01 μA cm^{-2}. The current study foresees many practical applications using cermet derived varistor samples which were developed through a simple and low cost approach. Thus the use of a partially avoided industrial by-product Zn dust is reported for the first time for high quality application like ZnO varistors.

6.2 Design and Fabrication of Flexible Poly (vinyl chloride) Dielectric Composite Incorporated with ZnO Micro-Varistors Derived from Zn dust

6.2.1 Abstract

Flexible Poly(vinyl chloride) **(**PVC) composite films reinforced with micro-varistor (MV) filler were processed through a facile solution casting approach. ZnO micro-varistor was prepared through solid state mixing of metallic Zn dust, an industrial by-product obtained from zinc alloy processing industry, with additive precursors by employing milling. Microvaristor particle loading are systematically varied to have better effect on the various properties of PVC composite. The variation of dielectric properties and conductivity of PVC/MV composite was studied over a broad range of frequency and the results are correlated with the loading of MV filler in the polymer matrix. The variation in dielectric properties is explained on the basis of interfacial polarization at polymer-filler boundary. The incorporation of microvaristor resulted in dielectric constant tunability (ε = 2–37) without any drastic change in the dielectric loss (0.02–0.05). It was seen that the addition of microvaristors also enhanced thermal and mechanical stability and UV resistance properties of the PVC/MV composites. The addition of MV filler in PVC enhanced the microhardness and maintained the tensile properties without any significant loss. After UV irradiation of PVC/MV composite film, remarkable mechanical stability retention by 95 % was obtained compared to pure PVC for which only 75 % retention of mechanical properties was observed. Thus, Zn dust-derived ZnO varistors could be potentially exploited to design functional PVC composites for electronic applications.

6.2.2 Introduction

Recently, ceramic fillers with high dielectric permittivity have become one of the basic requirements to design modern electronic and electrical power system components [51-

55]. The recent investigation on fabricating flexible electronic modules out of hybrid organic–inorganic designs from the solution processable polymers demand such dielectric ceramic filler to facilitate certain requirements for the respective applications [56-59]. Polymers possess high break down strength and can offer excellent opportunity for scale-up and shaping into intricate designs [60, 61]. Moreover, its wide availability at lower cost makes them a promising candidate for the fabrication of electronics and electrical power systems [60-64]. Poly (vinyl chloride) (PVC) is a widely used solution processable thermoplastic for electrical cable applications [65]. The main uniqueness of PVC is its exceptional durability with an almost unaffected functionality [66-68]. Even though it's high stiffness, chemical stability and inherent flame retardancy are truly lucrative, properties such as poor UV stability, low toughness, low heat-softening temperature, and thermal degradation during processing limits it's various industrial applications [69-73].

PVC is prone to several environmental effects like autocatalytic dehydrochlorination and related decolouration, photo-chemical decomposition under solar irradiation, and also attack of oxygen from the atmosphere through radical mechanism [74, 75]. Thus, there is an increasing demand for a variety of functional ceramic fillers which are not only able to absorb UV radiation and radical scavenging but also to produce desired dielectric properties good mechanical and thermal stability for PVC composites.

Towards these objectives several interesting studies have already been carried out reported. Several nano-fillers like polysiloxanes [76], clay [77], carbonates [78], and metal oxides [79] etc., have been reported to improve the thermo-mechanical properties of pure PVC. Cho and Choi and Kim *et al*. reported that the addition of TiO_2 to the PVC matrix can absorb harmful wavelengths in solar radiation and can protect the polymer matrix from the photochemical decomposition [80, 81]. UV radiation aging effect of

PVC/$CaCO_3$ and PVC/$CaCO_3$/macromolecular modified composites was investigated by Liu *et al*. [82]. The study confirmed that the modified nano $CaCO_3$ fillers are capable of resolving the issues connected with aging effect by UV radiation and its influence on the mechanical strength retention of polymer matrix. The ability of PVC matrix to hold-up UV aging behaviour by the addition of talc, $CaCO_3$ and SiO_2 was reported by Zhang *et al.* [83] PVC/Nano clay composite with both hectorite and bentonite based organically modified clays was formulated by Awad *et al*. and It was observed that the incorporation of nanoclay to PVC improved the thermal stability of PVC composite [69].

Flexible graphene/PVC film with improved mechanical and electrical properties was reported by Vadukumpully *et al.* [71]. An increase in Young's modulus by 58 % and an improvement in tensile strength by 130 % were obtained with very low loading of graphene. For 6.47 wt % of filler loading maximum conductivity of 0.058 $S.cm^{-1}$ was also noticed. The effect of CNT additives in PVC matrix was investigated by O'Connor *et al.* [84]. The resulting composite showed improved mechanical properties by 70 % and 50 % enhancement in Young's modulus and tensile strength respectively. However, due to the challenge in getting stable dispersion in organic solvents and their higher cost, the use of CNT based filler has been impeded [85]. By the addition of metal salt fillers such as $CuCl_2$, $CoCl_2$ and $FeCl_2$A a six fold increase in the electrical conductivity value of PVC composite is observed [86]. However, these fillers have bad effects on the thermal stability of the polymer.

For polymer composites the dielectric loss is a highly sensitive parameter. Fillers such as metal salts, CNT and graphene have remarkable effect on the desired low-dielectric loss of PVC composites [61]. Usually the addition of these fillers resulted in high dielectric loss in the PVC composites. For such linear-resistive fillers, an early breakdown of polymer composites is also seen [87]. In this scenario, nonlinear resistive filler [88] offer an additional way to supply some conductivity to insulating polymer matrix while still maintaining other multifunctional benefits.

From the previous literature it is clear that there is no single-filler available to solve the issue of UV attack maintaining high thermal, electrical, and mechanical stability of the PVC composites at the same time. In this contest, present study is devoted to explore the nonlinear, UV stable rare earth doped ZnO micro varistor fillers in PVC matrix, which is not yet reported. For this purpose, new high-energy/high-field varistor filler [89] is designed from the low cost Zn dust; which is another unique outcome of this work.

Thus, the present work is an attempt to explore the role of nonlinear resistive micro varistor (MV) filler derived from Zn dust on the thermal behaviour, UV stability, mechanical and dielectric performance of PVC matrix composite dielectric materials, which has not been previously studied or reported.

6.2.3 Experimental Section

6.2.3.1 Materials

Zinc dust (Binani Zinc Pvt. Ltd., India, 99.9 %, D_{avg} ~10 µm) was used as ZnO precursor. $Ce(NO_3)_3.6H_2O$ (Sigma Aldrich, 99 %), $La(NO_3)_3.6H_2O$ (Alfa Acer, 99.99 %), $Co(NO_3)_2.6H_2O$ (Sigma Aldrich, 99 %), SiO_2 (Sigma Aldrich, 99.5 %), $Cr(NO_3)_3.9H_2O$ (Sigma Aldrich, 99%), $(CH_3COO)_2Mn.4H_2O$ (Sigma Aldrich, 98 %), and $Al(NO_3)_3.9 H_2O$ (Merck, 95 %) were used as varistor additives. PVC K-67 suspension grade free flowing powder was used as polymer matrix. Tetrahydrofuran (THF) (Merck) was used as the solvent for PVC.

6.2.3.2 Preparation of Varistor Filler

Rare earth added nonlinear ZnO micro-varistor (MV) was first processed according to the procedure reported in section 6.1.3.2. Further, the calcined powder was pressed into cylindrical discs and then sintered at 1250 °C in air for 2 h to obtain the dense ZnO varistors as optimised in the previous study. The sintered varistors were crushed in order to get the ZnO MV grains. The MV grains wet ball milled again for 24 h in ethanol medium. After drying (100 °C, overnight), the milled varistor grains were directly used as micro-varistor filler for fabricating PVC/MV composites.

6.2.3.3 Fabrication of PVC/Varistor Composite Film

PVC composite incorporated with ZnO microvaristor filler was fabricated by simple solution blending method. To dissolve PVC granules THF was used as the solvent. PVC suspension in THF was obtained by magnetic stirring at room temperature (32 °C) for 60 min. The ZnO MV grains are dispersed in THF medium using an ultrasonic bath with frequency 40 kHz (GT Sonic, Ultra Instruments, India) (for 30 min). Subsequently the suspension of MV/THF and PVC/THF was mixed together under magnetic stirring for 3 h to achieve a uniform PVC/MV suspension in THF. After obtaining a homogeneous PVC/MV suspension, it was poured into a glass dish (Schott Duran petri dish) and dried at 40 °C in vacuum oven to obtain thin solid film of PVC/MV composite by solution casting method. The MV filler loading was varied from 0 to 70 wt % and the samples were marked as PVC 0, PVC 30, PVC 50, and PVC 70 with respect to the content of filler.

6.2.3.4 UV Irradiation

The UV irradiation of the PVC/MV composite film was performed inside a closed UV chamber having a UV light source with an intensity of 0.4 mW. cm^{-2} and wavelength 200–400 nm. Inside the UV chamber the films were vertically suspended for 12 h.

6.2.4 Results and Discussion

6.2.4.1 Varistor Properties of the Filler

In the previous study, described in the Section 6.1, the sintering temperature for varistors prepared through cermet route was optimised at 1250 °C/ 2 h. The XRD pattern of MV filler sintered at 1250 °C/ 2 h is shown in Figure 6.9(a). The XRD pattern showed well resolved characteristic peaks of crystalline ZnO. All the peaks observed were indexed according to the JCPDS file of wurtzite ZnO (No. 36–1451) and the major peaks are assigned to (100), (002), (101), (102), and (110) planes.

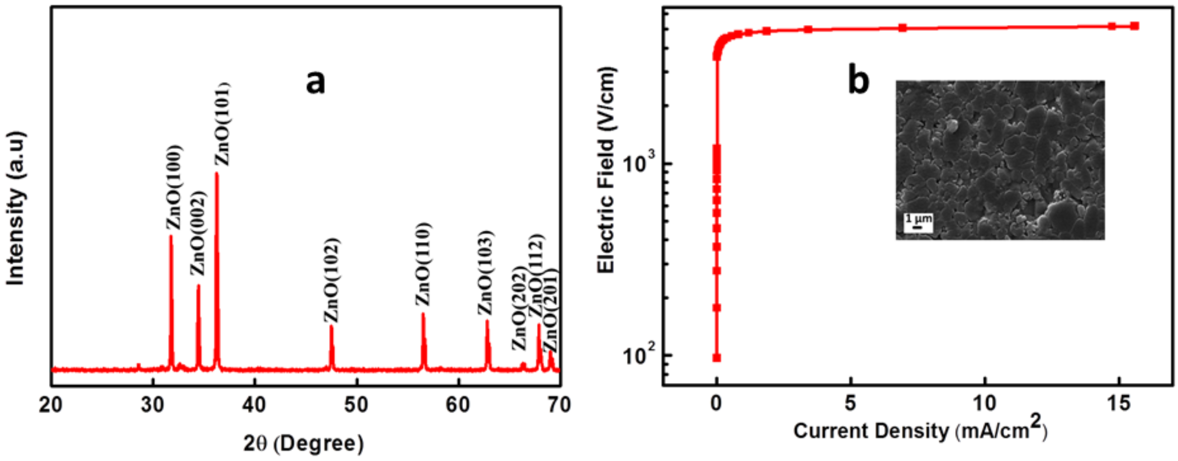

Figure 6.9: (a) XRD pattern and (b) E-J characteristics of ZnO varistor derived from cermet source sintered at 1250 °C/ 2h and microstructure of varistor sintered at 1250 °C/ 2h (b, inset)

The E–J characteristic of ZnO varistor derived *via* cermet route and sintered at 1250 °C is presented in Figure 6.9 (b). It resulted in good varistor performance with break down voltage (V_b) = 4778 V. cm^{-1}, leakage current (J_L) = 0.01 mA. cm^{-2}, nonlinear coefficient (α) = 38 and average grain size 1.5 µm. The corresponding microstructure is presented in the inset tile within Figure 6.9 (b).

6.2.4.2 Effect of Ball Milling on Micro-Varistor Filler Morphology

The SEM microstructure of MV filler after milling (24 h) is shown in Figure 6.10 (a). Milling leads to the breakdown of large agglomerates of MV filler particle. The particle size distribution of milled MV filler is shown in Figure 6.10 (b). After milling, the particles become finer and the size was significantly reduced to nearly 950 nm with narrow distribution.

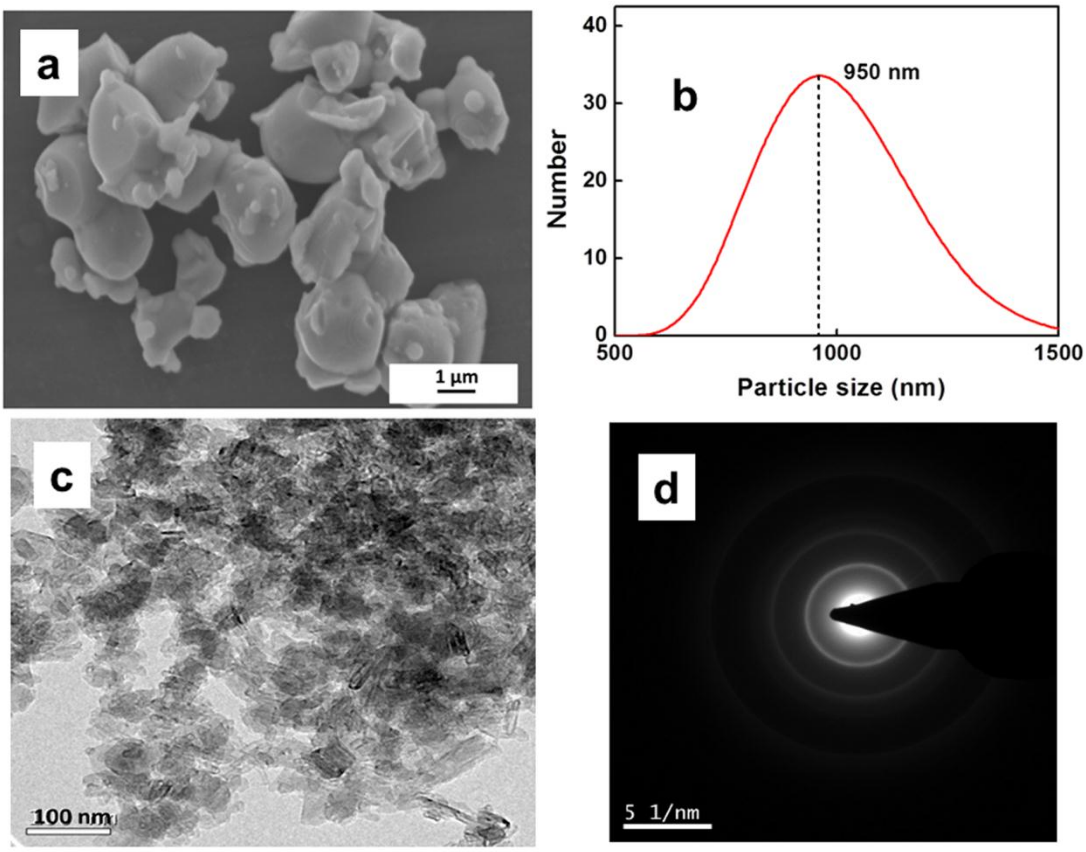

Figure 6.10: (a) SEM image, (b) The size distribution (c) TEM image and (d) SAED pattern of sintered MV filler after ball milling.

The grain-grain boundary junctions in the MV filler can be clearly seen from the micrograph. The TEM images of varistor filler is shown in the Figure 6.10 (c). It can be seen that the MV filler particle constitute both rod and spherical shaped particles. The good crystalline nature of the MV filler particle is well evident from the corresponding SAED pattern presented in Figure 6.10(d).

6.2.4.3 Structure, Phase and Thermal Analysis of PVC/MV Composites

The structure of PVC is depicted in Figure 6.11 (a). Normally, PVC exists in the amorphous state with polar Cl atom in its structure. It is synthesised by the free radical polymerization of vinyl chloride. Figure 6.11 (b) displays the processing of PVC/MV composite *via* solution blending approach. In the as-prepared PVC/MV suspension, MV grains are suspended well in PVC solution without any stabilizing agents, as shown in Figure 6.11(c).

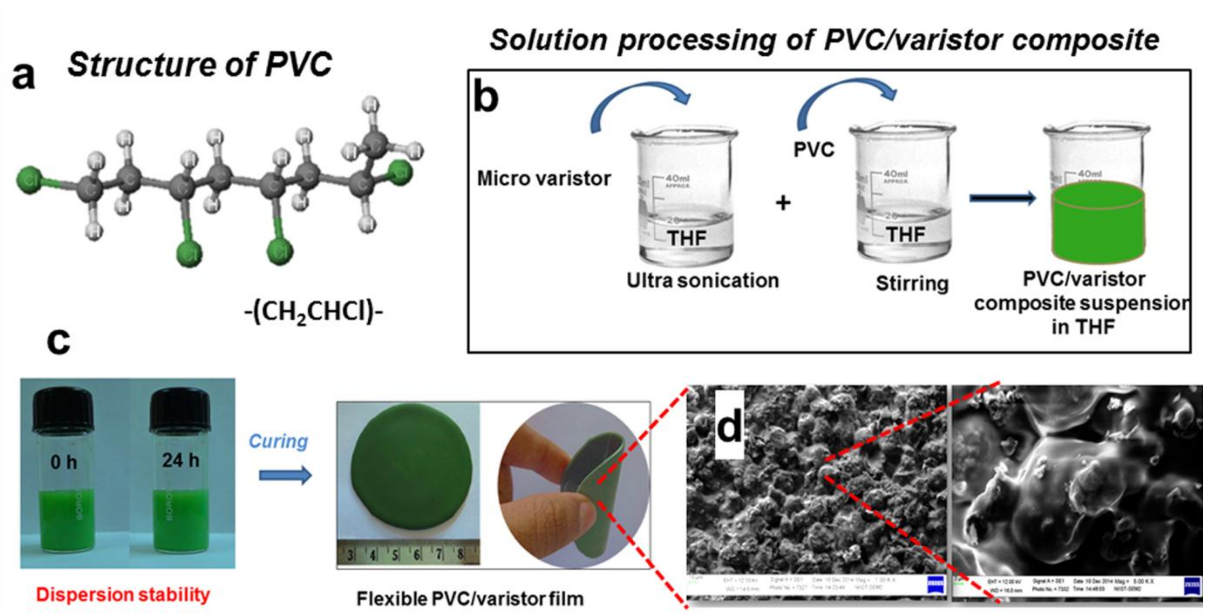

Figure 6.11: (a) Structure of PVC, (b) processing of PVC/MV composite, (c) stable suspension of PVC/MV composite and flexible PVC/MV composite film, and (d) SEM image of PVC/MV composite film.

The PVC/MV suspension kept undisturbed for 24 h. The uniform and stable suspension of PVC/MV composite is still observed, suggesting the stability of PVC/MV suspension. After curing at room temperature (32 ^{o}C) homogeneous PVC/MV composite film was obtained. The PVC/MV film obtained is flexible so that it could be bent easily in different directions. The SEM images of PVC/MV composite (Figure 6.11 (d)) showed highly rough surface of film, which is a clear indication of proper blending of filler in the matrix.

Figure 6.12 (a) shows the phase analysis of pure PVC and PVC/MV composite (PVC 50). The phase analysis of pure PVC reveals its highly amorphous characteristics. The phase analysis of PVC/MV composites shows distinct characteristic peaks of crystalline ZnO. The peaks are indexed based on the JCPDS file of hexagonal wurtzite

ZnO (no. 36–1451). The peaks are assigned to (100), (002), (101), (102), and (110) planes. The TG analysis of MV

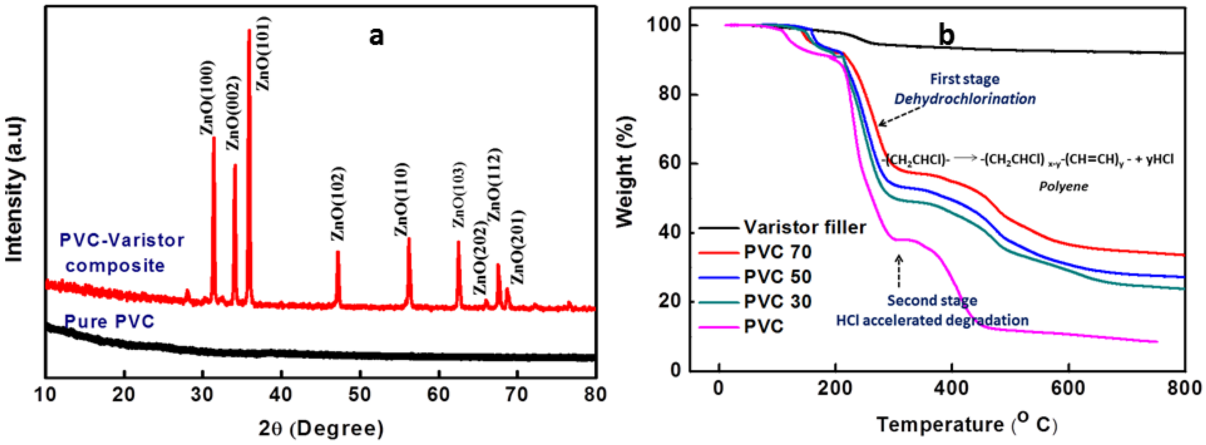

Figure 6.12: (a) XRD spectra and (b) thermo gravimetric analysis of varistor filler, PVC, and PVC/MV composites

filler, pure PVC, and PVC/MV composites are plotted in Figure 6.12 (b). At lower temperature the TGA curve of MV filler showed a minor weight loss (~7%) due to the loss of physically bound water on the surface of MV filler. For pure PVC, the weight loss caused by the degradation of PVC chain which takes place in two stages. The first stage decomposition which extends up to 300 ^{o}C is attributed to the dehydrochlorination of PVC, leaving behind conjugated polyene structures [90]. The second stage degradation that extends up to 750 ^{o}C the PVC degradation is further accelerated by the HCl evolved in the first stage degradation. It involves the decomposition of the polyene backbone structures and liberation of many aromatic compounds such as benzene and toluene [90, 91]. The TGA curves of PVC/MV composites also showed a similar weight loss pattern as that of pure PVC. With the addition of MV filler the onset decomposition temperature of PVC composite increased and the temperature corresponding to maximum degradation was also shifted to higher temperature. By the addition of inorganic filler, the oxidative tendency of the PVC chain is restricted and further decomposition is retarded [91]. Thus, for PVC polymer, MV filler acts as a co-stabilizer. The rate of mass loss of PVC/MV composite reduced significantly with increase in filler loading. This decreased mass loss is induced by the addition of inorganic particle which enhanced the thermal stability of polymer by impeding the out-diffusion of the volatile decomposition products and also by preventing the oxygen diffusion into the polymer matrix [92, 93]. Good dispersion and increased loading of MV filler in the PVC matrix forms a more effective obstacle to impede the progress of the degradation process of the composites.

6.2.4.4 Microstructural Analysis of PVC Composites

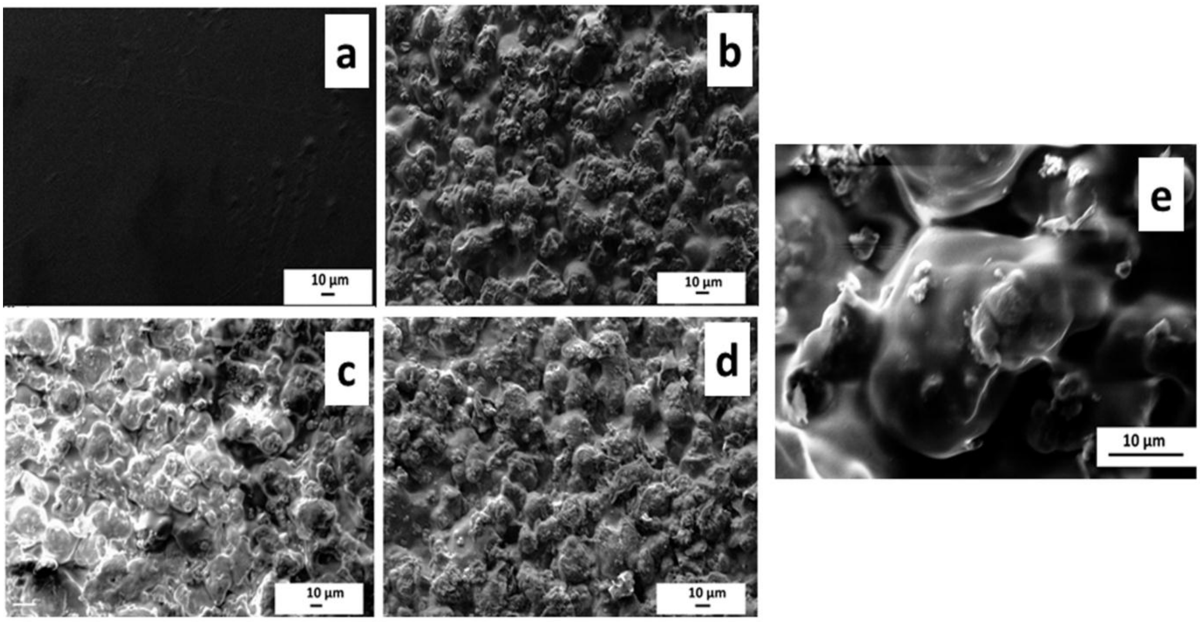

Figure 6.13: SEM images of surface of PVC/MV composites. (a) PVC 0, (b) PVC 30, (c) PVC 50, (d) PVC 70, and (e) PVC 30 at higher magnification.

Figure 6.13 (a–d) shows the SEM images of surface of pure PVC and PVC/MV composite films for different % of filler loading. The microstructure of pristine PVC reveals plane surface (Figure 6.13 (a)). With the addition of MV filler to PVC matrix, the microstructure analysis revealed rough surface and the roughness increased with increase in the filler content. Figure 6.13 (e) showed the higher magnification image of surface microstructure of PVC/MV composite film with 30 wt % filler loading. It reveals the good blending and proper interaction between matrix and MV filler particle.

6.2.4.5 Dielectric Characteristics

The frequency dependent variation of dielectric permittivity (ε_r) and loss tangent (tan δ) of the PVC/MV composites having different wt % MV filler were carefully investigated at room temperature (32 ^{o}C) and the results are given in Figure 6.14 (a) and (b). It is clear from the plots that all the PVC/MV compositions showed obviously improved dielectric properties compared with pure PVC in the frequency ranges (300 Hz to 3 MHz). The dielectric permittivity of PVC and PVC/MV composites was less dependent on frequency. As the frequency increases from 300 Hz to 3 MHz, for pure PVC the dielectric permittivity remains almost unaffected and for composite (PVC 70) dielectric permittivity is slightly decreased from 40 to 37. Thus with filler loading both dielectric permittivity and loss tangent shows an increasing tendency. At 1 MHz, the dielectric permittivity is increase to 37 for 70 % filler loading from a value 3 for pure PVC.

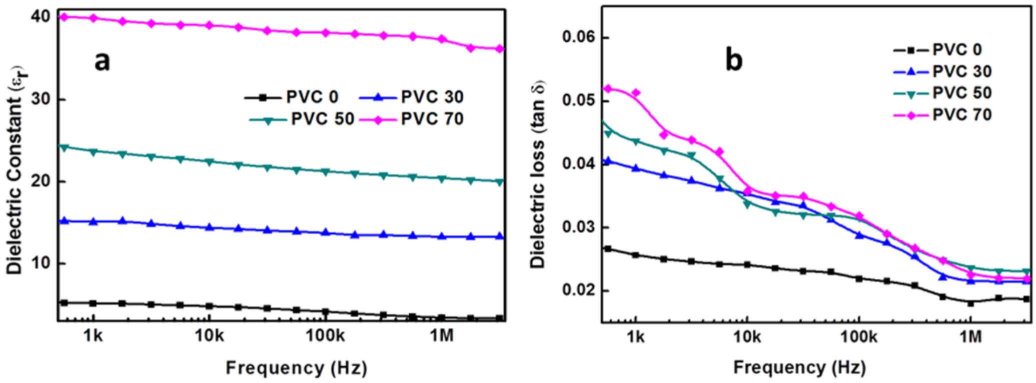

Figure 6.14: (a) Variation of dielectric permittivity and (b) dielectric loss with frequency for PVC/MV composites.

The increased dipole-dipole interaction in PVC/MV composite with the addition of MV filler leads to improved dielectric properties for PVC/MV composites. Due to the polarization at the interface (Maxwell–Wagner–Sillars effect) [94] the accumulated charge will be more in the case of PVC/MV composites. This will be an extra contribution to the amount of charge stored on either side of the sample surface and resulted in increase in the dielectric constant of PVC/MV composites. Thus, with the increase in the filler addition, the finer MV particle create large interface with PVC matrix and offer higher polarization effect to the composites. From SEM image [Figure 6.13 (a–d)] of PVC/MV composite, it is clear that the MV particles are homogeneously dispersed in the PVC matrix. Each filler particles are separated by an insulating layer of polymer matrix which act as a barrier layer between MV particles. This keeps the dielectric loss of PVC/MV composites at a relatively low level. Initially, at lower frequencies the dielectric loss decreases and at higher frequencies it is less dependent of frequency. At frequency 1 MHz, the dielectric loss was in the range 0.01–0.02 with increasing filler loading from 0–70 wt %. As the loading of MV filler increases the inter particle distance gets reduced and promote the electron tunnelling between the adjacent MV particle which in turn increases the dielectric loss.

6.2.4.6 Conductivity of the PVC/MV Composites

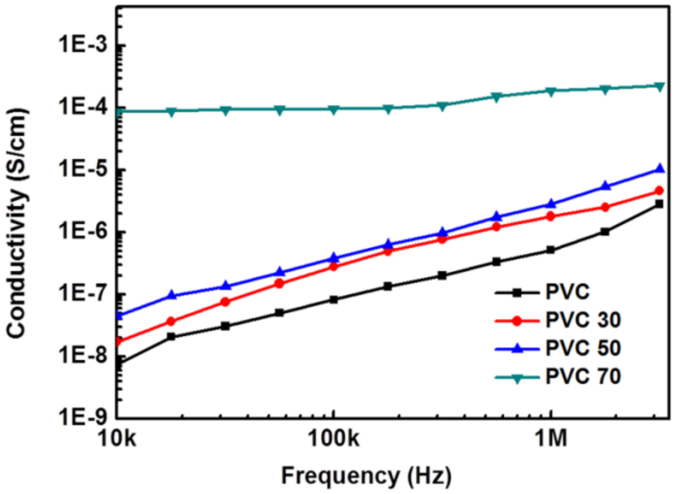

Figure 6.15: The variation of conductivity with frequency of PVC/MV composite for different loadings of MV particle.

The variation of conductivity of the PVC/MV composites as a function of the frequency for different filler loading is presented in Figure 6.15. The conductivity of the PVC/MV composites increases with increasing frequency, indicating the typical insulating behaviour of PVC/MV composites [95]. The formation of a continuous electrical conducting path due to the development of connection network between MV particles in the composites resulted from the increase in filler loading.

The variation of conductivity of PVC/MV composite for different filler loading is represented in Figure 6.16. The conductivity of the composite varies from 2.2 X 10^{-6} to 3.8 X 10^{-4} S.cm^{-1} as the filler loading increased from 0 to 70 wt %. Beyond 70 wt % loading of varistor filler in PVC matrix there is no significant change in conductivity of composite with frequency (linear dependency with the frequency). Hence, the electrical percolation is attained at 70 wt % loading of MV filler.

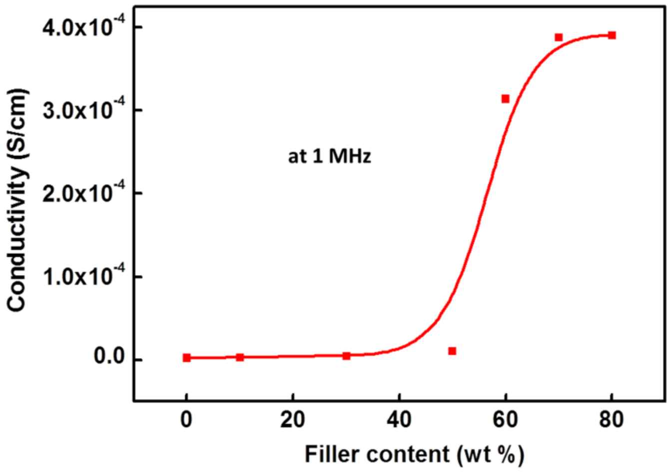

Figure 6.16: Variation of conductivity with loading of MV fillers.

6.2.4.7 Mechanical Properties of PVC/MV Composites

Along with the electronic properties, mechanical properties of PVC/MV composites are also an important prerequisite for various electronic applications. The tensile strength and elongation at break for pure PVC and PVC composites at different loading are measured and the results are shown in Figure 6.17 (a). The tensile strength and elongation at break of PVC composite did not show any drastic changes compared to pure PVC. Thus, by the MV filler addition the mechanical properties of PVC were not significantly affected. The enhancement in toughness of PVC composite resulted from the crack deflection induced by filler particle. The MV filler particle in PVC matrix forces the crack propagation in an irregular path leading to increased plastic deformation and rough fracture surface.

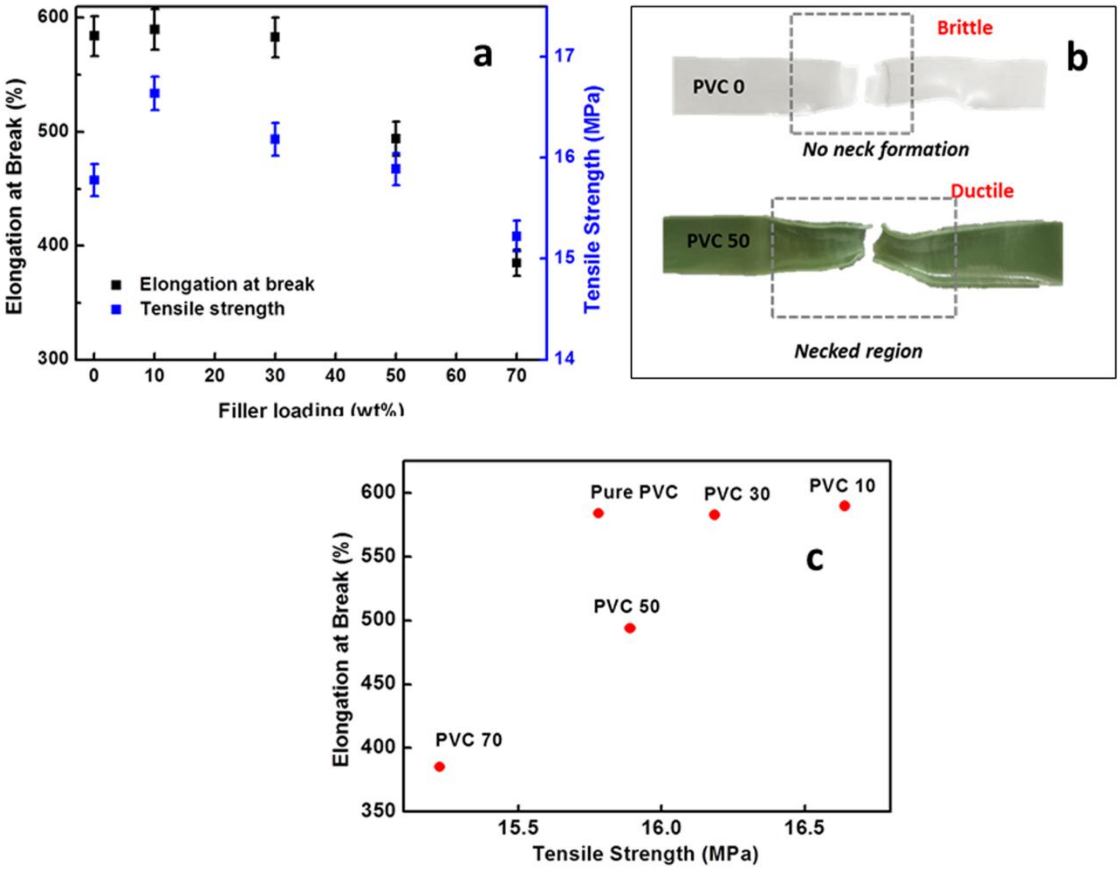

Figure 6.17: (a) Variation of tensile strength and elongation at break of PVC/MV composites with filler loading, (b) photographs of PVC 0 and PVC 50 of fractured surface samples after tensile test, and (c) variation of elongation at break with tensile strength for PVC/MV composite.

The tensile strength obtained for 10 wt % MV loading was16 MPa. Further increase in filler loading shows a decreasing trend in tensile strength value (15 MPa).

However, up to 50 wt % loading of MV filler, the tensile strength obtained for PVC composite was higher than that of pure PVC. Beyond 50 wt % increase in filler loading resulted in the lower tensile strength of PVC/MV composite than that of pure PVC. The same trend was observed for the elongation at break of PVC/MV composite with filler loading. With increase in filler loading, more surface area become available for the interaction between filler particles and PVC matrix and resulted in good interfacial adhesion between filler and matrix. However, the optimum filler loading observed was at 30 wt % beyond which the dilution effect was found to take place. The filler particles were no longer properly dispersed or wetted by the matrix phase, thus the tensile strength is reduced beyond 30 wt % loading of filler particle in PVC matrix.

The photographic image of the fractured samples after tensile test of PVC 0 and PVC 50 were presented in Figure 6.17 (b). For the sample PVC 0, during fracturing no neck formation was observed which clearly indicate the brittle fracture of PVC. In the case of PVC composite (PVC 50), neck formation during fracturing of samples was observed at both ends of the fractured surfaces of the sample. This is a clear indication of transition of PVC from brittle to ductile fracture with MV filler loading. Figure 6.17(c) presents the variation of elongation break with tensile strength for different PVC/MV composites.

Figure 6.18 (a–d) represent the SEM images of the fracture surface after tensile test of PVC and PVC/MV composite with 30, 50, and 70 wt % filler loading respectively. Figure 6.18 (a) clearly shows the brittle fracture pure PVC; but the PVC/MV composite showed ductile characteristics at the broken surface Figure 6.18 (c)-(d). A lot of dimples and long tearing edges were present at the fracture surfaces of all compositions. For PVC with 30 wt % loading longer tearing edges were observed compared to other compositions due to the adequate wetting or interaction of filler particle with polymer matrix.

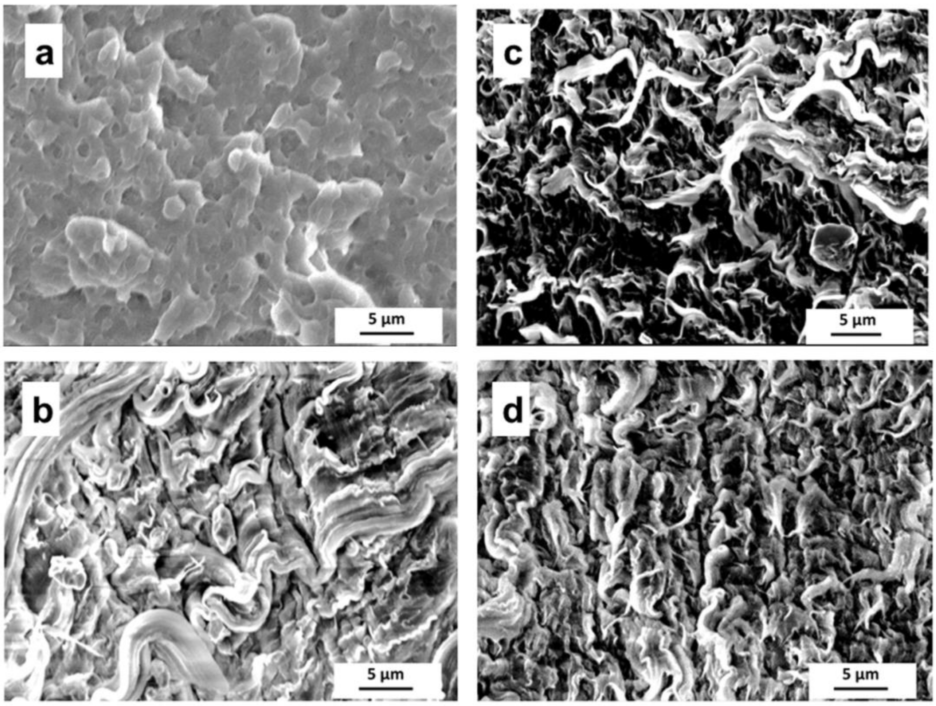

Figure 6.18: SEM images of fracture surface of (a) PVC 0, (b) PVC 30, (c) PVC 50, and (d) PVC 70.

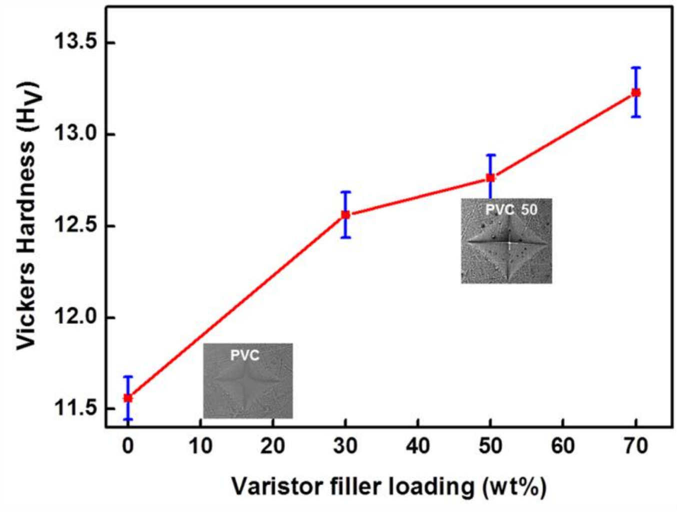

Figure.6.19: The variation of microhardness of PVC/MV composite (optical images of the indentation mark for PVC and PVC 50 are given as insets).

The variation of microhardness of the PVC composite with MV filler addition was studied and the results are presented in Figure 6.19. A load of 25 gf was applied for a dwell time of 14 s on finely polished samples. It was observed that the microhardness of the PVC/MV composites was found to increase linearly with an increase in loading. Only marginal increase (11.55–13.22 Hv) in the hardness value of the composites were observed. The relatively small increase in hardness value for PVC composites was due to the inherent soft nature of ZnO MV filler.

6.2.4.8 UV Shielding Properties of PVC/MV Composites and Mechanical Properties after UV Irradiation

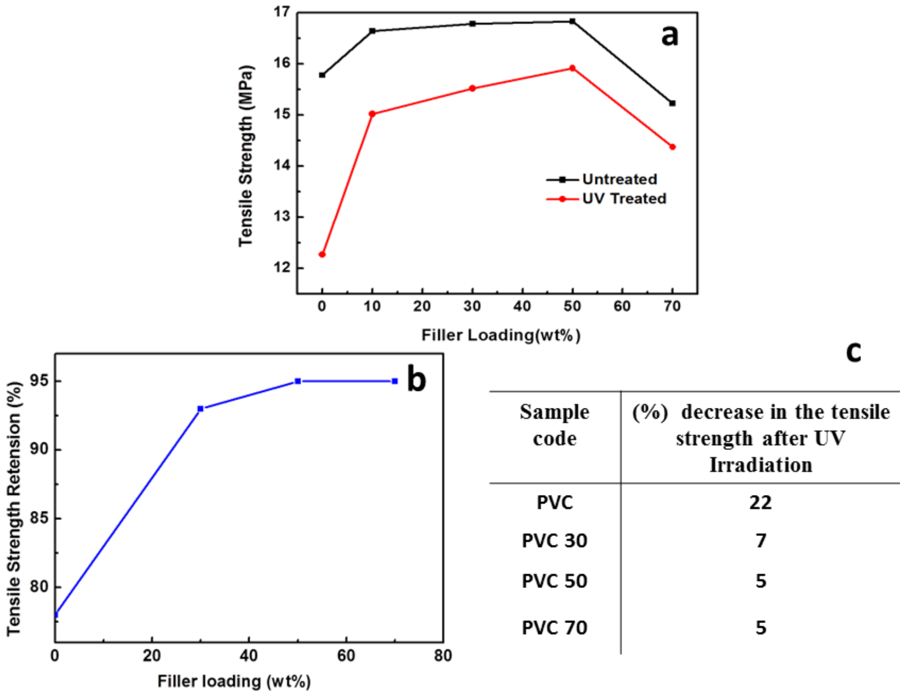

Sample code	(%) decrease in the tensile strength after UV Irradiation
PVC	22
PVC 30	7
PVC 50	5
PVC 70	5

Figure 6.20: (a) Variation of tensile strength of PVC/MV composite with filler loading before and after UV irradiation, (b) Tensile strength retention of PVC/ MV composite after UV treatment, and (d) decrease (%) in tensile strength of PVC/ MV composite after UV irradiation.

Wavelengths in the range 310–320 nm are considered as especially harmful to PVC and its composites [83]. When the MV filler particle is incorporated into PVC, a considerable share of UV light is absorbed by the MV particle which reduces the efficiency of excitation of polymer matrix compared to pure PVC.

It is well documented that inorganic fillers, such as ZnO, $CaCO_3$, and TiO_2 particles, can be used as UV light screening agents in polymer matrix [65, 96]. Between polymer matrix and light source, the UV active filler particle forms a barrier and thus prevents the polymer from photo degradation. The UV resistance of PVC/MV composite was evaluated by measuring the tensile strength of composite film after UV irradiation. Figure 6.20 (a) presents the tensile strength variation with filler loading before and after UV treatment. The effect of UV light on mechanical properties of composite film was reduced with increase in filler loading.

From the Figure 6.20 (b) it is well clear that after 12 h of UV irradiation, PVC/MV composite keeps better retention of tensile strength compared to pure PVC. In case of pure PVC during UV irradiation, the dechlorination of PVC results in the formation of chromophoric groups like conjugated double bond [96]. The percentage of tensile strength retention after UV irradiation of PVC/MV composite is presented in Figure 6.20 (b). After UV irradiation, 25 % decrease in the tensile strength for pure PVC was observed. This can be attributed to the effective scission process and the subsequent embrittlement that occurs to the PVC during the exposure of the UV radiation in oxygen atmosphere. With increase in filler loading the reduction in tensile strength is reduced below 10 %. It is remarkable that for the 50 % loaded sample the reduction is observed below 5 %. The decrease (%) in tensile strength of PVC/ MV composite film after UV irradiation is given in Figure 6.20 (c). Thus, MV particle in PVC matrix act as a bypass for the UV radiation and extend improved antiaging properties to PVC/MV composites.

6.2.5 Conclusions

A novel flexible PVC composite with nonlinear resistive MV particle as multifunctional filler was fabricated *via* simple solution casting technique. Systematic analysis of PVC/MV composites showed that the MV filler were uniformly distributed in the polymer matrix and resulting in good micro scale level compatibility with PVC matrix. The incorporation of MV filler in PVC matrix resulted in a dielectric constant of 37 without any drastic change in the dielectric loss (0.05). The thermal stability analysis of PVC composite clearly showed a significant improvement in the initial decomposition temperature and the temperature corresponding to maximum degradation is shifted to higher temperature with increase in filler loading. The excellent dispersion of MV particle in PVC resulted in mechanically stable PVC composite with no significant reduction either in tensile strength or in elongation at break with filler loading. The PVC/MV composite showed good UV resistance compared to pure PVC. This can be attributed to the fact that the MV particle effectively absorbs UV radiation especially in the wavelength range 310–320 nm, which is particularly harmful to PVC. After aging under UV light, the tensile strength has been retained more effectively in PVC/MV composites (95 % retention for 50 wt % loading) than in unfilled one (77 % retention). The combination of tunable dielectric properties along with mechanical robustness and thermal stability makes PVC/MV composites a potential candidate for electronic industry.

References

[1] Anas, S., Mahesh, K.V., Jobin, V., Prasanth, S. and Ananthakumar, S. "Nanofillers in ZnO based materials: a ‘smart’technique for developing miniaturized high energy field varistors." *Journal of Materials Chemistry C* 1.39 (2013): 6455-6462.

[2] Pillai, S.C., Kelly, J.M., McCormack, D.E. and Ramesh, R. "High performance ZnO varistors prepared from nanocrystalline precursors for miniaturised electronic devices." Journal of Materials Chemistry 18.33 (2008): 3926-3932.

[3] Pillai, S.C., Kelly, J.M., Ramesh, R. and McCormack, D.E. "Advances in the synthesis of ZnO nanomaterials for varistor devices." Journal of Materials Chemistry C 1.20 (2013): 3268-3281.

[4] Baraki, R., Zierep, P., Erdem, E., Weber, S. and Granzow, T. "Electron paramagnetic resonance study of ZnO varistor material." Journal of Physics: Condensed Matter 26.11 (2014): 115801.

[5] Anas, S., Metz, R., Sanoj, M.A., Mangalaraja, R.V. and Ananthakumar, S. "Sintering of surfactant modified ZnO–Bi_2O_3 based varistor nanopowders." Ceramics International 36.8 (2010): 2351-2358.

[6] Rahul, S.P., Mahesh, K.V., Sujith, S.S., Jeen Maria M. and S. Ananthakumar, s. Processing of La2O3 based rare earth non-linear resistors via combustion synthesis, Journal of Electroceramics. 32.4 (2013): 292–300.

[7] Matsuoka, M. "Nonohmic properties of zinc oxide ceramics." Japanese Journal of Applied Physics 10.6 (1971): 736.

[8] Einzinger, R. "Metal oxide varistors." *Annual Review of Materials Science* 17.1 (1987): 299-321.

[9] Metz, R., Delalu, H., Vignalou, J.R., Achard, N. and Elkhatib, M. "Electrical properties of varistors in relation to their true bismuth composition after sintering." *Materials Chemistry and Physics* 63.2 (2000): 157-162.

[10] Peiteado, M., Fernandez, J.F. and Caballero, A.C. Varistors based in the ZnO–Bi_2O_3 system: microstructure control and properties." *Journal of the European Ceramic Society* 27.13-15 (2007): 3867-3872.

[11] Oliveira, M.M., Bueno, P.R., Longo, E. and Varela, J.A. "Influence of La_2O_3, Pr_2O_3 and CeO_2 on the nonlinear properties of SnO_2 multicomponent varistors." *Materials chemistry and physics* 74.2 (2002): 150-153.

[12] Pillai, S.C., Kelly, J.M., McCormack, D.E., O'Brien, P. and Ramesh, R. "The effect of processing conditions on varistors prepared from nanocrystalline ZnO." *Journal of Materials Chemistry* 13.10 (2003): 2586-2590.

[13] Banerjee, A., Ramamohan, T.R. and Patni, M.J. "Smart technique for fabrication of zinc oxide varistor." *Materials research bulletin* 36.7-8 (2001): 1259-1267.

[14] Cheng, L.H., Zheng, L.Y., Meng, L., Li, G.R., Gu, Y., Zhang, F.P., Chu, R.Q. and Xu, Z.J. "Electrical properties of Al_2O_3-doped ZnO varistors prepared by sol–gel

process for device miniaturization." *Ceramics International* 38 (2012): S457-S461.

[15] Dong, X.U., JIANG, B., Lei, J., CUI, F.D., XU, H.X., YANG, Y.T., YU, R.H. and CHENG, X.N. "Sol–gel synthesis of Y2O3-doped ZnO thin films varistors and their electrical properties." *Transactions of Nonferrous Metals Society of China* 22 (2012): s110-s114.

[16] Anas, S., Mangalaraja, R.V., Poothayal, M., Shukla, S.K. and Ananthakumar, S. "Direct synthesis of varistor-grade doped nanocrystalline ZnO and its densification through a step-sintering technique." *Acta Materialia* 55.17 (2007): 5792-5801.

[17] Gupta, T.K. "Application of zinc oxide varistors." *Journal of the American Ceramic Society* 73.7 (1990): 1817-1840

[18] Viswanath, R.N., Ramasamy, S., Ramamoorthy, R., Jayavel, P. and Nagarajan, T. "Preparation and characterization of nanocrystalline ZnO based materials for varistor applications." *Nanostructured Materials* 6.5-8 (1995): 993-996.

[19] Pillai, S.C., Kelly, J.M., McCormack, D.E. and Ramesh, R. "Microstructural analysis of varistors prepared from nanosize ZnO." Materials science and technology 20.8 (2004): 964-968.

[20] Shojaee, S.A., Shahraki, M.M., Sani, M.A.F., Nemati, A. and Yousefi, A "Microstructural and electrical properties of varistors prepared from coated ZnO nanopowders." Journal of Materials Science: Materials in Electronics 21.6 (2010): 571-577.

[21] Nahm, C.W. "Electrical properties and stability of praseodymium oxide-based ZnO varistor ceramics doped with Er_2O_3." *Journal of the European Ceramic Society* 23.8 (2003): 1345-1353.

[22] Pillai, S.C., Kelly, J.M., McCormack, D.E. and Ramesh, R. "Effect of step sintering on breakdown voltage of varistors prepared from nanomaterials by sol gel route." *Advances in applied ceramics* 105.3 (2006): 158-160.

[23] Ji-le, L., Chen, G.H. and Yuan, C.L. "Microstructure and electrical properties of rare earth doped ZnO-based varistor ceramics." Ceramics International 39.3 (2013): 2231-2237.

[24] Ya, K.X., Diao, W.T., Han, Y., De, T.M. and Jing, T.M. "Sol-gel process doped ZnO nanopowders and their grain growth." Materials research bulletin 32.9 (1997): 1165-1171.

[25] Bai, S.N., Shieh, J.S. and Tseng, T.Y. "Characteristic analysis of ZnO varistors made with spherical precipitation powders." *Materials chemistry and physics* 41.2 (1995): 104-109.

[26] Hembram, K., Sivaprahasam, D. and Rao, T.N. "Combustion synthesis of doped nanocrystalline ZnO powders for varistors applications." *Journal of the European Ceramic Society* 31.10 (2011): 1905-1913.

[27] Westin, G., Ekstrand, Å., Nygren, M., Österlund, R. and Merkelbach, P. "Preparation of ZnO-based varistors by the sol–gel technique." *Journal of Materials Chemistry* 4.4 (1994): 615-621.

[28] Haile, S.M., Johnson, D.W., Wiseman, G.H. and Bowen, H.K. "Aqueous precipitation of spherical zinc oxide powders for varistor applications." *Journal of the American Ceramic Society* 72.10 (1989): 2004-2008.

[29] Alles, A.B. and Burdick, V.L. "The effect of liquid-phase sintering on the properties of Pr6O11-based ZnO varistors." *Journal of applied physics* 70.11 (1991): 6883-6890

[30] Furtado, J.G.D.M., Saléh, L.A., Serra, E.T., Oliveira, G.S.G.D. and Nóbrega, M.C.D.S. "Microstructural evaluation of rare-earth-zinc oxide-based varistor ceramics." Materials Research 8.4 (2005): 425-429.

[31] Chun, S.Y. and Mizutani, N. "Mass transport via grain boundary in Pr-based ZnO varistors and related electrical effects." *Materials Science and Engineering: B* 79.1 (2001): 1-5.

[32] Nahm, C.W., Park, C.H. and Yoon, H.S. "Highly stable nonohmic characteristics of ZnO-Pr_6O_{11}-CoO-Dy_2O_3 based varistors." *Journal of materials science letters*19.9 (2000): 725-727.

[33] Lee, Y.S. and Tseng, T.Y. "Phase identification and electrical properties in ZnO–glass varistors." *Journal of the American Ceramic Society* 75.6 (1992): 1636-1640

[34] Nahm, C.W. "La_2O_3 Addition Influence on Electrical Characteristics of Pr_6O_{11}-based ZnO Varistors." *Transactions on Electrical and Electronic Materials* 7.3 (2006): 123-128.

[35] Mukae, K. "Zinc Oxide Varistors with Praseodymium Oxide." AM. CERAM. SOC. BULL. Am. Ceram. Soc. Bull. 66.9 (1987): 1329.

[36] Ashraf, M.A., Bhuiyan, A.H., Hakim, M.A. and Hossain, M.T. "Microstructure and electrical properties of Sm_2O_3 doped Bi_2O_3-based ZnO varistor ceramics." Materials Science and Engineering: B 176.11 (2011): 855-860.

[37] Hongyu, L., Hui, K., Dongmei, J., Wangzhou, S. and Xueming, M. "Microstructure and electrical properties of Er_2O_3-doped ZnO-based varistor ceramics prepared by high-energy ball milling." Journal of rare earths 25.1 (2007): 120-123.

[38] Xu, D., Song, K., Li, Y., Jiao, L., Zhong, S., Ma, J., Bao, L., Zhang, L. and Song, J. "Sc_2O_3 doped Bi_2O_3-ZnO thin films varistor prepared by sol-gel method." Journal of Alloys and Compounds 746 (2018): 314-319.

[39] Liu, H., Ma, X., Jiang, D. and Shi, W. "Microstructure and electrical properties of $Y2O_3$-doped ZnO-based varistor ceramics prepared by high-energy ball milling." *Journal of University of Science and Technology Beijing, Mineral, Metallurgy, Material* 14.3 (2007): 266-270.

[40] Houabes, M. and Metz, R. "Rare earth oxides effects on both the threshold voltage and energy absorption capability of ZnO varistors." *Ceramics International* 33.7 (2007): 1191-1197.

[41] Cao, Z.C., Zheng, L.Y., Cheng, L.H., Tian, T. and Li, G.R. "Influence of CeO_2-Doping on the Electrical Properties of ZnO-Bi2O3-Based Varistor Ceramics." *Key Engineering Materials*. Vol. 697. Trans Tech Publications, 2016.

[42] Shichimiya, S., Yamaguchi, M., Furuse, N., Kobayashi, M. and Ishibe, S. "Development of advanced arresters for GIS with new zinc-oxide elements." IEEE Transactions on power Delivery 13.2 (1998): 465-471.

[43] Nahm, C.W. and Park, C.H. "Microstructure, electrical properties, and degradation behavior of praseodymium oxides-based zinc oxide varistors doped with Y_2O_3." Journal of Materials Science 35.12 (2000): 3037-3042

[44] Lei, M., Li, S., Jiao, X., Li, J. and Alim, M.A. "The influence of CeO_2 on the microstructure and electrical behaviour of ZnO–Bi_2O_3 based varistors." *Journal of Physics D: Applied Physics* 37.5 (2004): 804.

[45] Jiang, F., Peng, Z., Zang, Y. and Fu, X. "Progress on rare-earth doped ZnO-based varistor materials." Journal of Advanced Ceramics 2.3 (2013): 201-212.

[46] Haque, N., Hughes, A., Lim, S. and Vernon, C. "Rare earth elements: Overview of mining, mineralogy, uses, sustainability and environmental impact." *Resources* 3.4 (2014): 614-635.

[47] Kutty, T.R.N. and Ezhilvalavan, S. "The role of silica in enhancing the nonlinearity coefficients by modifying the trap states of zinc oxide ceramic varistors." Journal of Physics D: Applied Physics 29.3 (1996): 809.

[48] Antonov, M. and Hussainova, I. "Thermophysical properties and thermal shock resistance of chromium carbide based cermets." *Proc. Estonian Acad. Sci. Eng* 12.4 (2006): 358-367.

[49] Clarke, D. R. "Varistor ceramics." *Journal of the American Ceramic Society* 82.3 (1999): 485-502.

[50] Bueno, P.R., Varela, J.A. and Longo, E. "SnO_2, ZnO and related polycrystalline compound semiconductors: an overview and review on the voltage-dependent resistance (non-ohmic) feature." *Journal of the European Ceramic Society* 28.3 (2008): 505-529.

[51] Li, Q., Chen, L., Gadinski, M.R., Zhang, S., Zhang, G., Li, H.U., Iagodkine, E., Haque, A., Chen, L.Q., Jackson, T.N. and Wang, Q. "Flexible high-temperature dielectric materials from polymer nanocomposites." *Nature* 523.7562 (2015): 576.

[52] Deepa, K.S., Shaiju, P., Sebastian, M.T., Gowd, E.B. and James, J. "Poly (vinylidene fluoride)–La 0.5 Sr 0.5 CoO 3− δ composites: the influence of LSCO particle size on the structure and dielectric properties." *Physical Chemistry Chemical Physics* 16.32 (2014): 17008-17017.

[53] Zhou, Y., Han, S.T., Xu, Z.X., Yang, X.B., Ng, H.P., Huang, L.B. and Roy, V.A.L. "Functional high-k nanocomposite dielectrics for flexible transistors and inverters with excellent mechanical properties." *Journal of Materials Chemistry* 22.28 (2012): 14246-14253.

[54] Priyanka, K.P. and Sunny, J. "Dielectric properties and ac conductivity of nanocrystalline titania." *J. Basic Appl. Phys* 2 (2013): 105-108.

[55] Arbatti, M., Shan, X. and Cheng, Z.Y. "Ceramic–polymer composites with high dielectric constant." Advanced Materials 19.10 (2007): 1369-1372.

[56] Feng, Y., Li, W.L., Wang, J.P., Yin, J.H. and Fei, W.D. "Core–shell structured BaTiO 3@ carbon hybrid particles for polymer composites with enhanced

dielectric performance." Journal of Materials Chemistry A 3.40 (2015): 20313-20321.

[57] Pleşa, I., Noţingher, P.V., Schlögl, S., Sumereder, C. and Muhr, M. "Properties of polymer composites used in high-voltage applications." *Polymers* 8.5 (2016): 173.

[58] Barber, P., Balasubramanian, S., Anguchamy, Y., Gong, S., Wibowo, A., Gao, H., Ploehn, H.J. and Zur Loye, H.C. "Polymer composite and nanocomposite dielectric materials for pulse power energy storage." *Materials*2.4 (2009): 1697-1733.

[59] Ram, R., Rahaman, M. and Khastgir, D. "Mechanical, electrical, and dielectric properties of polyvinylidene fluoride/short carbon fiber composites with low-electrical percolation threshold." *Journal of Applied Polymer Science* 131.3 (2014)

[60] Dang, Z.M., Yuan, J.K., Zha, J.W., Zhou, T., Li, S.T. and Hu, G.H. "Fundamentals, processes and applications of high-permittivity polymer–matrix composites." Progress in Materials Science 57.4 (2012): 660-723.

[61] Ning, N., Bai, X., Yang, D., Zhang, L., Lu, Y., Nishi, T. and Tian, M. "Dramatically improved dielectric properties of polymer composites by controlling the alignment of carbon nanotubes in matrix." *RSC Advances* 4.9 (2014): 4543-4551.

[62] Hassan, A., Akbari, A., Hing, N.K. and Ratnam, C.T. "Mechanical and thermal properties of ABS/PVC composites: Effect of particles size and surface treatment of ground calcium carbonate." *Polymer-Plastics Technology and Engineering* 51.5 (2012): 473-479.

[63] Zhou, Y., Han, S.T., Xu, Z.X., Yang, X.B., Ng, H.P., Huang, L.B. and Roy, V.A.L. "Functional high-k nanocomposite dielectrics for flexible transistors and inverters with excellent mechanical properties." *Journal of Materials Chemistry* 22.28 (2012): 14246-14253.

[64] Bai, Y., Cheng, Z.Y., Bharti, V., Xu, H.S. and Zhang, Q.M. "High-dielectric-constant ceramic-powder polymer composites." *Applied Physics Letters* 76.25 (2000): 3804-3806.

[65] Abdul Nabi, M., Yusop, R.M., Yousif, E., Abdullah, B.M., Salimon, J., Salih, N. and Zubairi, S.I. "Effect of nano ZnO on the optical properties of poly (vinyl chloride) films." *International Journal of Polymer Science* 2014 (2014).

[66] Unar, I.N., Soomro, S.A. and Aziz, S. "Effect of various additives on the physical properties of polyvinylchloride resin." Pakistan Journal of Analytical & Environmental Chemistry 11.2 (2010): 7.

[67] Deshmukh, S.P., Rao, A.C., Gaval, V.R., Joseph, S. and Mahanwar, P.A. "Effect of particle size and concentration on mechanical and electrical properties of the mica filled PVC." *Journal of Minerals and Materials Characterization and Engineering* 9.09 (2010): 831.

[68] Schiller, M. *PVC additives: performance, chemistry, developments, and sustainability*. Carl Hanser Verlag GmbH Co KG, 2015.

[69] Awad, W.H., Beyer, G., Benderly, D., Ijdo, W.L., Songtipya, P., del Mar Jimenez-Gasco, M., Manias, E. and Wilkie, C.A. "Material properties of nanoclay PVC composites." Polymer 50.8 (2009): 1857-1867.

[70] Fang, Y., Wang, Q., Guo, C., Song, Y. and Cooper, P.A. "Effect of zinc borate and wood flour on thermal degradation and fire retardancy of polyvinyl chloride (PVC) composites." *Journal of Analytical and Applied Pyrolysis* 100 (2013): 230-236.

[71] Vadukumpully, S., Paul, J., Mahanta, N. and Valiyaveettil, S. "Flexible conductive graphene/poly (vinyl chloride) composite thin films with high mechanical strength and thermal stability." *Carbon* 49.1 (2011): 198-205.

[72] Liu, H., Dong, L., Xie, H., Wan, L., Liu, Z. and Xiong, C. "Ultraviolet light aging properties of PVC/$CaCO_3$ composites." *Journal of Applied Polymer Science* 127.4 (2013): 2749-2756.

[73] Starnes Jr, W. H. "Structural and mechanistic aspects of the thermal degradation of poly (vinyl chloride)." Progress in Polymer Science 27.10 (2002): 2133-2170.

[74] Tong, M., Chen, H., Yang, Z. and Wen, R. "The effect of Zn-Al-Hydrotalcites composited with calcium stearate and β-diketone on the thermal stability of PVC." *International journal of molecular sciences* 12.3 (2011): 1756-1766.

[75] Rosu, Dan, and P. M. Visakh, eds. *Photochemical Behavior of Multicomponent Polymeric-based Materials*. Springer International Publishing, 2016.

[76] Ogoshi, T. and Chujo, Y. "Synthesis of organic–inorganic polymer hybrids utilizing amphiphilic solvent as a compatibilizer." *Bulletin of the Chemical Society of Japan* 76.9 (2003): 1865-1871.

[77] Xu, W.B., Zhou, Z.F., Ge, M.L. and Pan, W.P. "Polyvinyl chloride/montmorillonite nanocomposites." Journal of Thermal Analysis and Calorimetry 78.1 (2004): 91-99.

[78] Xie, X.L., Liu, Q.X., Li, R.K.Y., Zhou, X.P., Zhang, Q.X., Yu, Z.Z. and Mai, Y.W. "Rheological and mechanical properties of PVC/$CaCO_3$ nanocomposites prepared by in situ polymerization." *Polymer* 45.19 (2004): 6665-6673.

[79] Cao, Y.M., Sun, J. and Yu, D.H. Preparation and properties of nano-Al_2O_3 particles/polyester/epoxy resin ternary composites. *Journal of Applied Polymer Science*, *83*(1), pp.70-77.

[80] Cho, S. and Choi, W. "Solid-phase photocatalytic degradation of PVC–TiO_2 polymer composites." *Journal of Photochemistry and Photobiology A: Chemistry*143.2-3 (2001): 221-228.

[81] Kim, S.H., Kwak, S.Y. and Suzuki, T. "Photocatalytic degradation of flexible PVC/TiO2 nanohybrid as an eco-friendly alternative to the current waste landfill and dioxin-emitting incineration of post-use PVC." *Polymer* 47.9 (2006): 3005-3016

[82] Liu, H., Dong, L., Xie, H., Wan, L., Liu, Z. and Xiong, C. "Ultraviolet light aging properties of PVC/CaCO3 composites." Journal of Applied Polymer Science 127.4 (2013): 2749-2756.

[83] Zhang, X., Pi, H. and Guo, S. The mechanism for inorganic fillers accelerating and inhibiting the UV irradiation aging behaviors of rigid poly (vinyl chloride). *Journal of Applied Polymer Science*, *122*(5), pp.2869-2875.

[84] O'Connor, I., Hayden, H., O'Connor, S., Coleman, J.N. and Gun'ko, Y.K. "Kevlar coated carbon nanotubes for reinforcement of polyvinylchloride." Journal of Materials Chemistry 18.46 (2008): 5585-5588.

[85] Zhao, X., Zhang, Q., Chen, D. and Lu, P. "Enhanced mechanical properties of graphene-based poly (vinyl alcohol) composites." *Macromolecules* 43.5 (2010): 2357-2363.

[86] Sivalingam, G., Karthik, R. and Madras, G. "Effect of metal oxides on thermal degradation of poly (vinyl acetate) and poly (vinyl chloride) and their blends." *Industrial & engineering chemistry research* 42.16 (2003): 3647-3653.

[87] Wang, Z., Nelson, J.K., Hillborg, H., Zhao, S. and Schadler, L.S. "Graphene oxide filled nanocomposite with novel electrical and dielectric properties." Advanced Materials 24.23 (2012): 3134-3137.

[88] Donzel, L., Greuter, F. and Christen, T. "Nonlinear resistive electric field grading Part 2: Materials and applications." *IEEE Electrical Insulation Magazine* 27.2 (2011).

[89] Maria, M.J., Balanand, S., Anas, S., Mohamed, A.P. and Ananthakumar, S. "Zn-dust derived ultrafine grained ZnO non-linear ceramic resistors via in-situ thermal oxidation of cermet reactant mixture." *Materials & Design* 92 (2016): 387-396.

[90] Endo, K. "Synthesis and structure of poly (vinyl chloride)." *Progress in Polymer science* 27.10 (2002): 2021-2054.

[91] Al-Sagheer, F.A. and Ahmad, Z. "PVC-silica hybrids: effect of sol–gel conditions on the morphology of silica particles and thermal mechanical properties of the hybrids." *Journal of sol-gel science and technology* 61.1 (2012): 229-235.

[92] Qin, H., Zhang, S., Zhao, C., Feng, M., Yang, M., Shu, Z. and Yang, S. "Thermal stability and flammability of polypropylene/montmorillonite composites." Polymer Degradation and Stability 85.2 (2004): 807-813.

[93] Dufresne, A. and Castano, J. "Polysaccharide nanomaterial reinforced starch nanocomposites: A review." *Starch‐Stärke* 69.1-2 (2017).

[94] Kuriakose, M., Longuemart, S., Depriester, M., Delenclos, S. and Sahraoui, A.H. "Maxwell-Wagner-Sillars effects on the thermal-transport properties of polymer-dispersed liquid crystals." *Physical Review E* 89.2 (2014): 022511.

[95] Barrau, S., Demont, P., Peigney, A., Laurent, C. and Lacabanne, C. "DC and AC conductivity of carbon nanotubes− polyepoxy composites." *Macromolecules* 36.14 (2003): 5187-5194.

[96] Unar, I.N., Soomro, S.A. and Aziz, S., "Effect of various additives on the physical properties of polyvinylchloride resin." *Pakistan Journal of Analytical & Environmental Chemistry* 11.2 (2010): 7

CHAPTER 7

Summary and Future Perspectives

7.1 Summary

The thrust for economic and environmental friendly production of nano ZnO from a cheap source is driven by its large scale applications in electronics, optoelectronics, pigments, paints, rubber industry, catalysis and agriculture.

The thesis entitled *"Investigations on the Evolution of Zn Dust into ZnO Nanostructures, Electroceramics and Polymer Matrix Composite Dielectrics"* has opened new avenues not only for the effective utilization of a partially neglected industrial by-product Zn dust but also for the bulk synthesis of high quality ZnO nanostructures and cermet architectures for technologically important electro ceramics and functional coatings.

In this chapter, the major conclusions derived from the various experiments carried out and the observations made in each working chapters are summarized. The highlights of the research accomplishment as well as the scientific and technological knowledge produced from the thesis are given below. The whole thesis is devoted for the efficient utilization of the low cost industrial by-product *Zn-dust.*

- **Processing of nano ZnO *via* aqueous mechanical oxidation of Zn dust:** The room temperature synthesis of nano ZnO *via* aqueous mechanical oxidation of Zn dust by employing mechanical milling was investigated first. By careful control of the milling parameters in aqueous medium, the micron sized Zn dust was found to be capable of producing nano ZnO without any catalyst, addition of chemical reagents and more importantly any further calcination reaction. The novel top-down approach reported in this study produced monocrystalline ZnO nanorods (aspect ratio ~ 5.2) in bulk. In addition to nano ZnO, production of H_2 gas also observed simultaneously by the catalyst free water splitting reaction. Thus the aqueous mechanical oxidation of Zn dust is a less expensive, facile and clean approach for the production of nano ZnO and H_2 gas. This mechanical approach seems to be a viable processing-route for today's industries which are looking for eco-friendly, effluent free, economical means to obtain bulk nano ZnO.

- **Evolution of nano ZnO *via* Surfactant assisted mechanical milling of Zn dust:** In the next stage of the thesis work, the role of surfactant was investigated on the evolution of ZnO nanostructures during top-down processing of Zn dust into nano ZnO. The surfactant (CTAB and PVP) assisted milling showed reduction in the particle size and agglomeration of nano ZnO during the synthesis *via* aqueous mechanical oxidation [48 h] of Zn dust followed by calcination at 450^oC. The evolution of thin circular plate like morphology without any agglomeration was observed for nano ZnO obtained when 10 wt % PVP was employed as surfactant. Interestingly, the nano ZnO produced *via* surfactant assisted milling resulted in fully sintered ZnO ceramics with exceptionally controlled microstructures. The sintering of cylindrical pellets of nano ZnO (obtained *via* 10 % PVP assisted milling) showed superior behaviour with 99 % theoretical density with grain size in the range 1.5-2 µm after sintering at 1200 ^oC/ 2 h. Since ultra-fine grained ZnO is technologically important for producing high energy varistors, the nano ZnO obtained from Zn dust has notable significance to produce high performance ZnO varistors. Further exploration of Zn dust derived ZnO varistors is taken for investigation in this thesis in subsequent chapters.
- **A comparative study on thermal oxidation of Zn dust in conventional route *vs* microwave assisted route**: The role of mechanical activation on the

morphological evolution of nano ZnO during thermal oxidation of Zn dust in conventional calcination as well as microwave assisted calcination routes was investigated systematically and the results are presented in a separate chapter. The ZnO seed layer developed on the surface of Zn dust in due course of milling accelerated the oxidation kinetics of Zn dust during thermal oxidation and resulted in a reduction of 100 ^{o}C is seen in the onset oxidation temperature of Zn dust. The conventional thermal oxidation at 1000 ^{o}C/ 2h of 72 h milled Zn dust resulted in the formation of nanowire having length of several tens of micrometre and multipods having legs with several micrometre lengths. In microwave assisted thermal oxidation, due to the ready absorption of microwave energy by the metallic Zn dust and graphite miture, the oxidation of mechanically activated Zn was seen within 15 min of microwave exposure reaction time. Compared to assorted morphology of nano ZnO obtained during conventional thermal oxidation, the microwave assisted thermal oxidation resulted in single morphology at a given experimental conditions. However, it was also seen that highly crystalline ZnO nanorod, tetrapod and multipod morphologies are possible under microwave assisted thermal oxidation when the reaction conditions are altered.

- **Application studies of Zn dust derived nano ZnO:** The Industrial application of nano ZnO obtained *via* thermal oxidation was tested for paint and coatings with corrosion resistance and NIR reflecting properties. A functional paint was prepared by dispersing the ZnO nanostructures processed in this study in naturally occurring organic resin; CNSL. The coating developed on glass substrate showed brown tinted transparent coating with the maximum NIR reflectance of 33 %. About 156% improvement in the corrosion resistance was also observed for the

Mg-alloy substrate coated with nano ZnO incorporated CNSL paint compared to the uncoated Mg-alloy surface.

- **Zn/ZnO cermet architecture for epoxy dielectrics**: Zn-ZnO cermet architecture was fabricated by simple heat treatment of raw Zn dust. The effect of Zn-ZnO cermet particles on the dielectric properties and thermal conductivity of epoxy composite was investigated. The epoxy composite incorporated with cermet particle (30 wt %) obtained at 500 ^oC/ 3h resulted in a dielectric constant of 102 and dielectric loss of 0.09 at 1 K Hz. The enhanced dielectric properties of epoxy/cermet composite were resulted from the duplex interfacial polarization induced by insulator-semiconductor interface and semiconductor-metal interface. The thermal conductivity was also found to be better because the thermal conductivity value of epoxy 0.18 $W.m^{-1}.K^{-1}$ was increased to 1.15 $W.m^{-1}\cdot K^{-1}$ with the addition of cermet filler. The excellent interfacial adhesion of cermet particle with epoxy matrix was favourable for heat dissipation in epoxy matrix. Thus the interface design in epoxy-cermet composite by controlling the metal to ceramic ratio of cermet particle introduces a new strategy for developing epoxy dielectric with enhanced thermal conductivity.
- **Fabrication of high performance ZnO varistor from metallic Zn *via* cermet route:** The evolution of ZnO varistor microstructure *via* cermet route with Zn dust as the starting material was compared with that of oxide route with commercial ZnO as the starting material. In cermet route the partial energy during heat treatment was utilized for oxidation of Zn dust. Thus the grain growth is suppressed to some extend and resulted in better varistor properties compared to oxide route derived sample. Out of different samples prepared the cermet route derived sample sintered at 1250 ^oC/ 2h showed best E–J characteristics with

markedly enhanced nonlinear properties, *viz.* V_b = 4778 V cm^{-1}, α = 38 and J_L = 0.01 μA cm^{-2} compared to its oxide route counterpart.

- **Fabrication of PVC composite incorporated with Zn dust derived microvaristor filler:** Flexible Poly (vinyl chloride) **(**PVC) composite films incorporated with micro-varistor (MV) filler was fabricated *via* solution casting method. The effect of Zn dust derived microvaristor filler on dielectric properties, mechanical and thermal stability and UV resistance behaviour of PVC composite film was systematically investigated by varying the filler loading. The microvaristor addition (0-70 wt %) resulted in dielectric constant tunability (ε = 2–37) without any significant change in the dielectric loss (0.02–0.05). The incorporation of microvaristor filler offer better UV resistance to PVC composite. After UV irradiation the PVC/MV composite showed 95 % retention of tensile strength where pure PVC showed 75 % retention of tensile strength. The addition of MV filler in PVC enhanced the microhardness but the enhancement was insignificant due to the soft nature of ZnO compared to other hard ceramics.

7.2 Future Perspectives

Some of the spin-off ideas generated during the course of research work which require further attention are given below.

- On-line production and storage of the H_2 gas during aqueous mechanical oxidation of Zn dust.
- A systematic look-out of the ZnO-CNSL paint coatings for NIR shielding window-glass without compromising the optical transparency. The studies may be extended further for developing antifouling coatings.
- The long length nanowire obtained during the thermal oxidation of Zn has a great potential for the fabrication of solar cell and sensors.

- Development of cermet varistor by the controlled heat treatment of metallic Zn can produce a new variety of thin film and flexible varistors.

List of Publications

Publications from the Thesis

[1] **Maria, M. Jeen**, S. Balanand, S. Anas, A. Peer Mohamed, and S. Ananthakumar. "Zn-dust derived ultrafine grained ZnO non-linear ceramic resistors via in-situ thermal oxidation of cermet reactant mixture." *Materials & Design* 92 (2016): 387-396

[2] Balanand, Santhosh, **Mathews Jeen Maria**, T. P. D. Rajan, A. Peer Mohamed, and S. Ananthakumar. "Bulk processing of ZnO nanostructures via microwave assisted oxidation of mechanically seeded Zn dust for functional paints and coatings." Chemical Engineering Journal 284 (2016): 657-667.

[3] **Mathews Jeen Maria,** Santhosh Balanand, Abdul Azeez Peer Mohamed, Solaiappan Ananthakumar. "Design and fabrication of flexible Polyvinyl Chloride dielectric composite reinforced with ZnO micro-varistors" Applied Polymer Science 135 (2018): 46031

[4] Santhosh Balanand, Kunnathuparambil Babu Babitha, **Mathews Jeen Maria,** Abdul Azeez Peer Mohamed and Solaiappan Ananthakumar. "Aqueous Mechanical Oxidation of Zn Dust: An inventive Technique for Bulk Production of ZnO Nanorods" ACS Sustainable Chemistry & Engineering 6(2018): 143−154.

[5] Enhanced dielectric properties of epoxy polymer composites induced by interface design *via* incorporation of Zn-ZnO cermet structures (Under preparation)

Publications Other than Thesis

[1] Rahul, Sasidharan Pillai, K. V. Mahesh, S. S. Sujith, **Mathews Jeen Maria**, and S. Ananthakumar. "Processing of La_2O_3 based rare earth non-linear resistors via combustion synthesis." **Journal of Electroceramics** 32, no. 4 (2014): 292-300.

Book Chapter

[1] Book: Sol-Gel Materials for Energy, Environment and Electronic Applications. Chapter: Anas, S., K. V. Mahesh, **M. Jeen Maria**, and S. Ananthakumar. "Sol-Gel Materials for Varistor Devices." In Sol-Gel Materials for Energy, Environment and Electronic Applications, pp. 23-59. Springer International Publishing, 2017.

Papers Presented in International/National Conferences

[1] **Jeen Maria Mathews**, K.P.Surendran and S. Ananthakumar "Rare Earth Doped ZnO Varistor Reinforced PVC Composites: - A Promising Field Grading Material for

High Voltage Applications" National conference on Material science and technology July 2015, IIST, Thiruvanandapuram, Kerala.

[2] **Jeen Maria Mathews**, Balanand Santhosh and S. Ananthakumar "Development of PVC Polymer Composite Reinforced with Non-Linear ZnO Micro Varistors Processed from Zn dust for High Performance Field Grading Application" NANO INDIA 2015 January 2015, SASTRA University, Thanjavur, Tamilnadu.

[3] **Jeen Maria Mathews**, Balanand Santhosh and S. Ananthakumar "Ultra Fine-Grained Zno Non-Linear Resistors from Metallic Zn-Dust" International Conference on Nano Science and Technology March 2014.

[4] **Jeen Maria Mathews,** Balanand Santhosh and S. Ananthakumar "Thermal Oxidation of Zn Dust and Fabrication of ZnO Varistors" NMAT-2013, November 2013 Thiruvanandapuram, Kerala. (Oral)